Title
Towards Grid-independent Dynamics in High-resolution Numerical Weather Prediction Models

Author
Simon, Jason Scot

Publication Date
2019

Peer reviewed|Thesis/dissertation

Towards Grid-independent Dynamics in High-resolution Numerical Weather Prediction Models

by

Jason Scot Simon

A dissertation submitted in partial satisfaction of the

requirements for the degree of

Doctor of Philosophy

in

Engineering – Civil and Environmental Engineering

in the

Graduate Division

of the

University of California, Berkeley

Committee in charge:

Professor Fotini Katopodes Chow, Chair
Professor Mark Stacey
Professor Dennis Baldocchi

Fall 2019

Towards Grid-independent Dynamics in High-resolution Numerical Weather Prediction Models

Abstract

Towards Grid-independent Dynamics in High-resolution Numerical Weather Prediction Models

by

Jason Scot Simon

Doctor of Philosophy in Engineering – Civil and Environmental Engineering

University of California, Berkeley

Professor Fotini Katopodes Chow, Chair

Since the beginning of numerical weather prediction (NWP), which was performed on $\mathcal{O}$(700 km) grids, advances in computing technology have driven corresponding advances in model resolution. In recent years, operational NWP efforts have reached $\mathcal{O}$(1 km) horizontal resolutions, leading to the use of large-eddy simulation (LES) to simulate the atmospheric boundary layer (ABL). However, the available turbulence closure models for atmospheric LES were designed to model the smallest scales of atmospheric turbulence, leaving operational forecasters and researches in many diverse fields alike without a turbulence model fit for the computing power available to them. This range of resolutions is known as the "gray zone" or *terra incognita* in the atmospheric turbulence literature, and will be the focus of much discussion in this dissertation. Further, the results will be presented in a way that is visual and digestible to a user of LES whose expertise is not necessarily in theoretical turbulence.

Here, the Weather Research and Forecasting (WRF) model is used to give a thorough and visual demonstration of the inadequacies of the more popular LES turbulence closure models, the Smagorinsky-Lilly and TKE-1.5 models, at gray-zone resolutions, and an explanation of the behavior is offered. Two alternatives, both with multiple flavors, the dynamic reconstruction model (DRM) and an alternative-anisotropic formulation of the classical eddy-viscosity models, are presented as potential remedies to the gray-zone issue. Studies are conducted first for an idealized free-convection case with constant surface heat flux and zero mean wind. A more realistic initial profile with an initial wind and geostrophic forcing is then considered. Finally, three more cases are considered with various surface heat flux values and initial wind profiles.

Both the DRM and alternative-anisotropic eddy-viscosity models are able to deliver much more consistent results at coarse resolutions when considering planar-averaged profiles of potential temperature and velocity, resolved velocity fields and resolved turbulent kinetic energy, and their performance inspires interesting topics of future work regarding the representation of

scales of energy in the atmosphere. The implementation of the anisotropic eddy-viscosity model in general, as well as the anisotropic Smagorinsky-Lilly model specifically, in the WRF model is also considered, resulting in a change in the WRF turbulent diffusion routines and a demonstration of improvement seen at coarse resolutions by reformulating the anisotropic Smagorinsky-Lilly model to partition stress terms into horizontal and vertical components. An additional chapter presents the gray zone problem as it relates to complex terrain.

To Papa.

Contents

Contents ii

List of Figures vi

List of Tables xv

1 Introduction 1
- 1.1 Notation . . . 1
- 1.2 Description and motivation . . . 2
- 1.3 Governing equations of fluid motion . . . 5
  - 1.3.1 Internal energy equation . . . 8
  - 1.3.2 Definition of potential temperature . . . 9
- 1.4 Weather Research and Forecasting (WRF) model governing equations . . . 9
- 1.5 Large-eddy Simulation (LES) equations . . . 11
  - 1.5.1 Numerical diffusion . . . 11
  - 1.5.2 LES filters . . . 12
- 1.6 Turbulence closure models . . . 13
  - 1.6.1 Isotropic eddy-viscosity models . . . 13
  - 1.6.2 Anisotropic eddy-viscosity models . . . 14
  - 1.6.3 The dynamic Wong-Lilly model (DWL) . . . 15
    - 1.6.3.1 The DWL test filter . . . 16
  - 1.6.4 The dynamic reconstruction model (DRM) . . . 16
    - 1.6.4.1 The "explicit" LES filter . . . 17
- 1.7 Overview . . . 18
- 1.8 Summary of contributions . . . 18

2 Idealized free convection 20
- 2.1 Introduction . . . 20
- 2.2 Case description . . . 22
- 2.3 Results . . . 23
  - 2.3.1 Mean CBL development . . . 23
  - 2.3.2 Turbulent vertical momentum stress profiles . . . 31

2.3.3 Vertical velocity fields . . . 32
2.3.4 Turbulent energy spectra . . . 37
2.3.5 Backscatter in the DRM . . . 41
2.3.6 Other considerations . . . 41
2.4 Summary and conclusions . . . 43

3 More on the formulation and performance of eddy-viscosity models in WRF-LES 45
3.1 Introduction . . . 45
3.2 Turbulent stress implementations in WRF . . . 46
3.3 Case description . . . 46
3.4 Results . . . 47
3.4.1 High-resolution cases . . . 47
3.4.2 Coarse grid with no explicit model . . . 51
3.4.3 Coarse Smagorinsky-Lilly flavors . . . 53
3.4.4 Coarse anisotropic-deformation Smagorinsky-Lilly flavors . . . 57
3.4.5 Coarse TKE-1.5 flavors . . . 59
3.5 Summary and conclusions . . . 60
3.A Changes to the turbulent stress tensor in the WRF code . . . 62
3.A.1 Original anisotropic Smagorinsky-Lilly implementation . . . 62
3.A.2 Modified anisotropic-deformation Smagorinsky-Lilly implementation . . . 64
3.B Full column planar-averaged profiles . . . 66

4 A promising alternative anisotropic formulation for eddy-viscosity models for atmospheric LES 69
4.1 Introduction . . . 69
4.1.1 Historical context for turbulence models . . . 70
4.1.2 An alternative formulation for anisotropic eddy-viscosity models . . . 71
4.2 Results . . . 73
4.2.1 Free convection . . . 74
4.2.1.1 At 1.2-km horizontal resolution . . . 74
4.2.1.2 At 5-km horizontal resolution . . . 79
4.2.2 Sheared convection . . . 84
4.2.2.1 At 1.2-km horizontal resolution . . . 84
4.2.2.2 At 5-km horizontal resolution . . . 88
4.2.3 Other cases . . . 90
4.2.3.1 For $\overline{w'\theta'_s} = 0.4$ m K s^{-1}, $u_0 = 0$ m s^{-1} . . . 92
4.2.3.2 For $\overline{w'\theta'_s} = 0.15$ m K s^{-1}, $u_0 = 8$ m s^{-1} . . . 95
4.2.3.3 For $\overline{w'\theta'_s} = 0.45$ m K s^{-1}, $u_0 = 8$ m s^{-1} . . . 98
4.3 Two interesting features of TKE spectra produced by the alternative-anisotropic eddy-viscosity model . . . 101
4.4 Summary and conclusions . . . 103

4.A Alternative-anisotropic eddy-viscosity implementations in the WRF code . . 104
4.A.1 TKE-1.5 model . . . 104
4.A.1.1 Original anisotropic TKE-1.5 implementation . . . 104
4.A.1.2 Alternative-anisotropic TKE-1.5 implementation . . . 108
4.A.2 Smagorinsky-Lilly model . . . 111
4.A.2.1 Original anisotropic Smagorinsky-Lilly implementation . . . 111
4.A.2.2 Alternative-anisotropic Smagorinsky-Lilly implementation . 113
4.B Full column planar-averaged profiles . . . 115
4.C Additional results . . . 116
4.C.1 No-wind case . . . 116
4.C.2 Wind case . . . 118

5 The gray zone of terrain representation in atmospheric models 119
5.1 Introduction . . . 119
5.2 MATERHORN . . . 121
5.3 IBM background . . . 121
5.4 Hypothesis/experiment . . . 122
5.5 Difference vs. horizontal resolution . . . 124
5.5.1 Model setup . . . 124
5.5.2 Results . . . 125
5.6 Increasing slope case . . . 125
5.6.1 Model setup . . . 126
5.6.2 Results . . . 128
5.7 Constant slope case . . . 129
5.7.1 Model setup . . . 129
5.7.2 Results . . . 129
5.8 Concluding remarks . . . 130
5.9 Acknowledgments . . . 132

6 Conclusions and future work 133

A Additional sheared test cases in WRF-LES 135
A.1 Results . . . 135
A.1.1 High-resolution cases . . . 135
A.1.2 Coarse DRM flavors . . . 138

B Additional test cases with terrain in WRF-LES 140
B.1 Results . . . 140
B.1.1 Coarse isotropic cases . . . 140
B.1.1.1 Smagorinsky-Lilly model . . . 142
B.1.1.2 TKE-1.5 model . . . 142
B.1.1.3 DRM model . . . 143

B.1.1.4 No model 143

C Relevant details of the WRF code **144**
C.1 Turbulent diffusion 144
C.1.1 Diffusion in WRF prior to 3.8.1 144
C.1.2 Diffusion in WRF 3.8.1 onwards 145
C.2 Ideal surface fluxes 145
C.2.1 Surface heat fluxes in WRF 145
C.2.2 Surface heat and momentum fluxes in the WRF code 146
C.2.3 Surface roughness-length implementation in the WRF code 152

D American Meteorological Society full copyright notices **154**
D.1 Full copyright notice for Ch. 2 154
D.2 Full copyright notice for Ch. 5 155

References **156**

List of Figures

2.1 Hourly horizontally domain-averaged potential temperature profiles using the Smagorinsky-Lilly (solid), TKE-1.5 (dashed), DRM0 (dash-dotted) and DRM2 (dotted) models for the 25-m resolution case. 26
2.2 Hourly horizontally domain-averaged potential temperature profiles using the Smagorinsky-Lilly model with $C_s = 0.25$ (left) and $C_s = 0.18$ (right) for $\Delta_{x,y} =$ 1 km, with profiles from the corresponding 25-m cases overlaid (dotted black). . 27
2.3 Mean value of resolved $w'\theta'$ in the 218-m plane (5th vertical level) using the Smagorinsky-Lilly model with $C_s = 0.25$ for resolutions from 25 m to 1 km. Planar averages are taken every 2 minutes initially and every 15 minutes once $\langle w'\theta' \rangle$ is approximately steady. 27
2.4 As in Fig. 2.2 but using the TKE-1.5 model with $C_k = 0.15$ (left) and $C_k = 0.10$ (right). 28
2.5 As in Fig. 2.3 but using the TKE-1.5 model with $C_k = 0.15$. 28
2.6 As in Fig. 2.2 but using the DRM0 (left) and DRM2 (right). 29
2.7 As in Fig. 2.3 but using the DRM0. 29
2.8 As in Fig. 2.3 but using the DRM2. 30
2.9 Planar-averaged total (resolved + modeled) vertical momentum flux ($\langle \overline{w}'\overline{w}' + \tau_{33} \rangle$), resolved vertical momentum flux ($\langle \overline{w}'\overline{w}' \rangle$), SFS vertical momentum flux ($\langle \tau_{33} \rangle$) for the TKE-1.5, DRM0, DRM2 and Smagorinsky-Lilly (resolved only) models after 6 hours when $\Delta_{x,y} = 500$ m (left) and $\Delta_{x,y} = 1$ km (right), compared to high-resolution cases ($\Delta_{x,y} = 25$ m) using the TKE-1.5 and DRM2 models filtered to the corresponding coarse resolution. 32
2.10 Resolved vertical velocity (w) field in the 218-m plane at hour 6 for $\Delta_{x,y} = 25$ m. All four models produced very similar fields; only the TKE-1.5 model is shown. . 34
2.11 Resolved vertical velocity (w) field in the 218-m plane at hour 6 using the Smagorinsky-Lilly ($C_s = 0.25$) model for $\Delta_{x,y} = 100$, 200, 500 and 1000 m. All cases are plotted as 20×20 km^2, but actual domain sizes follow Table 2.1. . . . 34
2.12 As in Fig. 2.11 but using the Smagorinsky-Lilly ($C_s = 0.18$) model for $\Delta_{x,y} = 500$ m and 1 km. 35
2.13 As in Fig. 2.11 but using the TKE-1.5 ($C_k = 0.15$) model. 35
2.14 As in Fig. 2.11 but using the TKE-1.5 ($C_k = 0.10$) model for $\Delta_{x,y} = 500$ m and 1 km. 35
2.15 As in Fig. 2.11 but using the DRM0. 36

2.16 As in Fig. 2.11 but using the DRM2. 36
2.17 Filtered resolved vertical velocity (w) field in the 218-m plane at hour 6 for the 25-m TKE-1.5 case, filtered to $\Delta_{x,y} = 500$ m (left) and $\Delta_{x,y} = 1$ km (right). . . . 36
2.18 Spectral energy density of w' as a function of k_h/L, where k_h is the horizontal wavenumber and L is the domain length, for the Smagorinsky-Lilly, TKE-1.5, DRM0 and DRM2 models in the 667-m plane after 6 hours at 25-m (dashed) and 1-km (solid) resolutions. Nyquist limits of the respective grids also shown (dashed black). . . . 39
2.19 Horizontal resolution vs. critical wavelength of resolved w' in the 218-m plane after 6 hours for Smagorinsky-Lilly, TKE-1.5, DRM0 and DRM2 for resolutions from 25 m to 1 km. Calculated by applying Eq. 2.2). . . . 40
2.20 Dissipation wavelength vs. critical wavelength of resolved $w'w'$ in the 218-m plane after 6 hours for Smagorinsky-Lilly, TKE-1.5, DRM0 and DRM2 for resolutions from 25 m to 1 km. Calculated by applying Eqs. 2.2 and 2.3. . . . 40
2.21 PDF of dissipation in 16 horizontal planes, from the 4th to 20th vertical level, at hour 6 for the Smagorinsky-Lilly, TKE-1.5, DRM0 and DRM2 models at 200-m (left) and 1-km (right) resolutions. The Smagorinsky-Lilly and TKE-1.5 models have only positive dissipation values while the DRM0 and DRM2 both show a large backscatter component. . . . 42

3.1 Planar-averaged resolved potential temperature and u-velocity profiles for the high-resolution ($\Delta_{x,y} = 100$ m) cases using the isotropic Smagorinsky-Lilly model, isotropic and anisotropic TKE-1.5 model, and no model (from left to right). Full-column profiles shown in Appx. 3.B. . . . 49
3.2 Resolved vertical velocity, $\overline{w}$, in the $z \approx 518$ m plane at $t = 4$ (top) and 9 (bottom) hours for the high-resolution ($\Delta_{x,y} = 100$ m) cases considered. . . . 50
3.3 Metrics of the resolved vertical velocity field, $\overline{w}$, averaged over the $z \approx 169$ m to 1.79 km planes for the high-resolution ($\Delta_{x,y} = 100$ m) cases with different model and isotropy settings: total resolved TKE ($\overline{w}'\overline{w}'$) in time (far left), the same in log-log scale (middle left), critical wavelength of $\overline{w}'\overline{w}'$ in time (middle right), and spectra of resolved TKE ($\overline{\mathcal{S}}_{33}$) averaged over the final two hours (far right). . . . 50
3.4 Contours of spectra of resolved TKE in the vertical velocity ($\overline{\mathcal{S}}_{33}$) in time for the high-resolution ($\Delta_{x,y} = 100$ m) cases with different isotropy settings, with the critical wavelength (dotted white) and horizontal Nyquist limit (dotted black) overlaid. . . . 50
3.5 Planar-averaged resolved potential temperature and u-velocity profiles for the $\Delta_{x,y} = 1.2$ km case using no model with the high-resolution ($\Delta_{x,y} = 100$ m) case overlaid for potential temperature (dotted black) and u-velocity (faded black). Full-column profiles shown in Appx. 3.B. . . . 52
3.6 As in Fig. 3.3 but when $\Delta_{x,y} = 1.2$ km using no model. . . . 52
3.7 Resolved vertical velocity, $\overline{w}$, in the $z \approx 518$ m plane at $t = 4$ (left) and 9 (right) hours for the $\Delta_{x,y} = 1.2$ km case using no model. . . . 52

3.8 Planar-averaged resolved potential temperature and u-velocity profiles for the $\Delta_{x,y} = 1.2$ km case using the Smagorinsky-Lilly model with isotropic and anisotropic lengthscales, with the high-resolution ($\Delta_{x,y} = 100$ m) case overlaid for potential temperature (dotted black) and u-velocity (faded black). Full-column profiles shown in Appx. 3.B. 55
3.9 Resolved vertical velocity, $\overline{w}$, in the $z \approx 518$ m plane at $t = 4$ (top) and 9 (bottom) hours for the $\Delta_{x,y} = 1.2$ km cases using the Smagorinsky-Lilly model with isotropic and anisotropic lengthscales. 56
3.10 Metrics of the resolved vertical velocity field, $\overline{w}$, averaged over the $z \approx 169$ m to 1.79 km planes for the $\Delta_{x,y} = 1.2$ km cases using the Smagorinsky-Lilly model with isotropic and anisotropic lengthscales: total resolved TKE ($\overline{w}'\overline{w}'$) in time (far left), the same in log-log scale (middle left), critical wavelength of $\overline{w}'\overline{w}'$ in time (middle right), and spectra of resolved TKE ($\overline{\mathcal{S}}_{33}$) averaged over the final two hours (far right). 56
3.11 Contours of spectra of resolved TKE in the vertical velocity ($\overline{\mathcal{S}}_{33}$) in time for the $\Delta_{x,y} = 1.2$ km cases using the Smagorinsky-Lilly model with isotropic and anisotropic lengthscales, with the critical wavelength (dotted white) and horizontal Nyquist limit (dotted black) overlaid. 56
3.12 As in Fig. 3.8 but using the anisotropic-deformation Smagorinsky-Lilly model. . 58
3.13 As in Fig. 3.9 but using the anisotropic-deformation Smagorinsky-Lilly model. . 58
3.14 As in Fig. 3.10 but using the anisotropic-deformation Smagorinsky-Lilly model. 58
3.15 As in Fig. 3.8 but using the TKE-1.5 model with isotropic and anisotropic lengthscales. 59
3.16 As in Fig. 3.9 but using the TKE-1.5 model with isotropic and anisotropic lengthscales. 60
3.17 As in Fig. 3.10 but using the TKE-1.5 model with isotropic and anisotropic lengthscales. 60
3.18 Full model height of planar-averaged resolved potential temperature and u-velocity profiles for the high-resolution ($\Delta_{x,y} = 100$ m) cases using the isotropic Smagorinsky-Lilly model, isotropic and anisotropic TKE-1.5 model, and no model (from left to right). 66
3.19 As in Fig. 3.18 but for $\Delta_{x,y} = 1.2$ km cases using no model. 66
3.20 As in Fig. 3.18 but for $\Delta_{x,y} = 1.2$ km cases using the Smagorinsky-Lilly model with isotropic and anisotropic lengthscales. 67
3.21 As in Fig. 3.20 but using the anisotropic-deformation Smagorinsky-Lilly model. 67
3.22 As in Fig. 3.20 but using the TKE-1.5 model. 68

4.1 Resolved potential temperature and u-velocity profiles for $\Delta_{x,y} = 1.2$ km using the current isotropic (far left) and anisotropic (middle left) TKE-1.5 implementations, compared to the alternative-anisotropic Smagorinsky-Lilly (middle right) and alternative-anisotropic TKE-1.5 (far right). High-resolution ($\Delta_{x,y} = 100$ m) isotropic TKE-1.5 case overlaid for resolved potential temperature (dotted black) and u-velocity (faded black). Full-column profiles shown in Appx. 4.B. 76
4.2 Resolved vertical velocity, $\overline{w}$, in the $z \approx 518$ m plane at $t = 4$ (top) and 9 (bottom) hours for the $\Delta_{x,y} = 1.2$ km cases using the current isotropic (far left) and anisotropic (middle left) TKE-1.5 implementations, compared to the alternative-anisotropic Smagorinsky-Lilly (middle right) and alternative-anisotropic TKE-1.5 (far right). 76
4.3 Metrics of the resolved vertical velocity field, $\overline{w}$, averaged over the $z \approx 169$ m to 1.79 km planes for the $\Delta_{x,y} = 1.2$ km cases using the Smagorinsky-Lilly model with current isotropic and anisotropic, as well as alternative-anisotropic, lengthscales: total resolved TKE ($\overline{w}'\overline{w}'$) in time (far left), the same in log-log scale (middle left), critical wavelength of $\overline{w}'\overline{w}'$ in time (middle right), and spectra of resolved TKE ($\overline{\mathcal{S}}_{33}$) averaged over the final two hours (far right) 77
4.4 Contours of spectra of resolved TKE in the vertical velocity ($\overline{\mathcal{S}}_{33}$) in time for the $\Delta_{x,y} = 1.2$ km cases using the Smagorinsky-Lilly model with current isotropic and anisotropic, as well as alternative-anisotropic, lengthscales, with the critical wavelength (dotted white) and horizontal Nyquist limit (dotted black) overlaid. 77
4.5 As in Fig. 4.3 but using the TKE-1.5 model. 77
4.6 As in Fig. 4.4 but using the TKE-1.5 model. 78
4.7 As in Fig. 4.1 but for $\Delta_{x,y} = 5$ km using versions of the Smagorinsky-Lilly model. 81
4.8 As in Fig. 4.1 but for $\Delta_{x,y} = 5$ km using versions of the TKE-1.5 model. 82
4.9 As in Fig. 4.3 but for $\Delta_{x,y} = 5$ km cases using the current isotropic Smagorinsky-Lilly model, isotropic and anisotropic TKE-1.5 model, the alternative-anisotropic Smagorinsky-Lilly and alternative-anisotropic TKE-1.5 models. 82
4.10 As in Fig. 4.4 but for $\Delta_{x,y} = 5$ km cases using the current isotropic Smagorinsky-Lilly, the anisotropic-deformation Smagorinsky-Lilly and the alternative-anisotropic Smagorinsky-Lilly models. 83
4.11 As in Fig. 4.4 but for $\Delta_{x,y} = 5$ km cases using the current isotropic and anisotropic TKE-1.5, and the alternative-anisotropic TKE-1.5 models. 83
4.12 Resolved potential temperature and u-velocity profiles for $\Delta_{x,y} = 1.2$ km using the current isotropic (far left) and anisotropic (middle left) TKE-1.5 implementations, compared to the alternative-anisotropic Smagorinsky-Lilly (middle right) and alternative-anisotropic TKE-1.5 (far right). High-resolution ($\Delta_{x,y} = 100$ m) isotropic TKE-1.5 case overlaid for resolved potential temperature (dotted black) and u-velocity (faded black). 85

4.13 Metrics of the resolved vertical velocity field, $\overline{w}$, averaged over the $z \approx 169$ m to 1.79 km planes for the $\Delta_{x,y} = 1.2$ km cases using the Smagorinsky-Lilly model with current isotropic and anisotropic, as well as alternative-anisotropic, lengthscales: total resolved TKE ($\overline{w}'\overline{w}'$) in time (far left), the same in log-log scale (middle left), critical wavelength of $\overline{w}'\overline{w}'$ in time (middle right), and spectra of resolved TKE ($\overline{\mathcal{S}}_{33}$) averaged over the final two hours (far right) 86
4.14 Contours of spectra of resolved TKE in the vertical velocity ($\overline{\mathcal{S}}_{33}$) in time for the $\Delta_{x,y} = 1.2$ km cases using the Smagorinsky-Lilly model with current isotropic and anisotropic, as well as alternative-anisotropic, lengthscales, with the critical wavelength (dotted white) and horizontal Nyquist limit (dotted black) overlaid. 86
4.15 As in Fig. 4.13 but using the TKE-1.5 model. 86
4.16 As in Fig. 4.14 but using the TKE-1.5 model. 87
4.17 As in Fig. 4.12 but for $\Delta_{x,y} = 5$ km cases using the current isotropic Smagorinsky-Lilly model, isotropic and anisotropic TKE-1.5 model, the alternative-anisotropic Smagorinsky-Lilly and alternative-anisotropic TKE-1.5 models. 88
4.18 Resolved vertical velocity, $\overline{w}$, in the $z \approx 518$ m plane at $t = 4$ (top) and 9 (bottom) hours for the $\Delta_{x,y} = 5$ km cases using the current isotropic Smagorinsky-Lilly model, isotropic and anisotropic TKE-1.5 model, the alternative-anisotropic Smagorinsky-Lilly and alternative-anisotropic TKE-1.5 models. 89
4.19 As in Fig. 4.13 but for $\Delta_{x,y} = 5$ km cases using the current isotropic Smagorinsky-Lilly model, isotropic and anisotropic TKE-1.5 model, the alternative-anisotropic Smagorinsky-Lilly and alternative-anisotropic TKE-1.5 models. 89
4.20 As in Fig. 4.1 but for $\overline{w'\theta'_s} = 0.4$ m K s^{-1}, $u_0 = 0$ m s^{-1} cases using the current isotropic and anisotropic Smagorinsky-Lilly model, and the alternative-anisotropic Smagorinsky-Lilly model. 92
4.21 As in Fig. 4.1 but for $\overline{w'\theta'_s} = 0.4$ m K s^{-1}, $u_0 = 0$ m s^{-1} cases using the current isotropic and anisotropic TKE-1.5 model, and the alternative-anisotropic TKE-1.5 model. 92
4.22 As in Fig. 4.2 but for $\overline{w'\theta'_s} = 0.4$ m K s^{-1}, $u_0 = 0$ m s^{-1} cases using the current isotropic and anisotropic Smagorinsky-Lilly model, and the alternative-anisotropic Smagorinsky-Lilly model. 93
4.23 As in Fig. 4.2 but for $\overline{w'\theta'_s} = 0.4$ m K s^{-1}, $u_0 = 0$ m s^{-1} cases using the current isotropic and anisotropic TKE-1.5 model, and the alternative-anisotropic TKE-1.5 model. 93
4.24 As in Fig. 4.3 but for $\overline{w'\theta'_s} = 0.4$ m K s^{-1}, $u_0 = 0$ m s^{-1} cases using the current isotropic Smagorinsky-Lilly model, isotropic and anisotropic TKE-1.5 model, the alternative-anisotropic Smagorinsky-Lilly and alternative-anisotropic TKE-1.5 models. 94
4.25 As in Fig. 4.4 but for $\overline{w'\theta'_s} = 0.4$ m K s^{-1}, $u_0 = 0$ m s^{-1} cases using different formulations of the Smagorinsky-Lilly (top) and TKE-1.5 (bottom) models. . . . 94

4.26 As in Fig. 4.1 but for $\overline{w'\theta'_s} = 0.15$ m K s^{-1}, $u_0 = 8$ m s^{-1} cases using the current isotropic and anisotropic Smagorinsky-Lilly model, and the alternative-anisotropic Smagorinsky-Lilly model. . . . 95
4.27 As in Fig. 4.1 but for $\overline{w'\theta'_s} = 0.15$ m K s^{-1}, $u_0 = 8$ m s^{-1} cases using the current isotropic and anisotropic TKE-1.5 model, and the alternative-anisotropic TKE-1.5 model. . . . 95
4.28 As in Fig. 4.2 but for $\overline{w'\theta'_s} = 0.15$ m K s^{-1}, $u_0 = 8$ m s^{-1} cases using the current isotropic and anisotropic Smagorinsky-Lilly model, and the alternative-anisotropic Smagorinsky-Lilly model. . . . 96
4.29 As in Fig. 4.2 but for $\overline{w'\theta'_s} = 0.15$ m K s^{-1}, $u_0 = 8$ m s^{-1} cases using the current isotropic and anisotropic TKE-1.5 model, and the alternative-anisotropic TKE-1.5 model. . . . 96
4.30 As in Fig. 4.3 but for $\overline{w'\theta'_s} = 0.15$ m K s^{-1}, $u_0 = 8$ m s^{-1} cases cases using the current isotropic Smagorinsky-Lilly model, isotropic and anisotropic TKE-1.5 model, the alternative-anisotropic Smagorinsky-Lilly and alternative-anisotropic TKE-1.5 models. . . . 97
4.31 As in Fig. 4.4 but for $\overline{w'\theta'_s} = 0.15$ m K s^{-1}, $u_0 = 8$ m s^{-1} cases using different formulations of the Smagorinsky-Lilly (top) and TKE-1.5 (bottom) models. . . . 97
4.32 As in Fig. 4.1 but for $\overline{w'\theta'_s} = 0.45$ m K s^{-1}, $u_0 = 8$ m s^{-1} cases using the current isotropic and anisotropic Smagorinsky-Lilly model, and the alternative-anisotropic Smagorinsky-Lilly model. . . . 98
4.33 As in Fig. 4.1 but for $\overline{w'\theta'_s} = 0.45$ m K s^{-1}, $u_0 = 8$ m s^{-1} cases using the current isotropic and anisotropic TKE-1.5 model, and the alternative-anisotropic TKE-1.5 model. . . . 98
4.34 As in Fig. 4.2 but for $\overline{w'\theta'_s} = 0.45$ m K s^{-1}, $u_0 = 8$ m s^{-1} cases using the current isotropic and anisotropic Smagorinsky-Lilly model, and the alternative-anisotropic Smagorinsky-Lilly model. . . . 99
4.35 As in Fig. 4.2 but for $\overline{w'\theta'_s} = 0.45$ m K s^{-1}, $u_0 = 8$ m s^{-1} cases using the current isotropic and anisotropic TKE-1.5 model, and the alternative-anisotropic TKE-1.5 model. . . . 99
4.36 As in Fig. 4.3 but for $\overline{w'\theta'_s} = 0.45$ m K s^{-1}, $u_0 = 8$ m s^{-1} cases using the current isotropic Smagorinsky-Lilly model, isotropic and anisotropic TKE-1.5 model, the alternative-anisotropic Smagorinsky-Lilly and alternative-anisotropic TKE-1.5 models. . . . 100
4.37 As in Fig. 4.4 but for $\overline{w'\theta'_s} = 0.45$ m K s^{-1}, $u_0 = 8$ m s^{-1} cases using different formulations of the Smagorinsky-Lilly (top) and TKE-1.5 (bottom) models. . . . 100
4.38 Resolved TKE in the vertical direction ($\overline{w}'\overline{w}'$) using the alternative-anisotropic TKE-1.5 model compared to PDFs and CDFs of two Beta($k; 3, 5$) distributions generated with differing toy units (i.e. with units finessed to fit visually). . . . 101
4.39 Resolved TKE in the vertical direction ($\overline{w}'\overline{w}'$) using the alternative-anisotropic TKE-1.5 model compared to Planck's law as a functional shape, generated with toy units (i.e. with units finessed to fit visually). . . . 102

4.40 Full model height of planar-averaged resolved potential temperature and u-velocity profiles for the $\Delta_{x,y} = 1.2$ km) cases using the isotropic and anisotropic TKE-1.5 model, and the alternative-anisotropic Smagorinsky-Lilly and alternative-anisotropic TKE-1.5 models (from left to right). 115
4.41 Resolved vertical velocity, $\overline{w}$, in the $z \approx 518$ m plane at $t = 4$ (top) and 9 (bottom) hours for the $\Delta_{x,y} = 5$ km cases using versions of the Smagorinsky-Lilly model. . 116
4.42 As in Fig. 4.41 but using versions of the TKE-1.5 model. 117
4.43 Resolved vertical velocity, $\overline{w}$, in the $z \approx 518$ m plane at $t = 4$ (top) and 9 (bottom) hours for the $\Delta_{x,y} = 1.2$ km cases using the current isotropic (far left) and anisotropic (middle left) TKE-1.5 implementations, compared to the alternative-anisotropic Smagorinsky-Lilly (middle right) and alternative-anisotropic TKE-1.5 (far right). 118
4.44 As in Fig. 4.14 but for $\Delta_{x,y} = 5$ km cases using the current isotropic Smagorinsky-Lilly model, isotropic and anisotropic TKE-1.5 model, the alternative-anisotropic Smagorinsky-Lilly and alternative-anisotropic TKE-1.5 models. 118

5.1 A mountain profile represented in terrain-following (top) and IBM coordinate systems. Note the distortion of grid cells when using terrain-following coordinates. 120
5.2 Satellite image of Northwestern Utah; Granite Mountain circled in red. Photo from NASA landsat. 121
5.3 Profile of Granite Mountain at 10m resolution, after smoothing. Note the complexity. To scale. 121
5.4 Visual description of the three types of nodes used in IBM-WRF. The blue line represents the terrain surface. The ghost node is the first node beneath the surface, and its image point is a reflection normal to the surface into the fluid domain. The green fluid nodes mark the values that are interpolated to find the image point value. The image point value and the boundary condition determine the value that the ghost node takes. In this example the value at the boundary is apart of the interplation process, which is the case only under Dirichlet boundary conditions. 122
5.5 Idealization of the relationships between WRF, IBM-WRF and horizontal resolution. 123
5.6 Velocity magnitude difference fields for cases where the horizontal resolution is (from top to bottom) 4, 3, 2, 1 0.5 km. Domains are zoomed in both horizontally and vertically. To scale. 126
5.7 Maximum difference as a function of grid spacing, plotted in semi-log. 127
5.8 Scales used on the terrain to achieve different slopes. Horizontal resolution is 500 m for all cases. 127
5.9 Velocity magnitude difference fields for cases where the terrain scale is (from top to bottom) 0.2, 0.4, 0.6, 0.8, 1.0. Domains are zoomed in both horizontally and vertically. To scale. 128
5.10 Maximum difference as a function of slope, plotted in reverse to mimic the shape expected when grid spacing is the independent variable. 129

5.11 Scales used on the terrain to achieve a maximum slope of 10 degrees for each horizontal resolution. 130
5.12 Velocity magnitude difference fields for cases where the horizontal resolution is (from top to bottom) 4km, 3km, 2km, 1km, 500m. Domains are zoomed in both horizontally and vertically. To scale. 131
5.13 Velocity magnitude fields for IBM-WRF (top) and WRF when the horizontal resolution is 2 km and the maximum slope is artificially set to 10 degrees. To scale. 131
5.14 Maximum difference as a function of horizontal resolution when the maximum slope is artificially set to 10 degrees. The two outliers are in red. 132

A.1 Resolved potential temperature and u-velocity profiles for the high-resolution ($\Delta_{x,y} = 100$ m) cases using the isotropic TKE-1.5 model, isotropic DRM2 model and no model. 136
A.2 Resolved vertical velocity, $\overline{w}$, in the $z \approx 518$ m plane at $t = 4$ (top) and 9 (bottom) hours for the high-resolution ($\Delta_{x,y} = 100$ m) cases using the isotropic TKE-1.5 model, isotropic DRM2 model and no model. 136
A.3 Metrics of the resolved vertical velocity field, $\overline{w}$, averaged over the $z \approx 169$ m to 1.79 km planes for the high-resolution ($\Delta_{x,y} = 100$ m) cases using the isotropic TKE-1.5 model, isotropic DRM2 model and no model: total resolved TKE ($\overline{w}'\overline{w}'$) in time (far left), the same in log-log scale (middle left), critical wavelength of $\overline{w}'\overline{w}'$ in time (middle right), and spectra of resolved TKE ($\overline{\mathcal{S}}_{33}$) averaged over the final two hours (far right). 137
A.4 Contours of spectra of resolved TKE in the vertical velocity ($\overline{\mathcal{S}}_{33}$) in time for the high-resolution ($\Delta_{x,y} = 100$ m) cases using the isotropic TKE-1.5 model, isotropic DRM2 model and no model, with the critical wavelength (dotted white) and horizontal Nyquist limit (dotted black) overlaid. 137
A.5 Resolved potential temperature and u-velocity profiles for the $\Delta_{x,y} = 1.2$ km using the DRM0 and DRM2 models with isotropic and anisotropic lengthscales. 138
A.6 Resolved vertical velocity, $\overline{w}$, in the $z \approx 518$ m plane at $t = 4$ (top) and 9 (bottom) hours for the $\Delta_{x,y} = 1.2$ km using the DRM0 and DRM2 models with isotropic and anisotropic lengthscales. 138
A.7 As in Fig. 3.3 but when $\Delta_{x,y} = 1.2$ km using the DRM0 and DRM2 models with isotropic and anisotropic lengthscales. 139
A.8 As in Fig. 3.4 but when $\Delta_{x,y} = 1.2$ km using the DRM0 and DRM2 models with isotropic and anisotropic lengthscales. 139

B.1 Vertical velocity, w, at $t = 4$ (top) and 9 (bottom) hours in the $z \approx 518$ m plane for the $\Delta_{x,y} = 1.2$ km cases considered. 140
B.2 Vertical velocity, w, at $t = 4$ (top) and 9 (bottom) hours in the $z \approx 1389$ m plane for the $\Delta_{x,y} = 1.2$ km cases considered. 141
B.3 Slice through the $y - z$ plane at $x = 190$ km using the isotropic Smagorinsky-Lilly model at $t = 4$ (top) and 9 (bottom) hours for the $\Delta_{x,y} = 1.2$ km case. 142

B.4 As in Fig. B.3 but for the isotropic TKE-1.5 model. 142
B.5 As in Fig. B.3 but for the isotropic DRM0 model. 143
B.6 As in Fig. B.3 but using no model. 143

List of Tables

2.1 Domain sizes for each horizontal resolution considered for all turbulence models unless stated otherwise (as noted in Sec. 2.32.3.1 and in Sec. 2.32.3.4). 23

Acknowledgments

Mother, Father, Mama, Mama and Papa.
Tina, Mark, Evan and Dennis.
Bowen and Jeff.
Dave, Diane, JINGYI, Alex, James and Mike.
Wayne, Y. Rachel, Madeline and Theresa.
Carol and Bob.
Lucas, Drew and Taylor.

Chapter 1

Introduction

1.1 Notation

Some of the more prevalent notation used in this manuscript is:

- arrows indicate vectors in vector notation, e.g. $\vec{u}$ is the velocity vector;
- bolded capital letters indicate tensors in vector notation, e.g. $\mathbf{T}$ is the stress tensor;
- single indices indicate vectors in summation notation, e.g. u_i is the velocity vector;
- double indices indicate tensors in summation notation, e.g. T_{ij} is the stress tensor;
- a variable not modified to indicate otherwise is assumed to be a "true" or correct value, e.g. u_i is the true velocity vector that our model is striving to produce;
- an overline indicates a field's value after filtering, e.g. $\overline{u}_i$ is the filtered velocity vector;
- angled brackets indicate some stated global averaging, e.g. $\langle \overline{u}_i \rangle$ could be the planar-averaged, resolved velocity field;
- a prime indicates a deviation from a stated mean value, e.g. $\overline{u}_i' = \overline{u}_i - \langle \overline{u}_i \rangle$ could be the resolved turbulent fluctuation from the planar-averaged resolved field;
- a product of primed values under a common filter implies a modeled value, as it could not be known otherwise (which is consistent with the notion that it is the "resolved" nonlinear term, in the sense that it is the value for the quantity under the filter), e.g. $\overline{w'\theta'}$ would be the modeled, sub-grid scale (SGS) vertical turbulent heat flux, contrasted to the resolved vertical turbulent heat flux, $\overline{w}'\overline{\theta}'$;
- a product of non-primed values under a common filter implies a theoretical value, e.g. $\overline{u_i u_j}$ would be the theoretical true value of the advective term (care will be taken in the text to avoid ambiguity in this and the previous notations);

- WRF input parameters are written in monospace font, e.g. `tke_heat_flux` is a setting for surface heat flux.

Other notation will be introduced where appropriate.

1.2 Description and motivation

Mesoscale atmospheric models used for numerical weather prediction (NWP) historically use coarse [$\mathcal{O}(1-10$ km)] horizontal resolutions relative to the dominant lengthscale of turbulent energy in the atmosphere, which scales with the planetary boundary layer (PBL) depth [$\mathcal{O}(0.1-1$ km)]. The separation between mesoscale grid spacing and turbulence lengthscale is a result of the balance between domain size, grid resolution and computational capability; i.e. forecasters must use coarse resolution to obtain a simulation that is fast enough and covers a large enough geospatial area to resolve relevant meteorological phenomena. Mesoscale models are based on Reynolds averaging, which uses an ensemble average to separate mean and fluctuating quantities of the Navier-Stokes equations,

$$\frac{\partial \langle u_i \rangle}{\partial t} + \frac{\partial \langle u_i \rangle \langle u_j \rangle}{\partial x_j} = -\frac{1}{\rho}\frac{\partial \langle p \rangle}{\partial x_i} + \nu \frac{\partial^2 \langle u_i \rangle}{\partial x_j \partial x_j} - \frac{\partial \tau_{ij}}{\partial x_j}. \tag{1.1}$$

The effect of turbulent motions is contained in the Reynolds stress term, $\tau_{ij} = \langle u_i' u_j' \rangle$, where $u_i' = u_i - \langle u \rangle_i$ is the fluctuating velocity field and the angled brackets represents an ensemble average. Inherent in this formulation is the assumption that the Reynolds stress term represents the effects of *all* of the unresolved scales of motion and that $\langle u' \rangle = 0$. Most mesoscale models use a one-dimensional parameterization for the turbulent stresses which cannot be resolved on coarse grids. Thus the assumption that RANS represents a mean flow solution results from the choice of grid resolution and/or the behavior of the chosen turbulence model.

In contrast to RANS, a large-eddy simulation (LES) resolves much of the turbulent energy (the "large eddies") in the flow. In an LES, the evolution of the PBL is well resolved and is not parameterized. A turbulence closure is used to model the subfilter-scale (SFS) motions which are smaller than a selected spatial filter width. With LES, the governing equations are typically written as

$$\frac{\partial \rho \overline{u}_i}{\partial t} + \frac{\partial \left(\rho \overline{u}_i \overline{u}_j\right)}{\partial x_j} = -\frac{\partial \overline{p}}{\partial x_i} - \frac{\partial \tau_{ij}}{\partial x_j}, \tag{1.2}$$

where the overbar indicates a spatial filter and $\tau_{ij} = \rho\left(\overline{u_i u_j} - \overline{u}_i \overline{u}_j\right)$ is the SFS turbulent stress. In LES, $\overline{u'} \neq 0$. LES parameterizations for τ_{ij} often contain a term representing the size of the filter, making the turbulence models "scale aware", in that the model will adjust when more or less energy is placed in the subfilter field. Commonly, there is no explicit filter defined and the grid itself and discretization schemes are considered to be the filter. Defining

an explicit filter allows reconstruction of scales between the filter and grid cutoffs, enabling more accurate representation of fine scales, as discussed further below.

Since LES requires a high-resolution grid to resolve the most energetic turbulent motions, LES has historically been limited to idealized atmospheric studies and small-scale engineering applications. Recently, many NWP models have adopted options for LES, enabling microscale weather simulations. Such models include the Advanced Regional Prediction System (ARPS) (Xue et al., 2000), the Naval Research Laboratory Coupled Ocean/Atmosphere Mesoscale Prediction System (COAMPS) (Golaz et al., 2005), the Consortium for Small-scale Modeling (COSMO) model (Langhans et al., 2012), the Colorado State University Regional Atmospheric Modeling System (RAMS) (Pielke et al., 1992), the United Kingdom Met Office Unified Model (UM) (Lean et al., 2008) and the Weather Research and Forecasting model (WRF) (Skamarock et al., 2008).

At the same time as offering LES capabilities, users are pushing mesoscale models to kilometer scale resolutions [$\mathcal{O}(1$ km)]. High resolution grids allow for a more accurate representation of many fields (e.g. terrain, land-use, urban effects). There are many recent examples in the literature of forecasting efforts reaching kilometer and finer scales for varying applications. Liu et al. (2011) used WRF with real-time four dimensional data assimilation for wind-energy forecasting, downscaling (nesting) from a 30-km grid to a 123-m grid, transitioning from a PBL scheme to LES at 500 m. Similarly, Zhu et al. (2010) used WRF to simulate stratocumulus clouds in the Southern Great Plains, nesting from 8.1 km to 100 m resolution using a PBL scheme and an LES closure. In another application, Taylor et al. (2016) used WRF to nest from 2.25-km resolution to 30-m resolution to model landfill methane emissions and assess potential observational strategies. Scalar plumes were studied by Klose and Shao (2013), who used WRF at a resolution of 100 m to model turbulent dust emissions using an LES closure. Garcia et al. (2014) used WRF to study the impact of using high-resolution forest harvesting data on high-resolution NWP, using grids from 30 km to 100 m. All of these examples describe nested LES case studies with short-term simulations on the order of a day.

Longer term or operational simulations are also moving to higher resolution. Kendon et al. (2014), for example, used the UM for a study on the United Kingdom's regional climate under climate change using an LES closure model at 1.5 km horizontal resolution. MeteoSwiss in Switzerland routinely performs NWP forecasts at kilometer-scale resolution (Leuenberger et al., 2005), as does the United Kingdom Met Office (Kendon et al., 2012).

It is clear that the resolution limits for NWP are changing rapidly, and it is only a matter of time before operational weather forecasts use a horizontal resolution $\Delta_{x,y} < 1$ km. This is problematic from a turbulence perspective, however, because kilometer-scale grids can be on the same order as the largest turbulent motions in the atmosphere [e.g. thermal plumes in the convective boundary layer (CBL)]. When an NWP grid cell size is similar in size to the largest eddies, the mesoscale modeling assumption that turbulent scales are all filtered out is no longer true. A natural progression would be to transition from mesoscale modeling to LES at finer resolutions, but LES has the opposite limitation that its filter is assumed to be much smaller than the turbulent eddies. This leaves forecasters with a range of resolutions where

there is no appropriate modeling procedure. This gap in turbulence parameterizations is often referred to as the *terra incognita* (Wyngaard, 2004). The term "gray/grey zone", a more general term, has also been adopted by the atmospheric turbulence community (Arakawa and Wu (2013) use the term to describe a similar issue in the cloud modeling community).

The gray zone has also been the subject of recent literature. Beare (2014) conducted an LES study on the gray zone for a CBL and proposed a gray zone criteria of $z_i/\lambda_d < 0.7$, where z_i is the inversion height and λ_d is a dissipation lengthscale based on the second moment of the TKE spectrum. This aims to capture the smallest lengthscale not filtered out by the combined turbulence model and numerical schemes. They found that the dissipation lengthscale is a much more accurate metric for considering gray zone dynamics than the simpler $z_i \sim \Delta_{x,y}$ criteria that is often used. Zhou et al. (2014) used the ARPS model and a TKE-based PBL scheme at grids progressively refined from 3.6 km to 400 m and compared to a 25-m LES case. They found that as the model enters the gray zone, from the mesoscale side, thermal structures begin to be resolved. This is problematic because the resolved thermal structures are nonphysically large due to the relatively coarse grid resolution, leading to physically inaccurate dynamics. Similar unrealistically large convective cells were seen using the UM with a PBL scheme for horizontal resolutions of 4- and 1-km by Lean et al. (2008), and again in WRF by Ching et al. (2014), who modified the BouLac PBL scheme to successfully suppress these large convective cells for 1-km and finer cases.

More generally, resolution sensitivity and requirements for LES have been studied from multiple perspectives. For example, Chow et al. (2006) used ARPS to simulate valley flows in the Swiss Alps nesting from 9 km to 150 m and found that many important features were not resolved until reaching a horizontal resolution of 350 m. Bryan et al. (2003) conducted a study on resolution requirements for LES to model deep moist convection by simulating squall lines at resolutions from 1 km to 125 m. They concluded that $\mathcal{O}(100$ m) resolution is required for modeling deep convection, however they did not reach convergence even at 125 m. Michioka and Chow (2008) used ARPS to nest from 45 km to 25 m, though results did not significantly improve with increased horizontal resolution beyond 190 m. Piotrowski et al. (2009) demonstrated heavy grid-dependence in convective structures and a large influence of numerical diffusion using the EULAG model (Prusa et al., 2008). Honnert et al. (2011) conducted an extensive study on the balance between resolved and SGS turbulent kinetic energy (TKE) at different resolutions. Efstathiou and Beare (2015) explored the gray zone of the Smagorinsky-Lilly turbulence model using the Met Office Large Eddy Model for a variety of shear and surface heating combinations. They observed a delay in the onset of resolved TKE in the gray zone, and that profiles of resolved TKE become unrealistic when $\Delta_{x,y} > 200$ m. van Stratum and Stevens (2015) conducted a gray zone study using the Smagorinsky-Lilly model for the nocturnal boundary layer, considering resolutions from 3.125 to 100 m, finding significant differences in the coarser cases.

In this dissertation, we examine the role of the turbulence closure model in LES on the behavior of convective boundary layer (CBL) simulations in the terra incognita. In particular, we examine two traditional LES closure models, Smagorinsky-Lilly and TKE-1.5, and a dynamic mixed model. Specifically, we study the performance of the dynamic reconstruction

model (DRM) (Chow et al., 2005) as implemented in WRF (Kirkil et al., 2012). Simulations of the CBL are performed at varying resolutions similar to Zhou et al. (2014) but at finer LES resolutions, with the aim of understanding the behavior of the model as it transitions from LES to RANS resolutions. Our goal here is to examine the role of the turbulence closure model in defining the gray zone, by examining the onset of convection, turbulence statistics, and mean profiles. In particular, it is hypothesized that the dynamic reconstruction model can be helpful in reducing grid-dependence in the gray zone by increasing the turbulence model's "awareness" of the resolved velocity field. The DRM has been shown to improve mean and turbulent profiles in neutral and stable boundary layer flows (Chow et al., 2005; Zhou and Chow, 2011). Moeng et al. (2010) conducted an *a priori* test on a cloud-resolving model with a horizontal resolution of 100 m and found that a mixed model, which is equivalent to a low-order reconstruction model (Chow, 2004), "greatly improves the representation of SGS fluxes of heat, moisture, and momentum" but the mixed model was not used in an *a posteriori* test. We proceed with the hypothesis that each closure model will behave differently in the gray zone, some models will be better at intermediate resolutions, and each model will require different guidelines for transitioning from LES to RANS. We also present an alternative formulation of anisotropic eddy-viscosity models which shows a great amount of potential at these scales.

1.3 Governing equations of fluid motion

The Navier-Stokes (N-S) equations are the most commonly used description of fluid motion. They can be, and have been, derived in a number of ways and their re-derivation is not necessary in the modern literature. However, in the context of the present analysis of highly-anisotropic grids being used to model the atmospheric boundary layer (which is often described as a compressible fluid behaving approximately incompressibly), it is helpful to point out the assumptions of a fluid's behavior that are made when using the N-S equations. Thus we will present one derivation that is particularly physically-revealing, which is to start with Cauchy's equations for motion in a continuum and then take Stokes' interpretation(s) of fluid motion. While this is not a rigorous presentation, as it begins by assuming the general equations of motion and the concept of a continuum and all of the mathematical assurances therein, the process of turning a general continuum into a "Stokesian fluid" is, in the author's opinion, the most elucidating part of the derivation. The rigor that is bypassed is so fundamental to all of classical mechanics that it may be taken for granted here. The presentation of this section will largely follow Truesdell (1952, 1954); Truesdell and Toupin (1960), Serrin (1959) and Aris (1962) (the latter two authors themselves being largely influenced by the former).

As justified above, we are quite comfortable with accepting Cauchy's equation of motion for a continuum, which can be written as

$$\rho\vec{a} = \rho\frac{D\vec{u}}{Dt} = \rho\vec{f} + \vec{\nabla}\cdot\mathbf{T}, \tag{1.3}$$

where ρ is the material's density, $\vec{a}$ is the material's acceleration vector (in time and three dimensions of space), D/Dt is the material derivative, $\vec{u}$ is the material's velocity vector, $\vec{f}$ is the external force per unit mass, $\vec{\nabla}\cdot$ is the divergence operator and $\mathbf{T}$ is the general stress tensor which has yet to be connected to either the composition or kinematic state of the material. Equation (1.3) is easy to accept due to its simplicity; the only visible assumptions are $\vec{F} = m\vec{a}$ and a very general notion of a continuum as a differentiable volume with a density and a boundary that can experience external forces and internal stresses.

Transitioning from a general continuum to a fluid requires making a few key assumptions about the nature of the internal stresses of the material. The first is Stokes' observation that a fluid's motion at any point, P, is proportional to the difference between the normal stresses on P by its immediate material surroundings and the normal stresses that P would experience in hydrostatic equilibrium. For now, let us call this proportionality to the difference in normal stresses anywhere in the continuum the "momentum potential", $\vec{p}$. Further, Stokes observed that a fluid has no preferred direction of motion when $\vec{p} \neq 0$, i.e. that the fluid's response to momentum potential is isotropic in space and thus our potential field, $\vec{p}$, is necessarily a scalar, p. For the desired behavior of divergent flow when $p > 0$, we can define this proportionality of relation to the equilibrium stress at a point to be $-p$, and redefine the stress tensor as

$$\mathbf{T} = -p\mathbf{I} + \mathbf{V}, \tag{1.4}$$

which has the trace

$$\mathrm{Tr}\left(\mathbf{T}\right) = -3p + \mathrm{Tr}\left(\mathbf{V}\right), \tag{1.5}$$

where $\mathbf{I}$ is the identity matrix and $\mathbf{V}$ will be called the viscosity tensor.

The relationship between the material and kinematic state of the fluid needs to be expressed in the definition of $\mathbf{T}$ (a "constitutive" relation), which Stokes did by deriving a linear relation between stress and strain of the form

$$\mathbf{V} = 2\mu\mathbf{S}, \tag{1.6}$$

where μ is the thermodynamic (or simply "dynamic") viscosity and $\mathbf{S}$ is the strain-rate tensor.[1] A key feature of this variable, μ, is that it is a thermodynamic property that is necessarily independent of pressure [proof not shown; see Stokes (1845)]. As an aside, it is nice to note that inherent in our assumptions thus far is the relation that $\mathbf{V} = 0$ when $\mathbf{S} = 0$, which implies that

$$\mathbf{T} = -p\mathbf{I} \tag{1.7}$$

when the fluid is in hydrostatic equilibrium, and when the only body force is gravity Eq. (1.3) reduces to

$$\frac{\partial p}{\partial z} = -\rho g, \tag{1.8}$$

[1] Equation 1.6 is known as Newton's viscosity law and its applicability distinguishes a "Newtonian" from a "non-Newtonian" fluid. Humorously, however, Stokes (1845) credits, in alphabetical order, Biot, Bossut, Cauchy, d'Alembert, Dubuat, Lagrange and Poisson ahead of Newton in validating his derivation of this relation.

where g is the scalar gravity magnitude.

Stokes (1845) also pointed out that a simple rotation of reference frame could re-frame components of T_{ij} to T_{ii}, thus from the assumptions of isotropic motion and Galilean invariance the remaining strain-rate tensor is necessarily symmetric, which can be written as

$$\mathbf{S} = \frac{1}{2}\big(\vec{\nabla}\vec{u} + \vec{\nabla}\vec{u}^{\intercal}\big), \tag{1.9}$$

where $\mathbf{S}$ is now the symmetric strain-rate tensor.

Note that this new dynamic variable for momentum potential, p, may only be taken to be the thermodynamic (thermostatic) pressure for a compressible (incompressible) fluid after further assumptions are made about $\mathbf{V}$ after removing the isotropic p component. For a compressible fluid, it must be assumed that the fluid is in thermodynamic equilibrium at all times, even while in motion. For an incompressible fluid, it must be assumed that $\mathrm{Tr}\,(\mathbf{V})$ vanishes in Eq. (1.5), which is ultimately true for an incompressible Newtonian fluid, but not by any assumptions made to this point (proof not shown; see Aris (1962), sec. 5.23). If no assumptions of this sort are made, we can write Eqs. (1.4) and (1.5) as

$$\mathbf{T} = \big(-p + \gamma\vartheta\big)\mathbf{I} + 2\mu\mathbf{S}, \tag{1.10}$$

and

$$\frac{1}{3}\mathrm{Tr}\,(\mathbf{T}) = -p + \gamma\vartheta + \frac{2}{3}\mu, \tag{1.11}$$

where γ is called the "second" or "bulk" viscosity and ϑ is the viscous dilation, an invariant of the deformation tensor that can be interpreted physically as a fractional rate of change of infinitesimal volume [see Sec. 4.43 of Aris (1962)]. Thus, the $\gamma\vartheta$ term represents the irreversible loss due to viscous resistance to expansion (contraction) for positive (negative) values of γ (akin to losses to shearing friction), which is separate from the reversible exchange with momentum potential, p.

Re-inserting our construction of $\mathbf{T}$ into Eq. (1.3) and assuming that gravity is the only body force and viscosity is (at least spatially) homogeneous, we can express the conservation of linear momentum in a Stokesian fluid as

$$\rho\frac{D\vec{u}}{Dt} = \rho\vec{g} - \vec{\nabla}p + \big(\gamma + \frac{2}{3}\mu\big)\vec{\nabla}\cdot\vec{u} + \mu\vec{\nabla}\cdot\big(\vec{\nabla}\vec{u} + \vec{\nabla}\vec{u}^{\intercal}\big). \tag{1.12}$$

To get from Eq. (1.12) to the N-S equation for linear momentum, we must find a way to neglect the bulk effects, i.e. to say

$$\big(\gamma + \frac{2}{3}\mu\big)\vec{\nabla}\cdot\vec{u} = 0. \tag{1.13}$$

If the fluid is assumed to be incompressible, then

$$\vec{\nabla}\cdot\vec{u} = 0 \tag{1.14}$$

and the bulk effects may be neglected, which is very justifiable for most liquids. Otherwise, the neglect of volume effects can be stated as

$$\gamma = -\frac{2}{3}\mu. \tag{1.15}$$

This can be interpreted either as that the dynamic variable p is the same as the (to now unrelated) thermodynamic pressure and that the fluid is always in thermodynamic equilibrium, or that viscous effects oppose shearing stress at a two-thirds rate that they oppose volume compression; either interpretation is justifiable for a monotonic gas. Older literature commonly refers to Eq. (1.15) as "Stokes' assumption," where modern literature typically takes this assumption for granted by beginning with the N-S equations.

Ultimately, the N-S equations for a compressible fluid together with the continuity equation are most often written as

$$\begin{aligned} \frac{\partial \rho u_i}{\partial t} + \frac{\partial \rho u_j u_i}{\partial x_j} &= -\frac{\partial p}{\partial x_i} + \mu\left(\frac{\partial^2 u_i}{\partial x_j \partial x_j}\right) + F_i \\ \frac{\partial \rho}{\partial t} + \frac{\partial \rho u_i}{\partial x_i} &= 0, \end{aligned} \tag{1.16}$$

where the indices imply summation notation and the variables are the same as before. It is perhaps only tangentially relevant but interesting to note that the density is often coupled to the velocity inside the derivative terms, as written here, which is not necessary mathematically (though it can be used to cleverly write both equations in one expression), but is instead a precursor to the numerical methods that will be used to solve these equations.

Brilliant and effective as the N-S equations are on the small and isotropic scales assumed in their derivation, for large-scale, highly-anisotropic grids in atmospheric boundary layer models, the assumptions related to stresses and especially to the equilibrium of the thermodynamic pressure should be considered, even if ultimately neglected, in any efforts to represent the internal viscous stresses experienced by the atmosphere.

1.3.1 Internal energy equation

If considerations are taken for energy in a fluid described by the N-S equations, we can follow Aris (1962), sec. 6.3 and say

$$\rho\frac{\partial E}{\partial t} = \vec{\nabla}\cdot\left(k\vec{\nabla}T\right) - p\left(\vec{\nabla}\cdot\vec{u}\right) + \mu\Upsilon, \tag{1.17}$$

where E is the specific internal energy, k is the conductance of heat, T is temperature and Υ is the viscous dissipation function which describes external energy converted to internal energy by viscous forces.

While such considerations are often taken for idealized cloud models [e.g. Romps (2008); Pressel et al. (2015)], most operational NWP models, including WRF, do not conserve, or even

track, internal energy explicitly in this way. WRF, specifically, prognosticates momentum, potential temperature, column mass and geopotential and uses a pressure-based vertical coordinate system. It is assumed that the energetics related to viscosity can be adequately dissipated by numerical effects associated with the numerical scheme, SGS model, or both. We do not intend to argue that the total energy should be conserved and accounted for as in Eq. (1.3.1), but rather that the entire implicit job of the SGS viscosity closure should be considered when it is formulated. Typically only the duties of the SGS model when the grid is in the inertial subrange and isotropic are considered in LES SGS closure model formulations, despite being commonly extended to $\mathcal{O}(1\text{ km})$ and highly anisotropic applications.

1.3.2 Definition of potential temperature

Potential temperature, θ, is a very useful variable in atmospheric modeling, as it is a buoyantly-relevant representation of temperature that encapsulates the effects of the local pressure of an air parcel. Potential temperature is defined as

$$\theta = T\left(\frac{p_0}{p}\right)^{R/c_p}, \tag{1.18}$$

where T is absolute temperature, p is local pressure, p_0 is a reference pressure (typically 100 kPa), R is the gas constant of air and c_p is the specific heat capacity of air at a constant pressure (Stull, 1988a).

1.4 Weather Research and Forecasting (WRF) model governing equations

The WRF model solves the flux-form Euler equations using a terrain-following hydrostatic-pressure vertical coordinate system, η, defined as

$$\eta = \frac{p_h - p_{ht}}{m}, \tag{1.19}$$

where

$$m = p_{hs} - p_{ht} \tag{1.20}$$

is the column mass per unit area,[2] p_h is the local hydrostatic pressure, p_{hs} is the hydrostatic pressure at the surface boundary and p_{ht} is the hydrostatic pressure at the top boundary.

The prognostic variables for momentum, $\vec{U} = (U, V, W)$, and mass-coupled potential temperature, Θ, are coupled to the column mass per area, m, and are defined as

$$\vec{U} = m\vec{u}, \tag{1.21}$$

$$\Theta = m\theta, \tag{1.22}$$

[2]The WRF documentation, namely Skamarock et al. (2008), uses μ for the column mass per area, but this manuscript has reserved μ for dynamic viscosity and will thus use m here.

where $\vec{u} = (u, v, w)$ is the velocity vector[3] and θ is the potential temperature.

For a dry atmosphere, following Sec. 2.2 of Skamarock et al. (2008), the governing prognostic equations are written for momentum,

$$\frac{\partial U}{\partial t} + \left(\vec{\nabla} \cdot \vec{U} u\right) - \frac{\partial}{\partial x}\left(p\frac{\partial \phi}{\partial \eta}\right) + \frac{\partial}{\partial \eta}\left(p\frac{\partial \phi}{\partial x}\right) = F_U, \tag{1.23}$$

$$\frac{\partial V}{\partial t} + \left(\vec{\nabla} \cdot \vec{U} v\right) - \frac{\partial}{\partial y}\left(p\frac{\partial \phi}{\partial \eta}\right) + \frac{\partial}{\partial \eta}\left(p\frac{\partial \phi}{\partial y}\right) = F_V, \tag{1.24}$$

$$\frac{\partial W}{\partial t} + \left(\vec{\nabla} \cdot \vec{U} w\right) - g\left(\frac{\partial p}{\partial \eta} - m\right) = F_W, \tag{1.25}$$

for potential temperature,

$$\frac{\partial \Theta}{\partial t} + \left(\vec{\nabla} \cdot \vec{U} \theta\right) = F_\Theta, \tag{1.26}$$

for column mass per area,

$$\frac{\partial m}{\partial t} + \left(\vec{\nabla} \cdot \vec{U}\right) = 0, \tag{1.27}$$

and for geopotential,

$$\frac{\partial \phi}{\partial t} + \frac{1}{m}\left[\left(\vec{U} \cdot \vec{\nabla}\phi\right) - gW\right] = 0, \tag{1.28}$$

where g is gravity, $\phi = gz$ is geopotential, p is the thermodynamic pressure, $\vec{\nabla}\cdot$ is the divergence operator for the vertical coordinate system used here [see Sec. 2.2 of Skamarock et al. (2008) for details], and F_U, F_V, F_W, and F_Θ are forcing terms from model physics, spherical projections, the Earth's rotation and turbulent mixing. The final consideration, turbulent mixing, is the focus of this manuscript and is the primary contribution to the $F_{\vec{U}}$ terms for the cases considered here.

These are combined with the equation of state,

$$p = p_0\left(\frac{R_d \theta}{p_0 \alpha}\right)^\gamma, \tag{1.29}$$

where p_0 is a reference pressure, $\gamma = c_p/c_v = 1.4$ is the ratio of heat capacities for dry air, R_d is the gas constant for dry air, and $\alpha = \rho^{-1}$ is the inverse density which is found from the diagnostic relation,

$$\alpha = -\frac{1}{m}\frac{\partial \phi}{\partial \eta}. \tag{1.30}$$

Only dry cases are considered in this work and the addition of moisture considerations does not significantly complicate the governing equations. As such the moist governing equations for WRF are not presented here [see Sec. 2.3 of Skamarock et al. (2008) for WRF's treatment of moisture].

[3] Again, Skamarock et al. (2008) uses $\vec{V}$ and $\vec{v}$, but $\vec{U}$ and $\vec{u}$ are used here for consistency with other discussions within the manuscript.

1.5 Large-eddy Simulation (LES) equations

To simplify the discussion of the large-eddy simulation (LES) turbulence closure models, consider perhaps the simplest form of the Euler momentum equations, written as

$$\frac{\partial \rho u_i}{\partial t} + \frac{\partial \left(\rho u_i u_j\right)}{\partial x_j} = -\frac{\partial p}{\partial x_i}, \tag{1.31}$$

where the subscripts imply summation notation, ρ is the fluid density and the other variables are the same as before. The neglect of the gravity term can be formally justified by declaring that p is now the deviation from the hydrostatic equilibrium pressure, if desired.

The derivation of the general LES equations from Eq. 1.31) is very straightforward. First, consider a general spatial filter, which will be indicated with an overbar, e.g. $\overline{u}_i$ would be the filtered value of the true u_i field. Applying this general filter and assuming that it may be distributed among linear terms and that the density may be treated as spatially homogeneous under the filter, the Euler equations can be written and manipulated as

$$\frac{\partial \rho \overline{u}_i}{\partial t} + \frac{\partial \left(\rho \overline{u_i u_j}\right)}{\partial x_j} = -\frac{\partial \overline{p}}{\partial x_i} \tag{1.32}$$

$$\frac{\partial \rho \overline{u}_i}{\partial t} + \frac{\partial \left(\rho \overline{u}_i \overline{u}_j\right)}{\partial x_j} = -\frac{\partial \overline{p}}{\partial x_i} - \frac{\partial \left(\rho \overline{u_i u_j} - \rho \overline{u}_i \overline{u}_j\right)}{\partial x_j} \tag{1.33}$$

$$\frac{\partial \rho \overline{u}_i}{\partial t} + \frac{\partial \left(\rho \overline{u}_i \overline{u}_j\right)}{\partial x_j} = -\frac{\partial \overline{p}}{\partial x_i} - \frac{\partial \tau_{ij}}{\partial x_j}, \tag{1.34}$$

where $\tau_{ij} = \rho\left(\overline{u_i u_j} - \overline{u}_i \overline{u}_j\right)$ is the turbulent stress tensor.

τ_{ij} represents both the internal effects of viscosity (which must be present to form eddies, at least theoretically) and any turbulent energy that was lost to turbulent dissipation at scales below the LES filter (which itself has yet to be defined). Most often the finite-difference scheme itself, and thus the grid itself, is considered to be the filter. When the numerical scheme for the advection term is chosen to have a diffusive error, this choice of using the grid as the filter includes an inherent diffusive term in the momentum equation, i.e. numerical diffusion. Thus this implicit filter that is formed by the grid combined with the implicit numerical dissipation sets the effective minimum resolution, below which the cumulative effect of numerical truncation errors so strongly impairs motions that they are essentially absent. It has been seen that different turbulence closure models have different associated implicit filter widths (Ch. 2).

1.5.1 Numerical diffusion

It is important to also consider the role of numerical diffusion when investigating turbulence closure models. A small amount of numerical diffusion is often considered beneficial since its magnitude is usually small and it tends to damp high wavenumbers, specifically 2Δ

waves, removing noise from the solution. Numerical diffusion is present when an odd-ordered, upwind scheme is used for discretizing the advection term in a transport equation for either momentum or scalars (Wang et al., 2009).

Use of an upwind scheme can be shown to be equivalent to a centered scheme with additional numerical diffusion. To demonstrate this, consider first- and second-order finite difference schemes, and their respective error terms, for a first derivative in the x-direction of a generic scalar, q. Following Skamarock et al. (2008), the error of the scheme is found by considering a Taylor series expansion:

$$q\left(x+\Delta_x\right) = q\left(x\right) + \Delta_x \frac{\partial q}{\partial x} + \frac{\Delta_x^2}{2}\frac{\partial^2 q}{\partial x^2} + \frac{\Delta_x^3}{6}\frac{\partial^3 q}{\partial x^3} + \text{higher order terms}, \tag{1.35}$$

and rearranging to define a finite difference approximation of a first derivative, $\partial q/\partial x$, with first-order accuracy, $\mathcal{O}(\Delta_x)$, which has the form

$$\underbrace{\frac{q(x+\Delta_x)-q(x)}{\Delta_x}}_{\text{finite difference scheme}} = \underbrace{\frac{\partial q}{\partial x}}_{\text{perfect solution}} + \underbrace{\frac{\Delta_x}{2}\frac{\partial^2 q}{\partial x^2} + \frac{\Delta_x^2}{6}\frac{\partial^3 q}{\partial x^3} + \text{higher order terms}}_{\text{error terms}}. \tag{1.36}$$

A second-order central scheme, $\mathcal{O}(\Delta_x^2)$, includes the point $q(x-\Delta_x)$ as well, taking the form

$$\frac{q(x+\Delta_x)-q(x-\Delta_x)}{2\Delta_x} = \frac{\partial q}{\partial x} + \frac{\Delta_x^2}{6}\frac{\partial^3 q}{\partial x^3} + \text{higher order terms}. \tag{1.37}$$

Note that the first-order scheme [Eq. 1.36)] contains an additional second derivative term, which is diffusive in nature, that is absent in the second-order scheme [Eq. 1.37)]. This is the first-order scheme's "numerical diffusion". Similarly, a third-order scheme will include an additional hyper-diffusive fourth-derivative term compared to a fourth-order scheme. Likewise a fifth-order scheme will have a hyper-diffusive sixth derivative in the leading error term. The diffusive error terms serve to smooth out the solution in much the same way as an eddy viscosity model would. Note, however, that these terms cannot be tuned, as they are the error that results from the finite difference scheme and depend on the size of the grid and the nature of q.

The default for momentum and scalar (e.g. potential temperature) advection in WRF is a 5th-order scheme in the horizontal directions and a 3rd-order scheme in the vertical direction, although WRF has 2nd through 6th order options available. The odd-ordered schemes are upwind-biased and numerically diffusive (Skamarock et al., 2008).

1.5.2 LES filters

Unlike RANS which is based on parameterizing fluctuations from a mean value, LES is based on simulating a "filtered" velocity field and parameterizing scales of turbulence that are

smaller than the filter. The typical representation of the most general LES filter is

$$\overline{u}_i(x) = \int_{-\infty}^{\infty} G(\tau)\, u_i(x+\tau)\, d\tau \tag{1.38}$$

where u_i is the "exact" or "perfect" velocity field, $\overline{u}_i$ is the filtered velocity field and G is the filter kernel to be defined later.

There are many ways to represent the LES filter that are used in practice, including both explicit and implicit methodologies. Often the only difference between a RANS mesoscale NWP model and an atmospheric LES is the behavior of the implemented turbulence closure model, where a RANS closure model will attempt to parameterize all of the turbulent energy in the atmospheric boundary layer and aloft, while an LES closure model will only attempt to parameterize the turbulent energy below the LES filter width.

The basis for the DRM is that there are potentially relevant scales of motion between the grid width and the filter width that can, theoretically, be reconstructed up to the grid's Nyquist limit by applying an inverse filter to the velocity field and using this reconstructed velocity in the scale similarity component of a mixed model. The eddy-viscosity model used in the DRM is the DWL model, which itself uses a test filter for its own scale-similarity component.

1.6 Turbulence closure models

1.6.1 Isotropic eddy-viscosity models

As described above, one of the few things that is known about τ_{ij} for atmospheric LES is that it contains the effects of turbulence on the resolved flow field. It is thus quite natural to assume that τ_{ij} has a diffusive form in a similar vein to molecular diffusion, an approach referred to as an eddy-viscosity model. Generally, eddy-viscosity turbulence closure models have the form

$$\tau_{ij} = -2K\overline{S}_{ij}, \tag{1.39}$$

where

$$\overline{S}_{ij} = \frac{1}{2}\left(\frac{\partial \overline{u}_i}{\partial x_j} + \frac{\partial \overline{u}_j}{\partial x_i}\right) \tag{1.40}$$

is the resolved, symmetric strain-rate tensor, K is the eddy viscosity and $\overline{u}_i$ is the resolved velocity vector. The eddy viscosity then must be modeled as well.

In the Smagorinsky-Lilly model (Lilly, 1962; Smagorinsky, 1963; Lilly, 1967) the eddy viscosity is diagnosed based, again, on the resolved strain rate. Specific implementations vary, but the WRF implementation, which is relatively simple, diagnoses K as

$$K = C_s^2 l^2 \overline{S}_\beta, \tag{1.41}$$

where C_s is the Smagorinsky tuning coefficient [typically $\mathcal{O}(0.1)$], l is a turbulent lengthscale and $\overline{S}_\beta$ is the magnitude of the resolved strain-rate tensor after some stability-based scaling,

typically based on the Richardson number. In WRF this is also implemented relatively simply as

$$\overline{S}_\beta = \max\left[0, \left(\overline{S}_{ij}\overline{S}_{ij} - \frac{N^2}{\mathrm{Pr}}\right)^{1/2}\right], \tag{1.42}$$

where N is the Brunt-Väisälä frequency and Pr is the turbulent Prandtl number ($\mathrm{Pr}^{-1} = 3$ is the typically-specified value).

Original eddy-viscosity formulations all used an isotropic lengthscale, typically defined as

$$l = (\Delta_x \Delta_y \Delta_z)^{1/3}. \tag{1.43}$$

Scalar diffusion is modeled with the turbulent Prandtl number mentioned above, as

$$K^{\mathrm{scalar}} = \frac{1}{\mathrm{Pr}} K. \tag{1.44}$$

The turbulent kinetic energy (TKE) order-1.5 model (often called TKE-1.5) solves a prognostic TKE equation which includes TKE advection and parameterizes sources and sinks from shear production, buoyancy, turbulent mixing and dissipation (Deardorff, 1972, 1974; Skamarock et al., 2008). The TKE-1.5 closure uses a grid-based lengthscale to define the eddy-viscosity as

$$K = C_k l \sqrt{e}, \tag{1.45}$$

where e is the SGS TKE and C_k is a constant [also typically $\mathcal{O}(0.1)$]. Scalar eddy diffusivities are defined for TKE-1.5 in the same way as the Smagorinsky-Lilly model above.

1.6.2 Anisotropic eddy-viscosity models

Most modern LES turbulence closure implementations also have some anisotropic option, with varying degrees of anisotropy. For instance, the WRF model will use anisotropic lengthscales such that

$$\begin{aligned} l_h &= (\Delta_x \Delta_y)^{1/2}, \\ l_v &= \Delta_z, \end{aligned} \tag{1.46}$$

and Eq. 1.41) is modified to indicate that the eddy-viscosity now takes different vertical and horizontal values using the respective lengthscales, but the other terms do not change, i.e.

$$K_h = C_s^2 l_h^2 \overline{S}_\beta, \tag{1.47}$$

$$K_v = C_s^2 l_v^2 \overline{S}_\beta. \tag{1.48}$$

Other codes have gone further, separating the strain terms anisotropically as well. For instance, the CM1 model uses

$$\begin{aligned} \overline{S}_h &= \sqrt{2}\left(\overline{S}_{11}^2 + \overline{S}_{22}^2 + \overline{S}_{33}^2 + \overline{S}_{12}^2 + \overline{S}_{21}^2\right)^{1/2}, \\ \overline{S}_v &= \sqrt{2}\left(\overline{S}_{13}^2 + \overline{S}_{23}^2 + \overline{S}_{31}^2 + \overline{S}_{32}^2\right)^{1/2}, \end{aligned} \tag{1.49}$$

and modifies Eqs. (1.47) and (1.48) to use the respective anisotropic strain rates after applying their particular implementation of Eq. 1.42) (Shi et al., 2019).

This re-formulation is not available in WRF as distributed, but is simple to implement and will be considered here as the "anisotropic-deformation Smagorinsky-Lilly" model, or "ad.Smag." in Ch. 3. The relevant original and modified WRF code is presented in Appx. 3.A.

The TKE-1.5 model is also often implemented anisotropically, generally as

$$K_{h,v} = C_k l_{h,v} \sqrt{e}, \tag{1.50}$$

where the horizontal and vertical lengthscales, l_h and l_v, are defined anisotropically. In WRF these lengthscales are defined as

$$l_h = \left(\Delta_x \Delta_y\right)^{1/2}, \tag{1.51}$$

$$l_v = \begin{cases} \min\left(\Delta_z, 0.76 N^{-1}\sqrt{e}\right) & : N^2 > 0 \\ \Delta_z & : N^2 \leq 0 \end{cases},$$

where the stability-based damping effect on the mixing length is similar to the damping applied to $\overline{S}_\beta$ in the Smagorinsky-Lilly model.

1.6.3 The dynamic Wong-Lilly model (DWL)

The DWL model, as presented by Wong and Lilly (1994), defines the turbulent stress tensor as

$$\tau_{ij} = -2 C_\epsilon \Delta^{4/3} \widetilde{\overline{S}}_{ij}. \tag{1.52}$$

The coefficient C_ϵ is then found dynamically as

$$2\Delta^{4/3} C_\epsilon \approx \frac{\left\langle \left(L_{ij} - \frac{1}{3}\delta_{ij} L_{kk}\right)\left(\widehat{\overline{S}}_{ij} - \frac{1}{3}\delta_{ij}\widehat{\overline{S}}_{kk}\right)\right\rangle}{(1-\alpha)\left\langle \left(\widehat{\overline{S}}_{lm} - \frac{1}{3}\delta_{lm}\widehat{\overline{S}}_{nn}\right)^2\right\rangle}, \tag{1.53}$$

where

$$\begin{aligned} \widehat{\overline{S}}_{ij} &= \frac{1}{2}\left(\frac{\partial \widehat{\overline{u}}_i}{\partial x_j} + \frac{\partial \widehat{\overline{u}}_j}{\partial x_i}\right), \\ L_{ij} &= \widehat{\overline{u}_i \overline{u}_j} - \widehat{\overline{u}}_i \widehat{\overline{u}}_j, \\ \alpha &= \left(\frac{\widehat{\Delta}}{\Delta}\right)^{4/3}, \end{aligned}$$

and Δ is the grid width, $\widehat{\Delta}$ is the test-filter width, the overbar represents the grid filter, the hat represents the test filter and $\langle\ \rangle$ indicates planar or local volume averaging.

When the DWL model is formulated isotropically, the resulting system is then solved in a least-squares manner for a single value of $2\Delta^{4/3} C_\epsilon$. When the DWL is formulated anisotropically, separate horizontal (consisting of 11, 22, 33, 12 components) and vertical (consisting of 13 and 23 components) systems are solved.

1.6.3.1 The DWL test filter

The "test filter" is specified to be

$$\widehat{u}_\iota = \frac{1}{2}u_{\iota-1} + \frac{1}{2}u_{\iota+1} \tag{1.54}$$

and is applied on top of the explicit filter, yielding

$$\widehat{\widetilde{u}}_\iota = \frac{1}{8}u_{\iota-2} + \frac{1}{4}u_{\iota-1} + \frac{1}{4}u_\iota + \frac{1}{4}u_{\iota+1} + \frac{1}{8}u_{\iota+2}, \tag{1.55}$$

which is a tophat filter that is twice the width of the explicit filter. This formulation is in agreement with the coefficients specified by Chow et al. (2005).

1.6.4 The dynamic reconstruction model (DRM)

The dynamic reconstruction model considers both the explicit and implicit filters involved in LES. The DRM allows for backscatter of energy from small to large scales, exhibits excellent correlation with turbulent stresses obtained from *a priori* tests, and reduces numerical errors in the solution (Chow et al., 2005; Zhou and Chow, 2011, 2012). The DRM uses an explicit filter (larger than the grid cell width) combined with velocity reconstruction, previously described by Chow et al. (2005) and Gullbrand and Chow (2003). Specifically, explicit filtering separates the role of the LES filter from the implicit grid discretization effects. This means there is a range of eddy motions between the grid's Nyquist limit and the LES filter. These motions are, by definition, resolvable, because they are larger than the minimum resolvable wavelength on the grid, and are referred to as RSFS motions.

Using the explicit filter (denoted by a wavy-overline) and the implicit grid filter (still denoted by an overbar), we define $\overline{u}_i$ as the resolved velocity field on the grid, $\widetilde{\overline{u}}_i$ as the filtered, resolved velocity field and $u_i^\star$ as the reconstructed velocity field (Gullbrand and Chow, 2003). (Note that the notation here differs from previous literature.) The explicit filter is chosen here to be a tophat filter and is used in a deconvolution step to reconstruct the velocity field,

$$u_i^\star = \underbrace{\underbrace{\underbrace{\widetilde{\overline{u}}_i}_{\text{Level 0}} + (I-G)*\widetilde{\overline{u}}_i}_{\text{Level 1}} + (I-G)*\left[(I-G)*\widetilde{\overline{u}}_i\right]}_{\text{Level 2}} + \ldots \tag{1.56}$$

where I is the identity matrix, G is the explicit filter and $*$ represents the convolution operator (Gullbrand and Chow, 2003). The DRM is characterized by the number of reconstruction terms included; level-n reconstruction includes the first $n+1$ terms in the series (as indicated in Eq. 1.56). In practice, only the first few terms in the series are retained for $u_i^\star$ (Chow et al., 2005; Shi et al., 2018). Once $u_i^\star$ is reconstructed, the Wong and Lilly (1994) dynamic

eddy-viscosity model (the Dynamic Wong-Lilly model) is combined with the RSFS term to create a mixed model. Together these become

$$\tau_{ij} = \left(\widetilde{u_i^\star u_j^\star} - \widetilde{u_i^\star}\ \widetilde{u_j^\star}\right) - 2C_\epsilon \Delta_f^{4/3} \widetilde{\overline{S}}_{ij}, \tag{1.57}$$

where C_ϵ is a dynamically-determined coefficient and Δ_f is the filter lengthscale (typically $2\Delta_{x,y}$, which is used here). To prevent unstable, anti-diffusive solutions, the dynamic coefficient of the eddy-viscosity term is constrained to $C_\epsilon \Delta_f^{4/3} > -1.5 \times 10^{-5}$. Scalar diffusion uses a similar mixed model, where the scalar RSFS term is found with the same filtering process as for momentum (Eq. 1.56) and the eddy-viscosity term is scaled by the same turbulent Prandtl number used with the Smagorinsky and TKE-1.5 models. For potential temperature, θ, the DRM SFS term is

$$\tau_{\theta j} = \left(\widetilde{\theta^\star u_j^\star} - \widetilde{\theta^\star}\ \widetilde{u_j^\star}\right) - \frac{1}{\mathrm{Pr}} 2C_\epsilon \Delta_f^{4/3} \frac{\partial \widetilde{\overline{\theta}}}{\partial x_j}. \tag{1.58}$$

When the DWL is used in concert with the reconstruction terms, as it is in the DRM, Eq. 1.53 is modified with a corresponding H_{ij} term, which is subtracted from L_{ij} in the numerator as

$$2\overline{\Delta}^{4/3} C_\epsilon \approx \frac{\left\langle \left(L_{ij} - \frac{1}{3}\delta_{ij}L_{kk} - H_{ij}\right)\left(\widehat{\overline{S}}_{ij} - \frac{1}{3}\delta_{ij}\widehat{\overline{S}}_{kk}\right)\right\rangle}{(1-\alpha)\left\langle \left(\widehat{\overline{S}}_{lm} - \frac{1}{3}\delta_{lm}\widehat{\overline{S}}_{nn}\right)^2\right\rangle}, \tag{1.59}$$

where

$$H_{ij} = \left(\widehat{\widehat{\overline{u}}_i \widehat{\overline{u}}_j} - \widehat{\overline{u}}_i \widehat{\overline{u}}_j\right) - \widehat{\tau_{ij}^{\mathrm{RSFS}}}.$$

Further details can be found in Chow et al. (2005).

When $u_i^\star = \widetilde{\overline{u}}_i$ (level-0 DRM), we obtain a dynamic mixed model similar to Zang et al. (1993). We will consider the level-0 and level-2 DRM cases here, referred to as DRM0 and DRM2, respectively. Mixed models have long been shown to improve the performance of LES. Moeng et al. (2010), for example, conducted an *a priori* test on a cloud-resolving model with a horizontal resolution of 100 m and found that a mixed model greatly improved the representation of SGS fluxes of heat, moisture, and momentum.

1.6.4.1 The "explicit" LES filter

The "explicit filter", denoted herein with a wavy-overline (e.g. $\widetilde{u}_i$), is the filter used to define the theoretical scales of the LES. Since the filtered fields must exist on the grid, the LES filter must be larger than the grid. It is so-named because in a maximally-rigorous LES the velocity field would first be solved on the grid and would then be filtered to some scale larger than the grid and the turbulence closure model would then parameterize turbulent

SFS energy. The numerics associated with solving the turbulent Navier-Stokes equations on a grid are often diffusive in nature, and additionally most LES turbulence closure models either have a diffusive eddy-viscosity component or are a purely diffusive model.

The step of applying this LES filter, if only implicitly, cannot be avoided without unstable, anti-diffusive behavior. However, this step is often ignored by practitioners and the grid itself is considered to be the entirety of the LES filter. In fact, the term "SGS" is often (incorrectly) considered to be synonymous with SFS and the SGS stress model is considered to be the entire turbulence closure model.

Although the WRF-LES model uses the grid as its implicit LES filter, the DRM is implemented as if the LES filter is a 3-point explicit tophat filter with coefficients

$$\widetilde{u}_\iota = \frac{1}{4}u_{\iota-1} + \frac{1}{2}u_\iota + \frac{1}{4}u_{\iota+1} \tag{1.60}$$

in each dimension, where ι denotes grid index.

1.7 Overview

Chapter 2 presents a detailed analysis of the behavior of anisotropic eddy-viscosity models and two levels of the DRM at 25-m to 1-km horizontal resolutions using the WRF-LES model to simulate an atmosphere under idealized free convection, showing the increasing importance of the turbulence closure model as the resolution becomes coarser.

Chapter 3 presents a further analysis of the behavior of both isotropic and anisotropic eddy-viscosity models at kilometer-scale resolutions for an increasingly realistic case, as well as considers the effects of different possible anisotropic implementations.

Chapter 4 presents a reformulation of the lengthscales used for anisotropic eddy-viscosity models which results in improved performance on anisotropic grids.

Chapter 5 presents an analysis of the representation of high-resolution terrain in kilometer-scale NWP models and the similarities to the challenges of representing high-resolution turbulent structures.

Chapter 6 summarizes the work presented here and makes recommendations for future studies.

Appendix A presents a similar analysis to Ch. 3 for two levels of the DRM.

Appendix B considers the performance of eddy-viscosity models and the DRM for a case with complex terrain by introducing a high-resolution representation of Granite Mountain.

1.8 Summary of contributions

In summary, the main contributions to the literature are:

1. A demonstration of the inadequacies of current isotropic and anisotropic eddy-viscosity models in modeling convective boundary layers in the atmosphere on anisotropic grids where $\Delta_{x,y}$ is $\mathcal{O}(1$ km$)$;

2. A demonstration of the ability of the DRM to generate consistent dynamics even at $\mathcal{O}(1$ km$)$ horizontal resolutions and on highly anisotropic grids;

3. An explanation for the dynamics seen at $\mathcal{O}(1$ km$)$ resolutions for eddy-viscosity and mixed models;

4. A thorough analysis of the formulation of turbulent stresses and the Smagorinsky-Lilly model in WRF;

5. A motivation for an alternative formulation of anisotropic eddy-viscosity models and a demonstration of the potential improvement introduced in the ability to create scale-consistent dynamics on different grid sizes and resolutions;

6. An investigation of similar "gray-zone" issues related to representing high-resolution terrain data on $\mathcal{O}(1$ km$)$ grids in NWP models.

Chapter 2

Idealized free convection[1]

2.1 Introduction

Mesoscale atmospheric models used for studying atmospheric dynamics and for numerical weather prediction (NWP) historically use horizontal resolutions that are $\mathcal{O}(1-10\text{ km})$, which are much larger than the dominant lengthscale of turbulence in the atmosphere. Since turbulent motions in the atmosphere cannot be resolved at such coarse horizontal resolutions, their effects are parameterized. The parameterizations used to represent the impact of turbulence on the mean flow are typically based on Reynolds averaging, which uses an ensemble average to separate mean and fluctuating quantities, of the Navier-Stokes equations,

$$\frac{\partial \overline{u}_i}{\partial t} + \frac{\partial \overline{u}_i \overline{u}_j}{\partial x_j} = -\frac{1}{\rho}\frac{\partial \overline{p}}{\partial x_i} - \frac{\partial \tau_{ij}}{\partial x_j} + \overline{F}_i. \tag{2.1}$$

where x_i represent x, y, z coordinates, $\overline{u}_i$ are the mean velocities, p is pressure, ρ is density, and molecular viscosity effects are neglected. The effect of turbulent motions is contained in the Reynolds stress term, $\tau_{ij} = \overline{u_i' u_j'}$, where u_i' is the fluctuating velocity field. Most mesoscale models use a planetary boundary layer (PBL) scheme to parameterize ensemble-averaged turbulent mixing in the boundary layer because it is assumed that PBL eddies cannot be resolved on a mesoscale grid.

In large-eddy simulation (LES), the large, energy-containing scales are resolved while smaller scales are parameterized. A turbulence closure is used to model the subfilter-scale (SFS) motions which are smaller than a selected spatial filter width. With LES, the overbar in Eq. 2.1) indicates a spatial filter and $\tau_{ij} = \overline{u_i u_j} - \overline{u}_i \overline{u}_j$ is now the SFS turbulent stress. Commonly, there is no explicit filter defined and the grid combined with the effects of the discretization schemes are considered to be an implicit filter. This implicit filter is effectively

[1]This chapter is a modified reproduction of the article "Explicit Filtering and Reconstruction to Reduce Grid Dependence in Convective Boundary Layer Simulations Using WRF-LES" by Jason S. Simon (the principle author), Bowen Zhou, Jeffrey D. Mirocha and Fotini Katopodes Chow, first published in *Monthly Weather Review*, May 2019, Volume 147(5), pages 1805 – 1821 (Simon et al., 2019),

wider than the grid's Nyquist limit, the smallest wavelength that can be resolved on a given grid. In contrast, defining an explicit filter allows reconstruction of resolvable subfilter-scale (RSFS) motions, enabling more accurate representation of fine scales (Gullbrand and Chow, 2003; Chow et al., 2005). Furthermore, by providing stresses from the missing scales, explicit filtering and reconstruction enable a more accurate representation of the more important energetic scales, as discussed further below.

Given the fine mesh spacing required to resolve turbulence, LES has historically been limited to idealized atmospheric studies and small-scale engineering applications where domain sizes are small enough to be manageable with the available computing power. As computational resources expand, users are now pushing mesoscale models to much higher resolutions, allowing for a more accurate representation of many properties (e.g., terrain, land-use, urban effects) as well as atmospheric features such as microfronts and terrain-induced flows, for example. As such, many NWP models have adopted options for LES, enabling microscale simulations. There are many recent examples in the literature of forecasting research reaching kilometer and finer scales for varying applications, such as wind energy (Liu et al., 2011), scalar dispersion (Klose and Shao, 2013; Taylor et al., 2016), cloud modeling (Zhu et al., 2010) and use of high-resolution surface data (Garcia et al., 2014). Longer term or operational simulations are also moving to higher resolution. This is problematic from a boundary-layer turbulence perspective, however, because kilometer-scale grids can be on the same order as the size of the largest turbulent eddies in the atmospheric boundary layer (ABL) (e.g., organized thermals in the convective boundary layer [CBL]). This leaves forecasters with a range of resolutions that are too coarse for LES and too fine for mesoscale turbulence modeling. This gap in turbulence parameterizations is often referred to as the gray zone or the *terra incognita* (Wyngaard, 2004). In the atmospheric boundary layer of depth z_i, it is often suggested that the gray zone consists of resolutions where $\Delta_{x,y} \sim z_i$ (though this definition will be examined here).

The gray zone has been the subject of many recent studies from multiple perspectives. Honnert et al. (2011) conducted an extensive study on the balance between resolved and sub-grid scale (SGS) turbulent kinetic energy (TKE) at different resolutions. Grid-dependent dynamics, in the form of nonphysically large convective cells, have been documented using multiple numerical models and turbulence closures (Lean et al., 2008; Piotrowski et al., 2009; Ching et al., 2014; Zhou et al., 2014; Shi et al., 2018).

Beare (2014) conducted an LES study on the gray zone for the CBL and proposed a gray zone criterion based on a dissipation lengthscale diagnosed from the second moment of the TKE. Efstathiou and Beare (2015) explored the gray zone of the Smagorinsky-Lilly turbulence model for a variety of shear and surface heating combinations, observing a delay in the onset of resolved TKE in the gray zone and that profiles of resolved TKE become unrealistic when $\Delta_{x,y} > 200$ m. Khani and Waite (2014, 2015) studied the Kraichnan, Smagorinsky-Lilly and dynamic Smagorinsky-Lilly models and found that different turbulence closures have different grid-spacing criteria for accurate simulations of stratified turbulence and proposed a gray zone criterion based on the buoyancy lengthscale. Multiple strategies for simulating the atmosphere in the gray zone have been proposed, including local grid refinement near the

surface (Zhou et al., 2017, 2018), distinguishing between updrafts and downdrafts (Thuburn et al., 2018), and improving eddy-viscosity models to better adapt to gray-zone resolutions (Efstathiou et al., 2016; Kurowski and Teixeira, 2018).

Here, we use the Weather Research and Forecasting (WRF) model to examine the role of the turbulence closure model in LES on the behavior of CBL simulations in the gray zone. Four LES closure models are tested: the Smagorinsky-Lilly model, the TKE-1.5 model, and the dynamic reconstruction model (DRM) with level-0 and level-2 reconstruction (see Sec. 2.11.6.4). Specifically, we study the performance of the DRM (Chow et al., 2005) as implemented in WRF (Kirkil et al., 2012). The DRM is built from an explicit filtering and reconstruction framework, which improves the representation of turbulent motions. Simulations of the CBL are performed at varying resolutions, in a process similar to Zhou et al. (2014) but using LES and at finer resolutions.

Our goal here is to examine the role of the turbulence closure model in the gray zone by examining mean profiles, the onset of convection, turbulence statistics, and velocity fields. In particular, it is hypothesized that the DRM can be helpful in reducing grid dependence in the gray zone by increasing the accuracy of the resolved scales and allowing for backscatter. The DRM has been shown to improve mean and turbulent profiles in multiple ABL regimes, including the neutral, stable, and stratocumulus-topped boundary layer when compared to eddy-viscosity models (Chow et al., 2005; Zhou and Chow, 2011; Shi et al., 2018). In addition to exploring the performance of the DRM in detail, we proceed with the hypothesis that each closure model will behave differently in the gray zone. This means that the resolution at which the model transitions from well-resolved LES to the gray zone will be different depending on the closure model used.

2.2 Case description

This study considers the development of the CBL, a key aspect of NWP, in an idealized model setup featuring a quiescent initial state with no forced mean wind, a flat bottom boundary with uniform roughness, and periodic lateral boundary conditions. The simulations are run for 9 hours with a constant sensible surface heat flux of 270 W m^{-2}, the default value for idealized convective cases in WRF-LES. This case was chosen primarily to isolate free convection, but also because it does not require any changes to the WRF code. The Wangara Day 33 case (Clarke et al., 1971) was also considered and yielded very similar results to those presented here (not shown).

A 3rd-order Runge-Kutta time-integration scheme, a 5th-order horizontal advection scheme and a 3rd-order vertical advection scheme are used (WRF default values). All cases use a time step of 0.1 s, a domain height of 3.5 km, and 65 vertical levels. The lowest vertical level is at $z = 24$ m and there are 10 levels below $z = 500$ m. The surface drag is computed using the Monin-Obukhov surface layer scheme in WRF for all of the turbulence models used.

Simulations are performed with horizontal resolutions ranging from $\Delta_{x,y} = 25$ m to 1 km (see Table 2.1). Domains with $\Delta_{x,y} \leq 200$ m are designed to have a size of 20 km $\times$ 20 km.

$\Delta_{x,y}$ (m)	$n_{x,y}$	Domain size (km^2)
25	800	20×20
50	400	20×20
100	200	20×20
200	100	20×20
500	80	40×40
1000	80	80×80

Table 2.1: Domain sizes for each horizontal resolution considered for all turbulence models unless stated otherwise (as noted in Sec. 2.32.3.1 and in Sec. 2.32.3.4).

The coarsest domains ($\Delta_{x,y} = 500$ m, 1 km) are larger in size to obtain adequate statistics with the lower resolution (Table 2.1). Different domain sizes are used for some cases in Secs. 2.32.3.1 and 2.32.3.4, as explained in the respective sections. Experiments were also conducted with finer and coarser vertical resolutions, but changes in vertical resolution had little to no impact on the results seen here. WRF version 3.8.1 is used for all cases.

The focus of this study is the grid dependence of large-eddy simulations, rather than the specific accuracy relative to field data. Therefore, the highest-resolution grid for a given turbulence model is considered to be the "true" solution for this idealized setup. A well-resolved solution for this convection-dominated case should show a shallow super-adiabatic layer at the surface, a well-mixed neutral layer above and resolved entrainment of the free atmosphere at the top of the CBL (Stull, 1988b). The finest grid spacing should put the filter-width well within the inertial subrange, and the next-finest grid should show a nearly identical solution to confirm that our study begins in a region of grid-independent dynamics.

2.3 Results

2.3.1 Mean CBL development

The evolution of the CBL is first evaluated by considering hourly mean potential temperature profiles for the Smagorinsky-Lilly, TKE-1.5, DRM0 and DRM2 models at the finest resolution ($\Delta_{x,y} = 25$ m). Smagorinsky-Lilly and TKE-1.5 here use the WRF default coefficients where $C_s = 0.25$ and $C_k = 0.15$, respectively. Figure 2.1 shows that for all four models, the 25-m cases show very good agreement in the development of the CBL. Specifically, they feature a well-mixed surface with a visible but shallow super-adiabatic layer, a deepening neutral layer, and entrainment at the CBL top, as expected (Stull, 1988b). For all models, the 50-m cases (not shown) exhibit the same development and are nearly identical to the 25-m cases.

Now considering the $\Delta_{x,y} = 1$ km case for the Smagorinsky-Lilly model using the WRF default value of $C_s = 0.25$ (Fig. 2.2a), the mixing is clearly not sufficient to create the desired neutral layer. This is especially true in the first four hours where the profile does not diverge

from the initial profile above a height of approximately 900 m. It should be noted that the potential temperature profiles for the Smagorinsky-Lilly model in the WRF, presented here, may be sensitive to model parameters. For example, Efstathiou and Beare (2015) presented results using the Smagorinsky-Lilly model in the Met Office Large Eddy Model, which uses different stability functions and a height-dependent lengthscale; their profiles, while still insufficiently mixed, appear better than the WRF results at coarse resolutions, especially near the surface.

Simulations using the Smagorinsky-Lilly model that are coarser than 50-m resolution are all associated with a deeper super-adiabatic layer at the surface, even in the later hours when the profiles appear to be somewhat well-mixed. The observed delay in resolved mixing for the Smagorinsky-Lilly model can be seen more clearly by considering the evolution of the mean resolved vertical heat flux, $\langle \overline{w}'\overline{\theta}' \rangle$, in a horizontal plane 218-m above the surface (Fig. 2.3). The 25-, 50- and 100-m cases show very similar behavior: resolved mixing begins approximately 15 minutes into the simulation, with the initially-trapped warm air being released in a burst of buoyancy-induced mixing. In the 200-m case, a 25-minute delay in the resolved heat flux onset is observed. Furthermore, the 500-m case is delayed a full hour, and the 1-km case is delayed 2.5 hours. For all resolutions, the onset of resolved mixing is associated with a spike in $\langle \overline{w}'\overline{\theta}' \rangle$. For $\Delta_{x,y} \leq 200$ m, $\langle \overline{w}'\overline{\theta}' \rangle$ reaches a quasi-steady value in the first hour, while the coarser resolutions take increasingly longer to reach a steady mean planar value. Reconsidering the Smagorinsky-Lilly model's mean potential temperature profiles with the knowledge of suppressed resolved turbulent mixing in the early hours of the simulation, we see that resolved mixing is very important to the potential temperature profiles. Before resolved turbulence begins, the surface heat flux is trapped in the lower atmosphere because the SFS turbulence model is only designed to provide local diffusion and is thus unable to mix the column when resolved mixing is absent. After resolved turbulence begins and the model is fully spun-up, the profiles change considerably in shape and it is clear that there is mixing throughout the column; however, these profiles are still very inaccurate in comparison with the higher-resolution simulations.

The TKE-1.5 model, using the WRF default value $C_k = 0.15$, appears to perform much better at coarser resolutions based on the potential temperature profiles, and even the 1-km case agrees relatively well with the 25-m case (Fig. 2.4a). There is a smaller delay in resolved vertical heat flux in the 218-m plane, with the onset of the 1-km case being delayed approximately 30 minutes and taking about 2 hours to become steady (Fig. 2.5).

Using smaller coefficient values of $C_s = 0.18$ and $C_k = 0.10$ for the Smagorinsky-Lilly and TKE-1.5 models, respectively, does show a small degree of improvement in potential temperature profiles for both models. The Smagorinsky-Lilly model has slightly different results with the lower $C_s = 0.18$ coefficient at coarser resolutions, where profiles show resolved mixing earlier (Fig. 2.2b). However, once both cases begin to resolve mixing, the $C_s = 0.18$ profiles are less neutral than their $C_s = 0.25$ counterparts, and both cases have a super-adiabatic layer that is very sharp and extends more than 200 m vertically. For the lower C_s, the delay in resolved $\langle \overline{w}'\overline{\theta}' \rangle$ is reduced by about an hour in the 1-km case and by 30 minutes in the 500-m case (not shown). The TKE-1.5 model, which already agrees relatively well

with its 25-m case at coarse resolutions, improves noticeably via sharper gradients in $\theta(z)$ resulting in shallower surface layers and sharper inversions (Fig. 2.4b). The TKE-1.5 model using the lower C_k also sees the delay in resolved $\langle \overline{w}'\overline{\theta}' \rangle$ reduced to only 15 minutes when $\Delta_{x,y} = 1$ km and shows no delay in the 500-m case (not shown).

In an attempt to improve the performance of the Smagorinsky-Lilly and TKE-1.5 cases, isotropic lengthscales ($l_h = l_v = (\Delta_x \Delta_y \Delta_z)^{1/3}$) were also considered. Results are not presented here as all cases performed worse than their anisotropic counterparts. This is expected given the improvements seen using lower $C_{s,k}$ values, because isotropic lengthscales effectively only serve to increase K_v.

Examining the DRM, we see that for DRM0 the potential-temperature profiles show a well-mixed structure throughout the simulation even at 1-km resolution. The super-adiabatic surface layer and inversion layer are much closer to the 25-m case compared to equivalent resolutions using either Smagorinsky-Lilly or TKE-1.5, even when using decreased values for C_s and C_k (Fig. 2.6a). Using the DRM0, the onset of resolved convection in the 218-m plane shows a delay of less than 30 minutes for the 1-km case, slightly better than the TKE-1.5 model (Fig. 2.7). The mean resolved heat flux in the 1-km case takes approximately two hours to become steady. The 500-m and 1-km cases show a similar burst of $\langle \overline{w}'\overline{\theta}' \rangle$ when resolved convection begins, though this is shorter-lived than in the TKE-1.5 case and much shorter than the Smagorinsky-Lilly case.

The $\Delta_{x,y} = 1$ km potential temperature profiles for the DRM2 case also show great agreement with the corresponding $\Delta_{x,y} = 25$ m case, producing the most accurate entrainment layer of any of the models considered (Fig. 2.6b). The two levels of additional reconstruction (from DRM0 to DRM2) do add a small kink to the potential-temperature profiles near the surface, but the overall performance is quite good considering the coarseness of the grid and the performance of the eddy-viscosity models at the same resolution. The time series of $\langle \overline{w}'\overline{\theta}' \rangle$ for the DRM2 show the earliest resolved convection at all resolutions, the smallest bursts of upward resolved heat flux at all resolutions, and the earliest steadying at all resolutions (Fig. 2.8). The coarse DRM0 and DRM2 potential temperature profiles show a very slight warm bias in the bulk of the CBL when compared to their 25-m profiles. As shown in Zhou and Chow (2014), increasing levels of reconstruction in the DRM allows the model to resolve more turbulent fluxes under stably-stratified environments. Compared to the DRM0 in Fig. 2.6a, the 1-km DRM2 predicts slightly larger boundary-layer-top entrainment due to its higher reconstruction level, resulting in a warmer CBL. The performance the DRM under stably-stratified conditions at kilometer scale resolution will be examined in a future study.

Considering the time series of $\langle \overline{w}'\overline{\theta}' \rangle$ of the four models, it is expected that an LES will resolve less of any flux as the grid spacing becomes larger, because more energy is present in the SFS motions. The DRM0 and especially the DRM2 exhibit this behavior clearly while the Smagorinsky-Lilly and TKE-1.5 models maintain a similar resolved vertical heat flux magnitude for all resolutions considered. This is due to gray-zone issues such as overly-energetic resolved thermals and inaccurate SFS stress magnitudes in the latter two models.

The time series for $\langle \overline{w}'\overline{\theta}' \rangle$ when $\Delta_{x,y} = 25$ and 50 m for all models are taken from smaller 80×80 domains with high temporal output to minimize data storage.

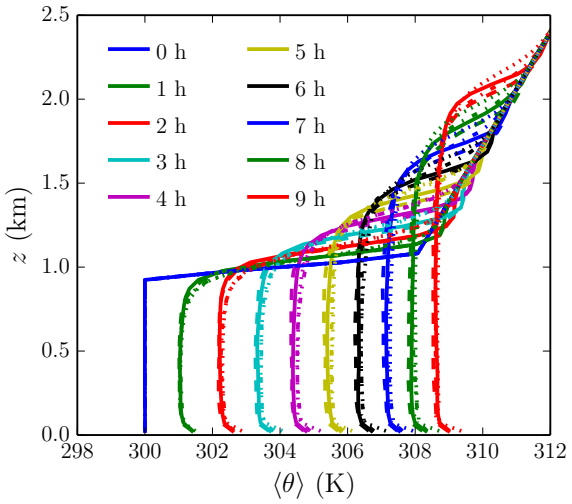

Figure 2.1: Hourly horizontally domain-averaged potential temperature profiles using the Smagorinsky-Lilly (solid), TKE-1.5 (dashed), DRM0 (dash-dotted) and DRM2 (dotted) models for the 25-m resolution case.

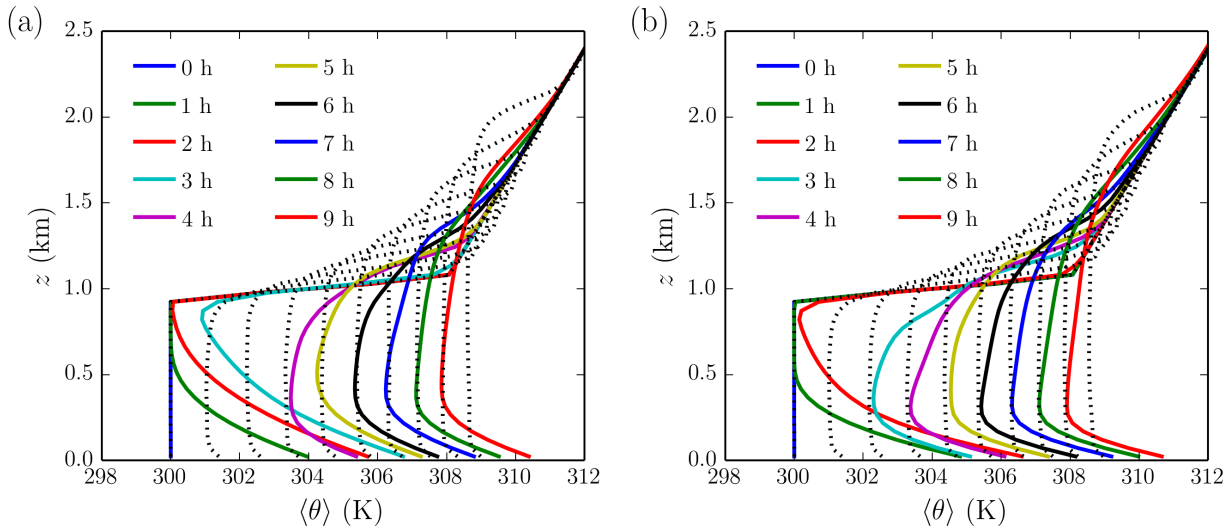

Figure 2.2: Hourly horizontally domain-averaged potential temperature profiles using the Smagorinsky-Lilly model with $C_s = 0.25$ (left) and $C_s = 0.18$ (right) for $\Delta_{x,y} = 1$ km, with profiles from the corresponding 25-m cases overlaid (dotted black).

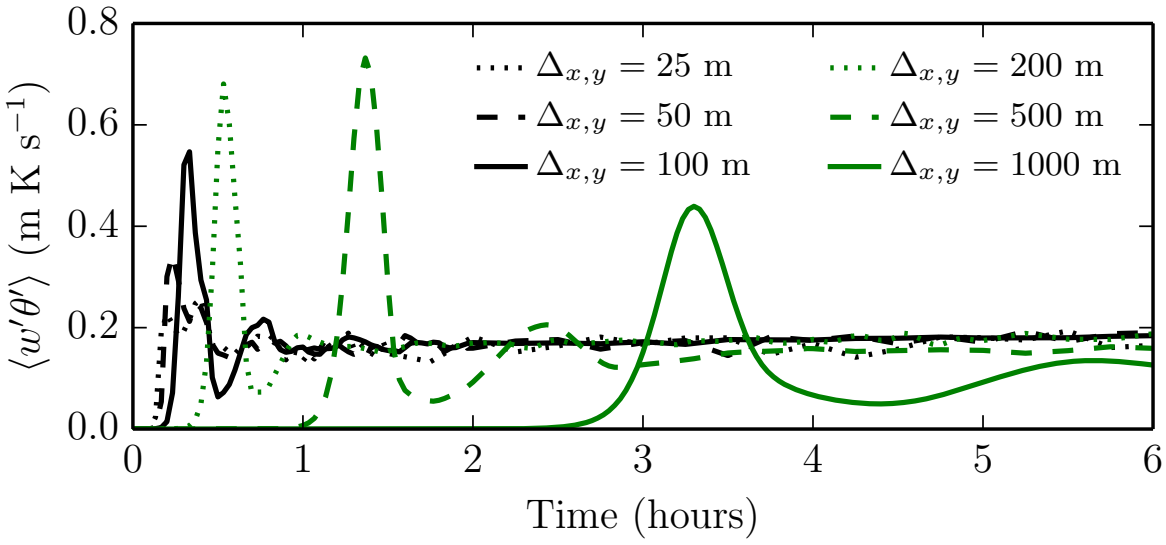

Figure 2.3: Mean value of resolved $w'\theta'$ in the 218-m plane (5th vertical level) using the Smagorinsky-Lilly model with $C_s = 0.25$ for resolutions from 25 m to 1 km. Planar averages are taken every 2 minutes initially and every 15 minutes once $\langle w'\theta' \rangle$ is approximately steady.

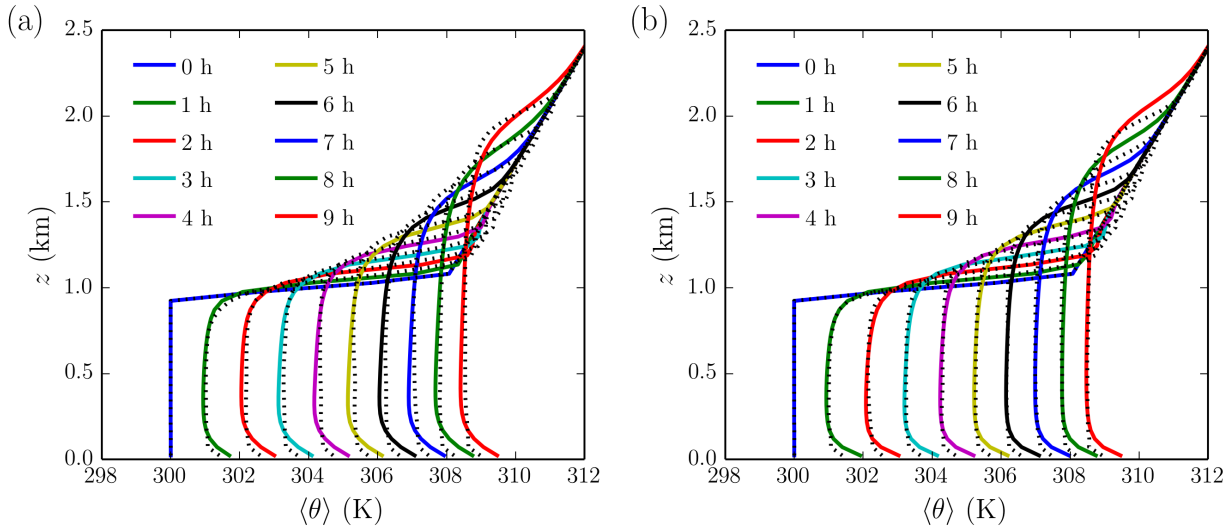

Figure 2.4: As in Fig. 2.2 but using the TKE-1.5 model with $C_k = 0.15$ (left) and $C_k = 0.10$ (right).

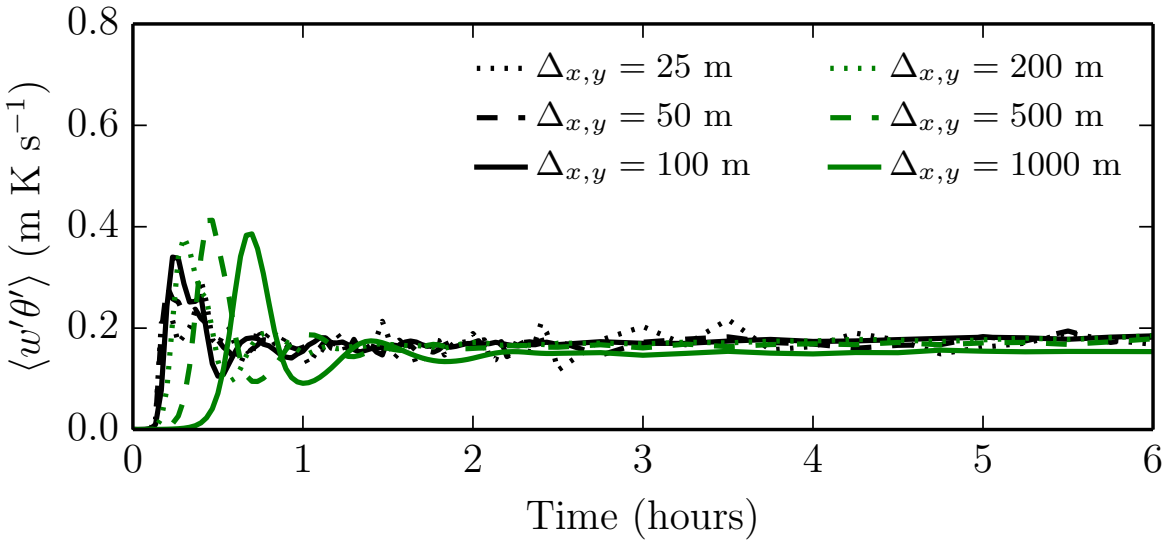

Figure 2.5: As in Fig. 2.3 but using the TKE-1.5 model with $C_k = 0.15$.

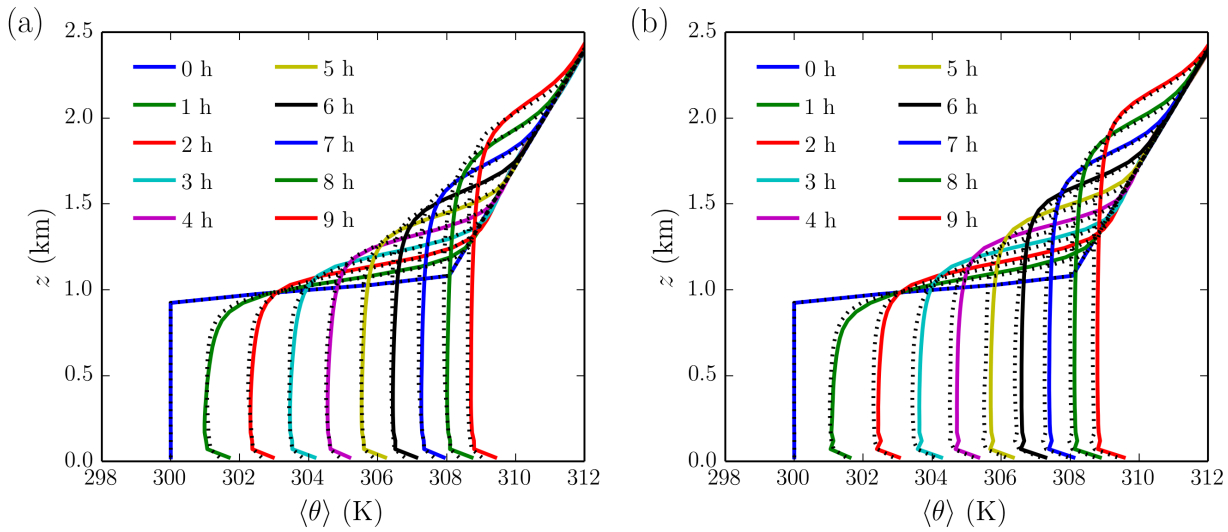

Figure 2.6: As in Fig. 2.2 but using the DRM0 (left) and DRM2 (right).

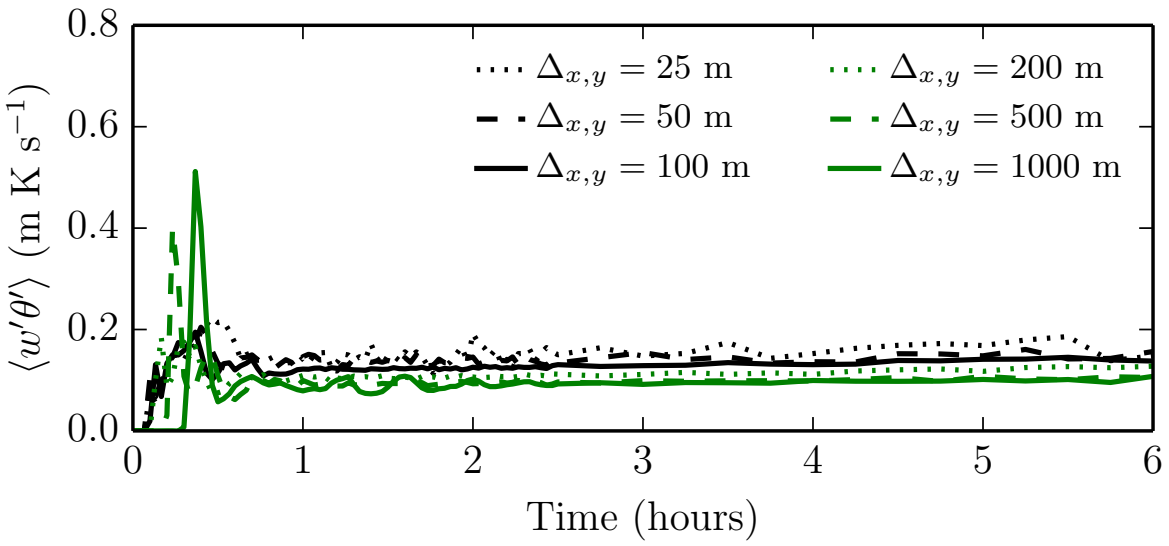

Figure 2.7: As in Fig. 2.3 but using the DRM0.

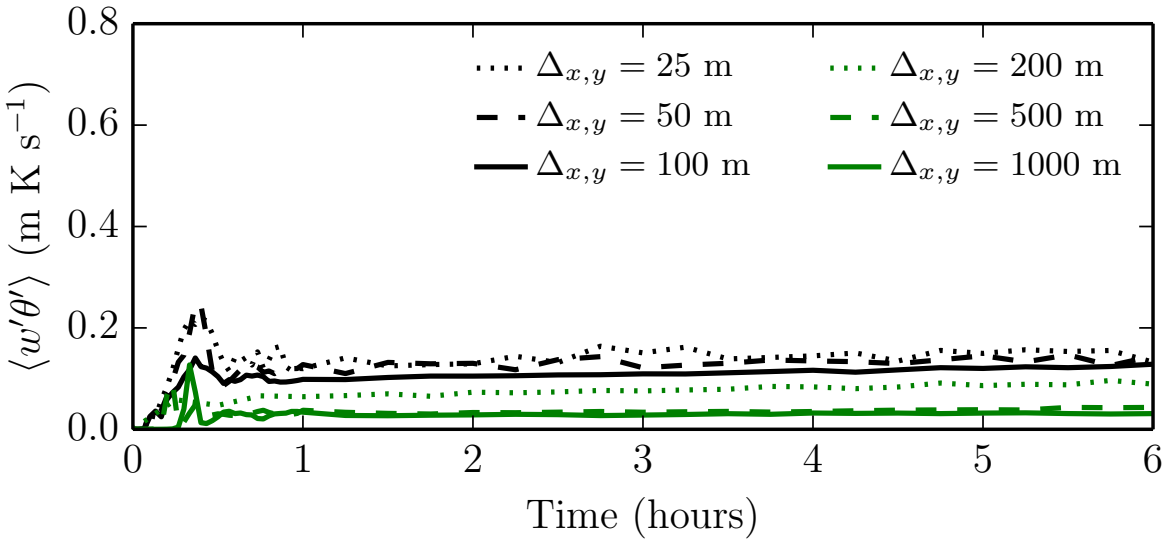

Figure 2.8: As in Fig. 2.3 but using the DRM2.

2.3.2 Turbulent vertical momentum stress profiles

Profiles of vertical turbulent momentum stresses ($w'w'$) at $t = 6$ h for the $\Delta_{x,y} = 500$ m and $\Delta_{x,y} = 1$ km cases are compared to filtered high-resolution cases for further evaluation in Fig. 2.9. Vertical fluxes of horizontal momentum ($u'w'$, $v'w'$) are not considered here because there is no mean wind present. The total (resolved + SFS) stress profiles should be consistent for different grid resolutions for the LES to be considered accurate. The resolved and SFS profiles are also shown individually for the TKE-1.5, DRM0 and DRM2 models to further illustrate their behavior as the grid coarsens. The high-resolution cases used for reference are the 25-m TKE-1.5 and DRM2 cases, which are filtered in each horizontal plane using a spectral cut-off filter where energy associated with a wavelength smaller than $2\Delta_{\text{filter}}$ is set to zero. The TKE-1.5 and DRM2 high-resolution cases are sufficient for comparison as the resolved stress profiles for the 25-m TKE-1.5 and Smagorinsky-Lilly cases are nearly indistinguishable, as are the total stress profiles for the 25-m DRM2 and DRM0 cases.

Only the resolved profiles are presented for the Smagorinsky-Lilly model because it does not store the isotropic portion of $\overline{S}_{ii}$ and thus an accurate τ_{33} term cannot be found. The Smagorinsky-Lilly model's resolved profile of $\langle \overline{w}'\overline{w}' \rangle$ is very similar to the DRM2 at $\Delta_{x,y} = 500$ m, and is similarly shaped to the DRM2 but approximately half the magnitude at $\Delta_{x,y} = 1$ km. It can be deduced from the resolved profiles and the model's poor overall performance in other metrics considered at coarse resolutions that the SFS contribution would not significantly improve its evaluation here. It will also be shown in later sections that the motions resolved by the Smagorinsky-Lilly model occur at wavelengths that are much larger than those in the high-resolution case.

The planar-averaged SFS stress profiles for the TKE-1.5 model are found as $\langle \tau_{33} + 2e/3 \rangle$ to account for the isotropic portion of $\overline{S}_{ii}$. Considering the planar-averaged total vertical momentum fluxes shown in Fig. 2.9, the TKE-1.5 model performs relatively poorly for both the 500-m and 1-km cases when compared to the high-resolution cases. The TKE-1.5 model produces the largest planar-averaged resolved flux ($\langle \overline{w}'\overline{w}' \rangle$) of all the models in the 500-m case and much more than any model except the DRM0 in the 1-km case. The 500-m TKE-1.5 case compares quite well to the filtered high-resolution TKE-1.5 case, however, later analysis shows that these motions again occur at much larger wavelengths. The TKE-1.5 planar-averaged SFS stress ($\langle \tau_{33} \rangle$) is the smallest of all of the models, however, generating a total flux profile that is much smaller in magnitude than either 25-m case, especially when $\Delta_{x,y} = 1$ km.

The SFS stress profiles for the DRM0 and DRM2 cases contain both the eddy-viscosity and the RSFS terms. The DRM0 has a much more significant SFS contribution than the TKE-1.5 model at both resolutions, leading to a total flux profile that is much closer to the TKE-1.5 and DRM2 high-resolution cases both in magnitude and shape, though still smaller than either high-resolution case in magnitude. The DRM2 has the largest SFS contribution of all the models due to the presence of the additional reconstruction terms representing the RSFS, resulting in the closest match to both high-resolution cases when considering the total flux profile. The DRM2 is especially accurate for the $\Delta_{x,y} = 500$ m case, where its total flux profile matches the DRM2 high-resolution case very closely.

Considering the total flux profiles, it is clear that the DRM2 is the closest match to the reference high-resolution cases of all four models at both resolutions, followed closely by the DRM0. The TKE-1.5 model performs much better than the Smagorinsky-Lilly model, but both perform poorly when compared to the DRM simulations.

Interestingly, filtering of the high-resolution TKE-1.5 case reveals a double-peak structure in the profile of τ_{33} that is much more exaggerated than for the DRM2, especially when filtered to $\Delta_{x,y} = 1$ km. The DRM's ability to produce single-peaked second moments of resolved vertical velocity has been noted in other studies as well (Shi et al., 2018).

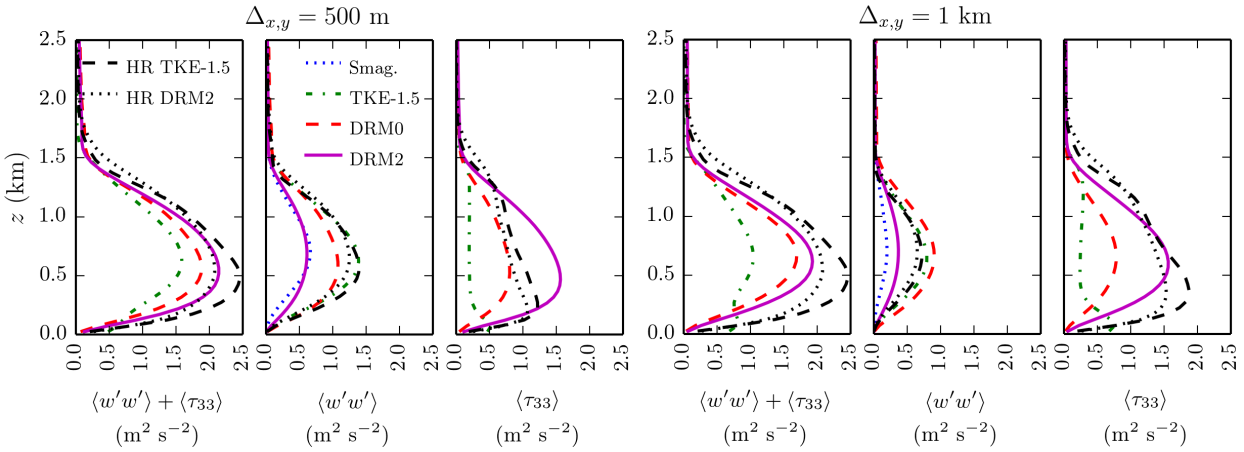

Figure 2.9: Planar-averaged total (resolved + modeled) vertical momentum flux ($\langle \overline{w}'\overline{w}' + \tau_{33} \rangle$), resolved vertical momentum flux ($\langle \overline{w}'\overline{w}' \rangle$), SFS vertical momentum flux ($\langle \tau_{33} \rangle$) for the TKE-1.5, DRM0, DRM2 and Smagorinsky-Lilly (resolved only) models after 6 hours when $\Delta_{x,y} = 500$ m (left) and $\Delta_{x,y} = 1$ km (right), compared to high-resolution cases ($\Delta_{x,y} = 25$ m) using the TKE-1.5 and DRM2 models filtered to the corresponding coarse resolution.

2.3.3 Vertical velocity fields

We next examine the vertical velocity field, $w(x, y)$, in the 218-m horizontal plane under coarsening horizontal resolution and compare to a high-resolution velocity field. The 218-m plane is chosen for its visual clarity of the convective cells formed near the surface. The coherent structures seen in w indicate the size of the convective cells formed at each resolution, which can then be compared to high-resolution results. A spectral filter applied to a high-resolution case is then used to examine the coarse models' ability to accurately capture the proper scales of motion at that grid size.

At high resolutions all four models appear very similar and demonstrate the thermal cells that are expected for a convectively-forced ABL with no mean wind. The TKE-1.5 model using 25-m horizontal resolution is shown in Fig. 2.10; the other three models are omitted because they are similar. As the horizontal resolution is coarsened, the size of the

convective cells should not change and the resolved motions should be similar to those of the spectrally-filtered high-resolution case.

Examining the resolved w fields of the coarser cases using the Smagorinsky-Lilly model ($C_s = 0.25$) shows the familiar cellular structure in the 100-m case (Fig. 2.11). The 200-m case looks similar, but the cells are visibly larger in their characteristic size. This pattern continues for the 500-m and 1-km cases, where very large cells are resolved on the grid. Also note that these cells are much larger than the grid's Nyquist limit. Reducing the Smagorinsky coefficient to $C_s = 0.18$ shows a reduction in the size of the thermal cells at coarser resolutions, though they remain extremely large compared to any of the high-resolution cases (Fig. 2.12). Note that all the w slices are shown over a 20 km $\times$ 20 km subdomain for comparison, though the actual simulations follow the domain sizes given in Table 2.1.

The resolved fields for the coarser cases using the TKE-1.5 model ($C_k = 0.15$) show a similar trend to the Smagorinsky-Lilly model but to a smaller degree (Fig. 2.13). For comparison, the cells on the 1-km grid using the TKE-1.5 model appear similar in size to the cells seen on the 200-m grid using the Smagorinsky-Lilly model, although the field is generally smoother between the updrafts of the thermal cells for the Smagorinsky-Lilly model. Reducing the coefficient for the TKE-1.5 model to $C_k = 0.10$ shows a similar reduction in the size of the thermal plumes, however the fields still contain very large structures (Fig. 2.14).

When using the DRM0 at fine resolutions ($\Delta_{x,y} \leq 200$ m) the resolved vertical velocity field shows a cellular nature, as expected (Fig. 2.15). As the grid coarsens, the resolved w field that the DRM0 produces becomes less coherent, in contrast to the large cells produced by standard eddy-viscosity models. The coarse DRM2 cases are qualitatively very similar to the DRM0 results, but with smaller magnitudes seen for both updrafts and downdrafts (Fig. 2.16). A quantitative comparison between the scales of energy present in the coarse cases and the scales present in the cellular, high-resolution cases is presented in Sec. 2.32.3.4.

For comparison to the coarser cases, the 25-m TKE-1.5 case is filtered in the same manner as in Sec. 2.32.3.2 (Fig. 2.17). The spectral filter selects the resolved large-scale motions present in the high-resolution cases, which should ideally be reproduced by the coarse-resolution LES simulations. Filtering the high-resolution case using different filter cut-offs shows a resolved field which loses its cellular nature after a horizontal resolution of approximately 200 m. The DRM0 and DRM2 are the only models which qualitatively agree with the filtered case at coarser resolutions, implying that the turbulent structures resolved by the two DRM models are more accurately represented than those from the eddy-viscosity models.

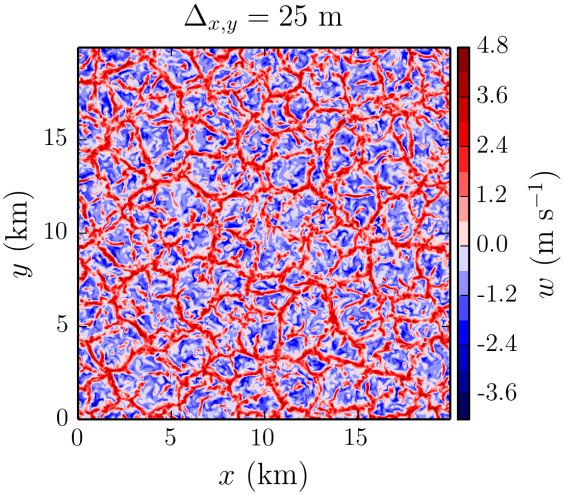

Figure 2.10: Resolved vertical velocity (w) field in the 218-m plane at hour 6 for $\Delta_{x,y} = 25$ m. All four models produced very similar fields; only the TKE-1.5 model is shown.

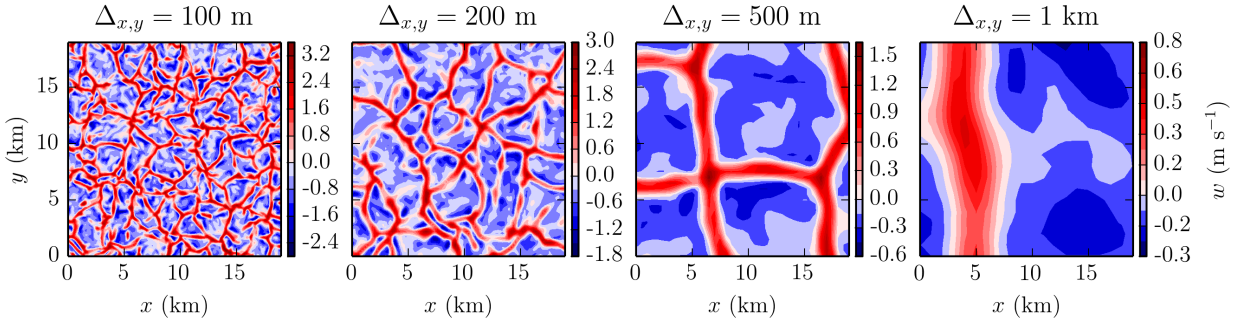

Figure 2.11: Resolved vertical velocity (w) field in the 218-m plane at hour 6 using the Smagorinsky-Lilly ($C_s = 0.25$) model for $\Delta_{x,y} = 100$, 200, 500 and 1000 m. All cases are plotted as 20×20 km^2, but actual domain sizes follow Table 2.1.

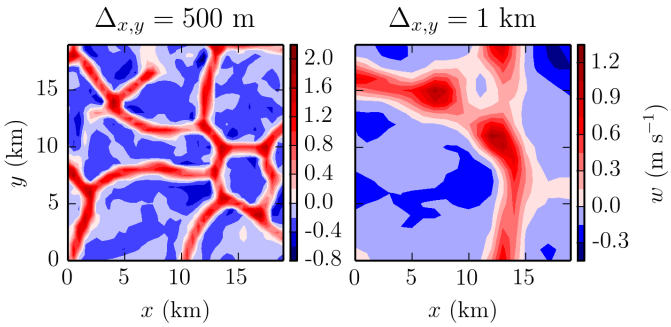

Figure 2.12: As in Fig. 2.11 but using the Smagorinsky-Lilly ($C_s = 0.18$) model for $\Delta_{x,y} =$ 500 m and 1 km.

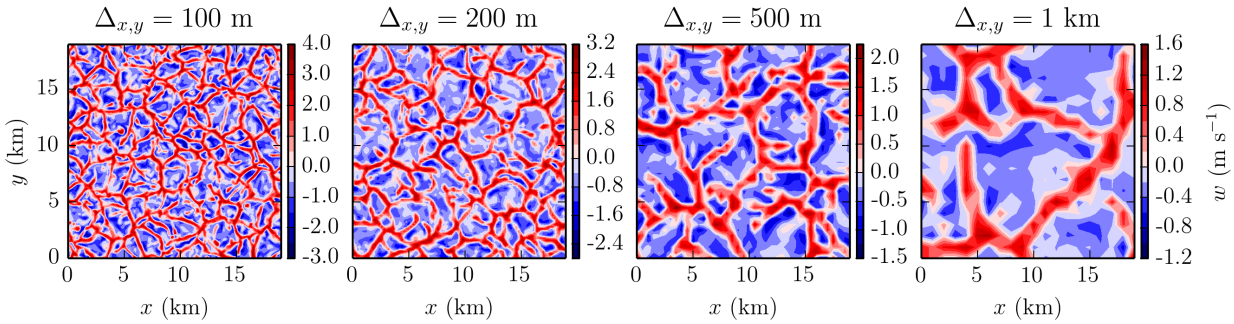

Figure 2.13: As in Fig. 2.11 but using the TKE-1.5 ($C_k = 0.15$) model.

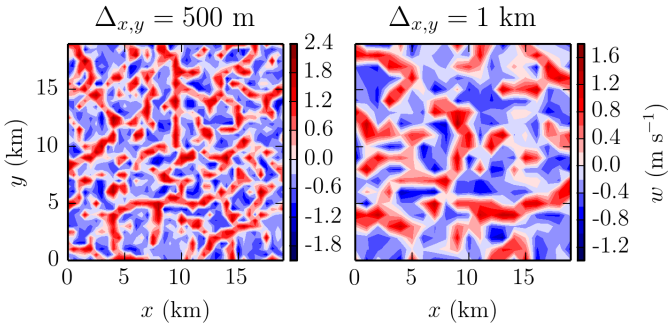

Figure 2.14: As in Fig. 2.11 but using the TKE-1.5 ($C_k = 0.10$) model for $\Delta_{x,y} =$ 500 m and 1 km.

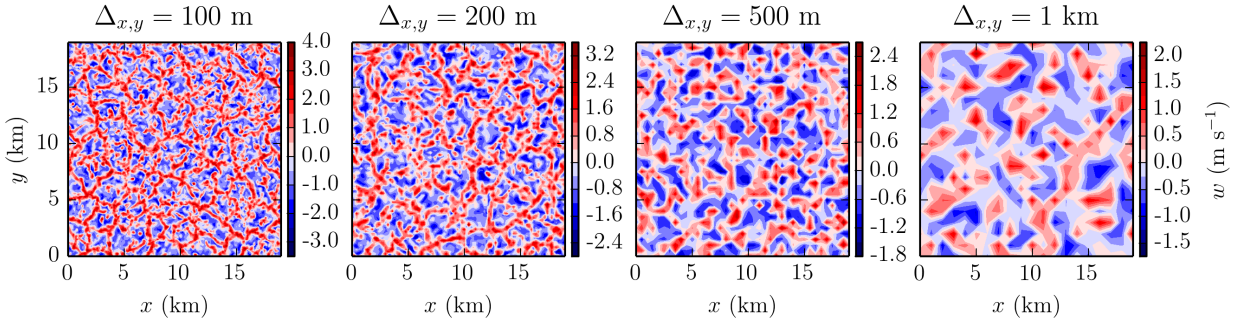

Figure 2.15: As in Fig. 2.11 but using the DRM0.

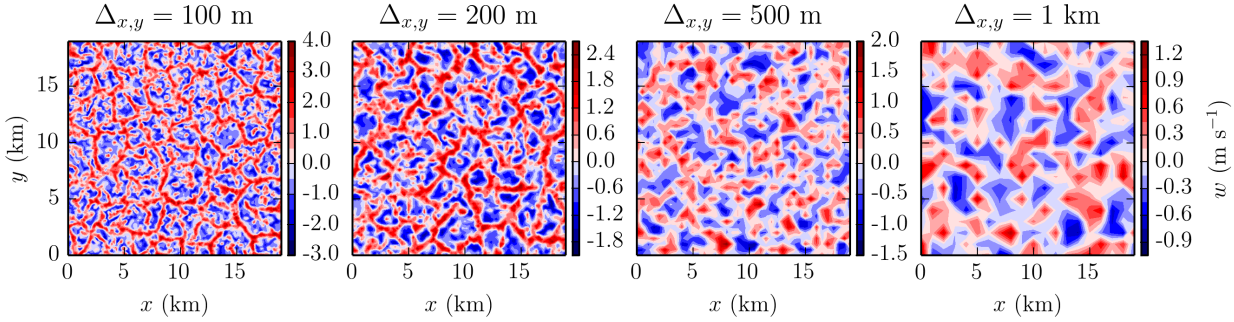

Figure 2.16: As in Fig. 2.11 but using the DRM2.

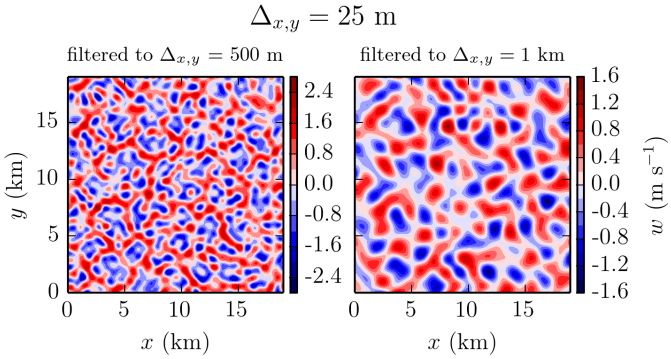

Figure 2.17: Filtered resolved vertical velocity (w) field in the 218-m plane at hour 6 for the 25-m TKE-1.5 case, filtered to $\Delta_{x,y} = 500$ m (left) and $\Delta_{x,y} = 1$ km (right).

2.3.4 Turbulent energy spectra

The one-dimensional spectral energy densities of w' as a function of the horizontal wavenumber $k_h = \left(k_x^2 + k_y^2\right)^{1/2}$ divided by the domain length, L, for the Smagorinsky-Lilly ($C_s = 0.25$), TKE-1.5 ($C_k = 0.15$), DRM0 and DRM2 models taken at $z = 667$ m (approximately the center of the CBL) after 6 hours are shown in Fig. 2.18. All models agree very closely with each other as well as with the theoretical $k^{-5/3}$ decay rate at high resolutions ($\Delta_{x,y} = 25$ m shown), but disagree significantly when $\Delta_{x,y} = 1$ km. The ideal spectrum at a coarse resolution would follow the high-resolution spectra until the grid's Nyquist limit (Skamarock, 2004). The Smagorinsky-Lilly model is so dissipative that very little energy is resolved other than at very coarse modes, resulting in too much energy at the grid's coarse scales and not enough energy at the grid's fine scales, as was seen qualitatively in Sec. 2.32.3.3. The TKE-1.5 model performs much better in that it allows much more energy to develop on the grid's finer scales. However, similar to Smagorinsky-Lilly, the TKE-1.5 model allows too much energy to build up at coarser resolutions, generating the larger, cohesive structures seen in the $w(x, y)$ fields. This can be addressed to some degree via changing the $C_{s,k}$ values for the Smagorinsky-Lilly and TKE-1.5 models, respectively, (spectra not shown) which reduces the energy in long waves and increases the energy in short waves, though this creates a very case-specific turbulence model that is still not particularly accurate. The DRM0 is the closest of the four models to matching the spectral density of the high-resolution cases, and excels both in terms of avoiding a buildup of energy at large scales and in allowing energy to develop on the grid's finer scales. The DRM0 also has the sharpest decay when approaching the grid's Nyquist limit, with a peak energy that is the closest of the four to the high-resolution cases.

It was seen in Sec. 2.32.3.2 that the DRM0 resolves more turbulent stress than the DRM2 due to the expected increase in the SFS term of the DRM2 from its RSFS terms. This relationship is seen again in the spectra, where the DRM0 and DRM2 agree closely at large scales but the DRM0 has more energy than the DRM2 at finer scales. This again is attributed to the DRM2 RSFS contribution, which is larger due to the higher level of velocity reconstruction (Chow et al., 2005). In Sec. 2.32.3.2, the TKE-1.5 and DRM0 models had very similar profiles of resolved variance, $\langle \overline{w}'\overline{w}' \rangle$, but we can see in the spectra (and in Sec. 2.32.3.3) that the TKE-1.5 model's resolved energy occurs at much larger wavelengths than the DRM0 despite their similar total resolved stress throughout the profile. This is consistent across energy spectra taken at different vertical levels (not shown).

To make a quantitative evaluation of the size of the thermal cells, the dominant wavelength of the resolved vertical velocity field is approximated by the critical wavelength $\lambda_c = 1/k_c$ (the 2π is omitted because we are interested in meters per cycle, rather than meters per radian, to get a better physical intuition of the quantities). k_c is defined as the wavenumber where 2/3 of the velocity variance seen in the physical field ($\langle w'w' \rangle$ in this case) is contained between k_c and k_N, the Nyquist limit, on the energy spectrum, S, of the turbulent velocity.

For w' using a discrete Fourier transform, we can say

$$\frac{2}{3}\langle \overline{w}'\overline{w}' \rangle = \sum_{k_c}^{k_N} \overline{\mathcal{S}}_{33}. \tag{2.2}$$

Values for λ_c are found here by considering the same one-dimensional energy spectra shown in Fig. 2.18 and finding the smallest k_c value where $2/3\langle \overline{w}'\overline{w}' \rangle \geq \sum_{k_c}^{k_N} \overline{\mathcal{S}}_{33}$ for each case. This can be considered similar to taking the median of a sample, and is used for its reduced sensitivity to noise in determining the peak of the spectrum (de Roode et al., 2004). The critical wavelength is computed in the same 218-m plane seen in Figs. 2.10 – 2.17. Calculating λ_c is sensitive to domain size and requires a domain large enough to have negligible energy at the largest scales. To this end, some cases required domains up to 25% larger in the horizontal to achieve statistics independent of domain size for λ_c.

In Fig. 2.19, all four models have a consistent dominant wavelength $\lambda_c \approx 1$ km for $\Delta_{x,y} \leq 100$ m, and agree very well with each other. At 200 m, the Smagorinsky-Lilly, TKE-1.5 and DRM2 models begin to show increasing dominant wavelengths and all four models begin to diverge from each other. When $\Delta_{x,y} = 500$ m the Smagorinsky-Lilly model's critical wavelength is greater than 6 km and by $\Delta_{x,y} = 1$ km the Smagorinsky-Lilly model's critical wavelength has increased 20-fold from the $\Delta_{x,y} = 25$ m case value of $\lambda_c = 1.0$ km to $\lambda_c = 19.8$ km. The TKE-1.5 model's increase from $\lambda_c = 1.1$ to $\lambda_c = 4.6$ km for the same change in resolution appears modest when compared to Smagorinsky-Lilly, but it is still nearly a 5-fold increase and is also more than twice the size of the grid's Nyquist limit of 2 km.

The DRM0 and DRM2 show a more consistent value for λ_c as horizontal resolution increases. The DRM2, as noted above, shows a small increase when $\Delta_{x,y} = 200$ m, but does not grow as quickly as TKE-1.5. Both DRM0 and DRM2 begin to show a notable increase in λ_c when $\Delta_{x,y} = 1$ km with $\lambda_c = 2.9$ km for DRM0 and $\lambda_c = 3.3$ km for DRM2. Note that some increase is inevitable because the $\Delta_{x,y} = 25$ m critical wavelength (~ 1 km) is smaller than the 1-km grid's Nyquist limit of 2 km. Interestingly, the DRM2 has a slightly larger critical wavelength than the DRM0 at coarse resolutions and is somewhat comparable to the TKE-1.5 model by the λ_c metric, especially at $\Delta_{x,y} = 500$ m, however the magnitude of the resolved energy is much lower than the TKE-1.5 model (seen in Figs. 2.9 and 2.18), resulting in a more accurate w field.

As we have seen, different LES turbulence models have varying responses to coarse (gray zone) resolutions due to differences in their formulation, implying that the models should not necessarily share criteria for being in the gray zone. Along these lines, Beare (2014) explored the lengthscales of the gray zone and suggested that the conventional wisdom that the gray zone begins when $z_i \sim \Delta_{x,y}$ (where z_i is the inversion depth) does not sufficiently capture the nuances of the turbulence model. They instead introduced the dissipation lengthscale, λ_d, which is the wavelength where turbulent dissipation begins in the energy spectrum. The result of the horizontal resolution and underlying numerical schemes on a turbulence model's performance can be encompassed by λ_d, defined as $\lambda_d = 1/k_d$, where

$$k_d^2 = \frac{\sum k^2 \overline{\mathcal{S}}_{33}}{\sum \overline{\mathcal{S}}_{33}}. \tag{2.3}$$

Beare (2014) found that the gray zone begins when $\lambda_p = 1.4\lambda_d$, where λ_p is the peak wavelength of the turbulent energy spectrum [here we are assuming $\lambda_p \approx \lambda_c$ from Eq. 2.2)]. When λ_c is considered as a function of λ_d, instead of a function of $\Delta_{x,y}$, the relationships for the four models essentially overlap, indicating that the dissipation lengthscale is a much more general predictor of the gray zone than horizontal resolution (Fig. 2.20). After considering the energy spectra and λ_c versus $\Delta_{x,y}$ for the four models, it is not surprising that the DRM0 and DRM2 also show the slowest increase in dissipation lengthscale as resolution coarsens.

Generally we agree with Beare (2014) that λ_c or λ_d are useful metrics for diagnosing the boundaries of the gray zone. Specifically, using λ_d as the characteristic lengthscale for a given grid resolution, in lieu of $\Delta_{x,y}$, provides a much more accurate measure of the limits of motions that can be represented numerically. The dissipation lengthscale is also useful for comparing the gray zones for different turbulence models because it includes the effects of the specific models on the energy spectra, which is crucial to turbulent dynamics in the gray zone.

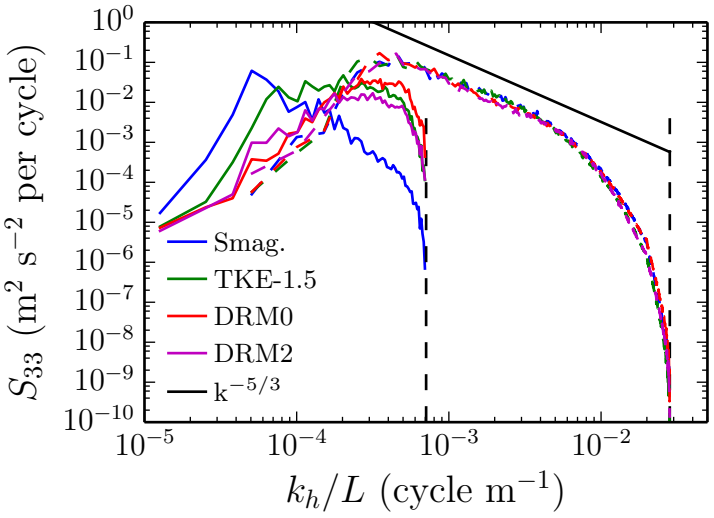

Figure 2.18: Spectral energy density of w' as a function of k_h/L, where k_h is the horizontal wavenumber and L is the domain length, for the Smagorinsky-Lilly, TKE-1.5, DRM0 and DRM2 models in the 667-m plane after 6 hours at 25-m (dashed) and 1-km (solid) resolutions. Nyquist limits of the respective grids also shown (dashed black).

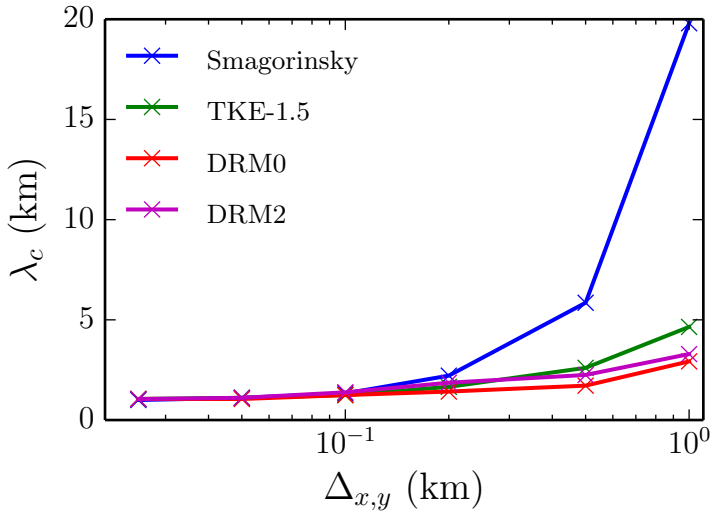

Figure 2.19: Horizontal resolution vs. critical wavelength of resolved w' in the 218-m plane after 6 hours for Smagorinsky-Lilly, TKE-1.5, DRM0 and DRM2 for resolutions from 25 m to 1 km. Calculated by applying Eq. 2.2).

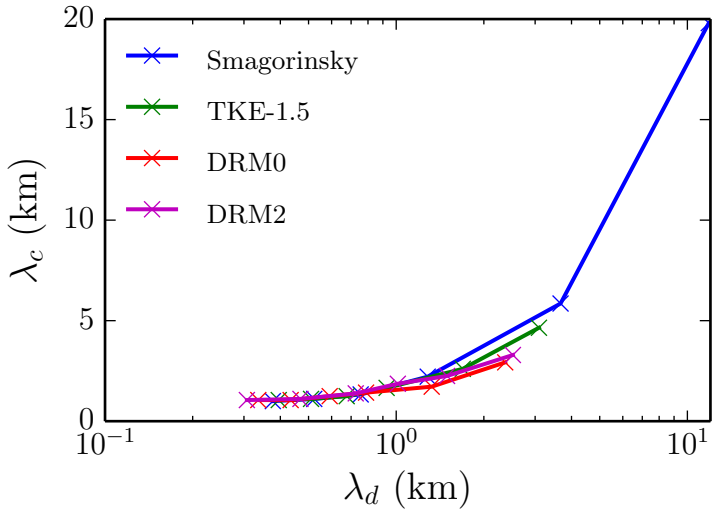

Figure 2.20: Dissipation wavelength vs. critical wavelength of resolved $w'w'$ in the 218-m plane after 6 hours for Smagorinsky-Lilly, TKE-1.5, DRM0 and DRM2 for resolutions from 25 m to 1 km. Calculated by applying Eqs. 2.2 and 2.3.

2.3.5 Backscatter in the DRM

Energy transfer between resolved and SFS scales is represented by the dissipation, Π, defined as

$$\Pi = -\tau_{ij}\overline{S}_{ij}. \tag{2.4}$$

When Π is positive it represents dissipation, i.e. energy transfer from resolved to SFS scales, which is a primary function of an LES turbulence model. Π is called dissipation because it is largely positive, although negative values (backscatter of energy from the SFS to the resolved scales) are also seen in atmospheric observations (Port-Agel et al., 2001; Carper and Porté-Agel, 2004). Eddy-viscosity models are purely dissipative by their formulation, which does not allow $K_{h,v}$ to take negative values. Because τ_{ij} and $\overline{S}_{ij}$ are always opposite in sign (or zero) for these models due to their definition of τ_{ij} [Eq. (1.39)], Π can never be negative. Scale-similarity models are not constrained in the same way, and do allow for energy transfer from SFS to resolved scales via negative dissipation values (Zhou and Chow, 2011).

PDFs of Π for all four models considered, normalized by their standard deviations, σ, are shown for the $\Delta_{x,y} = 200$ m (Fig. 2.21a) and $\Delta_{x,y} = 1$ km (Fig. 2.21b) cases. Data from the 4th to 20th vertical levels (from $z = 218$ m to $z = 976$ m) are used to compute the PDF of dissipation values within the well-mixed layer of the boundary layer. PDFs at other grid resolutions show similar behavior and are not shown here. The Smagorinsky-Lilly and TKE-1.5 models have only positive dissipation values, as expected. The DRM0 and DRM2 show a significant backscatter component and compare well to the observations of τ_{33} seen by Carper and Porté-Agel (2004). For the $\Delta_{x,y} = 200$ m ($\Delta_{x,y} = 1$ km) case, 42% (47 %) of the gridpoints produce backscatter accounting for 35% (47%) of the total stress by magnitude-weighted average using the DRM0, and 43% (52 %) of the gridpoints produce backscatter accounting for 41% (56%) of the total stress by magnitude-weighted average using the DRM2. Backscatter in the DRM is nearly entirely attributed to the scale-similarity term. The eddy-viscosity component of the DRM is not a significant contributor to backscatter because the dynamic coefficient is constrained to $c_\epsilon \Delta_f^{4/3} > -1.5 \times 10^{-5}$.

That the DRM creates backscatter is one reason that it performs well at coarse resolutions. Specifically, the DRM allows backscatter of energy from the SFS to the resolved scales, introducing resolved energy near the grid's Nyquist limit that is not seen in the eddy-viscosity models. The positive effects of backscatter are especially pronounced at the coarse resolutions considered here due to the important role of energy near the grid's Nyquist limit.

2.3.6 Other considerations

Given the sensitivity of the CBL evolution to the closure models, changes to several other aspects of the numerical configuration were also explored. Changing from 3rd- to 5th-order advection has little influence on the dynamics (not shown). Changing the vertical advection to an even, 4th-order scheme, which does not contain any numerical diffusion, does tend to reduce the delay of resolved mixing by a few minutes in both the 500-m and 1-km cases (not shown). While the eddy-viscosity model is primarily responsible for the grid-dependent

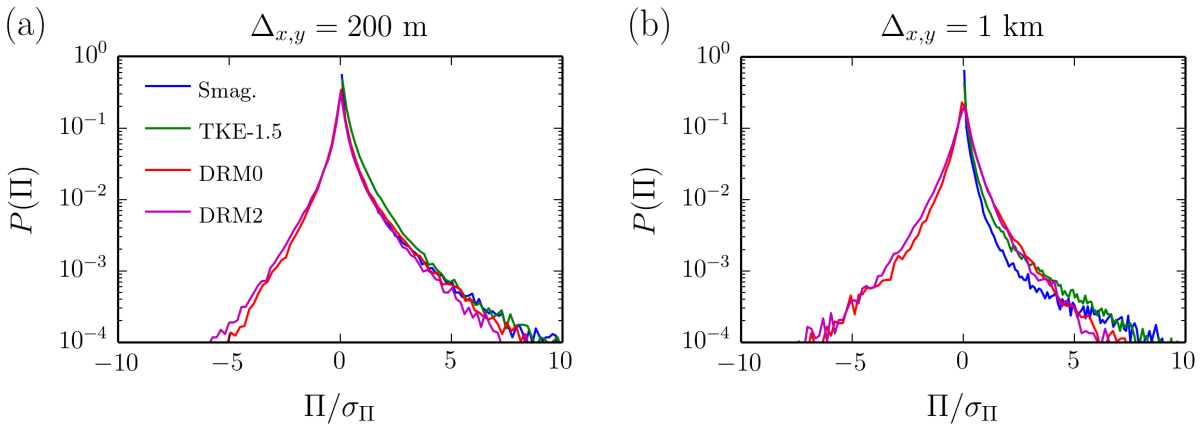

Figure 2.21: PDF of dissipation in 16 horizontal planes, from the 4th to 20th vertical level, at hour 6 for the Smagorinsky-Lilly, TKE-1.5, DRM0 and DRM2 models at 200-m (left) and 1-km (right) resolutions. The Smagorinsky-Lilly and TKE-1.5 models have only positive dissipation values while the DRM0 and DRM2 both show a large backscatter component.

effects seen, the numerical diffusion present in the default 3rd-order vertical advection term exacerbates the issue of overly damping the high wavenumbers. Changing the horizontal advection scheme between odd- and even-ordered does not have a noticeable effect on the dynamics for the convectively-driven case considered here.

Increasing the vertical resolution has little effect on the size of the resolved thermal cells or the delay in resolved turbulence. Coarser vertical-resolution cases were also tested, in accordance with Mirocha et al. (2010), who advise an aspect ratio ($\alpha = \Delta_{x,y}/\Delta_z$) of 2 – 4. Ultimately, even large changes in vertical resolution have little influence on the presence of large resolved thermal structures seen with coarse horizontal resolution. [Zhou et al. (2018) explored the use of increased horizontal refinement near the surface to alleviate the impact of unrealistic large thermal structures.]

Alternative surface-stress implementations [as in Mirocha and Lundquist (2017)] were used for the Smagorinsky-Lilly model but had minimal impact on its performance and are not shown here. The Dynamic Wong-Lilly eddy-viscosity model alone, without any scale-similarity or velocity reconstruction, outperforms the Smagorinsky-Lilly and TKE-1.5 models based on all of the criteria considered here, however it is inferior to the DRM0 and DRM2 and is thus not presented.

The current DRM implementation in WRF has not been optimized and requires approximately twice as long to run compared to the eddy-viscosity closure models. In other codes, the DRM has been found to increase computational cost by only 25 – 60% depending on the level of reconstruction (Chow et al., 2005; Kirkil et al., 2012; Shi et al., 2018).

2.4 Summary and conclusions

The gray zone refers to a range of resolutions where there exists no fundamentally appropriate turbulence model. The gray zone for a CBL simulation includes resolutions which lie between the traditional application of mesoscale PBL parameterizations and LES closure models, and is often generally defined to be the range when horizontal resolutions are $\mathcal{O}(1$ km). The gray zone is specific not only to the mesoscale and fine-scale turbulence models chosen, but also to the physics of the case being simulated. Here, simulations performed at various resolutions and with different closure models allowed a detailed examination of the gray zone for the convectively-forced atmospheric boundary layer. Vertical profiles of potential temperature and turbulent fluxes, time series of resolved fluxes, horizontal slices of vertical velocity fields and energy spectra of coarse simulations were compared to higher-resolution simulations.

Based on the dependence of the critical wavelength, λ_c, on horizontal resolution, the gray zone appears to begin at $\Delta_{x,y} \approx 200$ m for both the Smagorinsky-Lilly and TKE-1.5 models. This is in agreement with prior studies in the literature (Beare, 2014; Zhou et al., 2014; Efstathiou and Beare, 2015) which also include other numerical weather prediction models in addition to WRF. Both eddy-viscosity models are problematic at coarse resolutions because the fine-scale motions, relative to the grid, are damped, forcing the model to resolve turbulence at artificially large scales. The eddy-viscosity models also are unable to produce accurate total (resolved + SFS) stress profiles when compared to high-resolution LES statistics. However, the TKE-1.5 model, despite its deficiencies, is significantly superior to the Smagorinsky-Lilly model in the gray zone.

The DRM is a mixed model which allows backscatter of energy from small to large scales. In the DRM the scale-similarity component is designed to reconstruct structures that are large enough to be resolved on the grid but are removed due to the implicit filter of the LES. Because the filter width is explicitly included in the DRM, it provides a potential solution for turbulence modeling at both LES resolutions and in the gray zone. Due to the DRM's explicit filtering, numerical errors are overall reduced [see Gullbrand and Chow (2003)]. Then, reconstruction allows better representation of grid-scale turbulent motions (near the grid cutoff). Other dynamic model implementations have considered the choice of the test filter relative to the grid cutoff as a way to improve this further (Schaefer-Rolffs, 2017). For example, using either the DRM0 or DRM2 at resolutions coarser than 200 m shows a much better qualitative and quantitative agreement with the high-resolution simulation results than the standard Smagorinsky-Lilly or TKE-1.5 closures. The DRM2 especially excels at producing accurate total stress profiles at coarse resolutions when compared to high-resolution cases. By using the DRM turbulence closure, the extent of the gray zone is greatly reduced for this convective case. Explicit filtering and reconstruction using the DRM produces realistic dynamics using a horizontal resolution as coarse as 1 km without any tuning to account for either the coarseness of the grid or the physics of the case being considered. The ability of the DRM to produce realistic turbulence on a coarse grid by reconstructing RSFS motions is very encouraging and will be the subject of future work where more complex cases will be considered.

Acknowledgments. We are grateful for support from a Presidential Early Career Award for Scientists and Engineers (PECASE) and from National Science Foundation (NSF) grant ATM-0645784 (Physical and Dynamic Meteorology Program). JDM's contribution was supported by LLNL under Contract DE-AC52-07NA27344 and by the U.S. Department of Energys Wind Energy Technologies Office. BZ's contribution was supported by the National Key R&D Program of China under Grant 2018YFC1506802. Acknowledgement is also made to the National Center for Atmospheric Research (NCAR), which is sponsored by NSF, and to the Savio computational cluster provided by the Berkeley Research Computing program at the University of California, Berkeley (supported by the UC Berkeley Chancellor, Vice Chancellor for Research, and Chief Information Officer) for computing time used in this research. We also thank James Neher for updating DRM for WRF 3.8.1. Finally, a sincere thank you to the reviewers for their careful reading and thoughtful review of the first submission of this manuscript.

Chapter 3

More on the formulation and performance of eddy-viscosity models in WRF-LES

3.1 Introduction

The turbulent gray zone problem is typically defined in terms of the scale of $\Delta_{x,y}$ compared to the energetic scale of the atmospheric boundary layer (ABL). However, considering that fine-scale turbulence closure models typically assume isotropic turbulence in their derivations, and considering also that isotropic grids are only feasible in numerical weather prediction (NWP) models at very high resolutions, the gray zone could be conceptually re-cast as an inability to model scale-correct resolved turbulence on anisotropic grids (that is, on grids where $\Delta_{x,y} \approx \Delta_z$ cannot be said).

As well, there is not a consensus among models as to how to partition τ_{ij} in an anisotropic eddy-viscosity model (that is, a formulation that uses differing turbulent lengthscales depending on the orientation of the stress term). The effect of different implementations, especially for the Weather Research and Forecasting (WRF) model, is also not clear in the literature.

In Ch. 2 the anisotropic Smagorinsky-Lilly and TKE-1.5 models were compared to the DRM0 and DRM2 models for a purely convective case. The results seen there for the eddy-viscosity models will be elaborated on here by considering a more realistic initial profile as well as different potential formulations of Smagorinsky-Lilly and TKE-1.5 models.

In this chapter we outline how WRF currently partitions the deformations and lengthscales for anisotropic Smagorinsky-Lilly and TKE-1.5 model implementations, and the improvement or regression associated with differing, but justifiable, formulations relative to each other and isotropic formulations.

We also note that the current (prior to version 4.1.3) implementation of the turbulent stress tensor in the WRF model uses K_v to calculate τ_{13} and K_h to calculate τ_{31}, which the WRF development team considers to be incorrect but was unaware of prior to our notification.

3.2 Turbulent stress implementations in WRF

For any of these anisotropic eddy-viscosity formulations, it is not necessarily immediately clear which $K_{h,v}$ should be used for the calculation of τ_{31} (the $\partial w/\partial t$ term associated with $\partial u/\partial z$) and τ_{33} (the $\partial w/\partial t$ term associated with $\partial w/\partial z$). Arguments based on either scaling or symmetry could be made for using either value of K in either of the stress terms, and theoretical speculations seem unnecessary when numerical experiments could so easily be performed.

In the most recent release of WRF (version 4.1.2 at the time of writing), K_h is used when considering contributions to $\partial w/\partial t$ from both $\tau_{31,33}$. The use of K_h for τ_{31} could be justified by considering that the gradients of τ_{31} are taken over ∂x when considering $\partial w/\partial t$, which is reasonable. It could also be argued that K_v should be used instead to be consistent with τ_{13} for symmetry reasons, which seems equally reasonable.[1] The use of K_h for τ_{33} is ostensibly related to symmetry with $\tau_{11,22}$, but again the use of K_v or a different treatment entirely could be argued based on energetics [e.g. Wajsowicz (1993)]. It should be noted in both cases that any assumptions related to the forms of $\tau_{13,33}$ that assume an isotropic grid are most likely to be invalid in any NWP application, which is rarely performed on isotropic grids.

In an attempt to alleviate the general confusion on the roles and influences of each component of the turbulent stress tensor, we consider the effect of changing K_h for K_v in either or both of these stresses for the Smagorinsky-Lilly and TKE-1.5 models. Cases using the original WRF implementation, where τ_{13} (the $\partial u/\partial t$ contribution) uses K_v and τ_{31} (the $\partial w/\partial t$ contribution) uses K_h will be labeled simply as "anisotropic". Cases that instead use K_v for τ_{31} will be labeled as "anisotropic + alt13". Cases that use K_v (rather than the current K_h) for τ_{33} will be labeled as "anisotropic + alt33". Cases that make both modifications will be labeled as "anisotropic + alt13/33".

3.3 Case description

This study considers the development of the convective boundary layer (CBL), a key aspect of NWP, in an idealized model setup featuring a (dry) stable initial profile with a realistic initial mean column wind, a flat bottom boundary and periodic lateral boundary conditions. In preparation for future studies of LES over mountainous terrain, the ground elevation is 1315-m above-sea-level, though it does not noticeably affect the results shown here. The surface drag is set as $z_0 = 0.1$ m and is enforced with an *ad-hoc* modification of WRF's treatment of surface friction, replacing the `tke_drag_coefficient` parameter (see Sec. C.2.3).[2] The simulations are run for 9 hours with a constant sensible surface heat flux of $\overline{w'\theta'_s} = 0.3$ m K s^{-1}

[1] Jimy Dudhia (personal communication) has expressed that the WRF development team considers the existing implementation of τ_{31} to be an error which they will update in the next release owing to our notification (so that K_v will instead be used for both $\tau_{13,31}$), and the existing implementation of τ_{33}, which uses K_h, to be correct.

[2] Original modification made by Katherine A. Lundquist for IBM-WRF, as indicated by the "KAL" in the comments in Appx. C.2.3.

(~ 314 W m^{-2}) and an initial profile with a mean column wind $u = 4$ m s^{-1} in the lower 3 km, which is further forced with a geostrophic wind $u_g = 10$ m s^{-1}. The initial profile is based on reanalysis data rather than a completely idealized column, which was done to verify that none of the models were creating unrealistic mixing aloft where gradients in temperature and momentum can become quite large while the atmosphere remains thermodynamically stable [a known potential issue in NWP turbulence closures (Shi et al., 2018)]. The initial potential-temperature and u-velocity profiles can be seen in the full-column profiles for $t = 0$ hours in Appx. 3.B.

A 3rd-order Runge-Kutta time-integration scheme, a 5th-order horizontal advection scheme and a 3rd-order vertical advection scheme are used in all cases (WRF default values). All cases use a time step of 0.2 s. The domains have a total height of 9.5 km, the top 3 km of which is a Rayleigh damping layer with a coefficient 0.003 s^{-1} (the WRF default coefficient).

Simulations are performed with horizontal resolutions of $\Delta_{x,y} = 100$ m and 1.2 km. All grids have 55 vertical levels with the lowest u-level at $z = 58$ m AGL and Δ_z ranging from 100 – 150 m in the lower 4 km AGL, making the grid approximately isotropic in the finest case ($\Delta_{x,y} = 100$ m). This is a relatively coarse vertical resolution, but the results seen here appear consistent across different vertical resolutions; a more precise treatment on the sensitivity to vertical resolution will be the subject of future work.

WRF version 3.8.1 is used for all cases.

3.4 Results

A well-resolved solution for this convection-dominated case should show a shallow super-adiabatic layer at the surface, a well-mixed neutral layer above and resolved entrainment of the free atmosphere at the top of the CBL (Stull, 1988b). This is very similar to the case examined in 2, but with a more realistic initial profile with added complexity aloft, and a stronger constant surface heat flux.

3.4.1 High-resolution cases

Considering the Smagorinsky-Lilly and TKE-1.5 models for a relatively high-resolution case, $\Delta_{x,y} = 100$ m, with 801×401 grid points, there is a very similar development of mean potential temperature profiles in the isotropic Smagorinsky-Lilly (anisotropic Smagorinsky-Lilly model not run at high-resolution for cost reasons) and TKE-1.5 models, as well as the anisotropic TKE-1.5 model (Fig. 3.1). Recalling that $\Delta_z \approx 100$ m near the surface, this grid is approximately isotropic in the ABL, so the similarity between the isotropic and anisotropic formulations is the expected behavior. Planar slices of vertical velocity in the $z \approx 518$ m plane after 4 and 9 hours are similarly indistinguishable, where all three models produce the cellular convective structure expected for this idealized case (Fig. 3.2).

To make a quantitative evaluation of the size of the thermal cells, the dominant wavelength of the resolved vertical velocity field is approximated by the critical wavelength of de Roode

et al. (2004), λ_c, as used previously in Simon et al. (2019). For clarity it will be restated here that to find the critical wavelength,

$$\lambda_c = 1/k_c \tag{3.1}$$

where the 2π is omitted to find meters per cycle, rather than meters per radian, to get a better physical intuition of the quantities. Then define k_c as the wavenumber where 2/3 of the velocity variance seen in the physical field ($\langle \overline{w}'\overline{w}' \rangle$ in this case) is contained between k_c and k_N, the Nyquist limit, on the energy spectrum, $\mathcal{S}_{33}$, of the turbulent velocity. For TKE in the w-velocity using a discrete Fourier transform on the resolved field, the criteria can be written as

$$\frac{2}{3}\langle \overline{w}'\overline{w}' \rangle = \sum_{k_c}^{k_N} \overline{\mathcal{S}}_{33}. \tag{3.2}$$

Values for λ_c are found here by considering the same one-dimensional energy spectra shown in Fig. 3.3, but without averaging in time, and approximating k_c where Eq. 3.2) is satisfied by taking a weighted average between the two wavenumbers that bound k_c on our discrete spectrum, then taking Eq. 3.1). This can be considered similar to taking the median of a sample, and is used for its reduced sensitivity to noise in determining the peak of the spectrum (de Roode et al., 2004). It can seen that the one-dimensional energy spectra for the vertical component of resolved TKE ($\overline{w}'\overline{w}'$) are, again, indistinguishable between the three models, showing the same temporal development of critical wavelength and total $\overline{w}'\overline{w}'$, and showing overlapping spectra in wavenumber space when averaged over $z \approx 169$ m to 1.79 km over the final two hours (Fig. 3.3).

Considering, finally, the same one-dimensional energy spectrum (but as a function of wavelength, k_h^{-1}) as a contour in time for each model, it is seen again that the three models create nearly identical solutions (Fig. 3.4). These contours of energy in time give a visual insight into the development of the energy in the simulation and how the critical wavelength, λ_c, should grow with time as the dynamics develop. Specifically, the onset in energy is smooth in time and and tends to begin with the smallest wavelengths and grow to larger wavelengths, which is indeed the theoretical behavior of the development of a boundary layer.

As an aside, it is noteworthy how the utility and accuracy of the λ_c metric are so clearly visualized in Fig. 3.4. Also note that the Nyquist limit marked on the contours is the one-dimensional Nyquist limit in either Δ_x or Δ_y; as can be seen in Fig. 3.4, energy values at higher wavenumbers result due to the nature of the scalar wavenumber,

$$k_h = \sqrt{k_x^2 + k_y^2}. \tag{3.3}$$

While the three models considered appear indistinguishable at $\Delta_{x,y} = 100$ m, the performance of the no-model case also deserves mentioning. The profiles of planar-averaged potential temperature in Fig. 3.1 for the no-model case show no discernible difference to the other cases, and all cases show the expected development. The velocity profiles for the no-model case appear noticeably less mixed than in the cases using a turbulence model, but it is not clear which of the four profiles is the most accurate, and they are all quite similar;

the differences between the no-model case and the other cases is not much more pronounced than the differences between the other cases compared to each other.

Considering the slices of $\overline{w}$, the no-model case shows a qualitatively similar structure, but the no-model case does have visibly stronger updrafts at both times considered in Fig. 3.2. This is again seen in the resolved spectra, $\overline{\mathcal{S}}_{33}$, in Fig. 3.3, where the effect of the turbulence closure models is seen most clearly. Specifically, the no-model case shows more energy on the high wavenumbers at the expense of the coarser wavelengths.

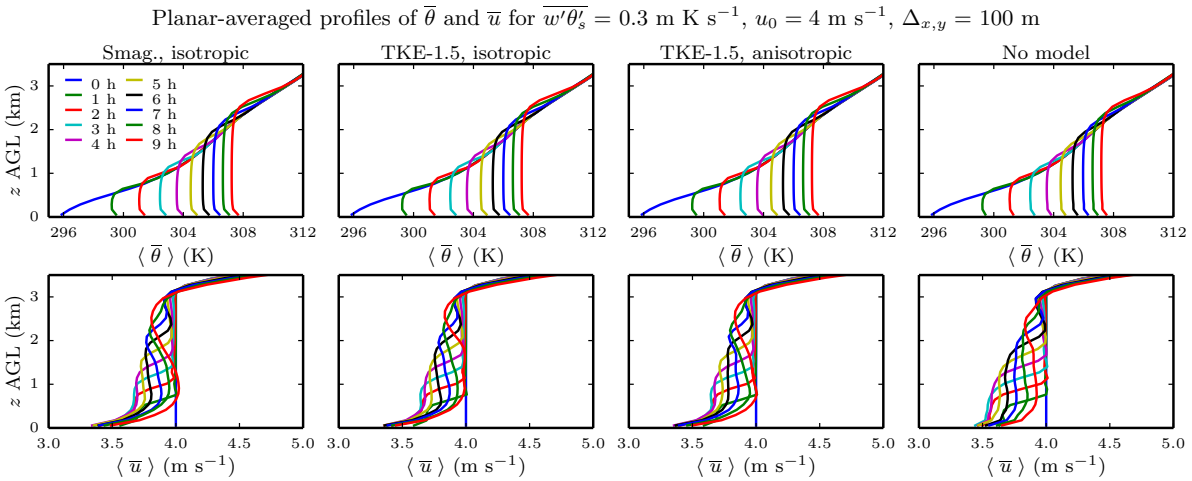

Figure 3.1: Planar-averaged resolved potential temperature and u-velocity profiles for the high-resolution ($\Delta_{x,y} = 100$ m) cases using the isotropic Smagorinsky-Lilly model, isotropic and anisotropic TKE-1.5 model, and no model (from left to right). Full-column profiles shown in Appx. 3.B.

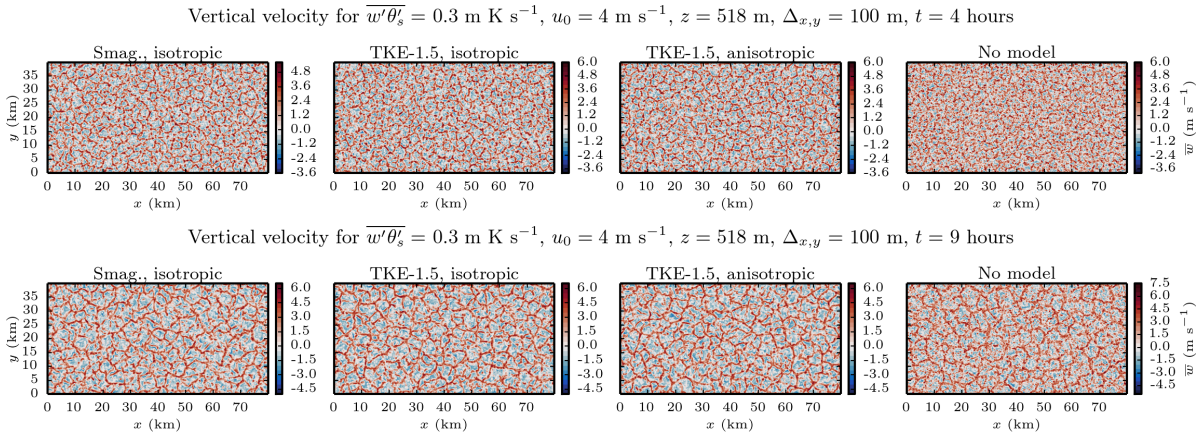

Figure 3.2: Resolved vertical velocity, $\overline{w}$, in the $z \approx 518$ m plane at $t = 4$ (top) and 9 (bottom) hours for the high-resolution ($\Delta_{x,y} = 100$ m) cases considered.

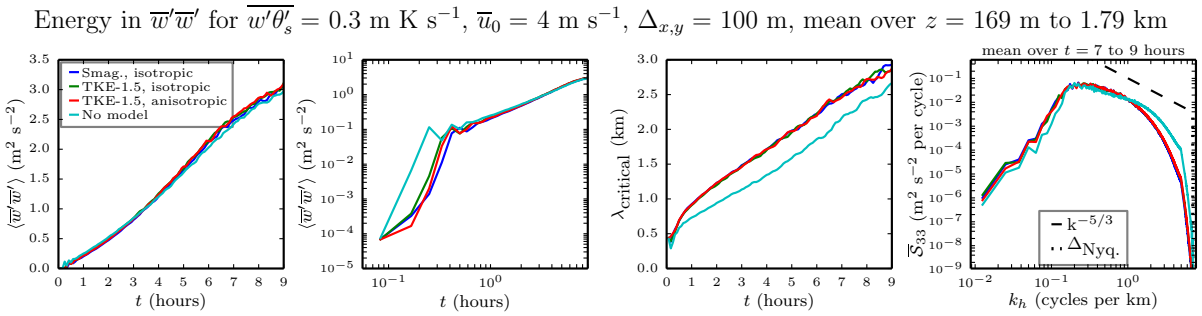

Figure 3.3: Metrics of the resolved vertical velocity field, $\overline{w}$, averaged over the $z \approx 169$ m to 1.79 km planes for the high-resolution ($\Delta_{x,y} = 100$ m) cases with different model and isotropy settings: total resolved TKE ($\overline{w}'\overline{w}'$) in time (far left), the same in log-log scale (middle left), critical wavelength of $\overline{w}'\overline{w}'$ in time (middle right), and spectra of resolved TKE ($\overline{\mathcal{S}}_{33}$) averaged over the final two hours (far right).

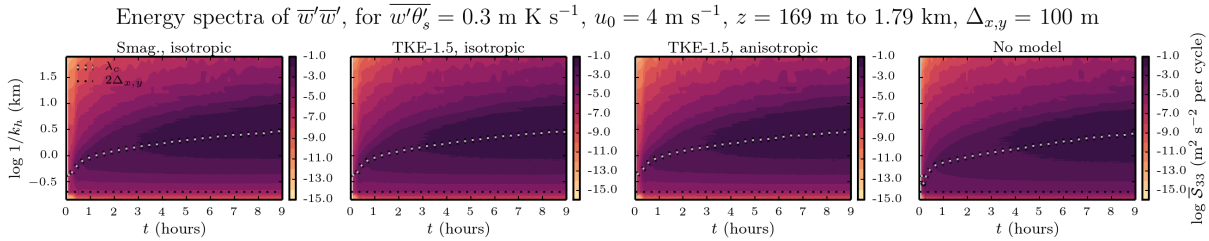

Figure 3.4: Contours of spectra of resolved TKE in the vertical velocity ($\overline{\mathcal{S}}_{33}$) in time for the high-resolution ($\Delta_{x,y} = 100$ m) cases with different isotropy settings, with the critical wavelength (dotted white) and horizontal Nyquist limit (dotted black) overlaid.

3.4.2 Coarse grid with no explicit model

Similar to the high-resolution case, the performance of the WRF model for the same physical case for $\Delta_{x,y} = 1.2$ km using no explicit SGS turbulence model, thus relying on numerical diffusion alone for SGS-mixing as well as viscous dissipation and numerical stability, warrants a brief discussion here for context during the evaluation of different formulations of different turbulence closure models that is to follow, so that the value the turbulence closure models are adding to the simulation is clear.

The planar-averaged profiles of resolved potential temperature and u-velocity show immediately the need for some explicit turbulence closure model, with profiles of $\langle \overline{\theta} \rangle$ that are under-mixed near the surface and profiles of $\langle \overline{u} \rangle$ are very visibly under-mixed throughout the ABL (Fig. 3.5). As well, both profiles show a significant kink near the surface. Note, though, that the entrainment at the top of the ABL shows an excellent agreement with the high-resolution profiles.

The familiar metrics of $\overline{w}'\overline{w}'$ are very informative to the added value that is expected from a turbulence model, where the no-model case resolves a very large proportion of the resolvable TKE seen in the high-resolution case (Fig. 3.6). Considering only the one-dimensional spectra of $\overline{\mathcal{S}}_{33}$, the no-model case compares very well to any of the high-resolution cases using a model (as those high-resolution cases are all indistinguishable). However, considering the temporal development of the resolved $\overline{w}'\overline{w}'$ on the grid, there is a very visible oscillation in the resolved TKE in the first two hours of the simulation. With the behavior of $\overline{w}'\overline{w}'$ in time and wave-space in mind, the visual nature of the resolved vertical velocity field, $\overline{w}$, which shows a large amount of resolved turbulence with no visible coherent structures, is not surprising (Fig. 3.7).

The conclusion to be drawn from both the high-resolution ($\Delta_{x,y} = 100$ m) and coarse ($\Delta_{x,y} = 1.2$ km) no-model cases is that an SGS closure model is not necessary to generate resolved mixing in a convective boundary layer simulation. Therefore, the role of the SGS turbulence closure model in a convectively-forced atmosphere is not to generate "mixing" but rather to reduce, or smooth, resolved mixing so that it may behave as similarly as possible to the high-resolution cases. However, it is clear from the spectrum of resolved vertical TKE, $\overline{\mathcal{S}}_{33}$, that the total amount of resolved energy is kept relatively stable by the grid-effects (i.e. numerical diffusion) alone; that is to say, any additional smoothing will come at the expense of reducing the accuracy of the resolved TKE. It will be seen that this balance between effectively smoothing the physical momentum and scalar fields without removing excessive amounts of resolvable TKE is the essence of the "gray zone".

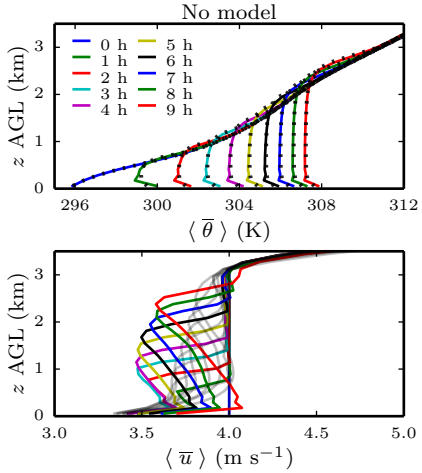

Figure 3.5: Planar-averaged resolved potential temperature and u-velocity profiles for the $\Delta_{x,y} = 1.2$ km case using no model with the high-resolution ($\Delta_{x,y} = 100$ m) case overlaid for potential temperature (dotted black) and u-velocity (faded black). Full-column profiles shown in Appx. 3.B.

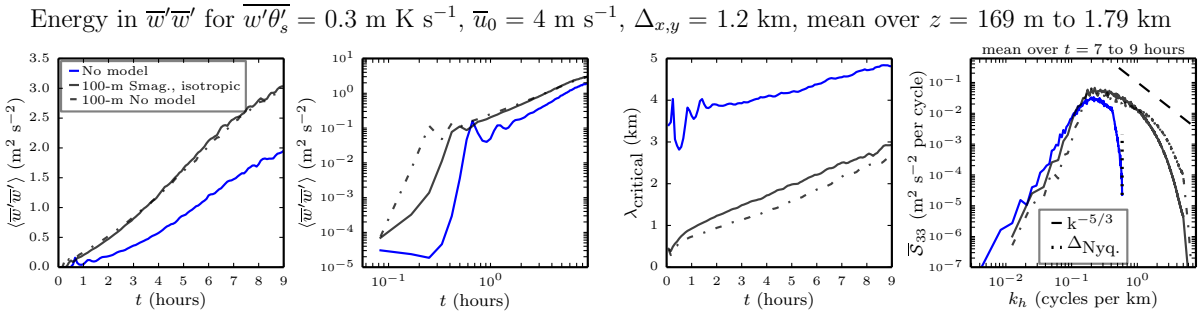

Figure 3.6: As in Fig. 3.3 but when $\Delta_{x,y} = 1.2$ km using no model.

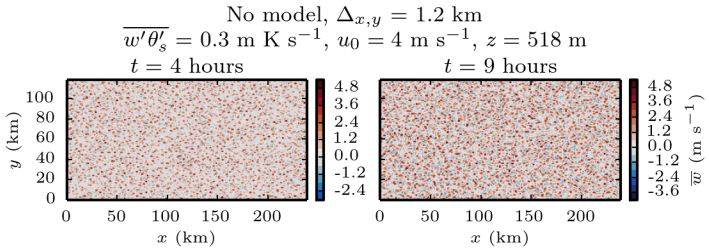

Figure 3.7: Resolved vertical velocity, $\overline{w}$, in the $z \approx 518$ m plane at $t = 4$ (left) and 9 (right) hours for the $\Delta_{x,y} = 1.2$ km case using no model.

3.4.3 Coarse Smagorinsky-Lilly flavors

The different formulations of the turbulent lengthscales, as outlined in Sec. 3.2, in the Smagorinsky-Lilly model show some significant differences that are worth discussing. The planar-averaged profiles of potential temperature and velocity show the first significant difference, which is that SGS-mixing of potential temperature is much more pronounced in the isotropic case (Fig. 3.8). Also noteworthy is the significantly-reduced response to the surface drag in the coarse isotropic case compared to all of the coarse anisotropic formulations, where the velocity profiles in the coarse isotropic case are notably different than in the reference high-resolution case, but the coarse isotropic case is not more extreme in its deviation from the initial profile in any sense, whereas all of the anisotropic formulations have velocity profiles with much larger deviations from the initial profile.

It is also perhaps interesting that, of the three permutations of changes to the anisotropic formulation considered, the most realistic $\langle \overline{\theta} \rangle$ profiles are produced when only τ_{33} is changed, which is the opposite of what is considered the correct formulation by the WRF team. While none of the coarse Smagorinsky-Lilly cases exhibit particularly good behavior, relative to the high-resolution cases, it must be said that the isotropic implementation is the most acceptable form based on the mean profiles. Note that all of the anisotropic formulations considered thus far still use the same $\overline{S}_\beta$ term, and so differences between the formulations are in the lengthscales used in Eqs. (1.47) and (1.48).

Considering planar slices of resolved vertical velocity ($\overline{w}$, Fig. 3.9) and the time-series and spectrum of TKE in the vertical direction ($\overline{w}'\overline{w}'$, Fig. 3.10) is again very revealing of the behavior of the Smagorinsky-Lilly model, and shows similar conclusions to the profiles. Specifically, the isotropic version does a lot more mixing of potential temperature on the SGS which results in much better-behaved profiles throughout the simulation, while all profiles are visibly flawed. Most notably, though, is that once resolved convection begins, i.e. $\overline{w}'\overline{\theta}' > \varepsilon$,[3] the lengthscale of the convective cells that form on the grid are very different in the isotropic version than the anisotropic version. In all formulations of the anisotropic version, the cells that develop are quite large and their horizontal lengthscale is visibly grid-dependent, where the isotropic cells are much smaller and closer in physical size to the high-resolution cases.

The behavior seen in the velocity contours is confirmed in the $\overline{\mathcal{S}}_{33}$ spectra, where the anisotropic versions essentially shift their spectra to longer wavelengths compared to the high-resolution case. In contrast, the isotropic version only resolves energy within the spectrum of the high-resolution case, though with notable energy missing on both ends of the spectrum. The temporal development of the energy is shown through the perspective of $\overline{\mathcal{S}}_{33}$ spectra contours in time, shown in Fig. 3.11. For the different implementations of the Smagorinsky-Lilly model the different energetic developments in time are very visible in the contours, where energy is resolved earlier in the anisotropic implementations but focused in very coarse wavelengths, compared to the isotropic formulation, which takes longer to begin

[3] It is somewhat interesting to note that while ε is ambiguous in this context, as it could be taken to be either some arbitrary minimum value or the energy dissipation rate, either definition would be equivalent here.

resolving turbulence, but does so at a much finer wavelength and in a much more broad spectrum once resolved turbulence is triggered.

It was previously reported in Simon et al. (2019) that isotropic implementations of eddy-viscosity models do not improve their performance at $\mathcal{O}(1\text{ km})$ horizontal resolutions, which does not appear to be true for the case considered here despite the deficiencies noted in the isotropic case. The original conclusion that using isotropic length scales does not improve the performance of the Smagorinsky-Lilly model on coarse grids was made for a case with a low surface heating rate and zero horizontal winds. These factors both increased the delay in generation of resolved turbulence so greatly that there was never resolved turbulence in that case. In contrast here, stronger surface heating and non-zero horizontal winds show a different behavior.

It must be confessed that the performance of the isotropic Smagorinsky-Lilly model is better, or at least more nuanced, than the author was aware after previous studies, and would be considered superior to the anisotropic Smagorinsky-Lilly model by any standard considered for the case presented, both before and after resolved turbulence is triggered. However, it is difficult to argue that the solution given by the isotropic Smagorinsky-Lilly model is correct, or even "good", because the Smagorinsky-Lilly model is not meant to generate a smooth profile via large SGS gradients and low levels of resolved turbulence, and any favorable results are, at best, a fortunate accident, as will be explained.

In the coarse, isotropic case, the initial mixing of the potential temperature profile is achieved by SGS diffusion, which is distinguishable by the shape of both the $\langle \overline{\theta} \rangle$ and $\langle \overline{u} \rangle$ profiles and lack of resolved entrainment until the seventh hour in Fig. 3.8. This can also be seen in the lack of resolved velocity at hour four in the vertical in Fig. 3.9, and most clearly in the time series of $\overline{w}'\overline{w}'$ in Fig. 3.10. While it may seem beneficial that the isotropic Smagorinsky-Lilly model creates a profile that appears mixed at coarse resolutions, this SGS diffusion is actually problematic for two reasons. The first is that this is simply not the design of the model, which is formulated with the assumption that the grid-scale is within the inertial subrange (Lilly, 1962). The result is, as indicated by our prior incorrect or incomplete assessment in 2, that the Smagorinsky-Lilly model cannot be relied upon to function as a robust SGS model at coarse resolutions. The second problem with this behavior is, related to the first, that the Smagorinsky-Lilly model is a fine-scale turbulence closure model designed to numerically dissipate scales of energy that may be assumed to be ultimately destined for viscous dissipation in the real atmosphere, while allowing appropriate scales of mechanical turbulence to be resolved. By generating such a large amount of SGS diffusion, the isotropic Smagorinsky-Lilly model is suppressing its own resolved mixing by generating SGS mixing. However, as can be seen in the improved profiles in Fig. 3.8 in the later hours and in the resolved velocity field at hour 9 in Fig. 3.9, resolved mixing is the superior method of mixing for the isotropic Smagorinsky-Lilly model, which is expected considering the design of the model.

In this way, the isotropic Smagorinsky-Lilly model for this case demonstrates the problem of the turbulent gray zone quite clearly. The LES turbulence closure model is unable to function as intended because it is too effective at mixing on the SGS, yet it is not effective

enough to create realistic profiles. Further, the stated intention of an LES is to resolve eddies on the grid, so while the mixing delivered by the SGS model before resolved mixing is triggered is impressive from one perspective, it is delaying the generation of resolved turbulence on the grid, which would create a much better-mixed profile and more realistic resolved fields. Even further, a smooth mean-profile solution is attainable with a PBL scheme at very coarse resolutions; to use a three-dimensional eddy-viscosity closure to ultimately generate a column-averaged solution is a significant waste of resources. However, the present anisotropic formulations, which do reduce the effectiveness of the SGS mixing and thus also reduce the delay in the onset of resolved turbulence, perform decidedly worse by any other metric considered here. There is a corresponding issue with planetary boundary layer (PBL) schemes, where on fine enough grids they can allow resolved mixing to be triggered (Zhou et al., 2014). This span of resolutions is what is referred to in the literature and throughout this manuscript as the turbulent gray zone, or the *terra incognita*.

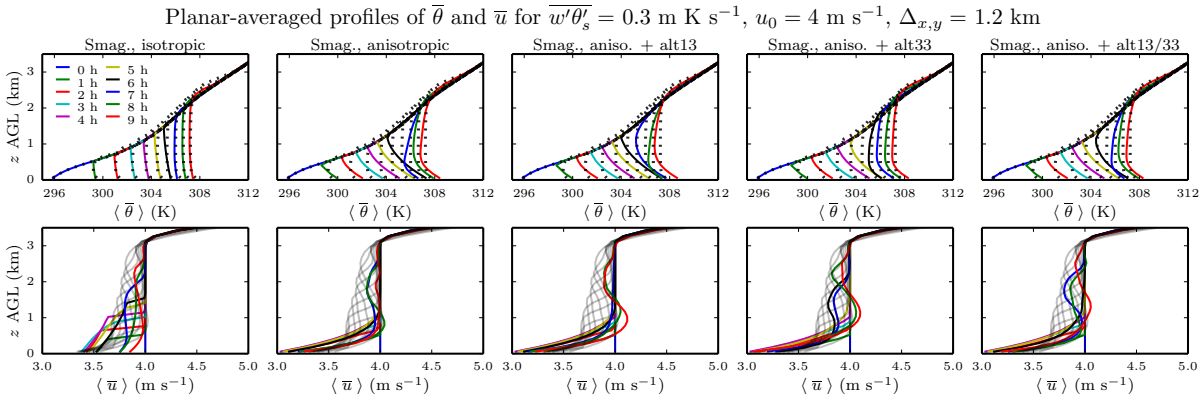

Figure 3.8: Planar-averaged resolved potential temperature and u-velocity profiles for the $\Delta_{x,y} = 1.2$ km case using the Smagorinsky-Lilly model with isotropic and anisotropic length-scales, with the high-resolution ($\Delta_{x,y} = 100$ m) case overlaid for potential temperature (dotted black) and u-velocity (faded black). Full-column profiles shown in Appx. 3.B.

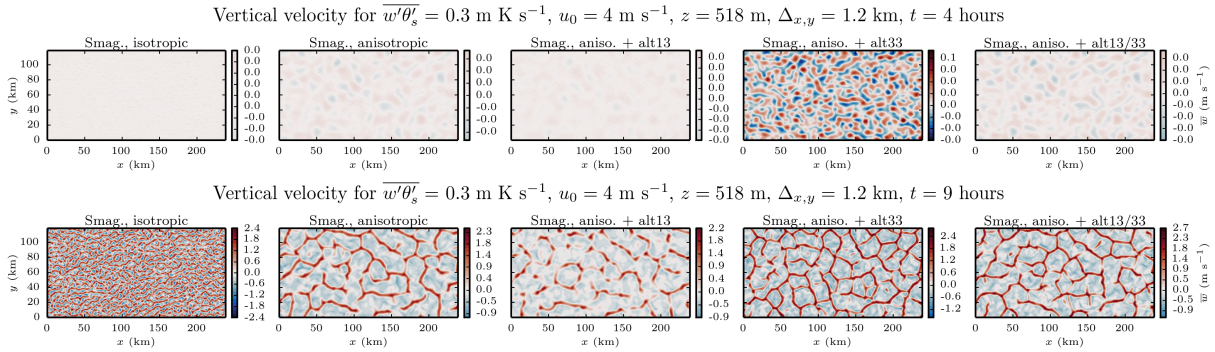

Figure 3.9: Resolved vertical velocity, $\overline{w}$, in the $z \approx 518$ m plane at $t = 4$ (top) and 9 (bottom) hours for the $\Delta_{x,y} = 1.2$ km cases using the Smagorinsky-Lilly model with isotropic and anisotropic lengthscales.

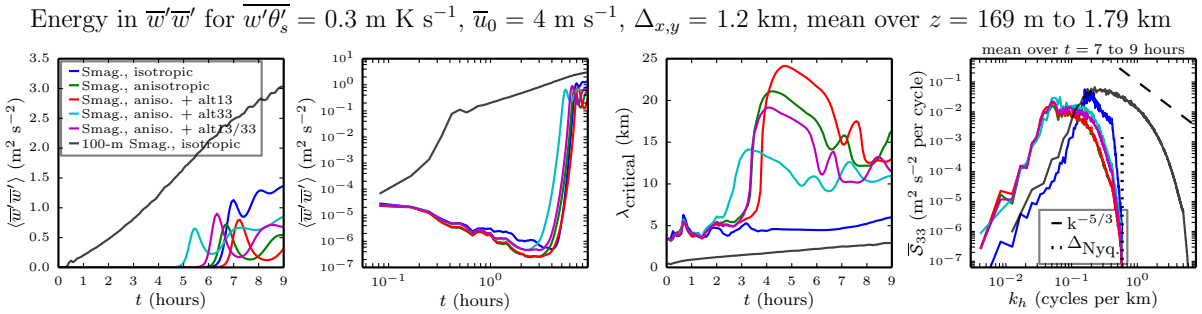

Figure 3.10: Metrics of the resolved vertical velocity field, $\overline{w}$, averaged over the $z \approx 169$ m to 1.79 km planes for the $\Delta_{x,y} = 1.2$ km cases using the Smagorinsky-Lilly model with isotropic and anisotropic lengthscales: total resolved TKE ($\overline{w}'\overline{w}'$) in time (far left), the same in log-log scale (middle left), critical wavelength of $\overline{w}'\overline{w}'$ in time (middle right), and spectra of resolved TKE ($\overline{\mathcal{S}}_{33}$) averaged over the final two hours (far right).

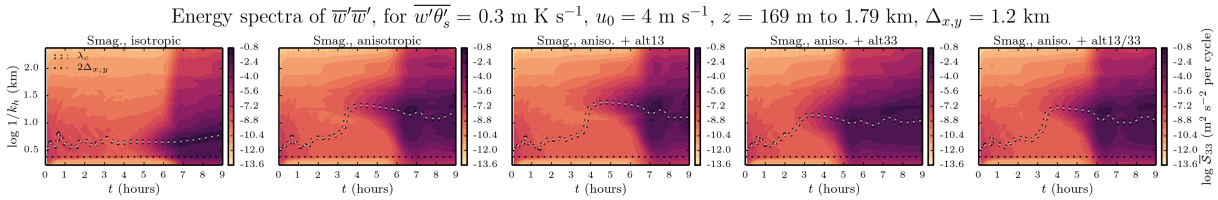

Figure 3.11: Contours of spectra of resolved TKE in the vertical velocity ($\overline{\mathcal{S}}_{33}$) in time for the $\Delta_{x,y} = 1.2$ km cases using the Smagorinsky-Lilly model with isotropic and anisotropic lengthscales, with the critical wavelength (dotted white) and horizontal Nyquist limit (dotted black) overlaid.

3.4.4 Coarse anisotropic-deformation Smagorinsky-Lilly flavors

As discussed in Sec. 1.6.2, the anisotropic Smagorinsky-Lilly model in WRF was modified to implement Eq. 1.49), which will be referred to as the "anisotropic-deformation Smagorinsky-Lilly" model, or "ad.Smag." model. The "anisotropic Smagorinsky-Lilly" model will always refer to the formulation that is currently implemented in the release version of WRF, where only the lengthscales are taken anisotropically.

The behavior of the planar-averaged mean profiles for this anisotropic-deformation Smagorinsky-Lilly model is much improved over any of the permutations of the original WRF anisotropic Smagorinsky-Lilly model. The ad.Smag version, it will be argued, is also better than the isotropic Smagorinsky-Lilly model.

The behavior of this formulation of the Smagorinsky-Lilly model is intuitive in that it greatly improves the performance of the anisotropic Smagorinsky-Lilly model, generating resolved TKE on the grid much earlier and at much smaller lengthscales than the previous anisotropic formulations, also generating significantly better-behaved planar-averaged profiles (Fig. 3.12). However it is also somewhat counter-intuitive, in that it makes the resolved velocity fields produced by the model largely insensitive to any permutations of alternative anisotropic lengthscales considered, i.e. alt13, alt33 and alt13/33 (Fig. 3.13). That is, when the strain-rate tensor is taken anisotropically, the resolved field is much less sensitive to the choice of K_h or K_v for either $\tau_{31,33}$.

The resolved velocity fields are not only less sensitive to the formulation of the lengthscales in K, they are also, visibly, significantly more coherent (cellular structures) than any formulation of the standard anisotropic Smagorinsky-Lilly model other than the anisotropic + alt33 case. The resolved cells are also visibly smaller in size than any permutation of the standard anisotropic Smagorinsky-Lilly model, though still much too large to be realistic for an ABL.

A final thought on the anisotropic-deformation Smagorinsky-Lilly model: it does an excellent job at generating coherent turbulent structures at the scales available on the grid (as seen in Fig. 3.13), which was the actual goal of the Smagorinsky-Lilly model (Lilly, 1962, 1967). Further, resolved TKE begins relatively early in the simulation and a $k^{-5/3}$ cascade is, more or less, generated even at very coarse resolutions. For scale-accurate dynamics, one should consider the dynamic Wong-Lilly model (Wong and Lilly, 1994).

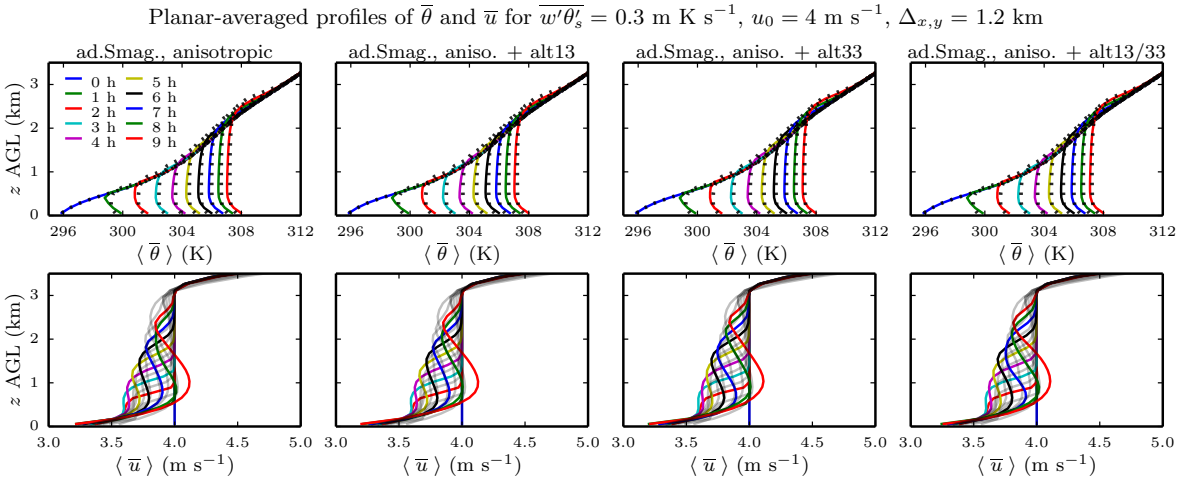

Figure 3.12: As in Fig. 3.8 but using the anisotropic-deformation Smagorinsky-Lilly model.

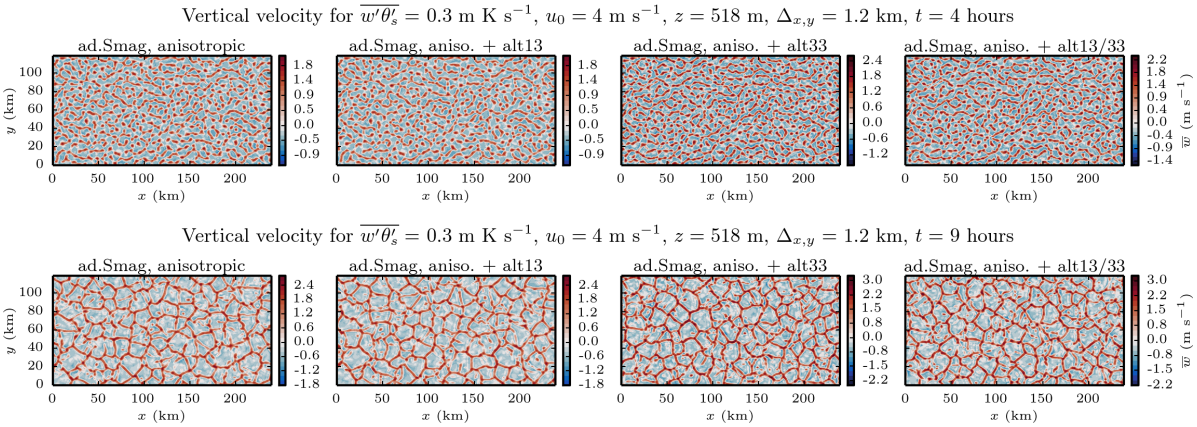

Figure 3.13: As in Fig. 3.9 but using the anisotropic-deformation Smagorinsky-Lilly model.

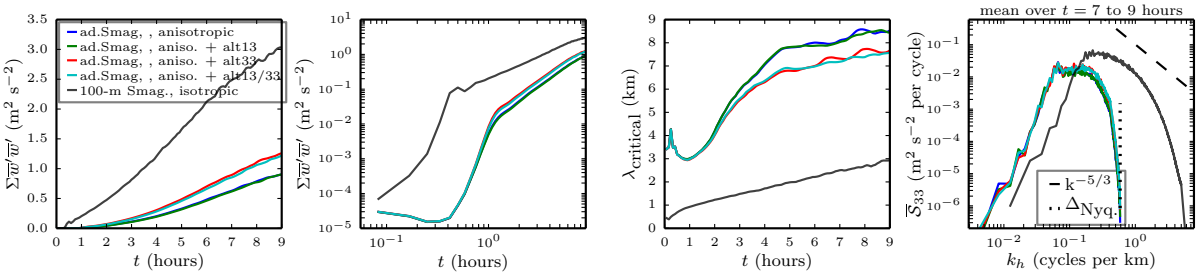

Figure 3.14: As in Fig. 3.10 but using the anisotropic-deformation Smagorinsky-Lilly model.

3.4.5 Coarse TKE-1.5 flavors

The isotropic TKE-1.5 model performs very similarly to the isotropic Smagorinsky-Lilly model in many ways (which is technically also the isotropic version of the anisotropic-deformation Smagorinsky-Lilly model), where the first few hours are dominated by SGS mixing of potential temperature. This creates an unrealistically sharp profile without any entrainment at the CBL top, but is still effective enough to suppress the onset of resolved turbulence (Fig. 3.15). Also similar to the isotropic Smagorinsky-Lilly model, the isotropic TKE-1.5 model shows much less dramatic velocity profiles and much smaller convective cells once resolved mixing does begin (Fig. 3.16). The behavior in time and wave-space of $\overline{w}'\overline{w}'$ is also very similar to the isotropic Smagorinsky-Lilly model, where there is a four-hour delay before the onset of resolved mixing, but the spectra seen over the final two hours are surprisingly accurate compared to the high-resolution TKE-1.5 case (Fig. 3.17). It is nice that a model formulated to model fine-scale, isotropic turbulence produces an acceptable resolved potential-temperature profile at such coarse resolutions. However, this could be achieved with a PBL scheme at even coarser resolution. But if this were a PBL scheme, then the onset of resolved turbulence is not desirable, so this is problematic behavior from either perspective. Thus the isotropic TKE-1.5 model is, yet again, a great example of the gray zone problem.

The anisotropic TKE-1.5 model behaves very similarly to the anisotropic-deformation Smagorinsky-Lilly model, both in the qualitative features of the resolved potential-temperature and u-velocity profiles, and in the nature of the resolved cells in the w-velocity field (Figs. 3.15, 3.16). Also similar to the anisotropic-deformation Smagorinsky-Lilly model, the anisotropic TKE-1.5 model is largely insensitive to different permutations of $\tau_{31,33}$. This is both in terms of the already-discussed profiles and velocity fields and in the metrics of $\overline{w}'\overline{w}'$ familiar to this manuscript, namely the resolved spectra, $\overline{\mathcal{S}}_{33}$, which show a very visible and consistent shift towards longer wavelengths when compared to the high-resolution counterpart for any of alt13, alt33 or alt13/33 (Fig. 3.17).

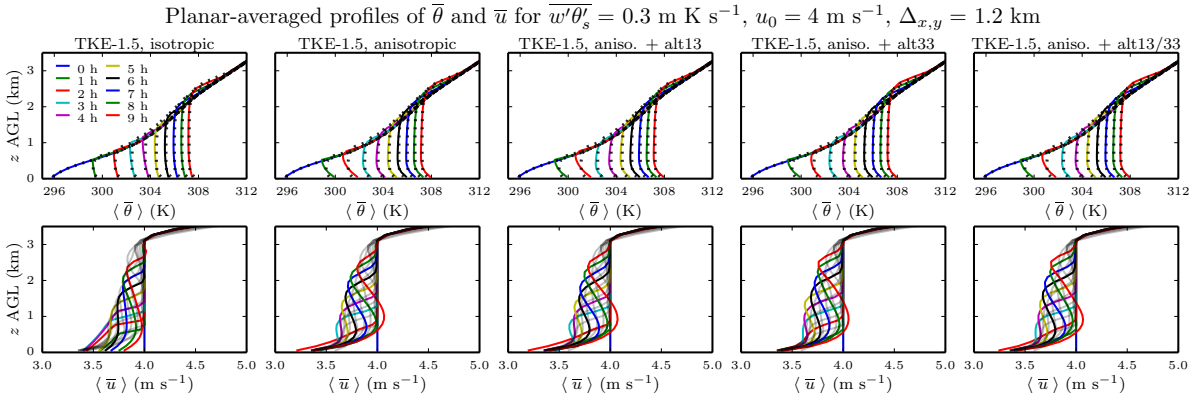

Figure 3.15: As in Fig. 3.8 but using the TKE-1.5 model with isotropic and anisotropic lengthscales.

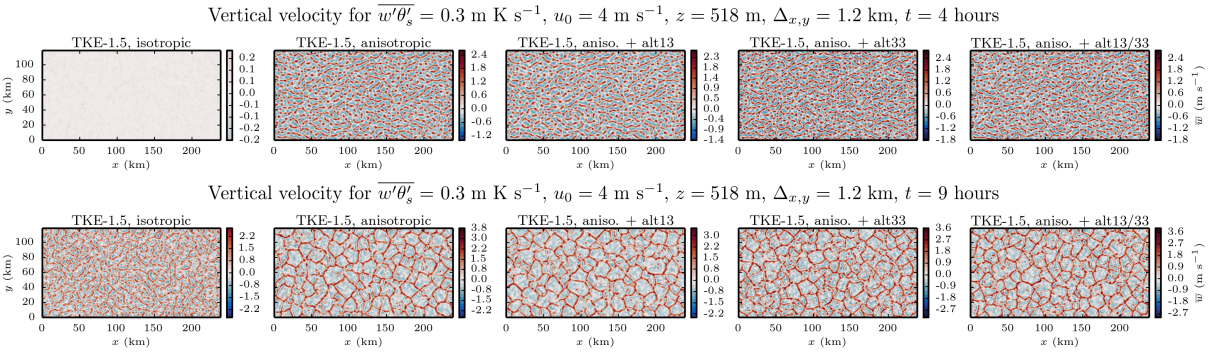

Figure 3.16: As in Fig. 3.9 but using the TKE-1.5 model with isotropic and anisotropic lengthscales.

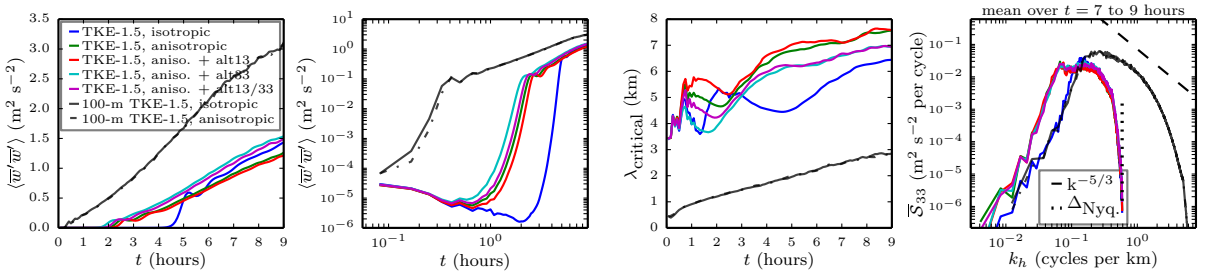

Figure 3.17: As in Fig. 3.10 but using the TKE-1.5 model with isotropic and anisotropic lengthscales.

3.5 Summary and conclusions

This chapter extended the analysis of the two eddy-viscosity models considered in Ch. 2, the Smagorinsky-Lilly and TKE-1.5 models, by considering isotropic and different anisotropic formulations as well as a more realistic initial column wind profile. The two models are also compared to using no model, relying entirely on the numerical diffusion of the grid discretization for SGS mixing, dissipation and for model stability.

It is seen that at high resolutions ($\Delta_{x,y}$ = 100 m) the isotropic Smagorinsky-Lilly, isotropic TKE-1.5 and anisotropic TKE-1.5 models all agree very closely, as expected. It is also seen at high resolutions that the turbulence closure models are providing a value to the simulation compared to using no model, which results in too much energy at high wavenumbers compared to theoretical dissipation rates (e.g. Fig. 3.3).

At coarse resolutions ($\Delta_{x,y}$ = 1.2 km), the isotropic Smagorinsky-Lilly and isotropic TKE-1.5 models provide a solution that appears decent in this case, but is largely driven by SGS mixing, and thus the ability of the model to produce a mixed mean-profile is not consistent or reliable. To this end, both models begin resolved mixing many hours into

the simulation, but at scales that compare better to the high-resolution cases than either model's anisotropic formulation. However, the isotropic models suppress their own resolved turbulence for too long initially to produce an accurate atmospheric simulation.

The anisotropic Smagorinsky-Lilly model, as implemented in release versions of WRF at the time of writing (where only the lengthscales are taken anisotropically), shows very poor behavior at coarse resolutions. However, if it is modified to also consider deformations anisotropically, as other NWP models have done, the behavior of the anisotropic-deformation Smagorinsky-Lilly model is significantly improved, and behaves very similarly to the anisotropic TKE-1.5 model.

Throughout the aforementioned analysis, considerations were made for different potential implementations of anisotropy, where the use of K_h or K_v is considered for τ_{31} and τ_{33}. Only the anisotropic Smagorinsky-Lilly model was sensitive to these permutations, where the anisotropic-deformation Smagorinsky-Lilly and anisotropic TKE-1.5 models show very consistent results for all implementations.

Finally, it is worth stating clearly that, in the author's opinion, both the anisotropic-deformation Smagorinsky-Lilly model and the anisotropic TKE-1.5 model do an excellent job of generating turbulent structures on the grid-scale which is, in fact, the original stated objective of both models (Lilly, 1962; Deardorff, 1972). The manner that they generate, more or less, the same momentum cascade on any grid is their intended functionality. Put another way, with the exception of the anisotropic Smagorinsky-Lilly model (which it has been argued here should be replaced by the anisotropic-deformation Smagorinsky-Lilly model) this chapter should be read as instructional to users and developers, rather than critical of anisotropic eddy-viscosity models.

Acknowledgments. Acknowledgement is made to the Savio computational cluster provided by the Berkeley Research Computing program at the University of California, Berkeley (supported by the UC Berkeley Chancellor, Vice Chancellor for Research, and Chief Information Officer) for computing time used in this research.

3.A Changes to the turbulent stress tensor in the WRF code

In this section, the reader will find the code for the Smagorinsky-Lilly model as-distributed in WRF 3.8.1 (Sec. 3.A.1), followed by the code for the anisotropic-deformation reformulation of the Smagorinsky-Lilly model (Sec. 3.A.2).

3.A.1 Original anisotropic Smagorinsky-Lilly implementation

```
SUBROUTINE smag_km(  config_flags ,xkmh,xkmv,xkhh,xkhv,BN2, &
                     div,defor11,defor22,defor33,defor12,          &
                     defor13,defor23,                              &
                     u, v, z, ht,                                  &
                     rdzw,dx,dy,dt,isotropic,                      &
                     mix_upper_bound, msftx, msfty,                &
                     ids,ide, jds,jde, kds,kde,                    &
                     ims,ime, jms,jme, kms,kme,                    &
                     its,ite, jts,jte, kts,kte                      )


!-------------------------------------------------------------------------
! Begin declarations.

   IMPLICIT NONE

   TYPE(grid_config_rec_type) , INTENT(IN    ) :: config_flags

  ! JSS: SKIPPING THE REST OF THE DECLARATIONS

      pr = prandtl
      c_s = config_flags%c_s

      do j=j_start,j_end
      do k=kts,ktf
      do i=i_start,i_end
         def2(i,k,j)=0.5*(defor11(i,k,j)*defor11(i,k,j) + &
                          defor22(i,k,j)*defor22(i,k,j) + &
                          defor33(i,k,j)*defor33(i,k,j))
      enddo
      enddo
      enddo

        do j=j_start,j_end
        do k=kts,ktf
        do i=i_start,i_end
         def2(i,k,j)=def2(i,k,j)+ defor12(i,k,j)*defor12(i,k,j)
        enddo
        enddo
        enddo

        do j=j_start,j_end
        do k=kts,ktf
        do i=i_start,i_end
```

```
45            def2(i,k,j)=def2(i,k,j)+ defor13(i,k,j)*defor13(i,k,j)
46          enddo
47          enddo
48          enddo
49
50          do j=j_start,j_end
51          do k=kts,ktf
52          do i=i_start,i_end
53            def2(i,k,j)=def2(i,k,j)+ defor23(i,k,j)*defor23(i,k,j)
54          enddo
55          enddo
56          enddo
57
58      IF (isotropic .EQ. 0) THEN
59         DO j = j_start, j_end
60         DO k = kts, ktf
61         DO i = i_start, i_end
62
63        mlen_h=sqrt(dx/msftx(i,j) * dy/msfty(i,j))
64        mlen_v= 1./rdzw(i,k,j)
65
66            tmp=max(0.,def2(i,k,j)-BN2(i,k,j)/pr)
67            tmp=tmp**0.5
68            xkmh(i,k,j)=max(c_s*c_s*mlen_h*mlen_h*tmp, 1.0E-6*mlen_h*mlen_h )
69            xkmh(i,k,j)=min(xkmh(i,k,j), mix_upper_bound * mlen_h * mlen_h / dt )
70            xkmv(i,k,j)=max(c_s*c_s*mlen_v*mlen_v*tmp, 1.0E-6*mlen_v*mlen_v )
71            xkmv(i,k,j)=min(xkmv(i,k,j), mix_upper_bound * mlen_v * mlen_v / dt )
72            xkhh(i,k,j)=xkmh(i,k,j)/pr
73            xkhh(i,k,j)=min(xkhh(i,k,j), mix_upper_bound * mlen_h * mlen_h / dt )
74            xkhv(i,k,j)=xkmv(i,k,j)/pr
75            xkhv(i,k,j)=min(xkhv(i,k,j), mix_upper_bound * mlen_v * mlen_v / dt )
76
77         ENDDO
78         ENDDO
79         ENDDO
80      ELSE
81
82        !JSS: REMOVED, NOT RELEVANT HERE
83
84      ENDIF
85
86  END SUBROUTINE smag_km
```

3.A.2 Modified anisotropic-deformation Smagorinsky-Lilly implementation

```
SUBROUTINE smag_jss_aniso( config_flags ,xkmh,xkmv,xkhh,xkhv,BN2, &
                    div ,defor11 ,defor22 ,defor33 ,defor12 ,      &
                    defor13 ,defor23 ,                             &
                    u, v, z, ht,                                   &
                    rdzw ,dx,dy,dt ,isotropic ,                    &
                    mix_upper_bound , msftx , msfty ,              &
                    ids ,ide , jds ,jde , kds ,kde ,               &
                    ims ,ime , jms ,jme , kms ,kme ,               &
                    its ,ite , jts ,jte , kts ,kte                 )

!-----------------------------------------------------------------------
! Begin declarations.

  IMPLICIT NONE

  TYPE(grid_config_rec_type) , INTENT(IN    ) :: config_flags

    ! JSS: SKIPPING THE REST OF THE DECLARATIONS

    pr = prandtl
    c_s = config_flags%c_s

    do j=j_start ,j_end
    do k=kts ,ktf
    do i=i_start ,i_end
      def2(i,k,j) = 0.5*( defor11(i,k,j)*defor11(i,k,j) + &
              defor22(i,k,j)*defor22(i,k,j) + &
              defor33(i,k,j)*defor33(i,k,j) )
    enddo
    enddo
    enddo

    do j=j_start ,j_end
    do k=kts ,ktf
    do i=i_start ,i_end
      def2(i,k,j) = def2(i,k,j) + defor12(i,k,j)*defor12(i,k,j)
    enddo
    enddo
    enddo

    do j=j_start ,j_end
    do k=kts ,ktf
    do i=i_start ,i_end
      def2v(i,k,j) = defor13(i,k,j)*defor13(i,k,j)
    enddo
    enddo
    enddo

    do j=j_start ,j_end
    do k=kts ,ktf
    do i=i_start ,i_end
      def2v(i,k,j) = def2v(i,k,j) + defor23(i,k,j)*defor23(i,k,j)
    enddo
```

```
54      enddo
55      enddo
56
57      DO j = j_start, j_end
58      DO k = kts, ktf
59      DO i = i_start, i_end
60
61         mlen_h = sqrt( dx/msftx(i,j)*dy/msfty(i,j) )
62         mlen_v = 1./rdzw(i,k,j)
63
64         tmp = max( 0.,def2(i,k,j) )
65         tmp = tmp**0.5
66
67         tmpv = max( 0.,def2v(i,k,j)-BN2(i,k,j)/pr )
68         tmpv = tmpv**0.5
69
70         xkmh(i,k,j) = max( c_s*c_s*mlen_h*mlen_h*tmp, 1.0E-6*mlen_h*mlen_h )
71         xkmh(i,k,j) = min( xkmh(i,k,j), mix_upper_bound*mlen_h*mlen_h/dt )
72         xkmv(i,k,j) = max( c_s*c_s*mlen_v*mlen_v*tmpv, 1.0E-6*mlen_v*mlen_v )
73         xkmv(i,k,j) = min( xkmv(i,k,j), mix_upper_bound*mlen_v*mlen_v/dt )
74         xkhh(i,k,j) = xkmh(i,k,j)/pr
75         xkhh(i,k,j) = min( xkhh(i,k,j), mix_upper_bound*mlen_h*mlen_h/dt )
76         xkhv(i,k,j) = xkmv(i,k,j)/pr
77         xkhv(i,k,j) = min( xkhv(i,k,j), mix_upper_bound*mlen_v*mlen_v/dt )
78
79      ENDDO
80      ENDDO
81      ENDDO
82
83  END SUBROUTINE smag_jss_aniso
```

3.B Full column planar-averaged profiles

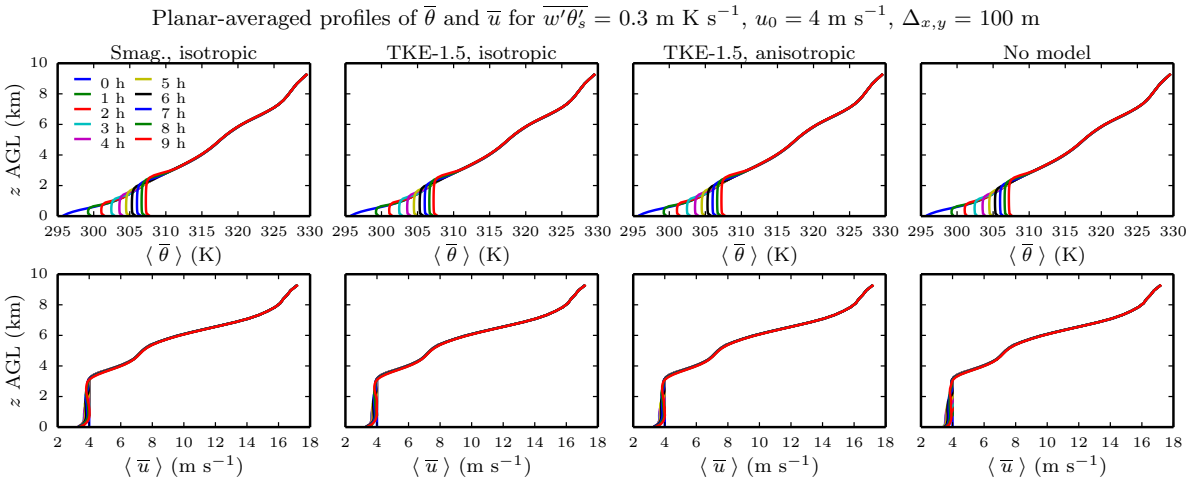

Figure 3.18: Full model height of planar-averaged resolved potential temperature and u-velocity profiles for the high-resolution ($\Delta_{x,y} = 100$ m) cases using the isotropic Smagorinsky-Lilly model, isotropic and anisotropic TKE-1.5 model, and no model (from left to right).

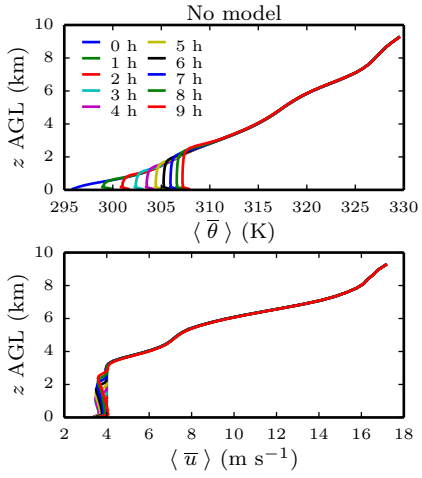

Figure 3.19: As in Fig. 3.18 but for $\Delta_{x,y} = 1.2$ km cases using no model.

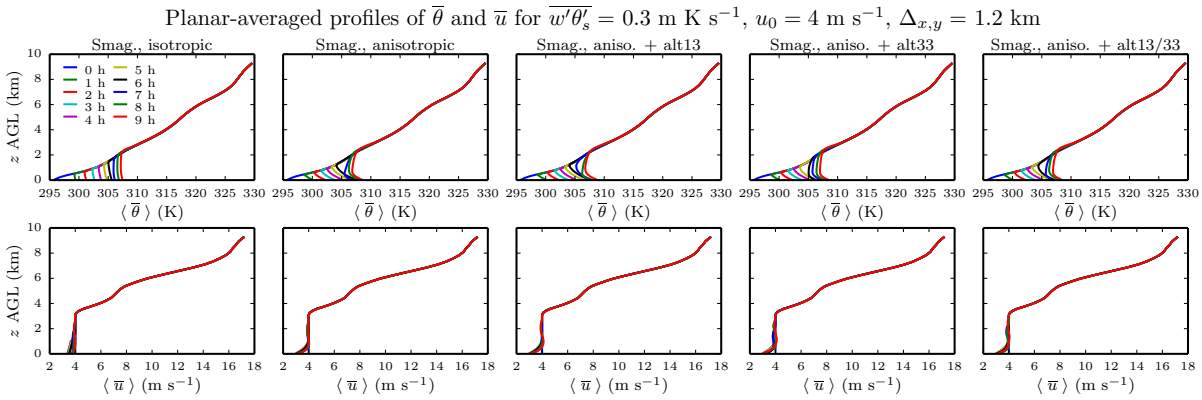

Figure 3.20: As in Fig. 3.18 but for $\Delta_{x,y} = 1.2$ km cases using the Smagorinsky-Lilly model with isotropic and anisotropic lengthscales.

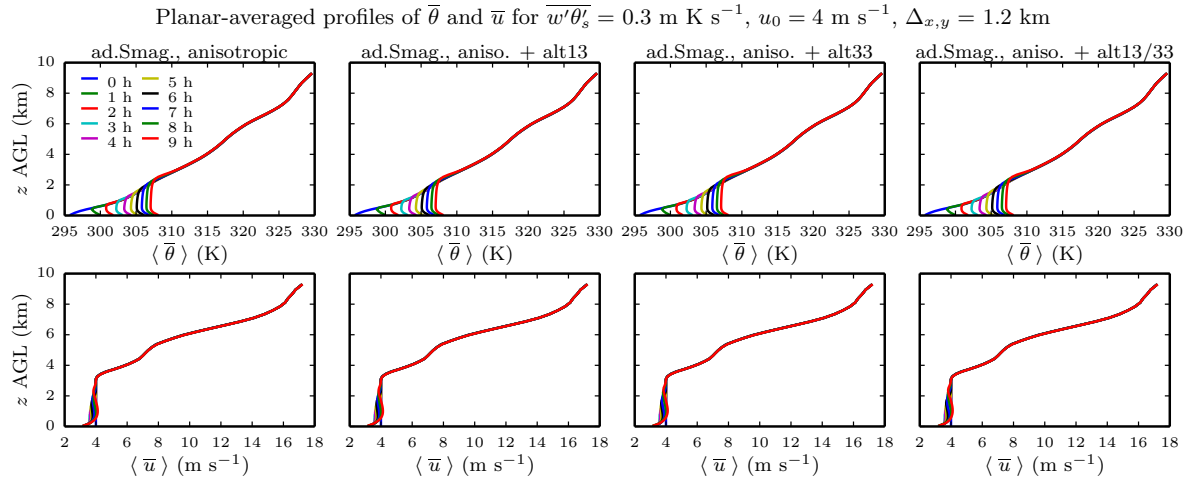

Figure 3.21: As in Fig. 3.20 but using the anisotropic-deformation Smagorinsky-Lilly model.

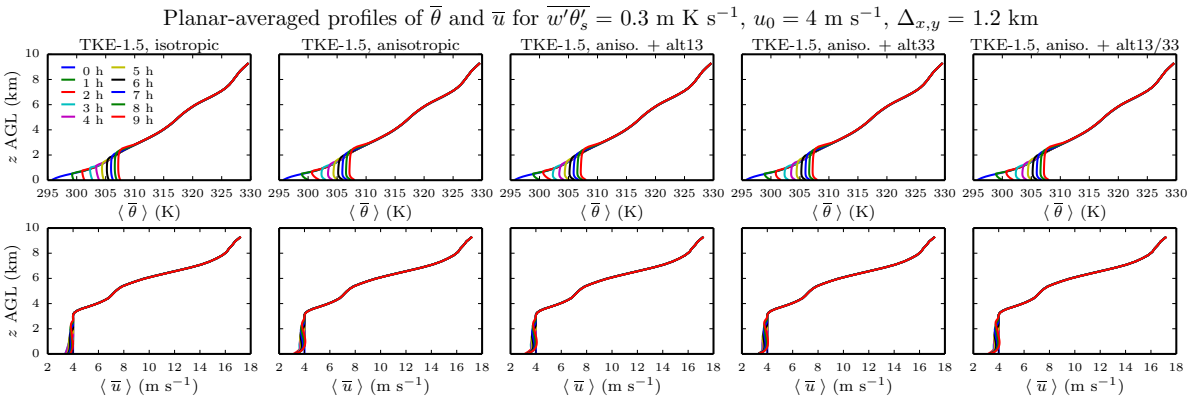

Figure 3.22: As in Fig. 3.20 but using the TKE-1.5 model.

Chapter 4

A promising alternative anisotropic formulation for eddy-viscosity models for atmospheric LES

4.1 Introduction

It has been seen in Chs. 2 and 3 that there is considerable work to be done, both in the area of improvement and in clarification, on the behavior of eddy-viscosity models for atmospheric large-eddy simulation (LES) when used for numerical weather prediction (NWP) applications, which are inherently performed on highly-anisotropic grids and likely will be for years to come.

With the results of Chs. 2 and 3 in mind, an alternative formulation is suggested for eddy-viscosity turbulence closure models when used on anisotropic grids for NWP, dubbed here the "alternative-anisotropic" formulation for the Smagorinsky-Lilly and TKE-1.5 models. It is shown that this alternative-anisotropic formulation performs well compared to the isotropic and anisotropic formulations of both models seen in Ch. 3 under the same criteria used there, and shows an interesting potential direction of study. The comparisons are made to the original formulations used in WRF v3.8.1 with the exception of the $\Delta_{x,y} = 5$ km free-convection case, where the anisotropic-deformation Smagorinsky-Lilly formulation from Ch. 3 is used (Sec. 4.2.1.2).

An analysis of the alternative-anisotropic formulation is presented for the previous case considered in Ch. 3 as well as a simpler, no-wind case that is similar, but not identical, to the case considered in Ch. 2. Then a shorter discussion is given on the results seen for three other cases where the surface heat flux is increased with no wind, the surface heat flux is decreased with high wind, and the surface heat flux is increased with high wind. The alternative-anisotropic eddy-viscosity models show an ability to generate qualitatively consistent planar-averaged profiles. As well, many questions are introduced related to the scales of production and dissipation of energy associated with buoyancy and shear and the

associated lengthscales, particularly in the $\overline{\mathcal{S}}_{33}$ spectra seen in the alternative-anisotropic TKE-1.5 model, which will be the subject of future work.

4.1.1 Historical context for turbulence models

The explicit goal of the LES turbulence closure model is often not stated, but there are many different objectives that may be attempted with LES, with different outcomes deemed satisfactory [see Pope (2004) for a detailed treatment of this topic]. The traditional eddy-viscosity models were generally designed to generate a turbulent cascade on the grid, and will only generate the correct scales of motion on high-resolution grids. In the case of atmospheric LES there is a lot of merit to the numerical studies of turbulence that these models were designed for, and the discussion here is in no way meant to diminish them. That said, for NWP with a stated goal of accurate physics, these formulations are only correct on very high-resolution grids. While the objectives for LES turbulence models have changed throughout their development, it is interesting to consider the original objectives at their development.

To give a very abbreviated history of LES turbulence closure models, Smagorinsky (1958, 1963) formulated his model for a very primitive two-level, vorticity-conserving general circulation code at a time when a viscous fluid had never before been numerically integrated on a computer. His intention was to generate a general circulation by dissipating vorticity in the xy-plane to surface friction in the lower layer, which would then be transported to the upper layer by the vorticity conservation inherent in his formulation. The two key points to note here are: first, that the original Smagorinsky (1958) SGS model's aim was to generate resolved circulations via local transport created by the dissipation of an explicitly conserved quantity (i.e. diffusion of vorticity); second, that his computing resources were so limited that generating physical features that appeared accurate was considered a bonus.

Lilly (1962) reformulated Smagorinsky's model for three-dimensional, fine-scale turbulence by adding a stability constraint in the vertical direction. Similar to Smagorinsky, Lilly was simply trying to simulate the turbulent momentum cascade observed by experiments on a grid, and was navigating uncharted territory and doing so with such limited resources that generating turbulence at all was considered a success. As well, Lilly (1962) is very clear that the grid is assumed within the inertial subrange in his SGS formulation. The three key points to note here are: first, that the Smagorinsky-Lilly SGS model's formulating assumption is that the grid-scale is in the inertial subrange; second, that generating eddies on the grid is prioritized over scale-correct dynamics in the formulation of the Smagorinsky-Lilly model; and third, that the classical formulation of the turbulent lengthscales in the Smagorinsky-Lilly model is only appropriate for modeling a physically-realistic atmosphere on very high-resolution grids.

Around the same time, Deardorff (1972) began developing models to prognosticate the advection, production and dissipation of SGS TKE to inform these fine-scale turbulence modeling efforts, leading to the familiar 1.5-order TKE model. The so-called TKE-1.5 model

is largely unchanged since its inception by Deardorff (1972), at least in its implementation into the WRF model.

Again, none of this is meant as a slight to the Smagorinsky-Lilly or TKE-1.5 models, as they are simple, elegant, cheap (the Smagorinsky-Lilly more so than the TKE-1.5 in this regard) and do exactly what they were designed to do. However, it is important to understand what they were intended to do, which is to generate as many eddies on the grid-scale as possible.

4.1.2 An alternative formulation for anisotropic eddy-viscosity models

As described in Sec. 4.1.1, the original isotropic Smagorinsky-Lilly turbulence closure model was formulated with the specific assumption "that the scale of the calculation mesh lies within the inertial range" (Lilly, 1967), and the model was originally formulated with the goal of producing a three-dimensional turbulent momentum cascade on a grid. Anisotropic efforts since have focused on the approach outlined in Sec. 1.6.2, the deficiencies of which were discussed in Chapter 3. The result is that eddies are resolved on the grid-scale by the turbulence closure model at resolutions that are too coarse to represent physically-realistic resolved motions (Ch. 2). with the anisotropic formulations. This is not without merit, as these models were designed to study turbulence via numerical simulation.

In the case of LES being used for high-resolution NWP, the objectives are quite different than those of the original formulators of the eddy-viscosity models. Instead of using the turbulence closure model to encourage resolving eddies on any grid, we would like to use the closure model to provide smoothing and/or dissipation when and where appropriate to develop accurate and consistent velocity and temperature fields at any resolution, but also to not overly suppress energy that would be resolved on a higher-resolution grid. That is, we want to develop appropriate scales of energy on whatever grid resolution is used; essentially to develop a consistent spectra of resolved TKE for whichever wavenumbers are available.

Considering, as a thought-experiment, the horizontal and vertical directions independently for an ABL, it a large coefficient on a diffusive term taken over $\partial^2/\partial x^2$, i.e. a large value for K_h, will result in a large amount of smoothing of waves over $\Delta_{x,y}$, starting with the wavelengths nearest to the grid's Nyquist limit in that direction, i.e. $\lambda \approx 2\Delta_{x,y}$. However, this is only desirable if it is desirable to enforce that $\Delta_{x,y}$ is in the inertial subrange. For an atmospheric LES, where scale-correct dynamics are preferential to developing a turbulent momentum cascade, the only waves that should be smoothed in either direction are those that are either "sub-filter scale" or those that are too energetic. Recalling that numerical diffusion increases with grid-spacing and the results seen in Ch. 3, the overly-energetic motions in the horizontal wavespace are adequately dissipated without any explicit SGS model. However, there are many wavenumbers that are resolvable in Δ_z on these highly-anisotropic grids that are smaller than the horizontal Nyquist limit, and thus are SFS motions in x but not in z. The vertical direction also receives much less numerical diffusion by virtue of being finer-scale,

so any stability-related efforts should be focused in the vertical direction. This is a fine balance of choosing the correct length scale and coefficients (e.g. Smagorinsky constant) to achieve the desired balance of resolved turbulence and SGS smoothing. This was also seen in the no-model results of Ch. 3, where the $\Delta_{x,y} = 1.2$ km resolved u-velocity profiles were significantly under-smoothed compared to the $\Delta_{x,y} = 100$ m case.

Following up said thought experiment with a numerical experiment, both the anisotropic Smagorinsky-Lilly and anisotropic TKE-1.5 models were modified to be formulated as

$$\begin{aligned} l_h &= \Delta_z, \\ l_v &= \Delta_{x,y}, \end{aligned} \tag{4.1}$$

where the lengthscales are then treated as they normally are in the anisotropic TKE-1.5 eddy-viscosity calculation. The implementations of the original and alternative-anisotropic TKE-1.5 models into the WRF code are presented in Appx. 4.A.1.2. Note that, currently, this adjustment in the TKE-1.5 model is made for the eddy-viscosity calculation only, and is not included in any calculations inside the prognosticated TKE equation. The impacts of this choice will be examined in future work.

The Smagorinsky-Lilly model was then adjusted further in its alternative-anisotropic formulation based on diagnosable deficiencies, until the following formulation was found. First, a partitioning similar to the anisotropic-deformation formulation discussed in Ch. 3 is taken, but recalling that the motivation is to mix vertically, the $\overline{S}_{33}$ term is moved to the $\overline{S}_v$ term, i.e.

$$\begin{aligned} \overline{S}_h &= \sqrt{2}\left(\overline{S}_{11}^2 + \overline{S}_{22}^2 + \overline{S}_{12}^2 + \overline{S}_{21}^2\right)^{1/2}, \\ \overline{S}_v &= \sqrt{2}\left(\overline{S}_{33}^2 + \overline{S}_{13}^2 + \overline{S}_{23}^2 + \overline{S}_{31}^2 + \overline{S}_{32}^2\right)^{1/2}, \end{aligned} \tag{4.2}$$

so that $\overline{S}_{33}$ will now be paired with the larger of the two lengthscales after applying the forthcoming re-definition of the lengthscales. Note that this is different than the partitioning used in the anisotropic-deformation Smagorinsky-Lilly formulation presented previously in Ch. 3. One possible explanation offered for the partitioning in Eq. (4.2) is that, recalling the discussions of Secs. 1.3 and 1.3.1, it may not be safe to assume a constant thermodynamic equilibrium in the pressure field on such anisotropic grids.

Finally, recalling the behavior of the no-model case in Chs. 2 and 3, where the no-model resolved TKE spectrum actually showed the most resolved TKE, the new lengthscale is formulated to scale with height in order to allow resolved mixing to be triggered at the surface, so that gradients may be smoothed out vertically by resolved mixing before being smoothed out horizontally by SGS mixing. Once the TKE is in the atmosphere, it may then be dissipated by the model, but it must first be allowed to enter into the resolved scale.

Thus, for the Smagorinsky-Lilly model, the alternative-anisotropic lengthscales are implemented as

$$\begin{aligned} l_h^2 &= \big(z\big)\big(\Delta_z\big), \\ l_v^2 &= \big(z\big)\big(\Delta_{x,y}\big), \end{aligned} \tag{4.3}$$

where z is height AGL. While the turbulent lengthscales are set alternatively [i.e. as in Eq.(4.3)], the numerical-stability-based upper limits for $K_{h,v}$ are set with the original grid lengths, as can be seen in the implementations of the original and alternative-anisotropic Smagorinsky-Lilly models into the WRF code presented in Appx. 4.A.2.2.

The alternative-anisotropic formulation is considered for both the Smagorinsky-Lilly and TKE-1.5 models. For convenience and simplicity, these reformulations will be referred to in figure labels as "alt.Smag." and "alt.TKE-1.5", respectively.

It is generally found that $C_s = C_k = 0.1$ works best for the alternative-anisotropic Smagorinsky-Lilly and alternative-anisotropic TKE-1.5 models, respectively, which is what is shown in this manuscript, though there is certainly room for improvement in the tuning of and further understanding of these coefficients. Other than this coefficient being lightly tuned (or simplified to be $C_s = C_k = 0.1$) and the re-defining of the turbulent lengthscales and the noted partitioning of deformations into anisotropic components in the Smagorinsky-Lilly model, there are no special changes made to the code for either model implementation.

It is worth pointing out that, while the alternative-anisotropic Smagorinsky-Lilly model does have some additional modifications other than the swapping of the lengthscales, the alternative-anisotropic TKE-1.5 model is only modified as Eq. (4.1) in the calculation of the final turbulent stresses, τ_{ij}, and not in the prognostic TKE equation. The alternative-anisotropic TKE-1.5 formulation is equivalent to the isotropic TKE-1.5 model on isotropic grids.

4.2 Results

Here the alternative-anisotropic formulation for the Smagorinsky-Lilly and TKE-1.5 models will be presented and compared to the standard isotropic and anisotropic formulations of the two models. They will be evaluated by the same criteria used for eddy-viscosity models in Ch. 3 for multiple combinations of surface heat flux and column mean wind. The first case considered is a free-convection version of the case from Ch. 3 (where $\overline{w'\theta'_s} = 0.3$ m K s^{-1}), using the same initial potential-temperature profile but with all velocities, as well as the geostrophic forcing, set to zero. The second case considered is the identical case to Ch. 3. Analysis is extended to coarser $\Delta_{x,y} = 5$ km grids here, in addition to the $\Delta_{x,y} = 1.2$ km already seen. At $\Delta_{x,y} = 5$ km the anisotropic Smagorinsky-Lilly model is replaced with the anisotropic-deformation Smagorinsky-Lilly model, as will be discussed. Other cases are also considered in less detail with larger and smaller heating rates and larger mean wind speeds, leading to some very interesting observations, conclusions and open questions for future work.

Some of the following analysis will consider only the standard isotropic and anisotropic TKE-1.5 model, as the TKE-1.5 performance was superior to the Smagorinsky-Lilly model in both formulations, as seen in Ch. 3. Analysis of the performance of the standard TKE-1.5 model, both in isotropic and anisotropic formulations, will not be heavily repeated here except as relevant as compared to the alternative-anisotropic models. Note that the standard versions used here are with the original WRF v3.8.1 implementation, before either of the

changes described in Ch. 3 (referred to as "alt13" and "alt33" there), with the exception of the 5-km simulations below which use the anisotropic-deformation Smagorinsky-Lilly formulation.

4.2.1 Free convection

4.2.1.1 At 1.2-km horizontal resolution

The first case presented is a wind-free (i.e. $u_0 = 0$ m s^{-1}) simplification of the case presented previously in Ch. 3, but all other model and grid settings remain identical. Considering first the planar-averaged resolved potential temperature and u-velocity profiles, the subtle but familiar signatures of the isotropic and anisotropic TKE-1.5 models are visible, though not strikingly so, in the potential-temperature profiles (Fig. 4.1). Those signatures are: in the first few hours the isotropic model has a profile that is visibly under-mixed and there is a lack of entrainment at the CBL top during the first few hours compared to the high resolution results. Resolved turbulence appears to begin in the $t = 5$ hours profile, after which the profiles appear very well mixed with visible entrainment, though with a near-surface adiabatic layer that has the appearance of being slightly too deep and gentle. The anisotropic TKE-1.5 model tends to be more severely under-mixed before resolved convection begins, but resolved convection begins earlier than in the isotropic case and develops a near-surface layer that is both too deep and too warm. For this wind-free case, neither model generates a significant mean-wind, which is the correct behavior.

The alternative-anisotropic models both perform similarly to each other, with the only noticeable differences in the planar-averaged resolved potential temperature profiles in the first couple of hours. The alternative-anisotropic Smagorinsky-Lilly model is more under-mixed in the first hour than the isotropic TKE-1.5 model, but less than the anisotropic TKE-1.5 model. The alternative-anisotropic TKE-1.5 model appears to be the most mixed profile of the four shown in the first hour, and there is visible entrainment in the CBL top, which cannot be said for the other three models. The second-hour profiles of the alternative-anisotropic models are interesting in that the alternative-anisotropic Smagorinsky-Lilly model generates a more-developed near-surface layer, while the TKE-1.5 version has not yet developed a clear near-surface layer, but is entraining aloft at a rate that appears similar the high-resolution case shown for comparison. By the third hour, both alternative-anisotropic models generate profiles that agree well with the high-resolution case, and continue to do so for the duration of the simulation.

Slices of the resolved vertical velocity ($\overline{w}$) through the $z \approx 518$-m plane at hours 4 and 6 are shown in Fig. 4.2. The familiar behavior of the isotropic and anisotropic TKE-1.5 model is presented for reference, showing that the alternative-anisotropic formulations for both the Smagorinsky-Lilly and TKE-1.5 models are generating smaller scales than both traditional formulations of the TKE-1.5 model. As well as resolving turbulence at a smaller scale, the $t = 4$ hour slices show high amounts of early resolved turbulence in both alternative-anisotropic models, unlike the isotropic TKE-1.5 model which appears very calm relative to the other three. The alternative-anisotropic models appear to combine the earlier onset of

resolved mixing seen in the traditional anisotropic formulations with the smaller scales of resolved TKE seen in the isotropic formulations, inspiring further consideration.

Considering the TKE in $\overline{w}'\overline{w}'$, as before, the alternative-anisotropic models both show an improved performance over the standard models for this case (Fig. 4.3 – 4.6). First discussing the alternative-anisotropic Smagorinsky-Lilly model, both the time-evolution of $\langle \overline{w}'\overline{w}' \rangle$ in space and the resolved energy spectra, $\overline{\mathcal{S}}_{33}$, over the final two hours show some unique qualities (Fig. 4.3). While the traditional models are both delayed longer than five hours before they begin resolving turbulence, the alternative-anisotropic model has triggered resolved turbulence by the first hour. As well, while the traditional models both begin with a very visible oscillation in the time series, the alternative-anisotropic case has a smoother onset of $\overline{w}'\overline{w}'$. The resulting critical wavelength in the alternative-anisotropic case is smoother versus time than the standard models, though it still shows a higher λ_c than the high-resolution case due to the coarser horizontal resolution in this test case. Considering the spectra of the three models, the alternative-anisotropic formulation appears to agree closest to the high-resolution control case. Compared to the high-resolution case, the isotropic model is visibly missing energy at both the lower and higher wavenumber ends of the spectrum, and the traditional anisotropic model has the same general shape as the high-resolution case but with a significant shift towards lower wavenumbers. The alternative-anisotropic case compared to the high-resolution case, however, shows a very high amount of agreement, and is only missing significant amounts of energy in the highest wavenumbers on the grid.

Contours of the resolved spectra, $\overline{\mathcal{S}}_{33}$, in time show that, again, the alternative-anisotropic Smagorinsky-Lilly model is visually the best-performing Smagorinsky-Lilly formulation (Fig. 4.3). The alternative-anisotropic model begins resolving TKE earlier than either other formulation, and at a smaller and more consistent scale.

The alternative-anisotropic TKE-1.5 model shows similar improvement compared to the traditional isotropic and anisotropic formulations, though less dramatic, partly owing to the traditional TKE-1.5 model performing better at $\Delta_{x,y} = 1.2$ km than the traditional Smagorinsky-Lilly model. Considering the time series of $\overline{w}'\overline{w}'$, the alternative-anisotropic TKE-1.5 model actually shows a slightly increased delay in resolved turbulence compared to the traditional anisotropic model and its onset of resolved TKE is not as smooth as the alternative-anisotropic Smagorinsky-Lilly model (Fig. 4.5. The alternative-anisotropic TKE-1.5 model produces a smaller critical lengthscale λ_c than the standard versions, though all versions show some oscillations with time. Improvement is also seen in the spectra of the resolved turbulence at the finest scales, $\overline{\mathcal{S}}_{33}$, however the improvement over the isotropic model is less pronounced due to the isotropic TKE-1.5 model delivering superior spectra to the isotropic Smagorinsky-Lilly model.

Contours of spectra for the TKE-1.5 models confirm what was seen above, where the alternative-anisotropic TKE-1.5 model shows the smoother and smaller-scale energy but is delayed in its onset compared to the traditional anisotropic TKE-1.5 model (Fig. 4.6). Considering that the delay in TKE is lesser in the traditional anisotropic model, this delay in resolved $\overline{w}'\overline{w}'$ for the alternative-anisotropic TKE-1.5 model is possibly due to the lengthscales in the SGS TKE-1.5 routines (prognosticated TKE equations) not being updated to correspond

to the eddy-viscosity calculation, and is the subject of future work.

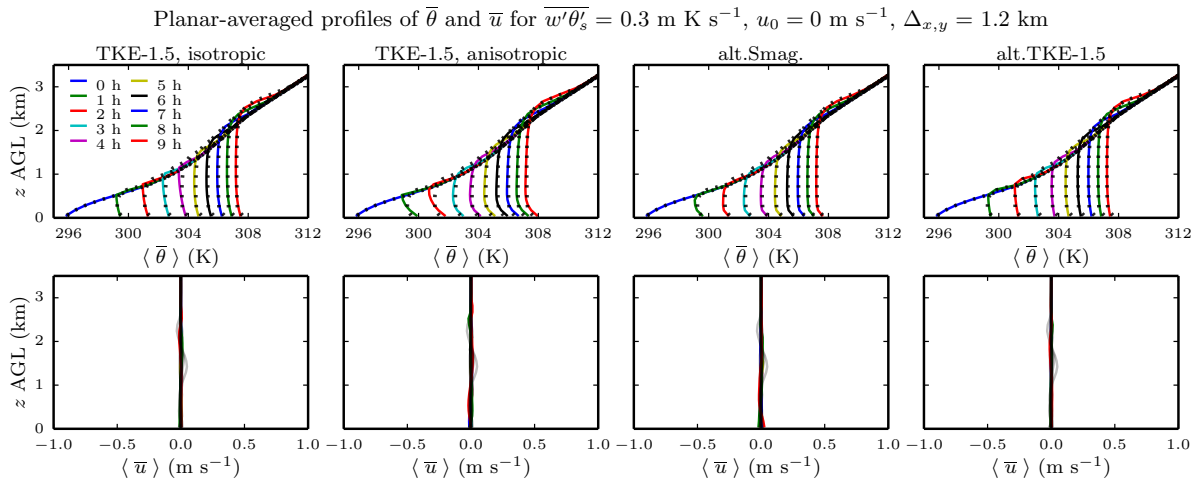

Figure 4.1: Resolved potential temperature and u-velocity profiles for $\Delta_{x,y} = 1.2$ km using the current isotropic (far left) and anisotropic (middle left) TKE-1.5 implementations, compared to the alternative-anisotropic Smagorinsky-Lilly (middle right) and alternative-anisotropic TKE-1.5 (far right). High-resolution ($\Delta_{x,y} = 100$ m) isotropic TKE-1.5 case overlaid for resolved potential temperature (dotted black) and u-velocity (faded black). Full-column profiles shown in Appx. 4.B.

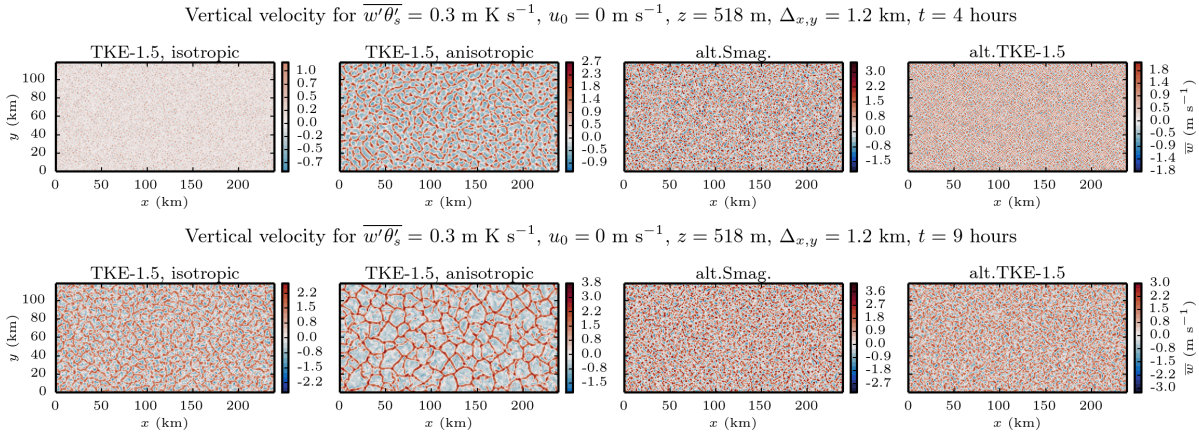

Figure 4.2: Resolved vertical velocity, $\overline{w}$, in the $z \approx 518$ m plane at $t = 4$ (top) and 9 (bottom) hours for the $\Delta_{x,y} = 1.2$ km cases using the current isotropic (far left) and anisotropic (middle left) TKE-1.5 implementations, compared to the alternative-anisotropic Smagorinsky-Lilly (middle right) and alternative-anisotropic TKE-1.5 (far right).

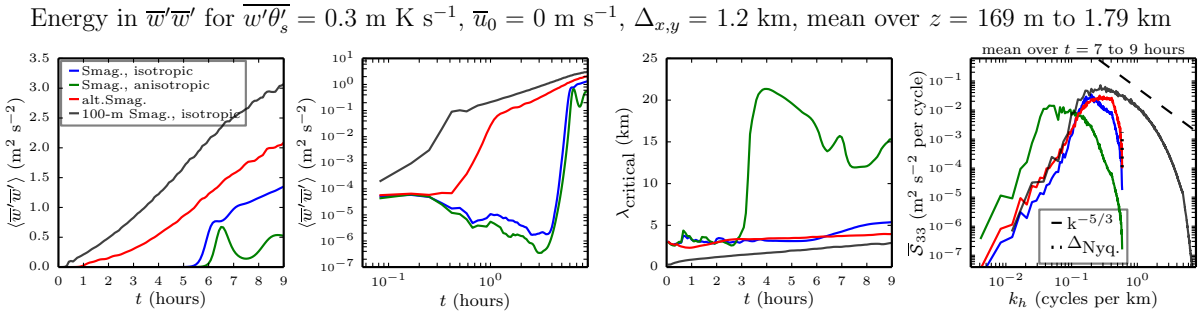

Figure 4.3: Metrics of the resolved vertical velocity field, $\overline{w}$, averaged over the $z \approx$ 169 m to 1.79 km planes for the $\Delta_{x,y} = 1.2$ km cases using the Smagorinsky-Lilly model with current isotropic and anisotropic, as well as alternative-anisotropic, lengthscales: total resolved TKE ($\overline{w}'\overline{w}'$) in time (far left), the same in log-log scale (middle left), critical wavelength of $\overline{w}'\overline{w}'$ in time (middle right), and spectra of resolved TKE ($\overline{\mathcal{S}}_{33}$) averaged over the final two hours (far right)

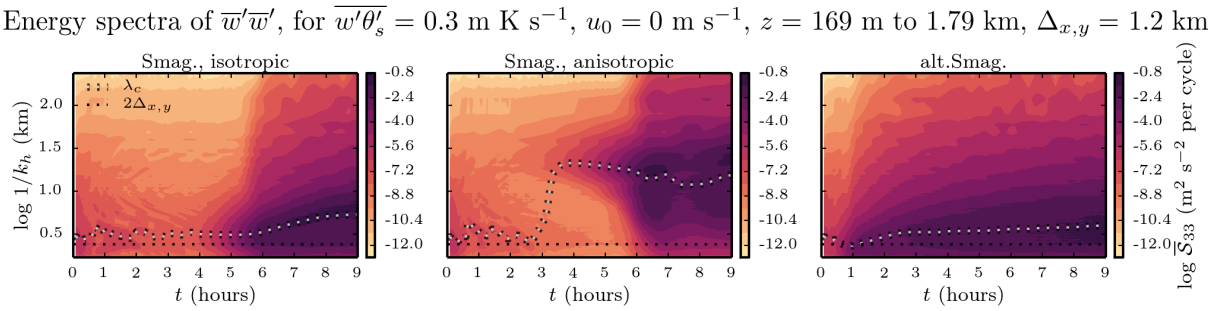

Figure 4.4: Contours of spectra of resolved TKE in the vertical velocity ($\overline{\mathcal{S}}_{33}$) in time for the $\Delta_{x,y} = 1.2$ km cases using the Smagorinsky-Lilly model with current isotropic and anisotropic, as well as alternative-anisotropic, lengthscales, with the critical wavelength (dotted white) and horizontal Nyquist limit (dotted black) overlaid.

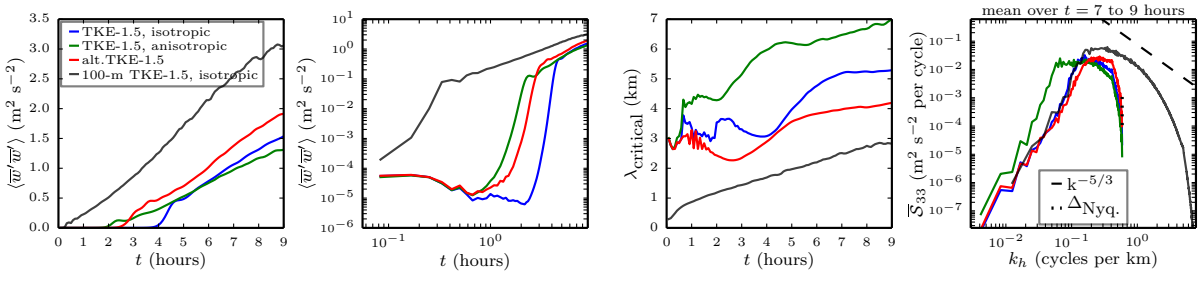

Figure 4.5: As in Fig. 4.3 but using the TKE-1.5 model.

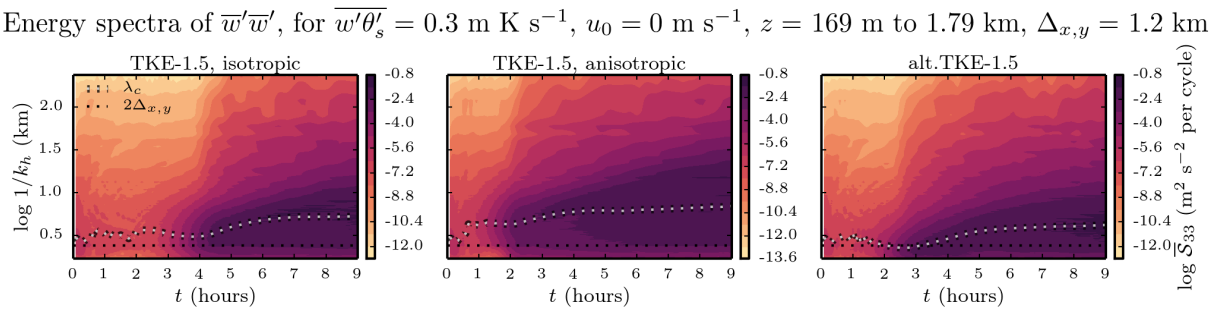

Figure 4.6: As in Fig. 4.4 but using the TKE-1.5 model.

4.2.1.2 At 5-km horizontal resolution

Considering the same case at $\Delta_{x,y} = 5$ km results in a very clear demonstration of the differences in the models considered, where each model behaves almost like a caricature of itself, in the planar-averaged profiles and velocity slices, but particularly in the energy spectra.

Considering the planar-averaged profiles first, following the precedent of the manuscript, the isotropic Smagorinsky-Lilly model shows planar averaged profiles of resolved potential temperature column that are fully mixed throughout the simulation but with no visible resolved surface layer or entrainment (Fig. 4.7). The anisotropic Smagorinsky-Lilly model (standard WRF version) was unable to complete the simulation and was thus replaced with the anisotropic-deformation Smagorinsky-Lilly model ("ad.Smag"), which, based on the profiles of potential temperature, appears to suppress mixing until approximately midway into the simulation, after which a very deep surface layer is resolved, with very minimal entrainment at the CBL top. The alternative-anisotropic Smagorinsky-Lilly model, like the other two Smagorinsky-Lilly formulations that produced a solution (i.e. the isotropic and anisotropic-deformation Smagorinsky-Lilly models), is unable to generate entrainment at the CBL top. However, in character, the near-surface layer is nicely resolved considering the horizontal resolution available. The velocity profiles show no mean wind as expected.

The planar-averaged profiles for the isotropic and alternative-anisotropic TKE-1.5 model appear very similar, with both showing very well-mixed profiles that are visibly too sharp (sharp gradients at the top of the boundary layer), the alternative-anisotropic version more so than the isotropic version (Fig. 4.8). Both the isotropic and alternative-anisotropic versions appear to under-develop the near-surface layer, consistent with the behavior seen by both models, but exhibit reasonable entrainment, with sharper gradients and the alternative-anisotropic slightly over-entraining at the CBL top. The anisotropic TKE-1.5 model struggles to mix the surface heat flux in the first 6 hours, and then produces a near-surface layer that is visibly much deeper than the reference high-resolution profile.

The slices of resolved vertical velocity at the same time and vertical-levels considered previously ($z \approx 518$ m and $t = 4$, 9 hours) show generally the same behavior as seen before and do not reveal anything particularly new. However, they are presented in Appx. 4.C.1 for the interested reader.

The TKE spectra for the resolved vertical velocity is very informative of the underlying behavior of the different models (Fig. 4.9). All four panels of the $\overline{w}'\overline{w}'$ diagnostic figure are presented for the familiar reader, but discussion will focus on the final panel considering the spectrum in wavespace, *osvv*. Compared to the $\Delta_{x,y} = 100$ m case using the isotropic TKE-1.5 model as a reference (recalling that all models produced largely the same spectra), the different behavior of the models is more pronounced than at finer resolutions, and is very aligned with everything learned about the models thus far. The two isotropic models, both Smagorinsky-Lilly and TKE-1.5 implementations, produce spectra that are largely flat across scalar wavespace (k_h), with the Smagorinsky-Lilly model staying flat past the largest wavelength of the isotropic and alternative-anisotropic TKE-1.5 models (which agree with

each other at the longest wavelengths). The isotropic TKE-1.5 model has a production-rate that is very visible, and in agreement with the rest of the models, but it both dissipates a lot of energy overall, and also, like the isotropic Smagorinsky-Lilly model, creates a spectrum that is largely flat across the present scales of k_h.

In contrast, the alternative-anisotropic TKE-1.5 model, which agrees with the isotropic TKE-1.5 model at the coarsest scales, continues producing TKE at the same production-rate until very close to the grid's Nyquist limit. The alternative-anisotropic Smagorinsky-Lilly model behaves much the same as the alternative-anisotropic TKE-1.5 model, but allows significantly more resolved energy on the grid and nearly overlaps with the reference high-resolution case. The low levels of resolved energy seen in Fig. 4.9 are because the simulations have not yet begun resolving turbulence, though it can be seen in the log-log time-series that all models appear to beginning to trigger mixing at the end of the 9-hour simulation. Longer simulations will be considered in future work.

The standard anisotropic implementations of both models show a very similar behavior to each other, and also fitting with their established behavior, where they have the same general aforementioned production rate, which all models other than the isotropic Smagorinsky-Lilly model seem to agree upon, but then resolve energy at the largest scales possible, rather than the finest scales possible. As has been stated previously in the analysis and criticism of the models considered, resolving a turbulent cascade on the grid is the objective of the traditional eddy-viscosity models, and to this end, again, they excel. Unfortunately, as has also been stated previously, in the case of NWP, this is the opposite behavior than is desired.

Contours of the $\overline{w}'\overline{w}'$ energy spectra, $\overline{\mathcal{S}}_{33}$, in time are also interestingly informative of the behavior of the models (Fig. 4.10 and 4.11). The isotropic Smagorinsky-Lilly model very visibly dissipates its seeded TKE in the first three hours and shows no signs of triggering significant amounts of resolved turbulence. The anisotropic-deformation Smagorinsky-Lilly model begins resolving TKE relatively early and the spectra develops in the correct nature, but, again, at too large of a scale for the physics driving this case, confirming what was seen from the time-averaged spectra of anisotropic-deformation Smagorinsky-Lilly model in Fig. 4.9. The alternative-anisotropic Smagorinsky-Lilly model does begin resolving turbulence at a very small scale, relative to the grid, and it was seen in the Fig. 4.9 that the resolved energy in $\overline{w}'\overline{w}'$ is in excellent agreement with the high-resolution case. However there is also a very visible delay in the onset of resolved turbulence compared to both a high-resolution case (see Ch. 3) and the anisotropic-deformation Smagorinsky-Lilly model at the same resolution.

The different versions of the TKE-1.5 model show a similar, but improved, behavior compared to the Smagorinsky-Lilly implementations. The isotropic TKE-1.5 model does also visibly dissipate a lot of its seeded TKE in the first hour, but it does not dissipate it all like the Smagorinsky-Lilly model, and appears as if it could trigger resolved turbulence if let to run longer (though that is largely speculative). The anisotropic TKE-1.5 model, similarly to the anisotropic-deformation Smagorinsky-Lilly model, begins resolving TKE earlier than either the isotropic or alternative-anisotropic formulations, however at a scale that is visibly much too large, and again similar to the anisotropic-deformation Smagorinsky-Lilly model, with a behavior that appears similar to the high-resolution case, rather than physically correct.

Unlike the anisotropic-deformation Smagorinsky-Lilly model, the anisotropic TKE-1.5 model takes nearly seven hours to to really start resolving TKE. Similar to the behavior seen in Sec. 4.2.1.1, it is hypothesized here that this behavior is related to, and can be addressed via, the lengthscales associated with different processes in the prognostic TKE calculation.

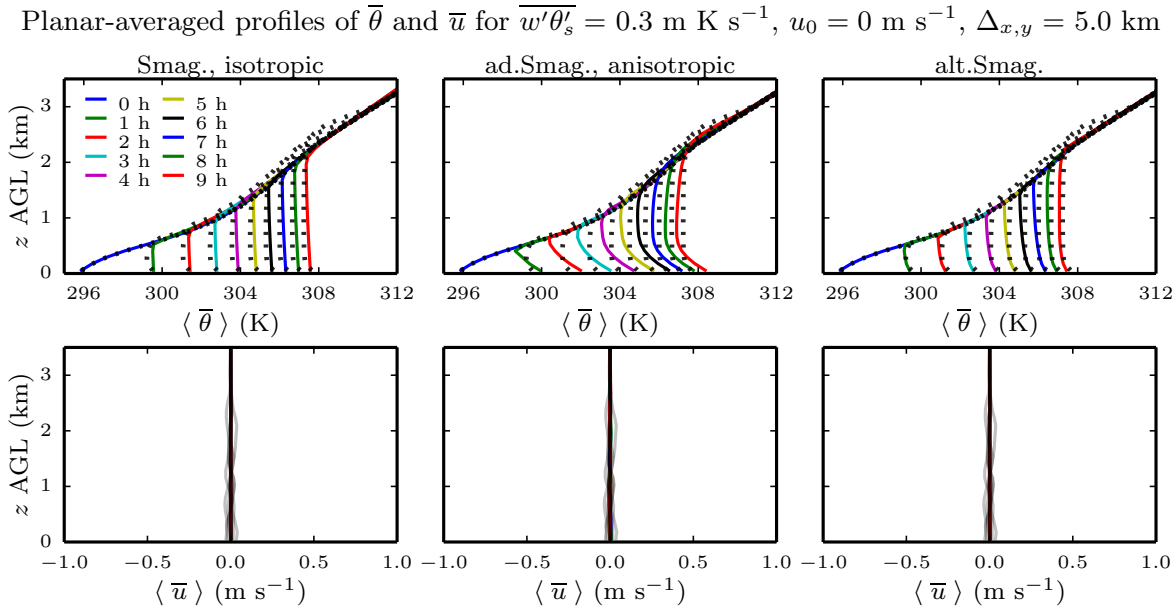

Figure 4.7: As in Fig. 4.1 but for $\Delta_{x,y} = 5$ km using versions of the Smagorinsky-Lilly model.

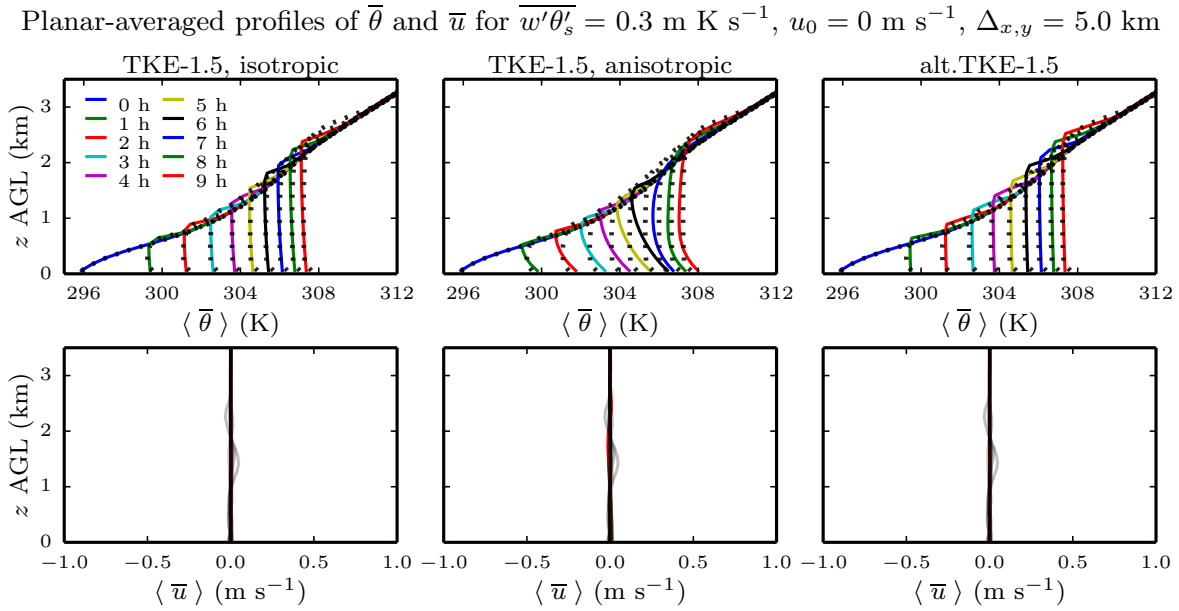

Figure 4.8: As in Fig. 4.1 but for $\Delta_{x,y} = 5$ km using versions of the TKE-1.5 model.

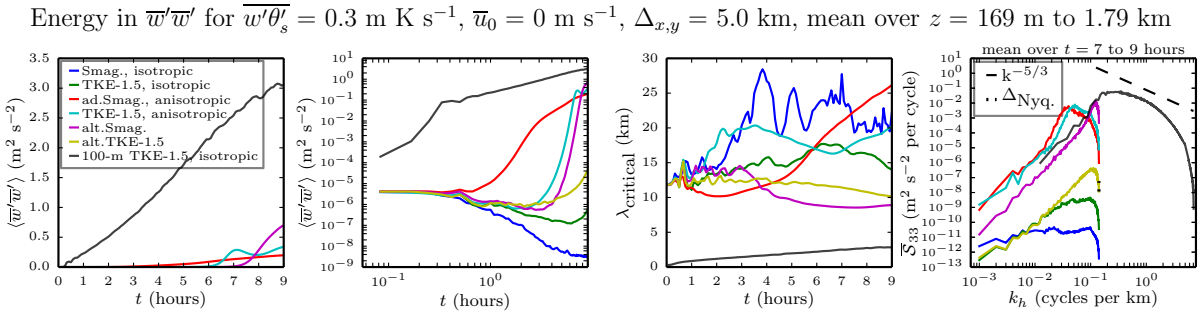

Figure 4.9: As in Fig. 4.3 but for $\Delta_{x,y} = 5$ km cases using the current isotropic Smagorinsky-Lilly model, isotropic and anisotropic TKE-1.5 model, the alternative-anisotropic Smagorinsky-Lilly and alternative-anisotropic TKE-1.5 models.

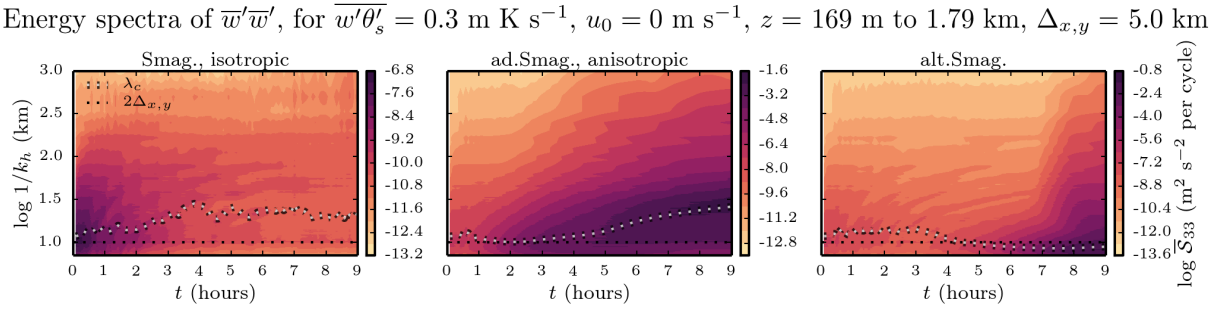

Figure 4.10: As in Fig. 4.4 but for $\Delta_{x,y} = 5$ km cases using the current isotropic Smagorinsky-Lilly, the anisotropic-deformation Smagorinsky-Lilly and the alternative-anisotropic Smagorinsky-Lilly models.

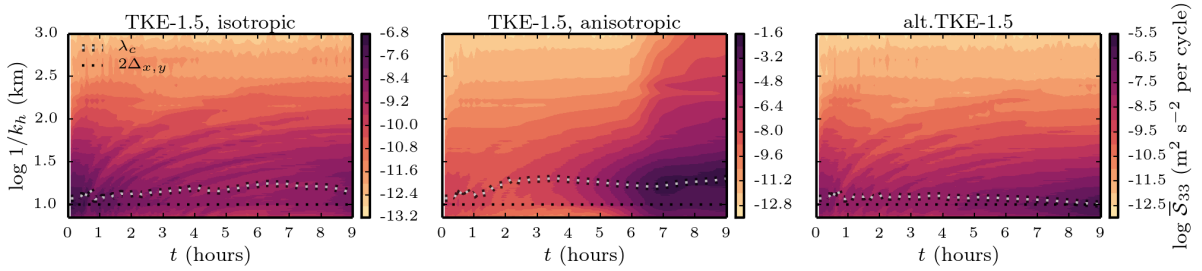

Figure 4.11: As in Fig. 4.4 but for $\Delta_{x,y} = 5$ km cases using the current isotropic and anisotropic TKE-1.5, and the alternative-anisotropic TKE-1.5 models.

4.2.2 Sheared convection

There are two pertinent questions features to examine when adding wind to the initial column. The first is whether or not the alternative-anisotropic models develop wind profiles as well as they develop potential-temperature profiles. The second is whether the presence of a mean wind and shear at the surface effects the potential-temperature development seen in the quiescent case.

4.2.2.1 At 1.2-km horizontal resolution

Considering the $\Delta_{x,y} = 1.2$ km grids, as to the first question above, the potential-temperature profiles appear actually improved, and certainly are not worse. The u-velocity profiles are interesting, where the alternative-anisotropic Smagorinsky-Lilly model appears to generally match the high-resolution case worse, in that its profile is not damped enough near the CBL top. However, the near-surface layer is better developed and thinner than any of the other cases considered, which is the same behavior that is seen in the potential-temperature profiles. The alternative-anisotropic TKE-1.5 model shows a well-developed potential-temperature profile compared to the high-resolution case, although it must be said the near-surface layer is not as well-defined as in the alternative-anisotropic Smagorinsky-Lilly model (which is also true in the u-velocity profiles). The u-velocity profile for the alternative-anisotropic TKE-1.5 model is well behaved compared to the high-resolution case, avoiding the increased velocity seen in the alternative-anisotropic Smagorinsky-Lilly profile. Based on the planar-averaged profiles of u-velocity alone, the alternative-anisotropic TKE-1.5 case is better than the anisotropic TKE-1.5 case, which is overly-effected by the drag at the surface, but appears very similar to the isotropic TKE-1.5 case here.

Velocity slices are not significantly different from the previous case to warrant analysis, but are presented for completeness in Appx. 4.C.2.

The energy spectra in the $\overline{w}'\overline{w}'$ field, $\overline{\mathcal{S}}_{33}$, for the different Smagorinsky-Lilly formulations shows the same behavior as before, where the isotropic case under-resolves energy on both ends of the spectrum and the anisotropic Smagorinsky-Lilly model shifts the entire spectrum towards longer wavelengths (Fig. 4.13). The alternative-anisotropic Smagorinsky-Lilly model, on the other hand, agrees much closer, at least visually, with the high-resolution case at the coarse end of the spectrum, and agrees relatively well with the high-resolution spectrum until very close to the grid's Nyquist limit, resolving visibly more energy than the isotropic Smagorinsky-Lilly model at both the low-wavenumber and high-wavenumber modes available on the $\Delta_{x,y} = 1.2$ km grid.

Contours of $\overline{\mathcal{S}}_{33}$ for the Smagorinsky-Lilly formulations show the same improved performance as seen before (Fig. 4.14).

Considering the familiar metrics of $\overline{w}'\overline{w}'$ for the isotropic, anisotropic and alternative-anisotropic TKE-1.5 model, the alternative-anisotropic TKE-1.5 model again appears very similar to the isotropic TKE-1.5 case, while the anisotropic TKE-1.5 case shows the undesirable behavior that was well-documented in Ch. 3 (Fig. 4.15). However, despite the general

similarities between the isotropic TKE-1.5 model and the alternative-anisotropic TKE-1.5 model, the alternative-anisotropic TKE-1.5 model begins resolving TKE more than an hour earlier than the isotropic TKE-1.5 model and develops in a smoother time-series than the isotropic TKE-1.5 model. As well, the alternative-anisotropic TKE-1.5 model generates visibly more energy on the finest scales of the $\overline{\mathcal{S}}_{33}$ spectrum compared to either of the other models, though the difference is not as drastic as for the Smagorinsky-Lilly model. The same can be said for the contours of $\overline{\mathcal{S}}_{33}$ in time (Fig. 4.16), which appear better for the alternative-anisotropic TKE-1.5 case by virtue of the TKE being triggered earlier than the isotropic case and at a finer scale than in the anisotropic case, however, like in the no-wind case before, the anisotropic TKE-1.5 model begins resolving turbulence before either of the other models. This once again leads to the conclusion that there is a better formulation of the alternative-anisotropic TKE-1.5 model possible, which will be the subject of future work.

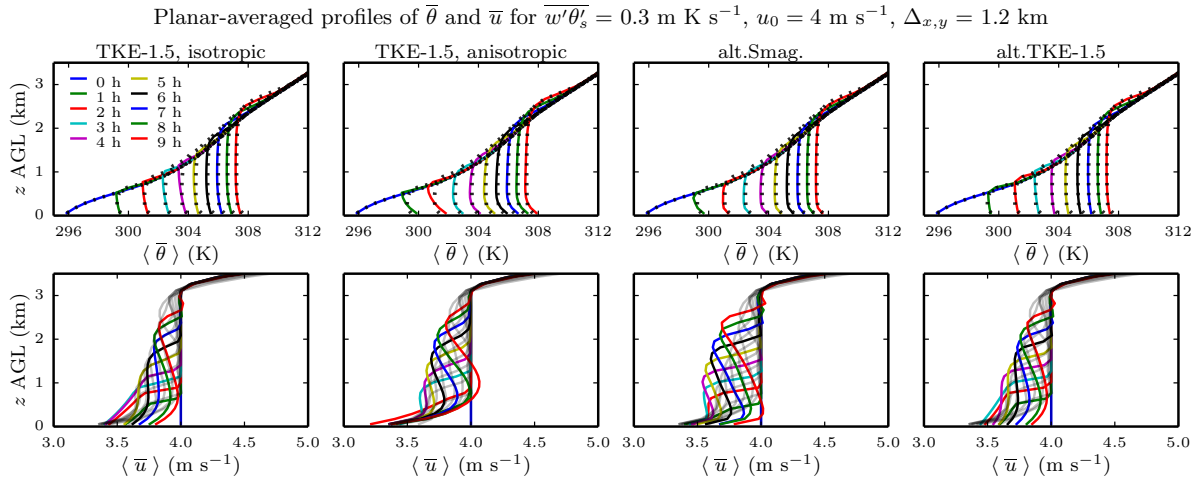

Figure 4.12: Resolved potential temperature and u-velocity profiles for $\Delta_{x,y} = 1.2$ km using the current isotropic (far left) and anisotropic (middle left) TKE-1.5 implementations, compared to the alternative-anisotropic Smagorinsky-Lilly (middle right) and alternative-anisotropic TKE-1.5 (far right). High-resolution ($\Delta_{x,y} = 100$ m) isotropic TKE-1.5 case overlaid for resolved potential temperature (dotted black) and u-velocity (faded black).

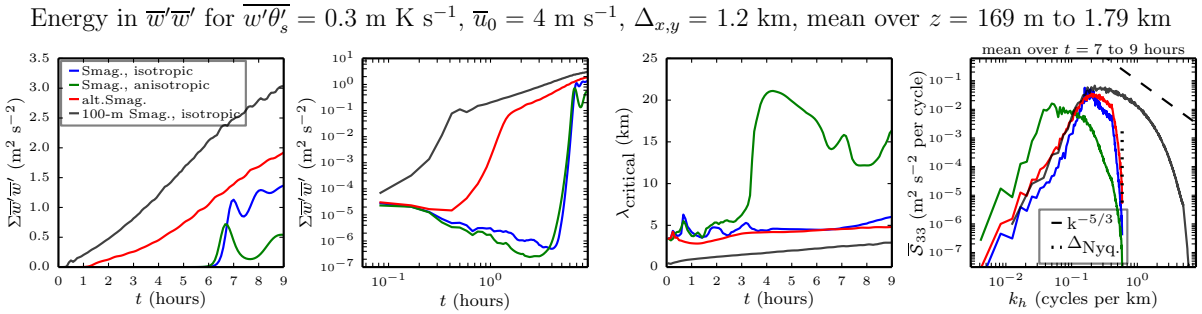

Figure 4.13: Metrics of the resolved vertical velocity field, $\overline{w}$, averaged over the $z \approx$ 169 m to 1.79 km planes for the $\Delta_{x,y} = 1.2$ km cases using the Smagorinsky-Lilly model with current isotropic and anisotropic, as well as alternative-anisotropic, lengthscales: total resolved TKE ($\overline{w}'\overline{w}'$) in time (far left), the same in log-log scale (middle left), critical wavelength of $\overline{w}'\overline{w}'$ in time (middle right), and spectra of resolved TKE ($\overline{\mathcal{S}}_{33}$) averaged over the final two hours (far right)

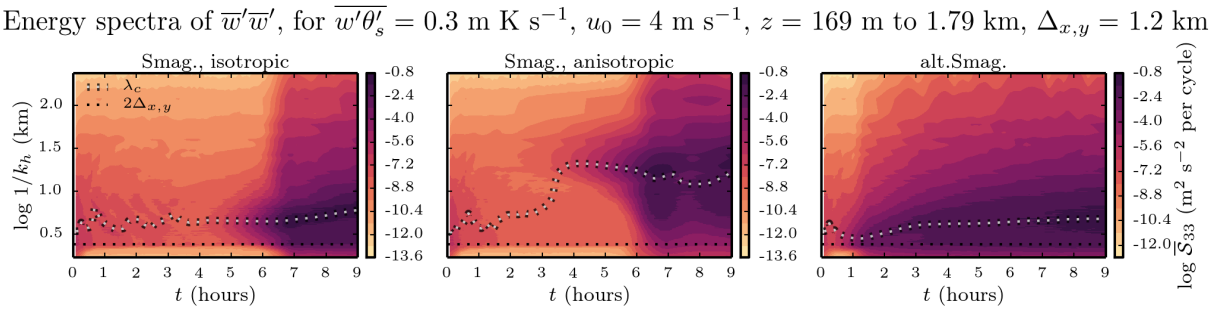

Figure 4.14: Contours of spectra of resolved TKE in the vertical velocity ($\overline{\mathcal{S}}_{33}$) in time for the $\Delta_{x,y} = 1.2$ km cases using the Smagorinsky-Lilly model with current isotropic and anisotropic, as well as alternative-anisotropic, lengthscales, with the critical wavelength (dotted white) and horizontal Nyquist limit (dotted black) overlaid.

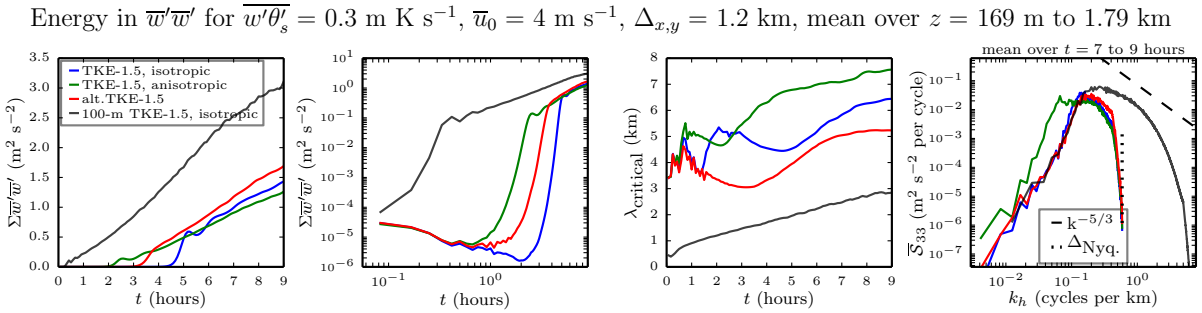

Figure 4.15: As in Fig. 4.13 but using the TKE-1.5 model.

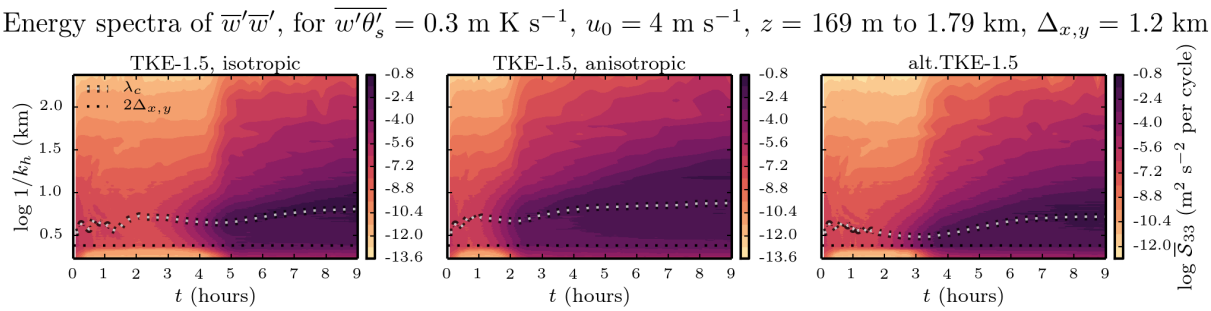

Figure 4.16: As in Fig. 4.14 but using the TKE-1.5 model.

4.2.2.2 At 5-km horizontal resolution

At $\Delta_{x,y} = 5$ km, the conclusions are much the same as before in both the $\Delta_{x,y} = 1.2$ km case with wind and the $\Delta_{x,y} = 5$ km case without wind. Specifically, the isotropic models produce a decent solution but by means of a mean-profile with minimal resolved turbulence, as seen in the planar-averaged profiles (Fig. 4.17), slices of resolved vertical velocity in the $z \approx 518$-m plane at $t = 4$ and 9 hours (Fig. 4.18).

Of more interest is that the same behavior is seen in the energy spectra for $\overline{w}'\overline{w}'$, i.e. $\overline{\mathcal{S}}_{33}$ (Fig. 4.19). Again, the isotropic Smagorinsky-Lilly and TKE-1.5 models create energy spectra that are essentially flat in wavenumber space. Interestingly, the presence of shear has shifted the 5-km $\overline{\mathcal{S}}_{33}$ spectrum for the alternative-anisotropic TKE-1.5 case towards lower wavenumbers, though not to the degree that the traditional anisotropic TKE-1.5 model is shifted to lower wavenumbers. The alternative-anisotropic Smagorinsky-Lilly model shows a similar behavior as at 5-km resolution without a mean wind, but does not resolve as much energy by the final two hours of the simulation. Generally, the same behavior is seen in the spectra, but the presence of shear is noticeably dissipating energy at the finest scales, even when there is not superfluous energy to be dissipated. Contours of $\overline{\mathcal{S}}_{33}$ in time show the same behavior and are included in Appx. 4.C.2.

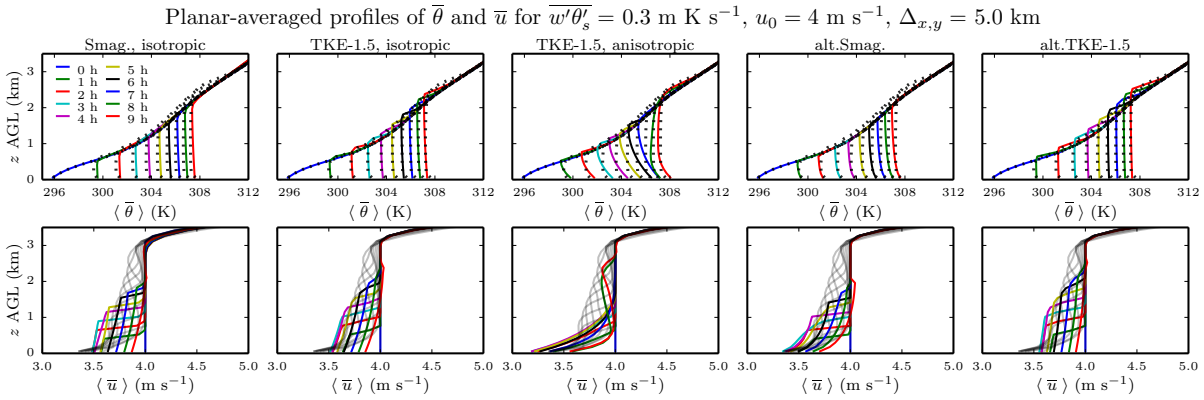

Figure 4.17: As in Fig. 4.12 but for $\Delta_{x,y} = 5$ km cases using the current isotropic Smagorinsky-Lilly model, isotropic and anisotropic TKE-1.5 model, the alternative-anisotropic Smagorinsky-Lilly and alternative-anisotropic TKE-1.5 models.

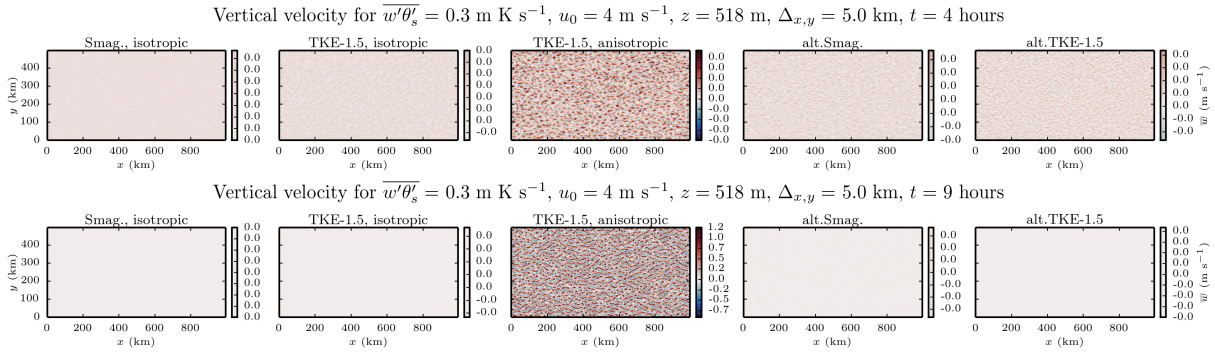

Figure 4.18: Resolved vertical velocity, $\overline{w}$, in the $z \approx 518$ m plane at $t = 4$ (top) and 9 (bottom) hours for the $\Delta_{x,y} = 5$ km cases using the current isotropic Smagorinsky-Lilly model, isotropic and anisotropic TKE-1.5 model, the alternative-anisotropic Smagorinsky-Lilly and alternative-anisotropic TKE-1.5 models.

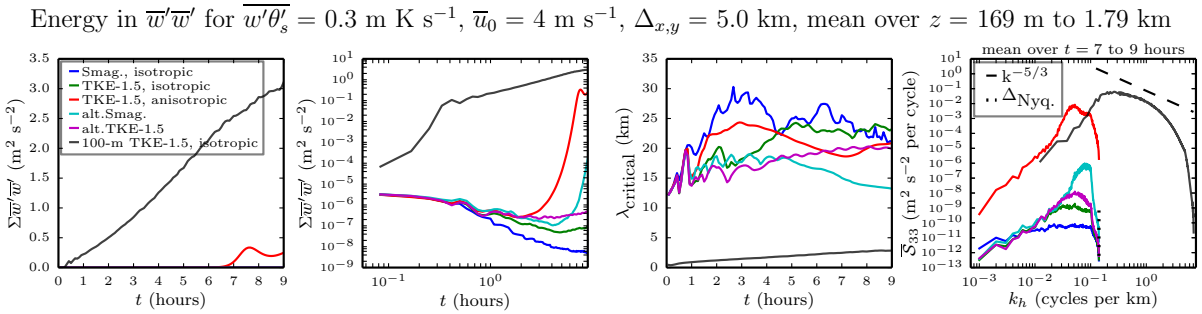

Figure 4.19: As in Fig. 4.13 but for $\Delta_{x,y} = 5$ km cases using the current isotropic Smagorinsky-Lilly model, isotropic and anisotropic TKE-1.5 model, the alternative-anisotropic Smagorinsky-Lilly and alternative-anisotropic TKE-1.5 models.

4.2.3 Other cases

Three other cases are considered to attempt to further isolate the different effects of buoyant and shear effects. Their results will be presented in Secs. 4.2.3.1 – 4.2.3.2, below, via the familiar figures of planar-averaged potential temperature and u-velocity, slices of resolved vertical velocity and energy spectra of TKE in the vertical direction, but will be discussed together here for the sake of brevity. For all cases shown here, the reference high-resolution control is a corresponding $\Delta_{x,y} = 100$ m case using the isotropic TKE-1.5 model.

In Sec. 4.2.3.1 the surface heat flux is increased to $\overline{w'\theta'_s} = 0.4$ m K s^{-1} for a case with no mean wind or geostrophic forcing. In brief, the results show similar promise. At $\Delta_{x,y} = 1.2$ km, resolved planar-averaged profiles show good visual agreement with the reference high-resolution case (Fig. 4.20 and 4.21), resolved velocities appear to be at the appropriate scale for the grid both visually (Fig. 4.22 and 4.23) and in the energetics (Figs. 4.24), and the contours of the resolved spectra begin resolving TKE early and smoothly, and at a consistent scale (Fig. 4.25). In summary, for a purely convective atmosphere the alternative-anisotropic model performs well for Smagorinsky-Lilly and TKE-1.5 implementations compared to both the other standard eddy-viscosity formulations considered and the reference high-resolution case and warrant further consideration.

In Sec. 4.2.3.2, the surface heat flux is reduced to $\overline{w'\theta'_s} = 0.15$ m K s^{-1} and the initial mean wind is increased to $u_0 = 8$ m s^{-1} near the surface. Considering the planar-averaged profiles, the alternative-anisotropic Smagorinsky-Lilly (Fig. 4.26) and alternative-anisotropic TKE-1.5 (Fig. 4.27) again show good agreement with the high-resolution case and the other cases, both developing visual entrainment and the alternative-anisotropic Smagorinsky-Lilly model developing the thinnest surface layer, as was seen before. The development of the resolved u-velocity profiles by the alternative-anisotropic models is of particular interest, where both isotropic eddy-viscosity models show very rigid, sharp profiles (which should be expected, in hindsight, considering that it is an isotropic model) and the anisotropic Smagorinsky-Lilly model generates a velocity profile that can only be described as incorrect in nearly every way, and appears to be actually reinforcing the xz-plane shear instead of mixing it upwards into the ABL. The anisotropic TKE-1.5 model shows this same behavior in the first few hours, before resolved mixing begins (as can be confirmed by both the shape of the resolved potential temperature profiles and later in time series of $\overline{w}'\overline{w}'$), but then reverts to the correct velocity profile after resolved mixing begins. The alternative-anisotropic TKE-1.5 model behaves like the isotropic TKE-1.5 model until resolved mixing begins, at which point it also begins resolving a velocity profile that compares, visually, relatively well to the high-resolution case though with overly-sharp gradients in velocity and potential temperature. Considering the resolved velocity fields shows the same conclusions as for every case thus far, but they do provide a nice visual confirmation (Figs. 4.28 and 4.29).

The time-series and spectra of $\overline{w}'\overline{w}'$ for this case show an interesting behavior that has yet to be seen in this manuscript (Fig. 4.36). The isotropic Smagorinsky-Lilly case shows a behavior that is clearly numerical in nature, showing bursts of energy across the entire spectrum that are immediately dissipated, as can also be seen in the time-contours of $\overline{\mathcal{S}}_{33}$

(Fig. 4.37). Both isotropic models show average resolved spectra over the final two hours (Fig. 4.36 far right panel) that appear to peak near an appropriate value, but with a very strange behavior at the highest wavenumbers of a decreased dissipation rate, and as well show an overly-sharp production rate on the lower wavenumbers. The alternative-anisotropic TKE-1.5 model shows a similar behavior but allows more energy to be resolved. The alternative-anisotropic Smagorinsky-Lilly model shows the best-looking spectra, but does not agree as well with previous high-resolution cases. This case warrants more computing resources for investigation, as it appears that the productive lengthscales are not yet fully resolved even on the high-resolution case (which contains 801×401 points. This could be said for most of the cases presented here, but this particular balance of high-shear and low-surface-heat appears to exacerbate the issue.

In Sec. 4.2.3.3, the surface heat flux is increased to $\overline{w'\theta'_s} = 0.45$ m K s^{-1} with the same initial profile as the previous section with a mean column profile of $u_0 = 8$ m s^{-1} near the surface. To be brief, the performance of the alternative-anisotropic eddy-viscosity models in this case show good agreement with the high-resolution control case without the large and very visible faults seen in the high-shear case.

The implications for future work by the behavior shown in the high-shear, low-heat case are, in the author's opinion, quite vast. The most immediate topics are further investigations of the lengthscales of buoyant and shear-driven production and dissipation in the TKE-1.5 turbulence closure model to deliver consistent results on highly anisotropic grids.

4.2.3.1 For $\overline{w'\theta'_s} = 0.4$ m K s^{-1}, $u_0 = 0$ m s^{-1}

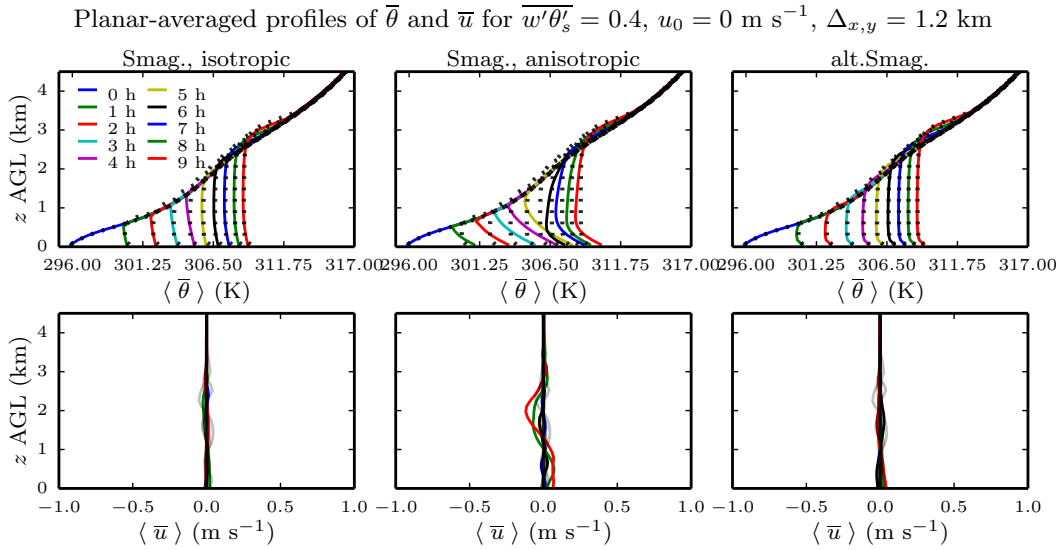

Figure 4.20: As in Fig. 4.1 but for $\overline{w'\theta'_s} = 0.4$ m K s^{-1}, $u_0 = 0$ m s^{-1} cases using the current isotropic and anisotropic Smagorinsky-Lilly model, and the alternative-anisotropic Smagorinsky-Lilly model.

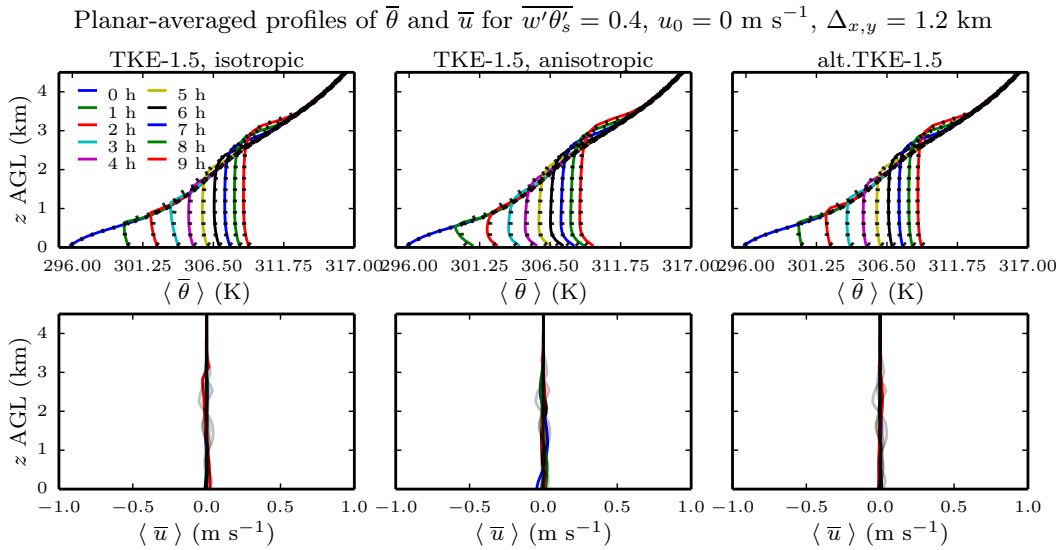

Figure 4.21: As in Fig. 4.1 but for $\overline{w'\theta'_s} = 0.4$ m K s^{-1}, $u_0 = 0$ m s^{-1} cases using the current isotropic and anisotropic TKE-1.5 model, and the alternative-anisotropic TKE-1.5 model.

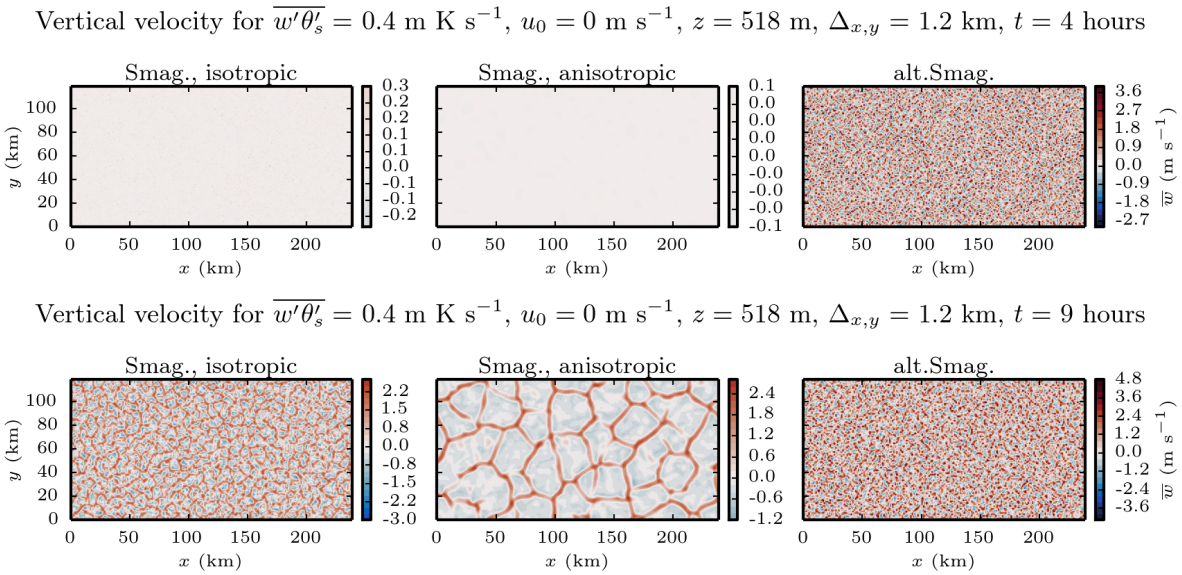

Figure 4.22: As in Fig. 4.2 but for $\overline{w'\theta'_s}$ = 0.4 m K s^{-1}, u_0 = 0 m s^{-1} cases using the current isotropic and anisotropic Smagorinsky-Lilly model, and the alternative-anisotropic Smagorinsky-Lilly model.

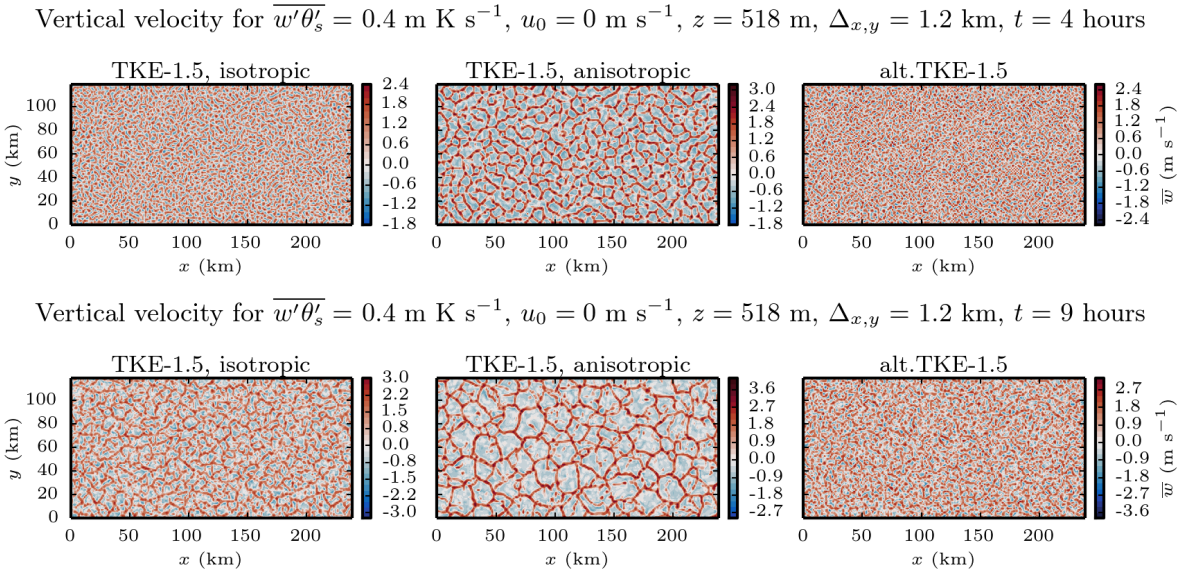

Figure 4.23: As in Fig. 4.2 but for $\overline{w'\theta'_s}$ = 0.4 m K s^{-1}, u_0 = 0 m s^{-1} cases using the current isotropic and anisotropic TKE-1.5 model, and the alternative-anisotropic TKE-1.5 model.

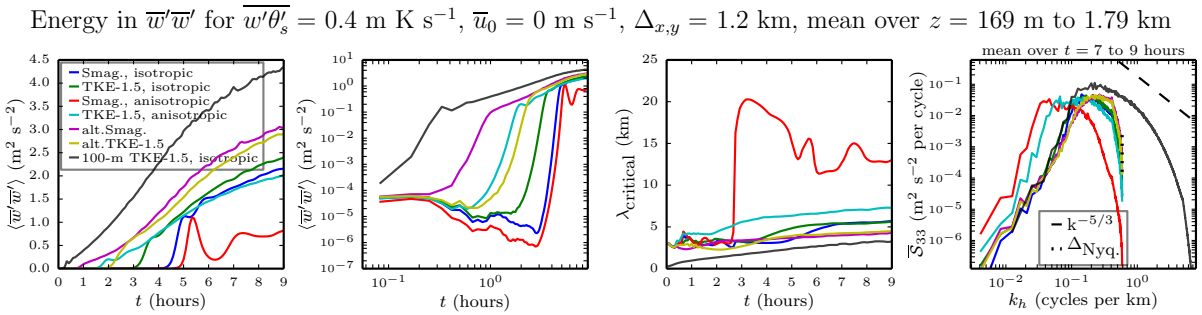

Figure 4.24: As in Fig. 4.3 but for $\overline{w'\theta'_s}$ = 0.4 m K s^{-1}, u_0 = 0 m s^{-1} cases using the current isotropic Smagorinsky-Lilly model, isotropic and anisotropic TKE-1.5 model, the alternative-anisotropic Smagorinsky-Lilly and alternative-anisotropic TKE-1.5 models.

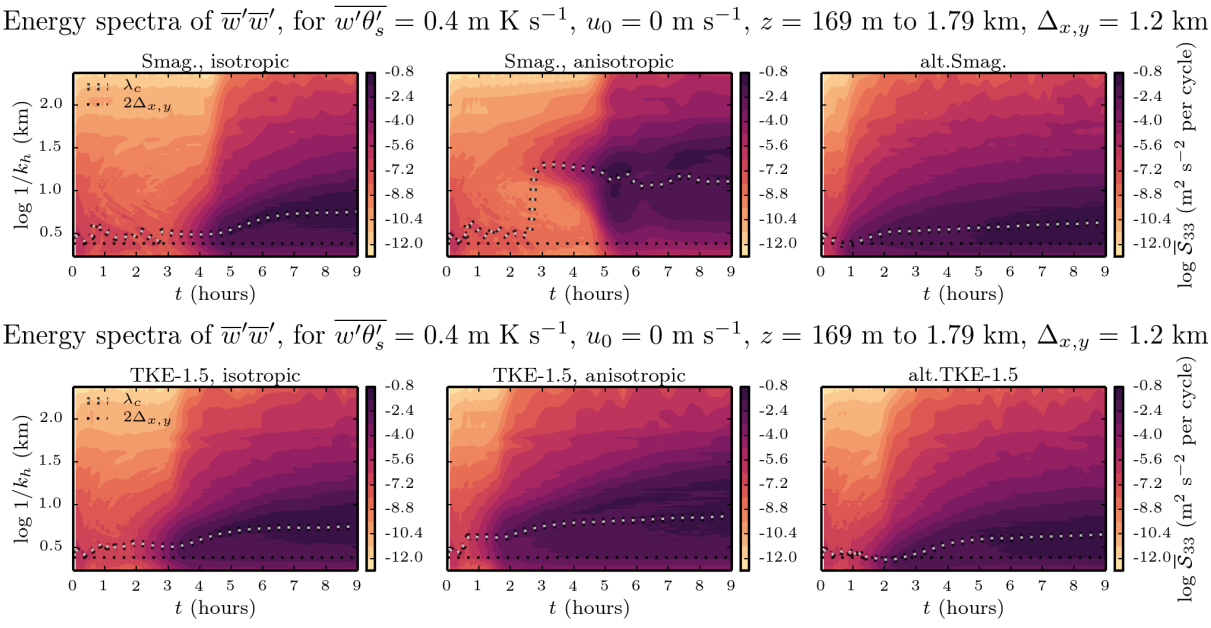

Figure 4.25: As in Fig. 4.4 but for $\overline{w'\theta'_s}$ = 0.4 m K s^{-1}, u_0 = 0 m s^{-1} cases using different formulations of the Smagorinsky-Lilly (top) and TKE-1.5 (bottom) models.

4.2.3.2 For $\overline{w'\theta'_s} = 0.15$ m K s^{-1}, $u_0 = 8$ m s^{-1}

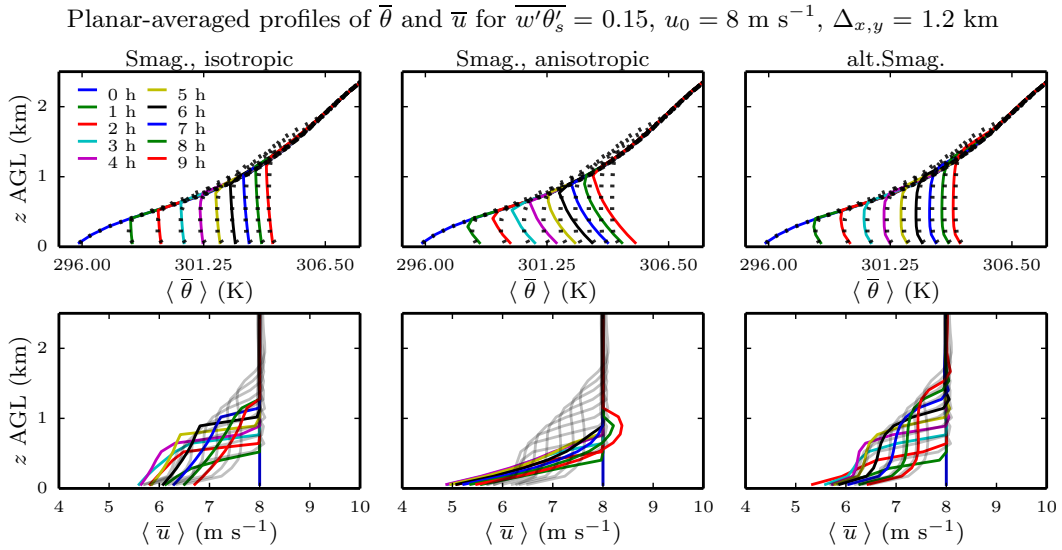

Figure 4.26: As in Fig. 4.1 but for $\overline{w'\theta'_s} = 0.15$ m K s^{-1}, $u_0 = 8$ m s^{-1} cases using the current isotropic and anisotropic Smagorinsky-Lilly model, and the alternative-anisotropic Smagorinsky-Lilly model.

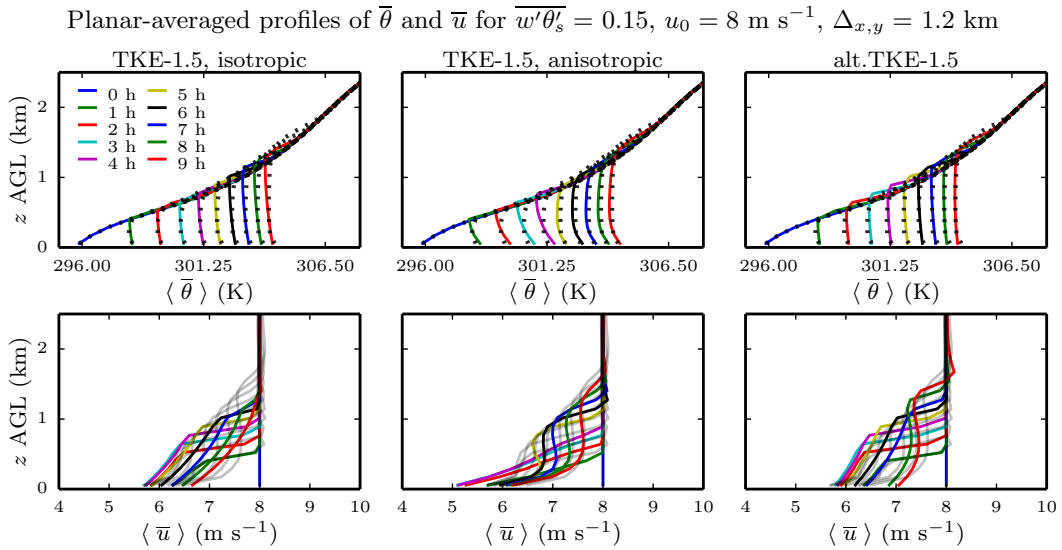

Figure 4.27: As in Fig. 4.1 but for $\overline{w'\theta'_s} = 0.15$ m K s^{-1}, $u_0 = 8$ m s^{-1} cases using the current isotropic and anisotropic TKE-1.5 model, and the alternative-anisotropic TKE-1.5 model.

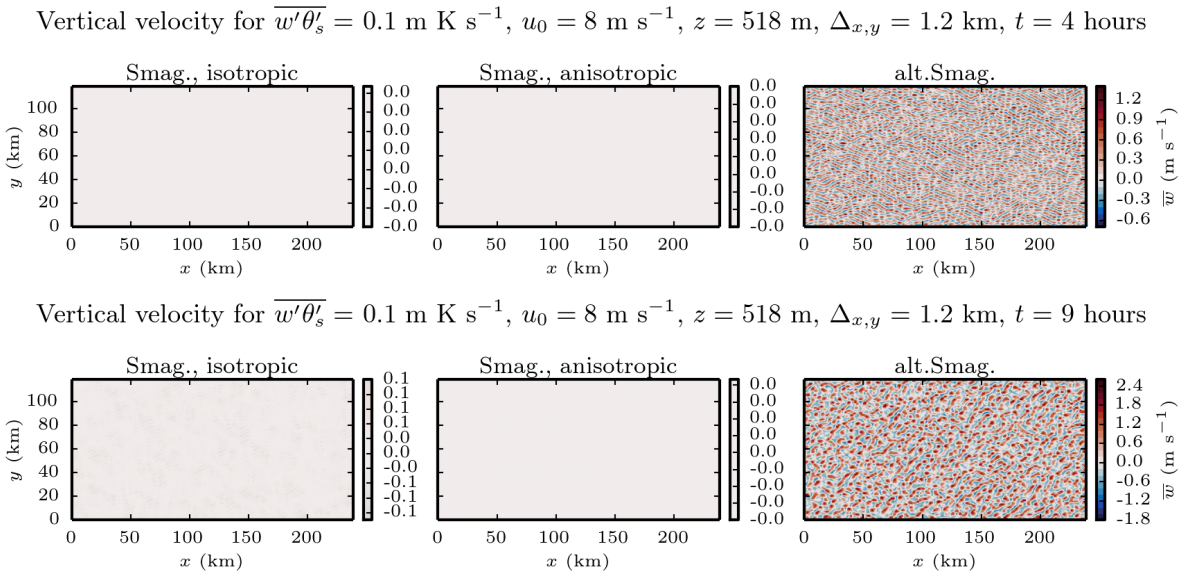

Figure 4.28: As in Fig. 4.2 but for $\overline{w'\theta'_s}$ = 0.15 m K s^{-1}, u_0 = 8 m s^{-1} cases using the current isotropic and anisotropic Smagorinsky-Lilly model, and the alternative-anisotropic Smagorinsky-Lilly model.

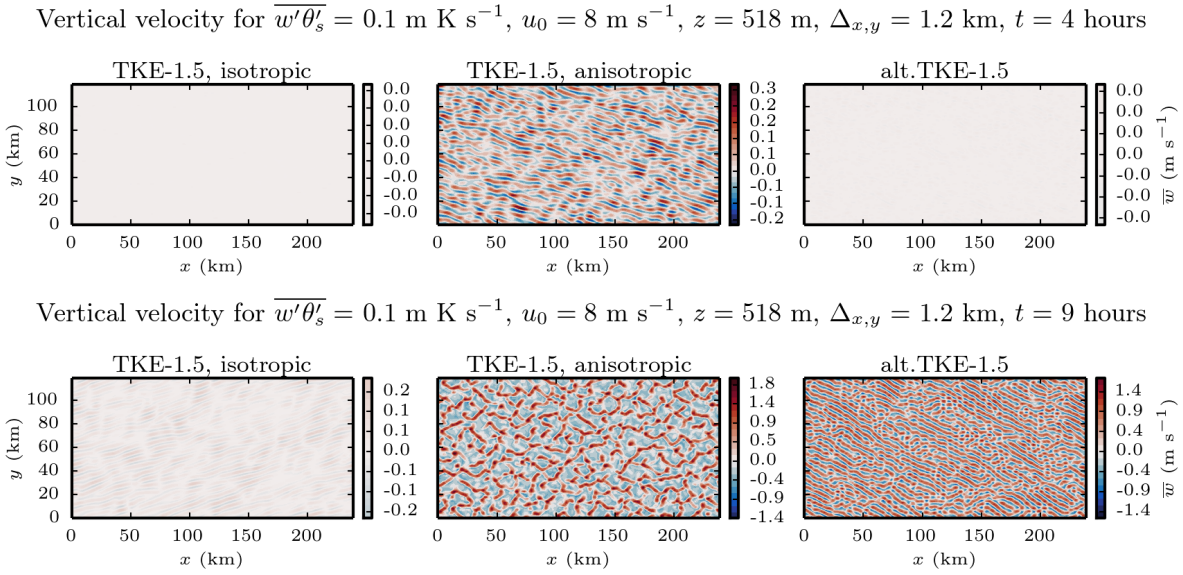

Figure 4.29: As in Fig. 4.2 but for $\overline{w'\theta'_s}$ = 0.15 m K s^{-1}, u_0 = 8 m s^{-1} cases using the current isotropic and anisotropic TKE-1.5 model, and the alternative-anisotropic TKE-1.5 model.

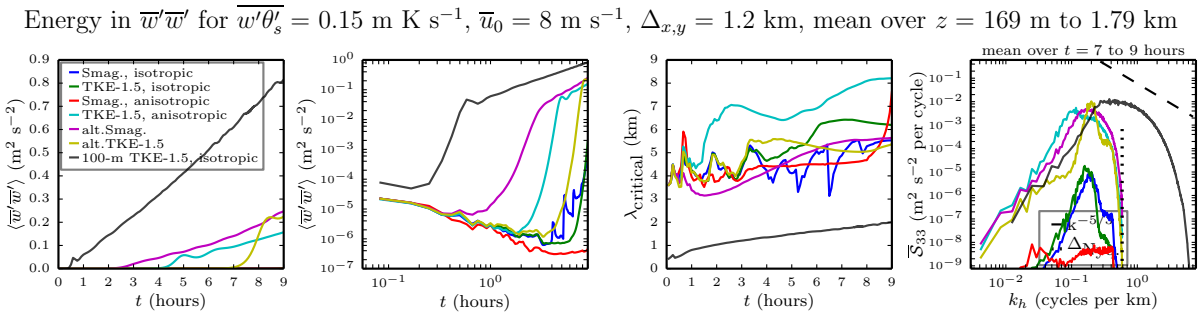

Figure 4.30: As in Fig. 4.3 but for $\overline{w'\theta'_s} = 0.15$ m K s^{-1}, $u_0 = 8$ m s^{-1} cases cases using the current isotropic Smagorinsky-Lilly model, isotropic and anisotropic TKE-1.5 model, the alternative-anisotropic Smagorinsky-Lilly and alternative-anisotropic TKE-1.5 models.

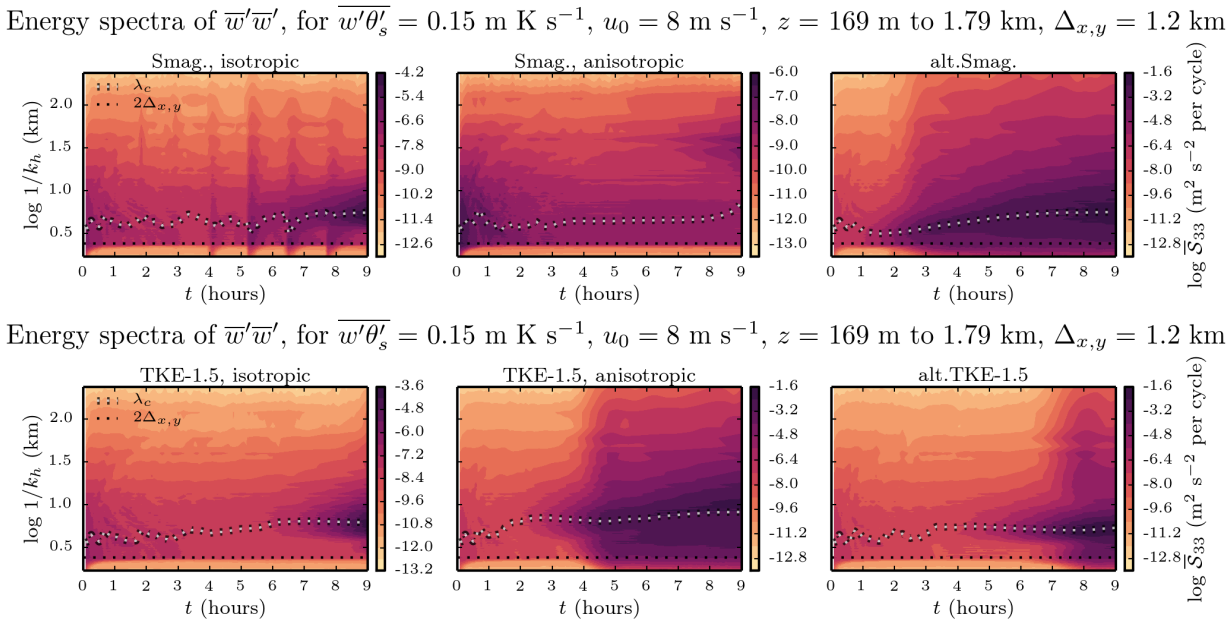

Figure 4.31: As in Fig. 4.4 but for $\overline{w'\theta'_s} = 0.15$ m K s^{-1}, $u_0 = 8$ m s^{-1} cases using different formulations of the Smagorinsky-Lilly (top) and TKE-1.5 (bottom) models.

4.2.3.3 For $\overline{w'\theta'_s} = 0.45$ m K s^{-1}, $u_0 = 8$ m s^{-1}

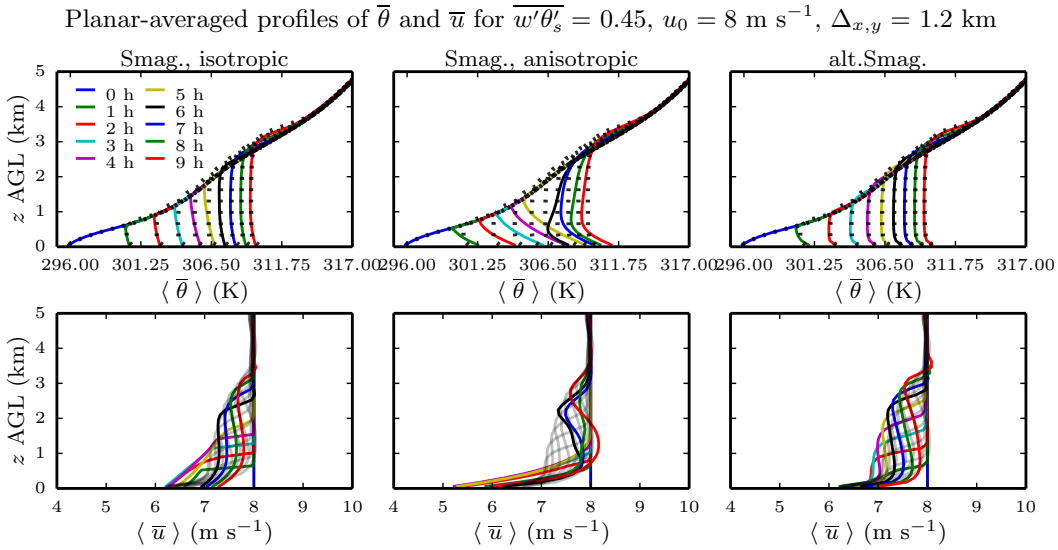

Figure 4.32: As in Fig. 4.1 but for $\overline{w'\theta'_s} = 0.45$ m K s^{-1}, $u_0 = 8$ m s^{-1} cases using the current isotropic and anisotropic Smagorinsky-Lilly model, and the alternative-anisotropic Smagorinsky-Lilly model.

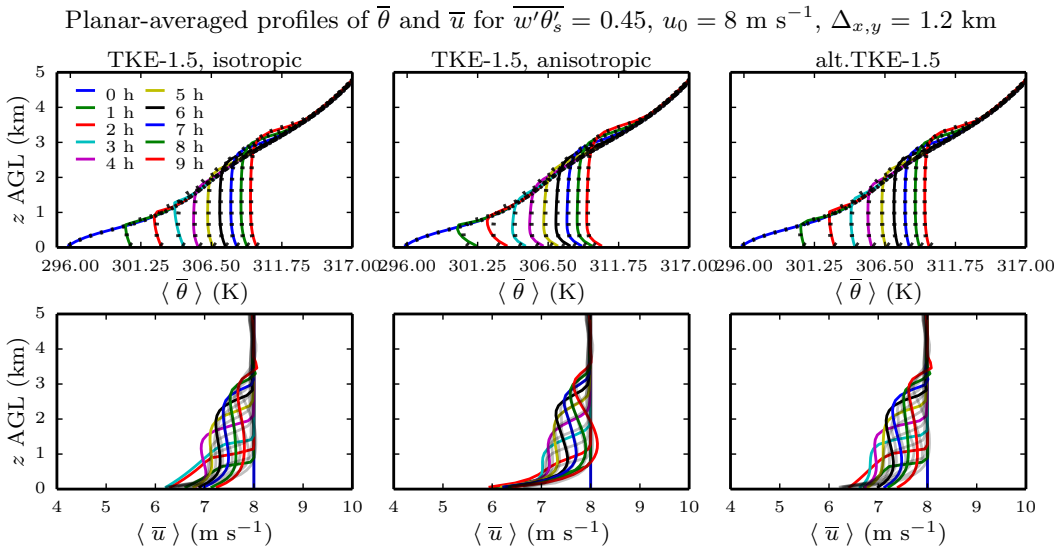

Figure 4.33: As in Fig. 4.1 but for $\overline{w'\theta'_s} = 0.45$ m K s^{-1}, $u_0 = 8$ m s^{-1} cases using the current isotropic and anisotropic TKE-1.5 model, and the alternative-anisotropic TKE-1.5 model.

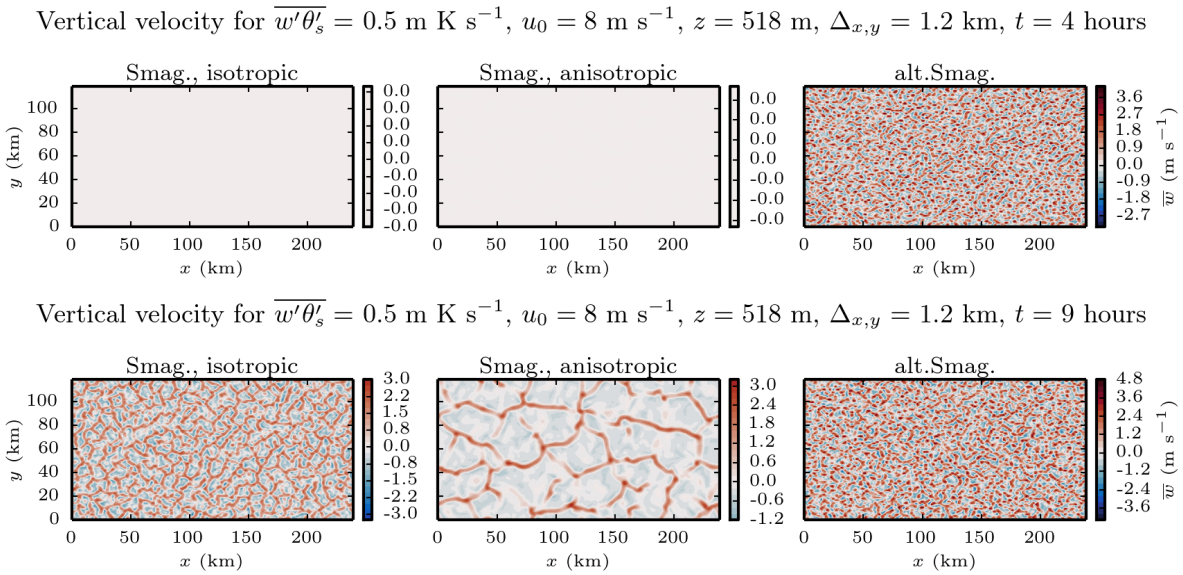

Figure 4.34: As in Fig. 4.2 but for $\overline{w'\theta'_s}$ = 0.45 m K s^{-1}, u_0 = 8 m s^{-1} cases using the current isotropic and anisotropic Smagorinsky-Lilly model, and the alternative-anisotropic Smagorinsky-Lilly model.

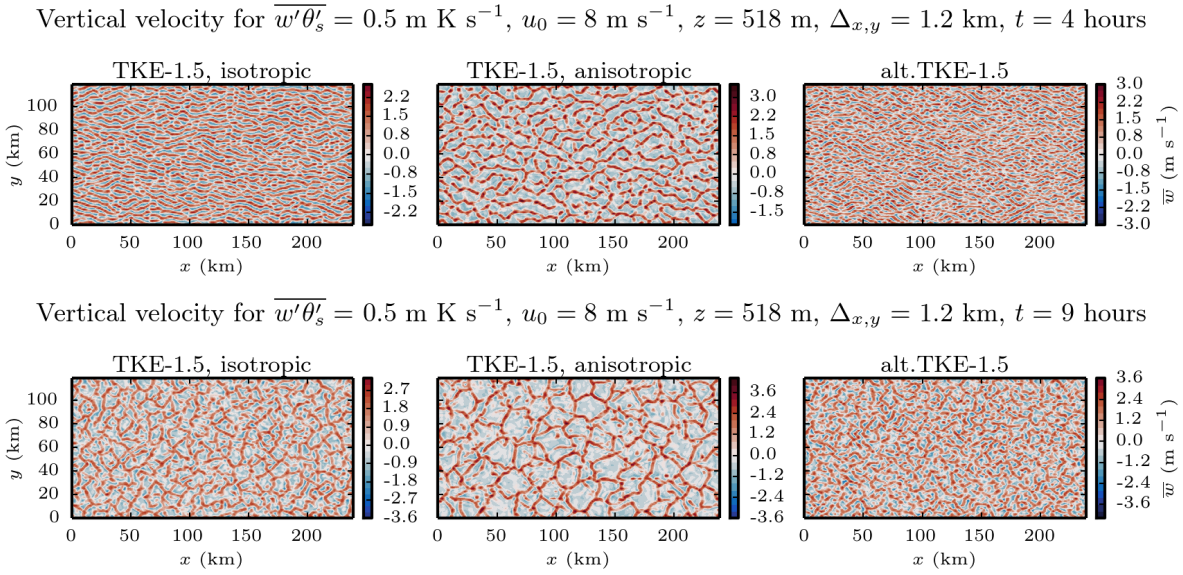

Figure 4.35: As in Fig. 4.2 but for $\overline{w'\theta'_s}$ = 0.45 m K s^{-1}, u_0 = 8 m s^{-1} cases using the current isotropic and anisotropic TKE-1.5 model, and the alternative-anisotropic TKE-1.5 model.

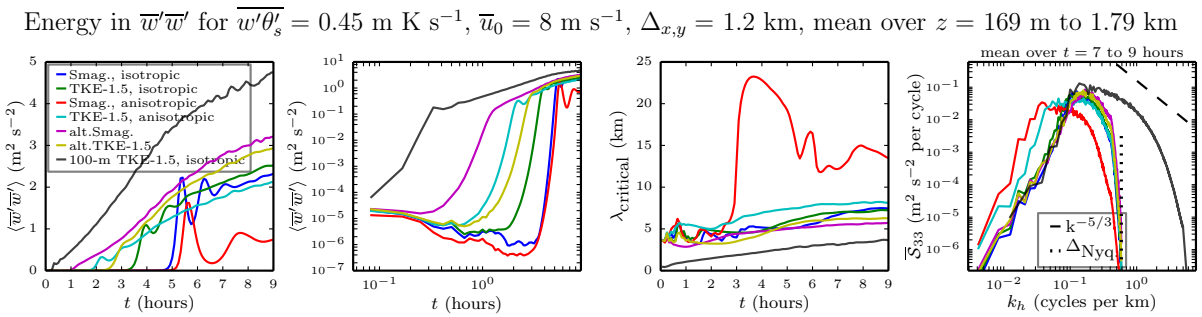

Figure 4.36: As in Fig. 4.3 but for $\overline{w'\theta'_s}$ = 0.45 m K s^{-1}, u_0 = 8 m s^{-1} cases using the current isotropic Smagorinsky-Lilly model, isotropic and anisotropic TKE-1.5 model, the alternative-anisotropic Smagorinsky-Lilly and alternative-anisotropic TKE-1.5 models.

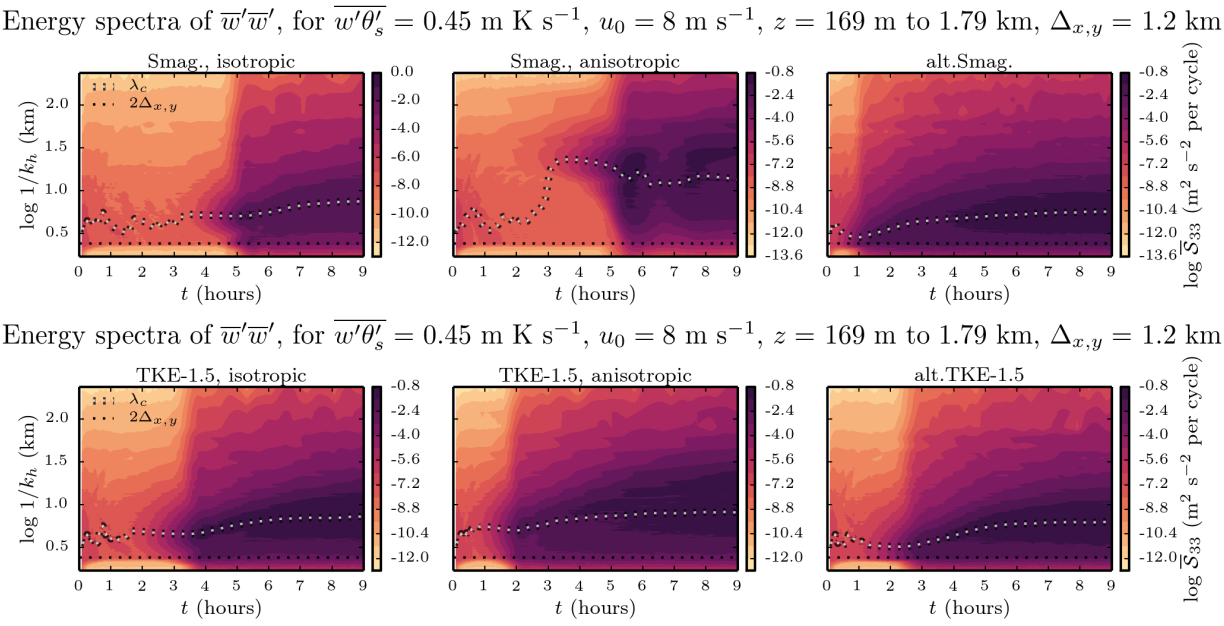

Figure 4.37: As in Fig. 4.4 but for $\overline{w'\theta'_s}$ = 0.45 m K s^{-1}, u_0 = 8 m s^{-1} cases using different formulations of the Smagorinsky-Lilly (top) and TKE-1.5 (bottom) models.

4.3 Two interesting features of TKE spectra produced by the alternative-anisotropic eddy-viscosity model

In a brief presentation that can only be described, in good conscience, as for fun, I would like to point out two features of the TKE spectra of $\overline{w}'\overline{w}'$ that are revealed by the consistent production lengthscales generated by the alternative-anisotropic TKE-1.5 model.

The first is that the spectra appears, in shape, to resemble the PDF of a beta distribution with parameters $\alpha = 3$, $\beta = 5$, though it is seemingly impossible to massage the units to fit both sides of the spectra simultaneously (Fig. 4.38, left two panels). It also appears, qualitatively, that the time series of $\langle \overline{w}'\overline{w}' \rangle$ in the WRF model is similar in shape to the CDF of the same Beta$(k; 3, 5)$ distribution (Fig. 4.38, right two panels).

This annoyance of not being able to fit both sides of a kinetic energy spectra to a single distribution being reminiscent of the "Ultraviolet Catastrophe", it was hypothesized that Planck's law may fit the spectrum, if in shape only. This appears, shockingly enough, to be true, as Planck's law can indeed be massaged into matching both ends of the resolved TKE spectrum if units are ignored (Fig. 4.39).

As noted, both figures presented in this section are a result of massaging functions to match on a plot; what I will refer to here as "toy units", or a "toy model". Despite its underdeveloped state as a theory, I find both of these plots fascinating and believe that this is interesting enough to share as a final thought here given the context and forum.

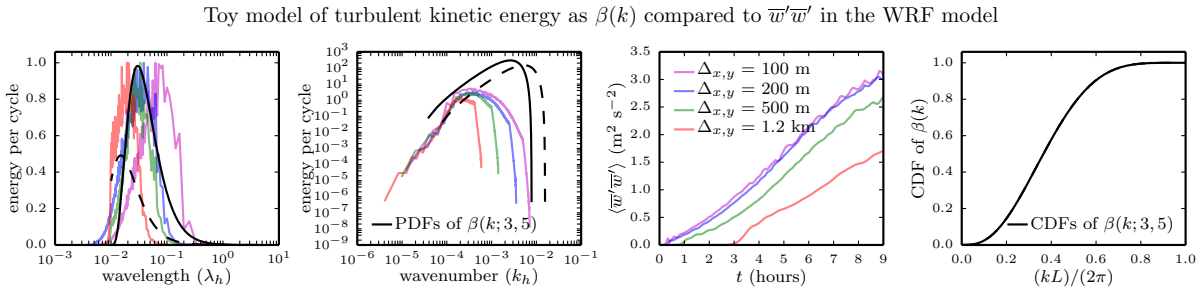

Figure 4.38: Resolved TKE in the vertical direction ($\overline{w}'\overline{w}'$) using the alternative-anisotropic TKE-1.5 model compared to PDFs and CDFs of two Beta$(k; 3, 5)$ distributions generated with differing toy units (i.e. with units finessed to fit visually).

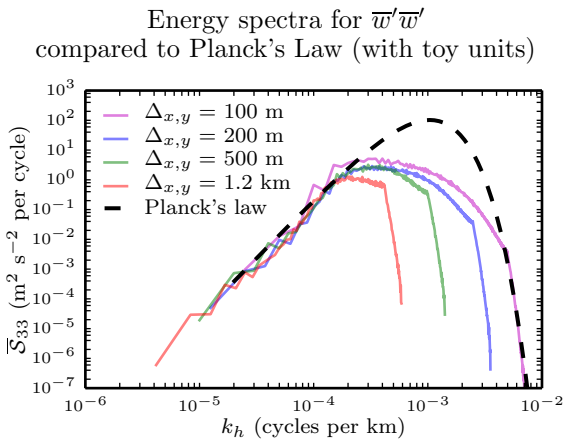

Figure 4.39: Resolved TKE in the vertical direction ($\overline{w}'\overline{w}'$) using the alternative-anisotropic TKE-1.5 model compared to Planck's law as a functional shape, generated with toy units (i.e. with units finessed to fit visually).

4.4 Summary and conclusions

An argument has been made that a reformulation of anisotropic eddy-viscosity models, referred to here simply as the "alternative-anisotropic" formulation, can potentially yield a turbulence closure model that generates more consistent resolved dynamics for atmospheric LES, the first steps towards this having been demonstrated with a first proof-of-concept of alternative-anisotropic formulations of the Smagorinsky-Lilly and prognostic TKE-1.5 turbulence closure models using the WRF-LES model.

It was shown that the alternative-anisotropic formulations are able to generate relatively consistent planar-averaged profiles for potential temperature and velocity, as well as resolve more energy compared to their respective isotropic formulations and resolve the correct scales of energy compared to their respective traditional anisotropic formulations.

Considering highly-sheared cases, it appears possible that the scales of production and dissipation for buoyant and shear modes may necessitate separate lengthscale considerations, as all model formulations show very clear deficiencies at coarse resolutions. It is seen that, despite the large amount of resources expended in the production of this manuscript, larger grid-sizes and higher resolutions are necessary to properly investigate the behavior of these eddy-viscosity models and their modes of energy representation.

In closing, between the performance of all versions of the two models, primarily the traditional anisotropic TKE-1.5 model and the alternative-anisotropic Smagorinsky-Lilly and TKE-1.5 models, there is an interesting potential for some formulation(s) of the Smagorinsky-Lilly and/or TKE-1.5 models that improve the treatment of buoyant and shear rates of production and dissipation to deliver an accurate solution in terms of planar-averaged mean profiles, resolved velocity fields and resolved TKE spectra.

Acknowledgments. Acknowledgement is made to the Savio computational cluster provided by the Berkeley Research Computing program at the University of California, Berkeley (supported by the UC Berkeley Chancellor, Vice Chancellor for Research, and Chief Information Officer) for computing time used in this research. Also a very sincere thanks to Professor Mark Stacey for additional computing time on the Savio cluster which made this research possible.

4.A Alternative-anisotropic eddy-viscosity implementations in the WRF code

4.A.1 TKE-1.5 model

4.A.1.1 Original anisotropic TKE-1.5 implementation

```
!=================================================================
!=================================================================

   SUBROUTINE tke_km( config_flags, xkmh, xkmv, xkhh, xkhv,          &
                      bn2, tke, p8w, t8w, theta,                     &
                      rdz, rdzw, dx,dy, dt, isotropic,               &
                      mix_upper_bound, msftx, msfty,                 &
                      ids, ide, jds, jde, kds, kde,                  &
                      ims, ime, jms, jme, kms, kme,                  &
                      its, ite, jts, jte, kts, kte                   )

! History:      Sep 2003    Changes by Jason Knievel and George Bryan, NCAR
!               Oct 2001    Converted to mass core by Bill Skamarock, NCAR
!               ...         ...

! Purpose:      This routine calculates the exchange coefficients for the
!               TKE turbulence parameterization.

! References:   Klemp and Wilhelmson (JAS 1978)
!               Chen and Dudhia (NCAR WRF physics report 2000)

!-----------------------------------------------------------------
! Begin declarations.

   IMPLICIT NONE

   TYPE( grid_config_rec_type ), INTENT( IN )  &
   :: config_flags

   INTEGER, INTENT( IN )  &
   :: ids, ide, jds, jde, kds, kde,  &
      ims, ime, jms, jme, kms, kme,  &
      its, ite, jts, jte, kts, kte

   INTEGER, INTENT( IN )  :: isotropic
   REAL, INTENT( IN )  &
   :: dx, dy, dt

   REAL, DIMENSION( ims:ime, kms:kme, jms:jme ), INTENT( IN )  &
   :: tke, p8w, t8w, theta, rdz, rdzw, bn2

   REAL, DIMENSION( ims:ime, kms:kme, jms:jme ), INTENT( INOUT )  &
   :: xkmh, xkmv, xkhh, xkhv

   REAL, INTENT( IN )  &
   :: mix_upper_bound

  REAL , DIMENSION( ims:ime, jms:jme), INTENT(IN    ) ::       msftx, &
```

```
49                                                                    msfty
50 ! Local variables.
51
52     REAL, DIMENSION( its:ite, kts:kte, jts:jte )  &
53     :: l_scale
54
55     REAL, DIMENSION( its:ite, kts:kte, jts:jte )  &
56     :: dthrdn
57
58     REAL  &
59     :: deltas, tmp, mlen_s, mlen_h, mlen_v, tmpdz,  &
60        thetasfc, thetatop, minkx, pr_inv, pr_inv_h, pr_inv_v, c_k
61
62     INTEGER  &
63     :: i_start, i_end, j_start, j_end, ktf, i, j, k
64
65     REAL, PARAMETER :: tke_seed_value = 1.e-06
66     REAL            :: tke_seed
67     REAL, PARAMETER :: epsilon = 1.e-10
68
69 ! End declarations.
70 !----------------------------------------------------------------------
71
72     ktf     = MIN( kte, kde-1 )
73     i_start = its
74     i_end   = MIN( ite, ide-1 )
75     j_start = jts
76     j_end   = MIN( jte, jde-1 )
77
78     IF ( config_flags%open_xs .OR. config_flags%specified .OR. &
79          config_flags%nested) i_start = MAX( ids+1, its )
80     IF ( config_flags%open_xe .OR. config_flags%specified .OR. &
81          config_flags%nested) i_end   = MIN( ide-2, ite )
82     IF ( config_flags%open_ys .OR. config_flags%specified .OR. &
83          config_flags%nested) j_start = MAX( jds+1, jts )
84     IF ( config_flags%open_ye .OR. config_flags%specified .OR. &
85          config_flags%nested) j_end   = MIN( jde-2, jte)
86       IF ( config_flags%periodic_x ) i_start = its
87       IF ( config_flags%periodic_x ) i_end = MIN( ite, ide-1 )
88
89     c_k = config_flags%c_k
90     tke_seed = tke_seed_value
91
92     DO j = j_start, j_end
93     DO k = kts+1, ktf-1
94     DO i = i_start, i_end
95       tmpdz         = 1.0 / rdz(i,k+1,j) + 1.0 / rdz(i,k,j)
96       dthrdn(i,k,j) = ( theta(i,k+1,j) - theta(i,k-1,j) ) / tmpdz
97     END DO
98     END DO
99     END DO
100
101    k = kts
102    DO j = j_start, j_end
103    DO i = i_start, i_end
104      tmpdz         = 1.0 / rdzw(i,k+1,j) + 1.0 / rdzw(i,k,j)
105      thetasfc      = T8w(i,kts,j) / ( p8w(i,k,j) / p1000mb )**( R_d / Cp )
```

```
106       dthrdn(i,k,j) = ( theta(i,k+1,j) - thetasfc ) / tmpdz
107     END DO
108     END DO
109
110     k = ktf
111     DO j = j_start, j_end
112     DO i = i_start, i_end
113       tmpdz         = 1.0 / rdz(i,k,j) + 0.5 / rdzw(i,k,j)
114       thetatop      = T8w(i,kde,j) / ( p8w(i,kde,j) / p1000mb )**( R_d / Cp )
115       dthrdn(i,k,j) = ( thetatop - theta(i,k-1,j) ) / tmpdz
116     END DO
117     END DO
118
119   IF ( isotropic .EQ. 0 ) THEN
120     DO j = j_start, j_end
121     DO k = kts, ktf
122     DO i = i_start, i_end
123       mlen_h = SQRT( dx/msftx(i,j) * dy/msfty(i,j) )
124       tmp    = SQRT( MAX( tke(i,k,j), tke_seed ) )
125       deltas = 1.0 / rdzw(i,k,j)
126       mlen_v = deltas
127       IF ( dthrdn(i,k,j) .GT. 0.) THEN
128         mlen_s = 0.76 * tmp / ( ABS( g / theta(i,k,j) * dthrdn(i,k,j) ) )
    **0.5
129         mlen_v = MIN( mlen_v, mlen_s )
130       END IF
131       xkmh(i,k,j)  = MAX( c_k * tmp * mlen_h, 1.0E-6 * mlen_h * mlen_h )
132       xkmh(i,k,j)  = MIN( xkmh(i,k,j), mix_upper_bound * mlen_h *mlen_h / dt
    )
133       xkmv(i,k,j)  = MAX( c_k * tmp * mlen_v, 1.0E-6 * deltas * deltas )
134       xkmv(i,k,j)  = MIN( xkmv(i,k,j), mix_upper_bound * deltas *deltas / dt
    )
135       pr_inv_h     = 1./prandtl
136       pr_inv_v     = 1.0 + 2.0 * mlen_v / deltas
137       xkhh(i,k,j)  = xkmh(i,k,j) * pr_inv_h
138       xkhv(i,k,j)  = xkmv(i,k,j) * pr_inv_v
139     END DO
140     END DO
141     END DO
142   ELSE
143     CALL calc_l_scale( config_flags, tke, BN2, l_scale,      &
144                        i_start, i_end, ktf, j_start, j_end,  &
145                        dx, dy, rdzw, msftx, msfty,           &
146                        ids, ide, jds, jde, kds, kde,         &
147                        ims, ime, jms, jme, kms, kme,         &
148                        its, ite, jts, jte, kts, kte          )
149     DO j = j_start, j_end
150     DO k = kts, ktf
151     DO i = i_start, i_end
152       tmp          = SQRT( MAX( tke(i,k,j), tke_seed ) )
153       deltas       = ( dx/msftx(i,j) * dy/msfty(i,j) / rdzw(i,k,j) )
    **0.33333333
154       xkmh(i,k,j)  = c_k * tmp * l_scale(i,k,j)
155       xkmh(i,k,j)  = MIN( mix_upper_bound * dx/msftx(i,j) * dy/msfty(i,j) /
    dt,  xkmh(i,k,j) )
156       xkmv(i,k,j)  = c_k * tmp * l_scale(i,k,j)
```

```
157           xkmv(i,k,j)   = MIN( mix_upper_bound / rdzw(i,k,j) / rdzw(i,k,j) / dt ,
      xkmv(i,k,j) )
158           pr_inv        = 1.0 + 2.0 * l_scale(i,k,j) / deltas
159           xkhh(i,k,j)   = MIN( mix_upper_bound * dx/msftx(i,j) * dy/msfty(i,j) /
    dt, xkmh(i,k,j) * pr_inv )
160           xkhv(i,k,j)   = MIN( mix_upper_bound / rdzw(i,k,j) / rdzw(i,k,j) / dt,
    xkmv(i,k,j) * pr_inv )
161         END DO
162         END DO
163         END DO
164       END IF
165
166       END SUBROUTINE tke_km
```

4.A.1.2 Alternative-anisotropic TKE-1.5 implementation

```
!=================================================================
!=================================================================

   SUBROUTINE tke_km( config_flags, xkmh, xkmv, xkhh, xkhv,          &
                      bn2, tke, p8w, t8w, theta,                     &
                      rdz, rdzw, dx,dy, dt, isotropic,               &
                      mix_upper_bound, msftx, msfty,                 &
                      ids, ide, jds, jde, kds, kde,                  &
                      ims, ime, jms, jme, kms, kme,                  &
                      its, ite, jts, jte, kts, kte                   )

! History:      Sep 2003    Changes by Jason Knievel and George Bryan, NCAR
!               Oct 2001    Converted to mass core by Bill Skamarock, NCAR
!               ...         ...

! Purpose:      This routine calculates the exchange coefficients for the
!               TKE turbulence parameterization.

! References:   Klemp and Wilhelmson (JAS 1978)
!               Chen and Dudhia (NCAR WRF physics report 2000)

!-----------------------------------------------------------------
! Begin declarations.

   IMPLICIT NONE

   TYPE( grid_config_rec_type ), INTENT( IN )  &
   :: config_flags

   INTEGER, INTENT( IN )  &
   :: ids, ide, jds, jde, kds, kde,  &
      ims, ime, jms, jme, kms, kme,  &
      its, ite, jts, jte, kts, kte

   INTEGER, INTENT( IN )  :: isotropic
   REAL, INTENT( IN )  &
   :: dx, dy, dt

   REAL, DIMENSION( ims:ime, kms:kme, jms:jme ), INTENT( IN )  &
   :: tke, p8w, t8w, theta, rdz, rdzw, bn2

   REAL, DIMENSION( ims:ime, kms:kme, jms:jme ), INTENT( INOUT )  &
   :: xkmh, xkmv, xkhh, xkhv

   REAL, INTENT( IN )  &
   :: mix_upper_bound

  REAL , DIMENSION( ims:ime, jms:jme), INTENT(IN    ) ::      msftx, &
                                                              msfty
! Local variables.

   REAL, DIMENSION( its:ite, kts:kte, jts:jte )  &
   :: l_scale

   REAL, DIMENSION( its:ite, kts:kte, jts:jte )  &
```

```
56      :: dthrdn
57
58      REAL  &
59      :: deltas, tmp, mlen_s, mlen_h, mlen_v, tmpdz,  &
60         thetasfc, thetatop, minkx, pr_inv, pr_inv_h, pr_inv_v, c_k
61
62      INTEGER  &
63      :: i_start, i_end, j_start, j_end, ktf, i, j, k
64
65      REAL, PARAMETER :: tke_seed_value = 1.e-06
66      REAL            :: tke_seed
67      REAL, PARAMETER :: epsilon = 1.e-10
68
69  ! End declarations.
70  !----------------------------------------------------------------------
71
72      ktf     = MIN( kte, kde-1 )
73      i_start = its
74      i_end   = MIN( ite, ide-1 )
75      j_start = jts
76      j_end   = MIN( jte, jde-1 )
77
78      IF ( config_flags%open_xs .OR. config_flags%specified .OR. &
79           config_flags%nested) i_start = MAX( ids+1, its )
80      IF ( config_flags%open_xe .OR. config_flags%specified .OR. &
81           config_flags%nested) i_end   = MIN( ide-2, ite )
82      IF ( config_flags%open_ys .OR. config_flags%specified .OR. &
83           config_flags%nested) j_start = MAX( jds+1, jts )
84      IF ( config_flags%open_ye .OR. config_flags%specified .OR. &
85           config_flags%nested) j_end   = MIN( jde-2, jte)
86        IF ( config_flags%periodic_x ) i_start = its
87        IF ( config_flags%periodic_x ) i_end = MIN( ite, ide-1 )
88
89      c_k = config_flags%c_k
90      tke_seed = tke_seed_value
91
92      DO j = j_start, j_end
93      DO k = kts+1, ktf-1
94      DO i = i_start, i_end
95        tmpdz          = 1.0 / rdz(i,k+1,j) + 1.0 / rdz(i,k,j)
96        dthrdn(i,k,j) = ( theta(i,k+1,j) - theta(i,k-1,j) ) / tmpdz
97      END DO
98      END DO
99      END DO
100
101     k = kts
102     DO j = j_start, j_end
103     DO i = i_start, i_end
104       tmpdz          = 1.0 / rdzw(i,k+1,j) + 1.0 / rdzw(i,k,j)
105       thetasfc       = T8w(i,kts,j) / ( p8w(i,k,j) / p1000mb )**( R_d / Cp )
106       dthrdn(i,k,j) = ( theta(i,k+1,j) - thetasfc ) / tmpdz
107     END DO
108     END DO
109
110     k = ktf
111     DO j = j_start, j_end
112     DO i = i_start, i_end
```

```
113         tmpdz          = 1.0 / rdz(i,k,j) + 0.5 / rdzw(i,k,j)
114         thetatop       = T8w(i,kde,j) / ( p8w(i,kde,j) / p1000mb )**( R_d / Cp )
115         dthrdn(i,k,j) = ( thetatop - theta(i,k-1,j) ) / tmpdz
116       END DO
117       END DO
118
119
120
121         DO j = j_start, j_end
122         DO k = kts, ktf
123         DO i = i_start, i_end
124           mlen_v = SQRT( dx/msftx(i,j) * dy/msfty(i,j) )
125           tmp    = SQRT( MAX( tke(i,k,j), tke_seed ) )
126           deltas = 1.0 / rdzw(i,k,j)
127           mlen_h = deltas
128           IF ( dthrdn(i,k,j) .GT. 0.) THEN
129             mlen_s = 0.76 * tmp / ( ABS( g / theta(i,k,j) * dthrdn(i,k,j) ) )
    **0.5
130             mlen_v = MIN( mlen_v, mlen_s )
131           END IF
132           xkmh(i,k,j)  = MAX( c_k * tmp * mlen_h, 1.0E-6 * mlen_h * mlen_h )
133           xkmh(i,k,j)  = MIN( xkmh(i,k,j), mix_upper_bound * mlen_h *mlen_h / dt
     )
134           xkmv(i,k,j)  = MAX( c_k * tmp * mlen_v, 1.0E-6 * deltas * deltas )
135           xkmv(i,k,j)  = MIN( xkmv(i,k,j), mix_upper_bound * deltas *deltas / dt
     )
136           pr_inv_h     = 1./prandtl
137           pr_inv_v     = 1./prandtl
138           xkhh(i,k,j)  = xkmh(i,k,j) * pr_inv_h
139           xkhv(i,k,j)  = xkmv(i,k,j) * pr_inv_v
140         END DO
141         END DO
142         END DO
143
144       END SUBROUTINE tke_km
```

4.A.2 Smagorinsky-Lilly model

4.A.2.1 Original anisotropic Smagorinsky-Lilly implementation

```
SUBROUTINE smag_km( config_flags ,xkmh,xkmv,xkhh,xkhv,BN2, &
                    div ,defor11 ,defor22 ,defor33 ,defor12 , &
                    defor13 ,defor23 , &
                    u, v, z, ht, &
                    rdzw ,dx,dy,dt ,isotropic , &
                    mix_upper_bound , msftx , msfty , &
                    ids ,ide , jds ,jde , kds ,kde , &
                    ims ,ime , jms ,jme , kms ,kme , &
                    its ,ite , jts ,jte , kts ,kte )


!-----------------------------------------------------------------------
! Begin declarations.

   IMPLICIT NONE

   TYPE(grid_config_rec_type) , INTENT(IN    ) :: config_flags

  ! JSS: SKIPPING THE REST OF THE DECLARATIONS

      pr = prandtl
      c_s = config_flags%c_s

      do j=j_start ,j_end
      do k=kts ,ktf
      do i=i_start ,i_end
         def2(i,k,j)=0.5*(defor11(i,k,j)*defor11(i,k,j) + &
                          defor22(i,k,j)*defor22(i,k,j) + &
                          defor33(i,k,j)*defor33(i,k,j))
      enddo
      enddo
      enddo

        do j=j_start ,j_end
        do k=kts ,ktf
        do i=i_start ,i_end
         def2(i,k,j)=def2(i,k,j)+ defor12(i,k,j)*defor12(i,k,j)
        enddo
        enddo
        enddo

        do j=j_start ,j_end
        do k=kts ,ktf
        do i=i_start ,i_end
         def2(i,k,j)=def2(i,k,j)+ defor13(i,k,j)*defor13(i,k,j)
        enddo
        enddo
        enddo

        do j=j_start ,j_end
        do k=kts ,ktf
        do i=i_start ,i_end
         def2(i,k,j)=def2(i,k,j)+ defor23(i,k,j)*defor23(i,k,j)
```

```
54          enddo
55          enddo
56          enddo
57
58      IF (isotropic .EQ. 0) THEN
59         DO j = j_start, j_end
60         DO k = kts, ktf
61         DO i = i_start, i_end
62
63        mlen_h=sqrt(dx/msftx(i,j) * dy/msfty(i,j))
64        mlen_v= 1./rdzw(i,k,j)
65
66            tmp=max(0.,def2(i,k,j)-BN2(i,k,j)/pr)
67            tmp=tmp**0.5
68            xkmh(i,k,j)=max(c_s*c_s*mlen_h*mlen_h*tmp, 1.0E-6*mlen_h*mlen_h )
69            xkmh(i,k,j)=min(xkmh(i,k,j), mix_upper_bound * mlen_h * mlen_h / dt )
70            xkmv(i,k,j)=max(c_s*c_s*mlen_v*mlen_v*tmp, 1.0E-6*mlen_v*mlen_v )
71            xkmv(i,k,j)=min(xkmv(i,k,j), mix_upper_bound * mlen_v * mlen_v / dt )
72            xkhh(i,k,j)=xkmh(i,k,j)/pr
73            xkhh(i,k,j)=min(xkhh(i,k,j), mix_upper_bound * mlen_h * mlen_h / dt )
74            xkhv(i,k,j)=xkmv(i,k,j)/pr
75            xkhv(i,k,j)=min(xkhv(i,k,j), mix_upper_bound * mlen_v * mlen_v / dt )
76
77         ENDDO
78         ENDDO
79         ENDDO
80      ELSE
81
82       !JSS: REMOVED, NOT RELEVANT HERE
83
84      ENDIF
85
86  END SUBROUTINE smag_km
```

4.A.2.2 Alternative-anisotropic Smagorinsky-Lilly implementation

```
SUBROUTINE alt_smag_km( config_flags ,xkmh,xkmv,xkhh,xkhv,BN2, &
                        div ,defor11 ,defor22 ,defor33 ,defor12 ,          &
                        defor13 ,defor23 ,                                 &
                        u, v, z, ht,                                       &
                        rdzw ,dx,dy,dt ,isotropic ,                        &
                        mix_upper_bound , msftx , msfty ,                  &
                        ids ,ide , jds ,jde , kds ,kde ,                   &
                        ims ,ime , jms ,jme , kms ,kme ,                   &
                        its ,ite , jts ,jte , kts ,kte                     )


!-------------------------------------------------------------------------
! Begin declarations.

   IMPLICIT NONE

   TYPE(grid_config_rec_type) , INTENT(IN    ) :: config_flags

  ! JSS: SKIPPING THE REST OF THE DECLARATIONS

   pr = prandtl
   c_s = config_flags%c_s

   do j=j_start ,j_end
   do k=kts ,ktf
   do i=i_start ,i_end
      def2(i ,k,j)=0.5*(defor11(i ,k,j)*defor11(i ,k,j) + &
                        defor22(i ,k,j)*defor22(i ,k,j))
      def2v(i ,k,j)=0.5*(defor33(i ,k,j)*defor33(i ,k,j))
   enddo
   enddo
   enddo


      do j=j_start ,j_end
      do k=kts ,ktf
      do i=i_start ,i_end
         tmp=0.25*(defor12(i   ,k,j)+defor12(i   ,k,j+1)+ &
                   defor12(i+1,k,j)+defor12(i+1,k,j+1))
       def2(i ,k,j)=def2(i ,k,j)+tmp*tmp
      enddo
      enddo
      enddo

      do j=j_start ,j_end
      do k=kts ,ktf
      do i=i_start ,i_end
       tmp=0.25*(defor13(i   ,k+1,j)+defor13(i   ,k,j)+ &
                 defor13(i+1,k+1,j)+defor13(i+1,k,j))
       def2v(i ,k,j)=def2v(i ,k,j) + tmp*tmp
      enddo
      enddo
      enddo

      do j=j_start ,j_end
```

```
56          do k=kts,ktf
57          do i=i_start,i_end
58           tmp=0.25*(defor23(i,k+1,j   )+defor23(i,k,j   )+ &
59                     defor23(i,k+1,j+1)+defor23(i,k,j+1))
60           def2v(i,k,j)=def2v(i,k,j)+tmp*tmp
61          enddo
62          enddo
63          enddo
64
65          DO j = j_start, j_end
66          DO k = kts, ktf
67          DO i = i_start, i_end
68
69         tmpz = z(i,k,j) - ht(i,j)
70
71         mlen_h=sqrt(dx/msftx(i,j) * dy/msfty(i,j))
72         mlen_v= 1./rdzw(i,k,j)
73
74             tmp=max(0.,def2(i,k,j))
75             tmp=tmp**0.5
76
77             tmpv=max(0.,def2v(i,k,j)-BN2(i,k,j)/pr)
78             tmpv=tmpv**0.5
79
80             xkmh(i,k,j)=max( c_s*c_s*mlen_v*tmpz*tmp, 1.0E-6*mlen_h*mlen_h )
81             xkmh(i,k,j)=min(xkmh(i,k,j), mix_upper_bound * mlen_h * mlen_h / dt )
82             xkmv(i,k,j)=max( c_s*c_s*mlen_h*tmpz*tmpv, 1.0E-6*mlen_v*mlen_v )
83             xkmv(i,k,j)=min(xkmv(i,k,j), mix_upper_bound * mlen_h * mlen_h / dt )
84             xkhh(i,k,j)=xkmh(i,k,j)/pr
85             xkhh(i,k,j)=min(xkhh(i,k,j), mix_upper_bound * mlen_h * mlen_h / dt )
86             xkhv(i,k,j)=xkmv(i,k,j)/pr
87             xkhv(i,k,j)=min(xkhv(i,k,j), mix_upper_bound * mlen_v * mlen_v / dt )
88          ENDDO
89          ENDDO
90          ENDDO
91
92 END SUBROUTINE alt_smag_km
```

4.B Full column planar-averaged profiles

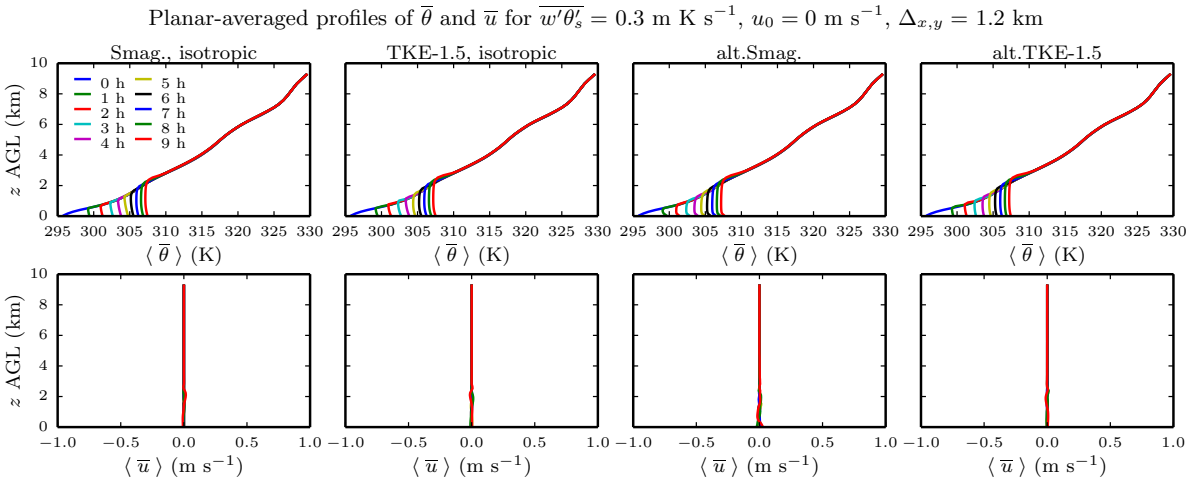

Figure 4.40: Full model height of planar-averaged resolved potential temperature and u-velocity profiles for the $\Delta_{x,y} = 1.2$ km) cases using the isotropic and anisotropic TKE-1.5 model, and the alternative-anisotropic Smagorinsky-Lilly and alternative-anisotropic TKE-1.5 models (from left to right).

4.C Additional results

4.C.1 No-wind case

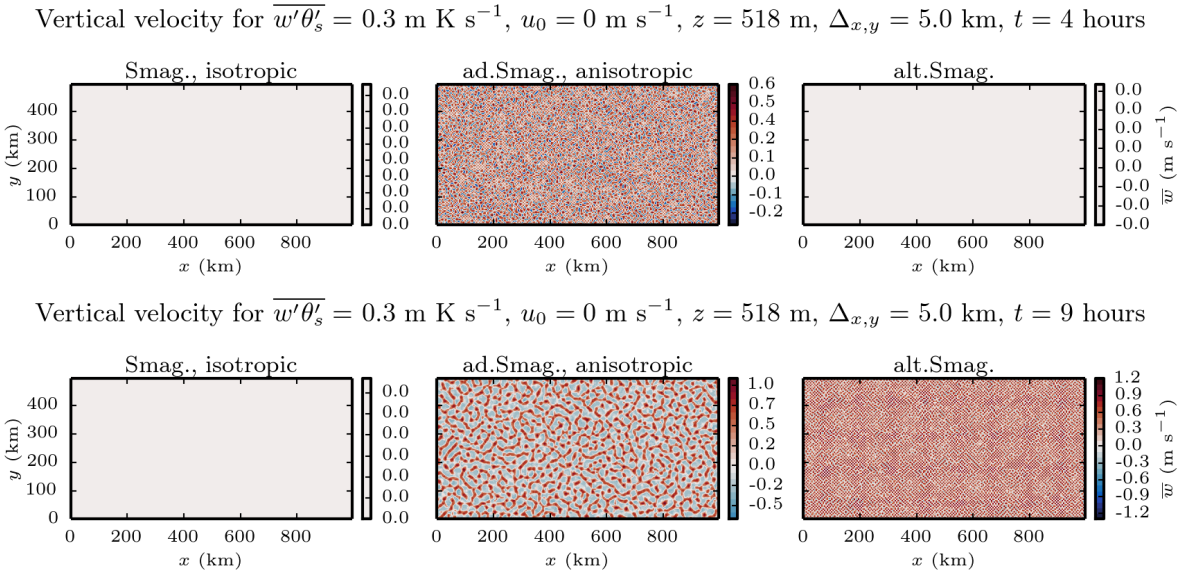

Figure 4.41: Resolved vertical velocity, $\overline{w}$, in the $z \approx 518$ m plane at $t = 4$ (top) and 9 (bottom) hours for the $\Delta_{x,y} = 5$ km cases using versions of the Smagorinsky-Lilly model.

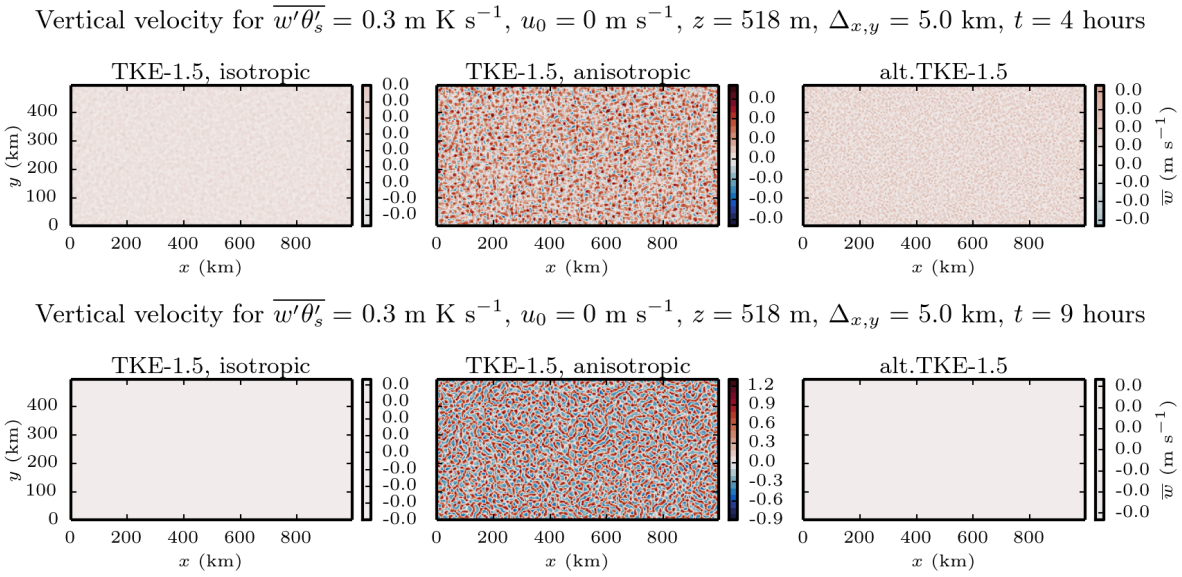

Figure 4.42: As in Fig. 4.41 but using versions of the TKE-1.5 model.

4.C.2 Wind case

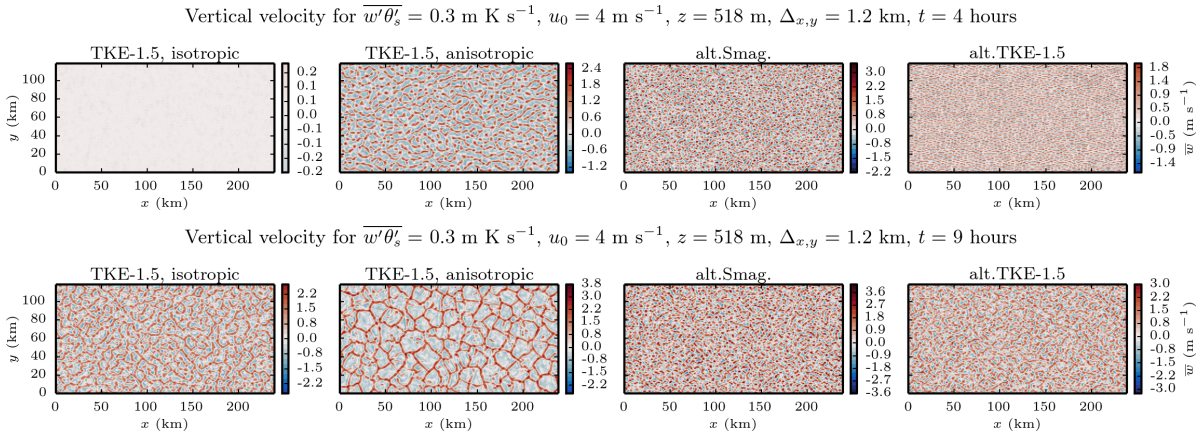

Figure 4.43: Resolved vertical velocity, $\overline{w}$, in the $z \approx 518$ m plane at $t = 4$ (top) and 9 (bottom) hours for the $\Delta_{x,y} = 1.2$ km cases using the current isotropic (far left) and anisotropic (middle left) TKE-1.5 implementations, compared to the alternative-anisotropic Smagorinsky-Lilly (middle right) and alternative-anisotropic TKE-1.5 (far right).

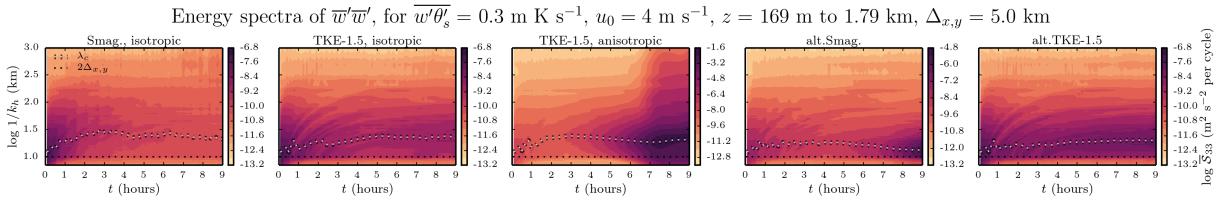

Figure 4.44: As in Fig. 4.14 but for $\Delta_{x,y} = 5$ km cases using the current isotropic Smagorinsky-Lilly model, isotropic and anisotropic TKE-1.5 model, the alternative-anisotropic Smagorinsky-Lilly and alternative-anisotropic TKE-1.5 models.

Chapter 5

The gray zone of terrain representation in atmospheric models[1]

5.1 Introduction

Mesoscale models have traditionally been used for predictions of atmospheric flow at regional scales. For higher-resolution, microscale simulations, computational fluid dynamics (CFD) codes are frequently used with the large-eddy simulation (LES) technique. Generally, mesoscale codes solve the Reynolds-averaged Navier-Stokes (RANS) equations with features for operational weather prediction such as using analysis and observational boundary conditions and extensive parameterization schemes of atmospheric physics processes. Traditional mesoscale codes also use a terrain-following coordinate system, where the bottom boundary of the grid is mapped to the terrain and metric terms arise from the coordinate transformation. This makes the application of the bottom boundary condition straightforward and works well at resolutions too coarse to resolve the more complex features of the terrain. Terrain-following coordinate systems generate some numerical errors in the presence of any slope due to the metric terms (Janjic, 1977; Klemp et al., 2003). For low slopes this is error is negligible but at high slopes model errors become large and can cause stability problems (Lundquist et al., 2010b).

On the other hand, traditional the CFD codes that are used for high-resolution studies of microscale atmospheric dynamics often have simplistic boundary conditions and do not use atmospheric physics parameterizations. The trade-off is that CFD codes, and specifically LES codes, are able to resolve turbulent eddies and thus study their evolution in the atmospheric boundary layer (ABL). These models can handle complex terrain well through use of conformal

[1]This chapter is a reproduction of the manuscript "Application of the Immersed Boundary Method to Simulations of Flow Over Steep, Mountainous Terrain" by Jason S. Simon (the principle author), Katherine A. Lundquist and Fotini Katopodes Chow, first published in *the proceedings of the 15th Conference on Mountain Meteorology*, American Meteorological Society, August 2012 (Simon et al., 2012)

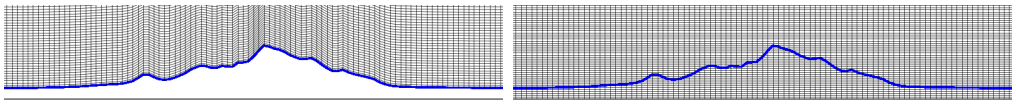

Figure 5.1: A mountain profile represented in terrain-following (top) and IBM coordinate systems. Note the distortion of grid cells when using terrain-following coordinates.

grid generation techniques, which are not terrain-following. The difference between the grids for each coordinate system is illustrated in Figure 5.1.

For ABL simulations, the massive historical costs of computing resources has meant that mesoscale codes cannot be run at high resolutions if they are to cover a sufficiently large geographic region and LES codes cannot be run for large geographic regions if they are to be sufficiently resolved.

A model capable of representing a range of scales is needed to seamlessly integrating from the meso to the microscale. This work continues development of such a framework, using the Weather Research and Forecasting (WRF) model.

WRF is capable as both a mesoscale model and an LES model, and is widely used for both operational and research applications (Skamarock et al., 2008). WRF is currently configurable as an LES code, and is able to nest between mesoscale and LES domains, albeit in a terrain-following coordinate system. Thus, WRF in its standard form is unable to handle very steep and complex terrain at fine resolution. We have therefore introduced an immersed boundary method (IBM) into WRF to allow for complex terrain to be represented at high resolutions within the WRF model (Lundquist et al., 2010a, 2012). IBM uses a Cartesian coordinate system and immerses the terrain boundary within this, using interpolation methods to represent the effect of the boundary on the flow. This then makes the IBM-WRF framework an excellent candidate for a model which can capture meso and microscales over steep and complex terrain.

Questions remain regarding the appropriate application of IBM-WRF over complex terrain. At coarse resolutions, the terrain-following coordinates native to WRF are appropriate, but at fine resoluions over complex terrain these break down, needing the use of the IBM features to represent the terrain. For a framework which uses grid nesting from meso to fine scales, the appropriate transition zone from terrain-following to IBM coordinates must be determined.

In this manuscript we present three simple experiments conducted on two-dimensional domains to compare WRF and IBM-WRF and evaluate how they each perform for different grid scales. (We use "WRF" to indicate the traditional form of WRF using terrain-following coordinates and "IBM-WRF" to indicate the use of the IBM coordinates.) These preliminary results will be used to guide more costly efforts to describe the relationship between WRF and IBM-WRF in three dimensions. The experiments are designed to illustrate the numerical errors associated with both the terrain-following coordinates and the IBM coordinates and design a strategy to mitigate these errors by appropriately transitioning between WRF and IBM-WRF.

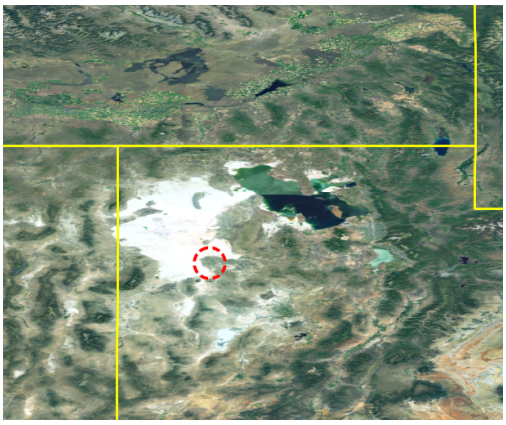

Figure 5.2: Satellite image of Northwestern Utah; Granite Mountain circled in red. Photo from NASA landsat.

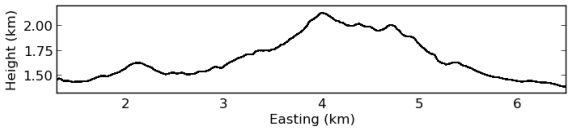

Figure 5.3: Profile of Granite Mountain at 10m resolution, after smoothing. Note the complexity. To scale.

5.2 MATERHORN

The general goal of the MATERHORN campaign is to study the predictability of meteorological events in complex, mountainous terrain. The MATERHORN observational campaign will take place at the Granite Mountain Atmospheric Science Testbed (GMAST), located on Dugway Proving Grounds in Utah. Granite Mountain is a relatively isolated mountain on the playa, southwest of the Great Salt Lake (Figure 5.2). This creates a nearly ideal topography of a complex mountain sitting on otherwise flat topography. Figure 5.3 shows a line profile, to scale, of an easterly cross-section of Granite Mountain to illustrate the complexity of the surface.

5.3 IBM background

IBM is used to represent the effects of boundaries on nonconforming, structured grids. There are many possible implementations of IBM, but the most common form is to add a body force term to the governing equations that takes a zero value away from the boundary and a non-zero value near the boundary. The IBM used in IBM-WRF is a direct forcing method,

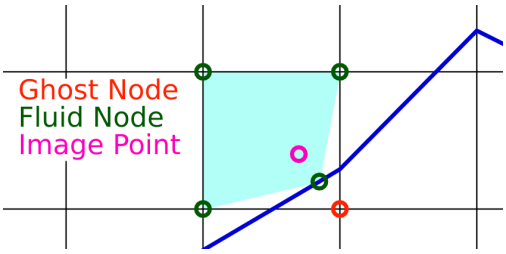

Figure 5.4: Visual description of the three types of nodes used in IBM-WRF. The blue line represents the terrain surface. The ghost node is the first node beneath the surface, and its image point is a reflection normal to the surface into the fluid domain. The green fluid nodes mark the values that are interpolated to find the image point value. The image point value and the boundary condition determine the value that the ghost node takes. In this example the value at the boundary is apart of the interplation process, which is the case only under Dirichlet boundary conditions.

where solutions at nodes near the boundary are calculated specifically to enforce the boundary condition, eliminating the need to calculate the body force explicitly (Mohd-Yusof, 1997). IBM-WRF uses a finite-difference approach which applies this forcing at ghost nodes (nodes that take a value only to enforce a correct solution in an adjacent node, and are not included in the physical solution) located just below the boundary. Nodes below the boundary are referred to as solid nodes.

Prognostic variables are reconstructed on the ghost node by finding a fit between the ghost node, the boundary condition and the image point (reflection of the ghost node across the boundary). The value of the image point is found via interpolation from surrounding nodes in the fluid domain. In this work, the image point is found using a unique bilinear reconstruction scheme for two-dimensional terrain, but three-dimensional interpolation methods are found to be tractable in the literature. An illustrative schematic of this method is shown in Figure 5.4.

A detailed description of the implementation of IBM-WRF is presented by (Lundquist, 2010).

5.4 Hypothesis/experiment

The mesoscale model WRF uses a terrain-following coordinate system. As previously discussed, this becomes an issue in steep topography. Terrain data is often available at very high resolutions ($\sim$ 5 m), therefore the steepness of the terrain represented in the model is essentially determined by the horizontal resolution of the simulation. Thus, we can assume that the hypothetical "error" that originates in the numerics of WRF's coordinate system increases as the grid spacing decreases. IBM-WRF, on the other hand, relies on interpolation

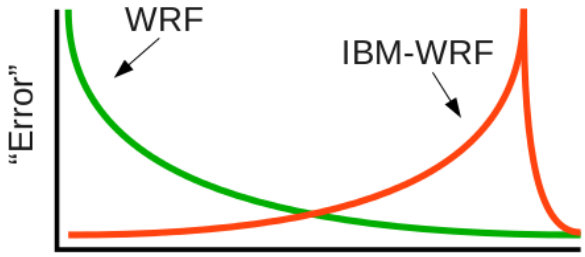

Figure 5.5: Idealization of the relationships between WRF, IBM-WRF and horizontal resolution.

at the terrain boundary. Therefore, when modeling complex terrain at the mesoscale, terrain-following coordinates are preferable because the numerical errors from the coordinate transformation are smaller than the numerical errors introduced by the interpolation scheme. This is only an issue when the coarse terrain retains enough steepness to be heterogeneous. Once the grid spacing is larger than the terrain scale, the surface is approximately flat and IBM-WRF's interpolation is adequate. This creates a hypothetical error inherent in the IBM's numerics that is very low at high resolutions, regardless of the presence of steep terrain, and high at coarse resolutions. At the point where the terrain is coarse enough to be essentially a flat plate the error returns to a low value.

While the performance of terrain-following coordinates in steep terrain is well studied, the horizontal resolutions appropriate for WRF and IBM-WRF relative to each other are not known. Given the inverse effect of resolution on the numerical errors of the two coordinate systems, when nesting from coarse to fine domains in a WRF/IBM-WRF framework, there should exist a horizontal resolution where the modeler should change from WRF to IBM-WRF.

A simple analysis of the relationship between the two models and horizontal resolution (and thus, indirectly, slope) can be done to estimate the nature of the two models' appropriate spatial scales. Figure 5.5 shows an idealization of the numerical errors of each coordinate system compared to an unknown exact solution. It follows that, if the shapes are correct, the difference between the solutions from WRF and IBM-WRF should relatively follow the sum of the two individual curves, and the resolution to switch from WRF to IBM-WRF should be the point where the two curves intersect (after IBM-WRF is adjusted for performance cost considerations). Note that in this idealization of the error curve WRF is shown to have a value across the entire spectrum of resolutions, and indeed this is how we expect the theoretical error associated with terrain-following coordinates to behave. In reality, though, we expect that WRF will have stability problems at very steep slopes (fine resolutions) so the error will not be measurable.

5.5 Difference vs. horizontal resolution

To estimate the behavior of the numerical error, WRF and IBM-WRF are run in complex terrain at different horizontal resolutions to compare differences in the resulting velocities. The terrain being used for this and the following experiments is an idealization of Granite Mountain created by prescribing a minimum elevation in the domain and removing all features other than the mountain. The result is an isolated mountain on a perfectly flat playa, which is a relatively realistic representation at the microscale. A two-dimensional east-west slice is taken through one of the highest points on Granite Mountain, and is used as the domain in all experiments.

The solutions from WRF and IBM-WRF are compared by interpolating the velocity magnitude field from IBM-WRF to the terrain-following coordinate system and taking the difference at each node in the domain. The difference between the two coordinate systems will be represented by the largest difference, in magnitude, present in the domain. For convenience, hereafter this interpolated velocity difference field between WRF and IBM-WRF will simply be referred to as the difference and will be a surrogate for the theoretical error in the system. This assumes that for any horizontal resolution one of the coordinate systems is appropriate and can give an accurate solution.

5.5.1 Model setup

All cases are two-dimensional in the east-west direction with 50 horizontal grid points. The horizontal resolutions used range from 450m to 4km. The finest grid is determined by the point where WRF becomes numerically unstable for this configuration, and the coarsest grid is the point where the difference between WRF and IBM-WRF starts decreasing. WRF has 90 vertical grid points, covering a vertical span from 1315 m to 7000 m above sea-level (ASL). IBM-WRF has 92 vertical grid points, to account for the two necessary solid nodes below the terrain, and covers a vertical span from 1215 m to 7000 m ASL. The cases are run for 6 hours with a 0.25 s timestep, with 5 m s^{-1} geostrophic forcing. The initial temperature profile is neutral and the initial velocity profile is a uniform 5m/s westerly flow. The eddy viscosity for all cases is 100 m^2 s^{-1}, to allow the solution to reach steady-state faster. Coriolis is neglected. A no-slip bottom boundary condition is used and a Rayleigh damping layer is present at the top 2km of the grid. The lateral boundary conditions are periodic. Terrain data is obtained from the Utah AGRC's 5 m Auto-Correlated Digital Elevation Model (DEM) with aforementioned adjustments; minimum elevation has been set to 1315 m. The DEM is interpolated to the model domain using the WRF Preprocessing System (WPS) average grid cell interpolation and smoothing-desmoothing.

Of the aforementioned settings, the results are most sensitive to vertical resolution and eddy viscosity.

The horizontal resolutions used range from 450 m to 4 km. This range, found empirically, contains the scales that we are interested in. The smallest resolution used is determined by the point where WRF becomes numerically unstable, and the largest resolution is the

determined by the point where the error decreases to global minimum levels after a local maximum.

5.5.2 Results

Figure 5.6 shows the maximum difference of five representative resolutions. The figures have a horizontal span of 60 km, centered on Granite Mountain, and extend vertically to 4km ASL (from a base of 1315 m). In all cases the maximum difference is on the lee side of the mountain and spreads quite far downstream. The general trend is illustrated in these cases: the largest error is present in the 3 km domain, with a decreasing trend in either direction. Notice that in the coarsest case the error is centered on the downstream edge of the mountain and spreads downstream, while in the finer two cases the error is located more directly over the mountain and does not spread nearly as far.

Figure 5.7 shows the maximum difference as a function of grid spacing. The error increases at coarser resolutions, as expected. With coarser grids, the terrain slope is lower, hence the WRF solution does a better job. The increase in error is due to interpolation errors in the IBM-WRF solution, which become larger at coarse resolution because the distance between grid points increases. Thus, the shape seen is approximately what we would expect to see if only evaluating the error from IBM-WRF. Once the resolution is so coarse that the terrain "looks" entirely flat to the model, the difference between the results becomes quite small, leading to a sharp dropoff in the curve at very coarse resolutions. These results therefore capture the orange curve in the Figure 5.5 schematic above. The green curve requires very fine resolutions where WRF may not be able to accurately run, especially in two dimensions.

5.6 Increasing slope case

The previous experiment was conducted at coarse resolutions where IBM-WRF has not previously been tested. At these coarse resolutions, the above results imply that the terrain-following coordinates are more accurate than coordinates using the IBM. This result is dominated by the effects of grid spacing on IBM-WRF, and it is very difficult to discern the impact that the slope has on WRF. The point where slope issues begin to dominate is of great interest, since it likely plays a large role in defining the edge of both WRF and IBM-WRF's preferred scale. The scale that is dominated by terrain slopes is not present due to numerical limitations. This limitation is case-specific, and a relationship between slope and error is still desirable. Since this is a two-dimensional domain it should not be assumed that horizontal resolutions that are too fine for WRF under these settings remain problematic in real, three-dimensional cases.

A second experiment is conducted to evaluate this slope/error relationship where the horizontal resolution remains constant (at 500 m) and the terrain is scaled from zero to one. The scaling factor is applied only to heights above the artificial floor of the topography. When the scale is zero, our domain is reduced to flat terrain and the two coordinate systems should

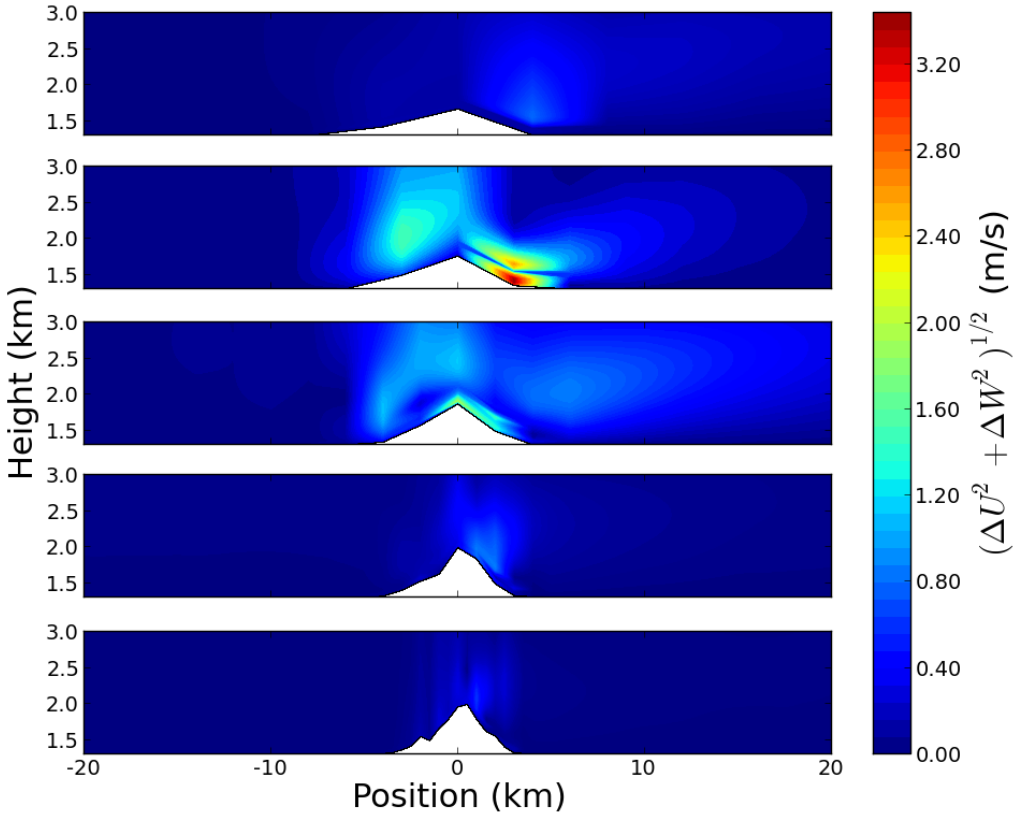

Figure 5.6: Velocity magnitude difference fields for cases where the horizontal resolution is (from top to bottom) 4, 3, 2, 1 0.5 km. Domains are zoomed in both horizontally and vertically. To scale.

yield nearly identical results. When the scale is one, we know from our first experiment that the maximum difference for this setup at 500 m horizontal resolution should be approximately 0.6 m s^{-1} (Figure 5.7). Since the resolution here is not changing, the variability in the error associated with grid points catching peaks and troughs in the terrain is not in play, and thus the trend should be very clear.

5.6.1 Model setup

The setup from the first experiment where dx = 500 m is scaled to coefficients of 0, 0.1, 0.2, 0.4, 0.6, 0.8 and 1.0. Since such strong trends are produced by this experiment, it is conducted for different eddy viscosities as well (K = 20, 30, 40, 50, 100 m^2 s^{-1}). All other settings are consistent throughout all runs. The coefficients used for each resolution are shown in Figure 5.8.

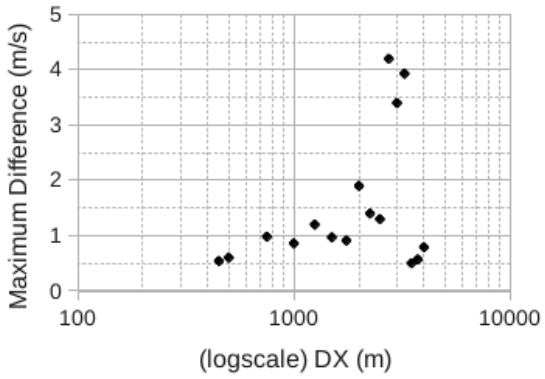

Figure 5.7: Maximum difference as a function of grid spacing, plotted in semi-log.

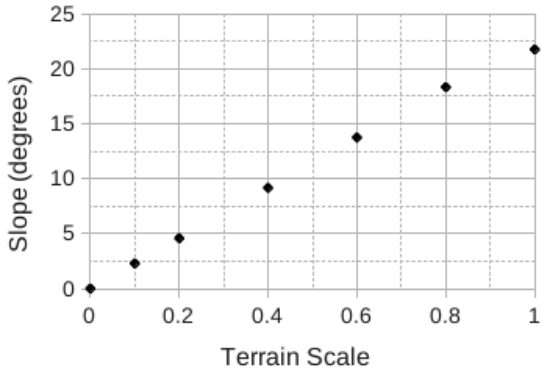

Figure 5.8: Scales used on the terrain to achieve different slopes. Horizontal resolution is 500 m for all cases.

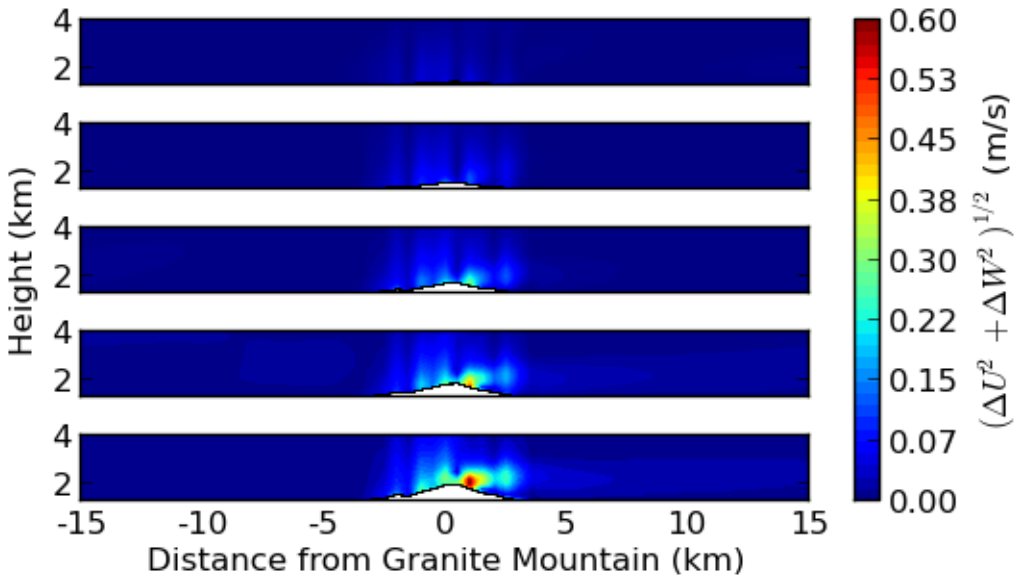

Figure 5.9: Velocity magnitude difference fields for cases where the terrain scale is (from top to bottom) 0.2, 0.4, 0.6, 0.8, 1.0. Domains are zoomed in both horizontally and vertically. To scale.

5.6.2 Results

Figure 5.9 shows five of the seven terrain scales (for $K = 100$ m^2 s^{-1}) and their difference field. A clear pattern, focused just on the lee side of the peak, emerges as the height of the mountain is increased. Even in the most consistent case, the location of the mountain can be made out easily by the location of nonzero difference values.

The maximum difference values seen in each domain, and for each eddy viscosity, follow a very strong increasing trend with slope. In Figure 5.10 the maximum differences are plotted against slope, with the slope axis reversed to mimic the pattern that would emerge were grid spacing used on the independent axis. Despite the altering of the x-axis, Figure 5.10 closely resembles the green curve in Figure 5.5 above.

This experiment is the only of the ones presented to vary eddy viscosity (all values are included in Figure 5.10). The isotropic eddy viscosity is a measure of how quickly momentum disperses in the atmosphere. When the eddy viscosity is high this momentum dispersion is rapid and the effects of the terrain are felt over shorter temporal and spatial scales. Thus the expected result is that for any scenario, a larger eddy viscosity will always yield a smaller maximum error. This was indeed the case for these results.

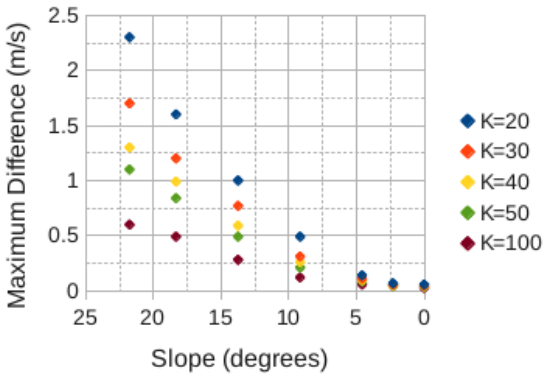

Figure 5.10: Maximum difference as a function of slope, plotted in reverse to mimic the shape expected when grid spacing is the independent variable.

5.7 Constant slope case

In this experiment 19 different horizontal resolutions between 4 km and 450 m are used. For each resolution, the height of Granite Mountain is scaled so that the maximum slope seen over any set of adjacent grid point is 10 degrees. All other factors remain constant. This is the same experiment as the initial case, except that we are removing a mechanism that is believed to limit the difference that we see as the grid spacing increases. This is very similar to the initial experiment, but attempts to isolate grid spacing as a variable and the impact it has on IBM-WRF.

5.7.1 Model setup

The base model setup the same as the previous case, with a scaling factor used to maintain a maximum slope of 10 degrees at each resolution. Figure 5.11 shows the scales used at each resolution to achieve the necessary maximum slope.

5.7.2 Results

Difference fields for five representative domains are shown in Figure 5.12. Unlike in Figure 5.9, where the difference seems to radiate directly from the mountain, the differences here are much more sporadic and concentrated to the side of the mountain. Such patterns, especially the one shown for the dx = 2 km case, indicate an interpolation error. This is visually confirmed in Figure 5.13 by comparing the velocity magnitude fields of WRF and IBM-WRF.

The resulting relationship between maximum difference and horizontal resolution is shown in Figure 5.14. The difference follows a similar trend as the initial experiment, but shows no

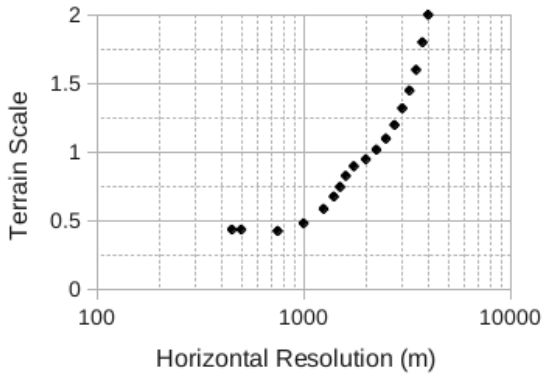

Figure 5.11: Scales used on the terrain to achieve a maximum slope of 10 degrees for each horizontal resolution.

sign of a tail. Two outliers are very visible (noted in Figure 5.14), but the trend is clearly present. Interestingly, the outliers are both at horizontal resolutions where the scaling factor is < 1, which is counter-intuitive. A decrease in the scale of the terrain is expected to be accompanied by an improvement in mutual agreement between the two systems. These outliers seem to be a result of a variable nature possessed by IBM-WRF at coarse resolutions, and are an example of an issue that the implementation of a log-law could potentially address.

5.8 Concluding remarks

The IBM-WRF framework is potentially a very powerful atmospheric model, capable of ranging across essentially all scales of the globe. Of note is the improved capability of joint observational and modeling studies of the atmosphere, especially studies of atmospheric turbulence. The meso-to-micro scale nesting capability would allow for LES at the finest scales to consider regional weather effects associated with observational data. The general spatial scale where each coordinate system is appropriate is known, however the specific relationships between numerical errors in the different systems and the multiple factors that control these errors are not known. If these two systems are to be used in a single modeling framework, the nature of the two systems relative to each other and their model settings must be investigated in more detail.

In this work we have presented a hypothetical model for the behavior of WRF's terrain-following coordinate system and IBM-WRF's immersed boundary method and conducted three simple experiments to evaluate this model. The presented hypothesis seems to have merit, although the relative location of WRF showing signs of numerical instabilities is not accurately predicted. The hypothesis is that as grid spacing decreases WRF and IBM-WRF

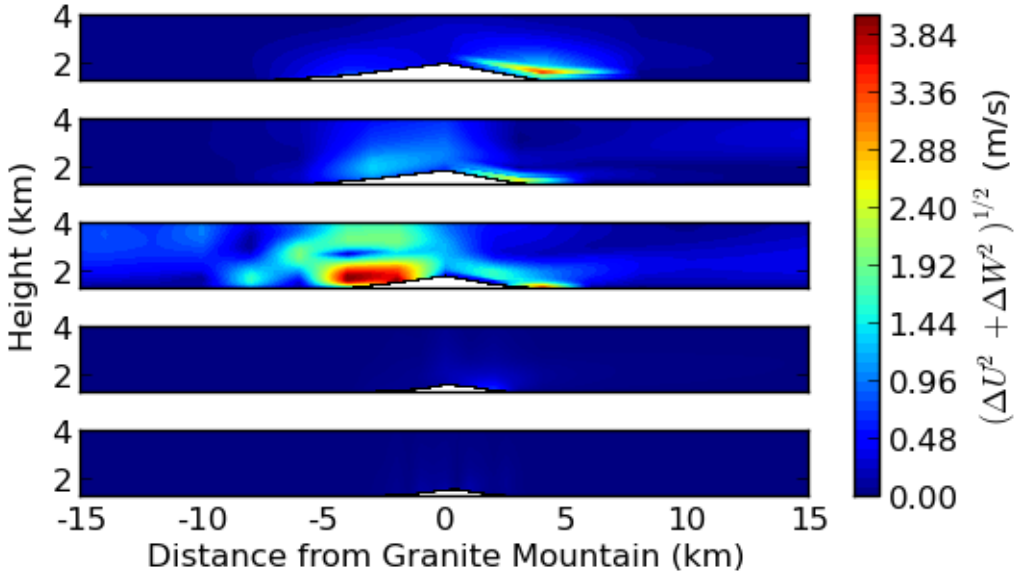

Figure 5.12: Velocity magnitude difference fields for cases where the horizontal resolution is (from top to bottom) 4km, 3km, 2km, 1km, 500m. Domains are zoomed in both horizontally and vertically. To scale.

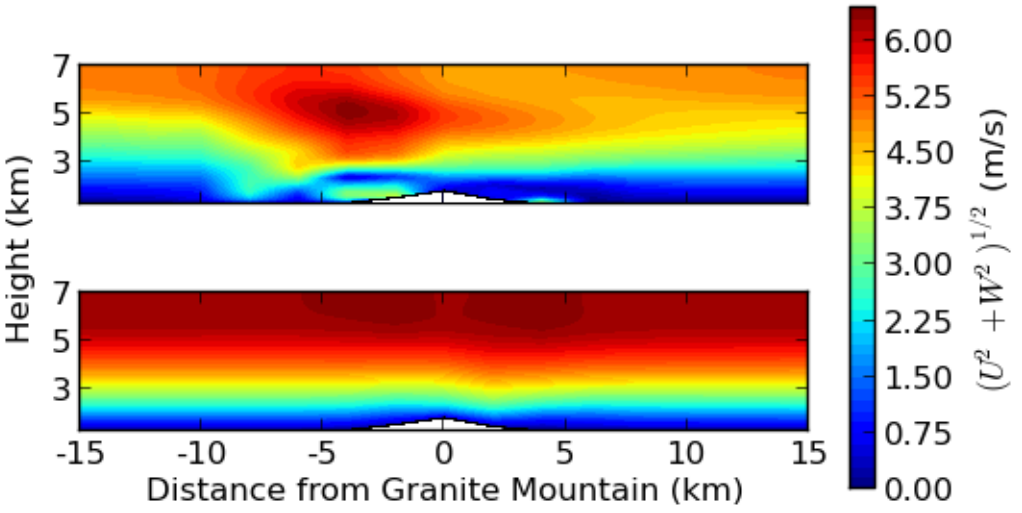

Figure 5.13: Velocity magnitude fields for IBM-WRF (top) and WRF when the horizontal resolution is 2 km and the maximum slope is artificially set to 10 degrees. To scale.

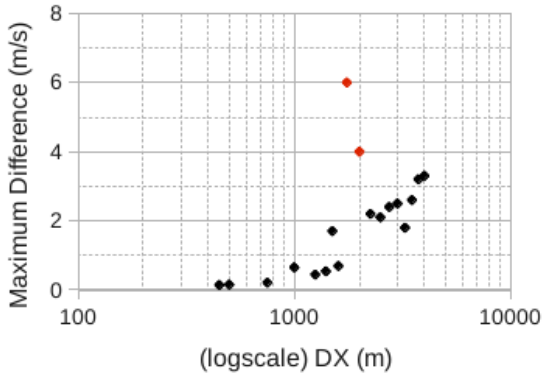

Figure 5.14: Maximum difference as a function of horizontal resolution when the maximum slope is artificially set to 10 degrees. The two outliers are in red.

will begin to diverge before WRF cannot continue. In these experiments WRF's range is at its minimum before a fine-scale divergence is seen. This is not concerning considering the two-dimensional setup used, since this is a considerable constrain on the solution that very well may cause premature instability.

From these results it can be deduced firstly that the choice of coordinate system is highly dependent on horizontal resolution and terrain slope. It is also concluded that, for two dimensions, there is a range of notably low difference between WRF and IBM-WRF which marks the location of the desired transition between the two. In two dimensions this transition is made necessary by numerical instabilities in WRF, but that result is not necessarily expected in three dimensions.

The errors generated by IBM-WRF are primarily a result of inaccurate interpolation caused by large spatial distances between grid points. This can likely be alleviated with the implementation of a log-law to reconstruct image point values. Indeed, this is a subject of ongoing work that is expected to increase the flexibility of IBM-WRF to be extended to coarser resolutions. The specific impact that a log-law will have on the results found here is not known.

5.9 Acknowledgments

This research was funded by Office of Naval Research Award #N00014-11-1-0709, Mountain Terrain Atmospheric Modeling and Observations (MATERHORN) Program.

Chapter 6

Conclusions and future work

A thorough investigation is presented on the behavior of isotropic and various implementations of anisotropic versions of the three-dimensional Smagorinsky-Lilly model of Lilly (1962); Smagorinsky (1963), the 1.5-order prognostic turbulent kinetic energy (TKE) model of Deardorff (1972), and the dynamic reconstruction model (DRM) using zero and two levels of reconstruction for large-eddy simulation (LES) of the atmospheric boundary layer (ABL). Cases considered began with an idealized free-convection case with $\overline{w'\theta'_s} = 0.24$ m K s^{-1} and $u_0 = 0$ m s^{-1}. A more realistic initial profile with an initial wind and geostrophic forcing was then considered with $\overline{w'\theta'_s} = 0.3$ m K s^{-1}. Finally, three more cases were considered with $\overline{w'\theta'_s} = 0.4$ m K s^{-1} and $u_0 = 0$ m s^{-1}, $\overline{w'\theta'_s} = 0.15$ m K s^{-1} and $u_0 = 8$ m s^{-1}, $\overline{w'\theta'_s} = 0.45$ m K s^{-1} and $u_0 = 8$ m s^{-1}.

For eddy-viscosity models, it is shown that, on the highly-anisotropic grids common to numerical weather prediction (NWP), classical isotropic formulations generate a TKE spectrum of resolved vertical velocity that is generally flat in wavenumber space, while classical anisotropic formulations generate a TKE spectrum of $\overline{w}'\overline{w}'$ that is skewed towards the longest wavelengths possible on the grid, which may be acceptable behavior for numerical studies of dimensionless turbulence but not applicable to forecasting applications where physical scales should be consistent across grids. It is also shown that the DRM generates a more consistent energy spectrum across different grids, as well as more consistent planar-averaged profiles of potential temperature and velocity and planar slices of vertical velocity.

A new alternative-anisotropic formulation (a swapping of l_h and l_v) is then proposed and shown to generate a TKE spectrum that is skewed towards the smallest wavelengths possible on the grid. The behavior of this new formulation is evaluated for multiple levels of surface heating and geostrophic forcing. It is seen that, while the performance is generally very good and an improvement over either traditional isotropic or anisotropic formulations, there are some very interesting follow-up questions about the different lengthscales of production and dissipation for heat and momentum in the atmosphere, and their partitioning in sub-grid scale (SGS) turbulent models. From the results seen, it seems very optimistic to think that there is some formulation of the prognostic TKE-1.5 model that is able to generate highly-consistent results across all grid scales, as well as provide insights into the scales of TKE production

and dissipation.

Analysis is also extended for the DRM, which is shown to improve the performance of NWP models in the presence of both increased shear and orographic drag (in the Appendices), with simulations of turbulence around a high-resolution representation of Granite Mountain (Utah) shown and compared to the traditional models.

Finally, a brief treatment of a similar gray-zone problem in the representation of complex terrain is given, highlighting that the general issues outlined here for representing atmospheric turbulence, where the extreme ends of the micro and macro scales are both easily modeled, but at the most relevant scales there is a conflict between the representation of the terrain complexity and the representation of the flow complexity that can lead to large errors in the solution.

This work has addressed many outstanding questions and has also led to many new and interesting questions which will be the subject of future work. First and foremost, considerations will be made for the inclusion of moisture, which is not only the most natural and obvious next step, but is the next step in the author's career as well. Other future considerations include the further development of the DRM and alternative anisotropic eddy-viscosity models, particularly in the lengthscales used in the prognostic TKE equations for the alternative-anisotropic TKE-1.5 model, as well as further theoretical insights to the scales of production and dissipation of TKE in the atmosphere that may be gained from these investigations.

Appendix A

Additional sheared test cases in WRF-LES

This appendix includes additional test cases comparing the DRM to the Smagorinsky-Lilly and TKE-1.5 models for sheared convection cases. The setup of these cases follows the cases in Chs. 3 and 4.

A.1 Results

A.1.1 High-resolution cases

High-resolution results (100 m) are given first using the same familiar figures to show the evolution of mean and turbulent fields.

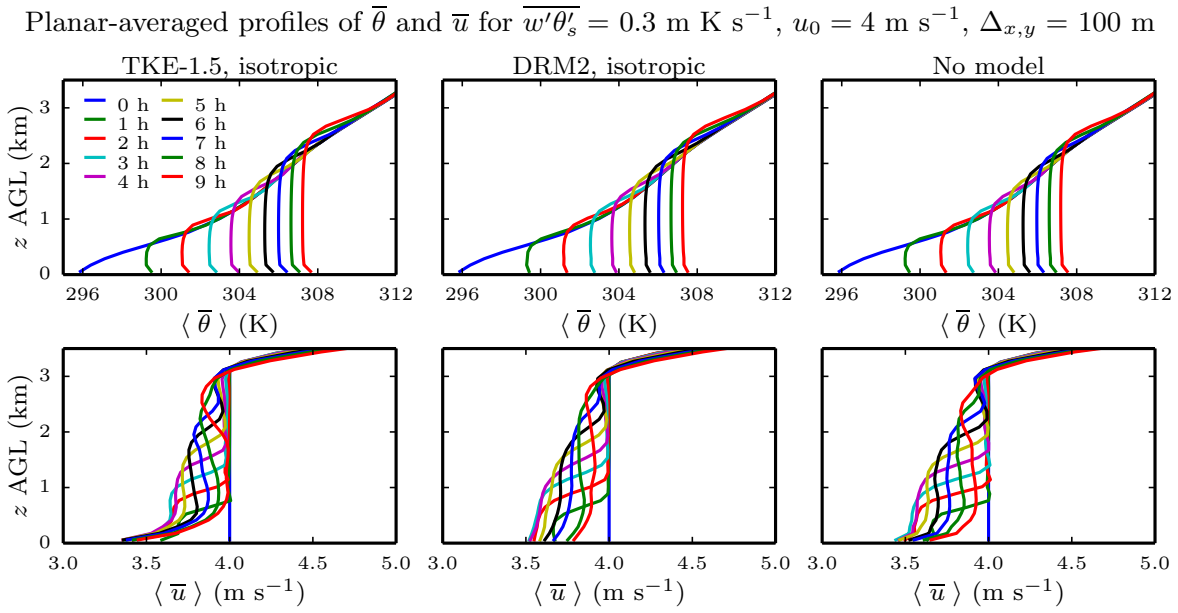

Figure A.1: Resolved potential temperature and u-velocity profiles for the high-resolution ($\Delta_{x,y} = 100$ m) cases using the isotropic TKE-1.5 model, isotropic DRM2 model and no model.

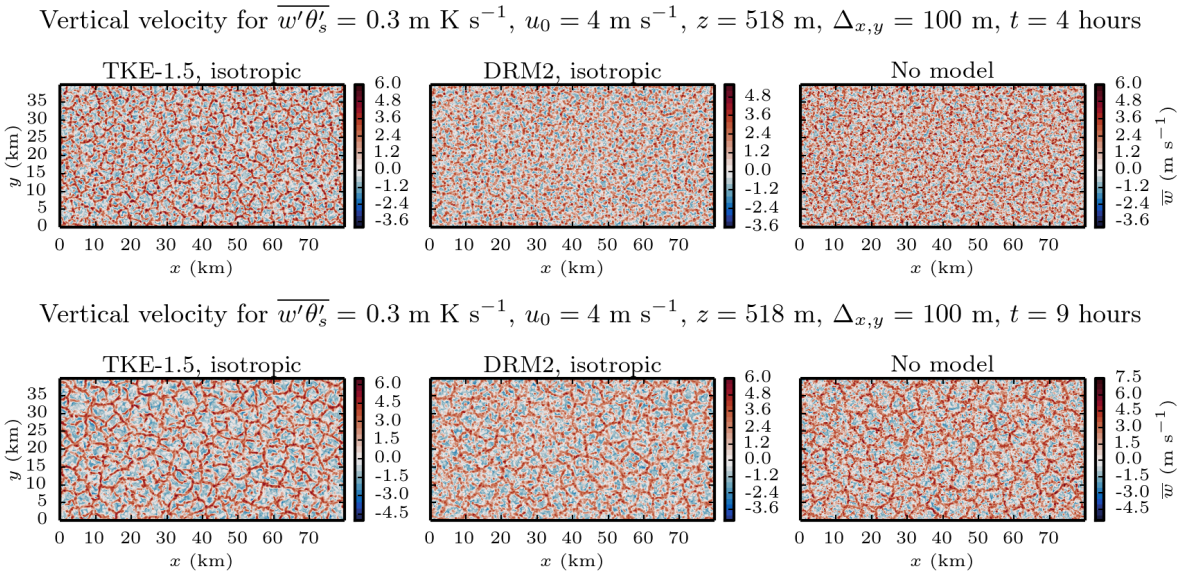

Figure A.2: Resolved vertical velocity, $\overline{w}$, in the $z \approx 518$ m plane at $t = 4$ (top) and 9 (bottom) hours for the high-resolution ($\Delta_{x,y} = 100$ m) cases using the isotropic TKE-1.5 model, isotropic DRM2 model and no model.

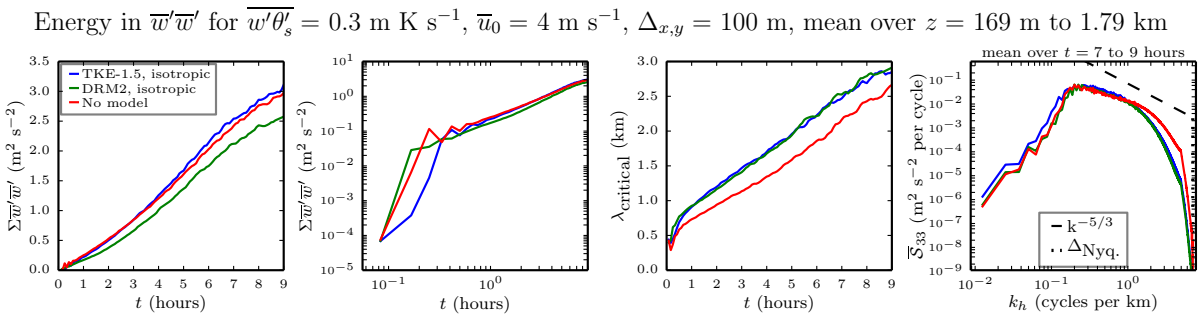

Figure A.3: Metrics of the resolved vertical velocity field, $\overline{w}$, averaged over the $z \approx$ 169 m to 1.79 km planes for the high-resolution ($\Delta_{x,y} = 100$ m) cases using the isotropic TKE-1.5 model, isotropic DRM2 model and no model: total resolved TKE ($\overline{w}'\overline{w}'$) in time (far left), the same in log-log scale (middle left), critical wavelength of $\overline{w}'\overline{w}'$ in time (middle right), and spectra of resolved TKE ($\overline{\mathcal{S}}_{33}$) averaged over the final two hours (far right).

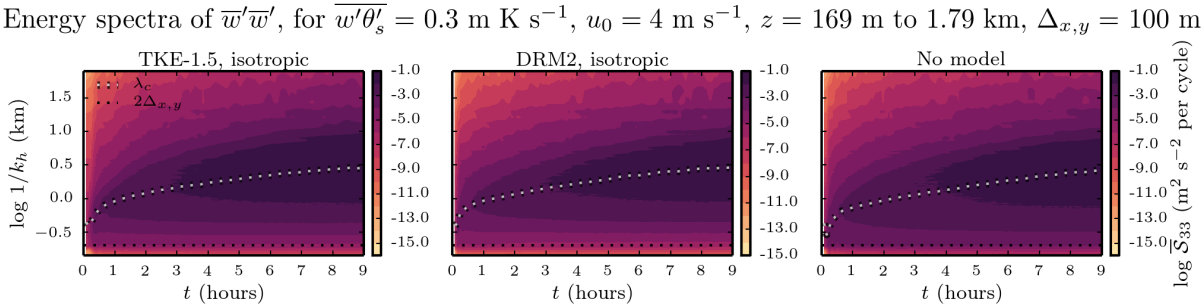

Figure A.4: Contours of spectra of resolved TKE in the vertical velocity ($\overline{\mathcal{S}}_{33}$) in time for the high-resolution ($\Delta_{x,y} = 100$ m) cases using the isotropic TKE-1.5 model, isotropic DRM2 model and no model, with the critical wavelength (dotted white) and horizontal Nyquist limit (dotted black) overlaid.

A.1.2 Coarse DRM flavors

This section includes results from test cases at 1.2-km resolutions with level-0 and level-2 reconstruction using isotropic and anisotropic versions of the DWL.

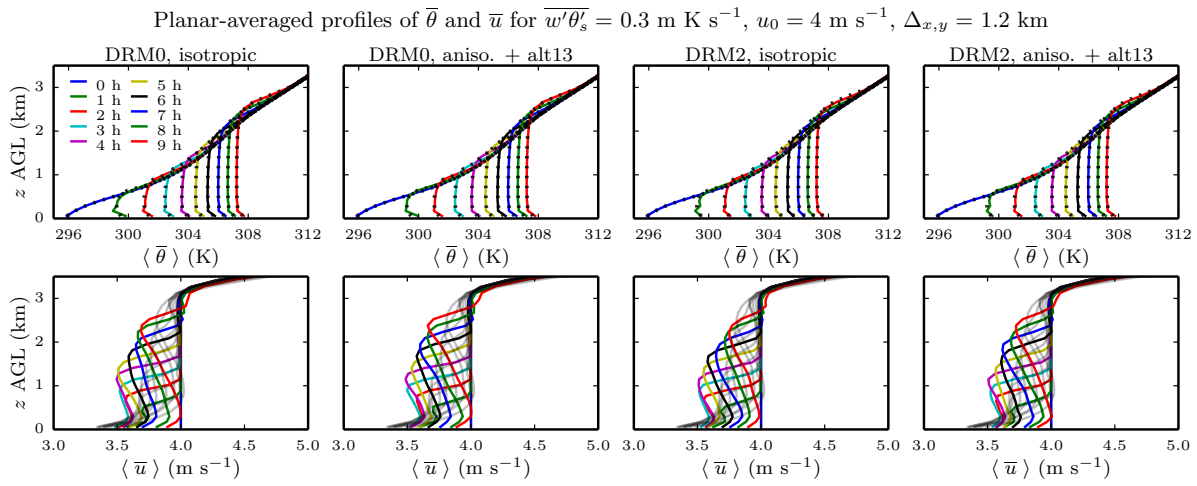

Figure A.5: Resolved potential temperature and u-velocity profiles for the $\Delta_{x,y} = 1.2$ km using the DRM0 and DRM2 models with isotropic and anisotropic lengthscales.

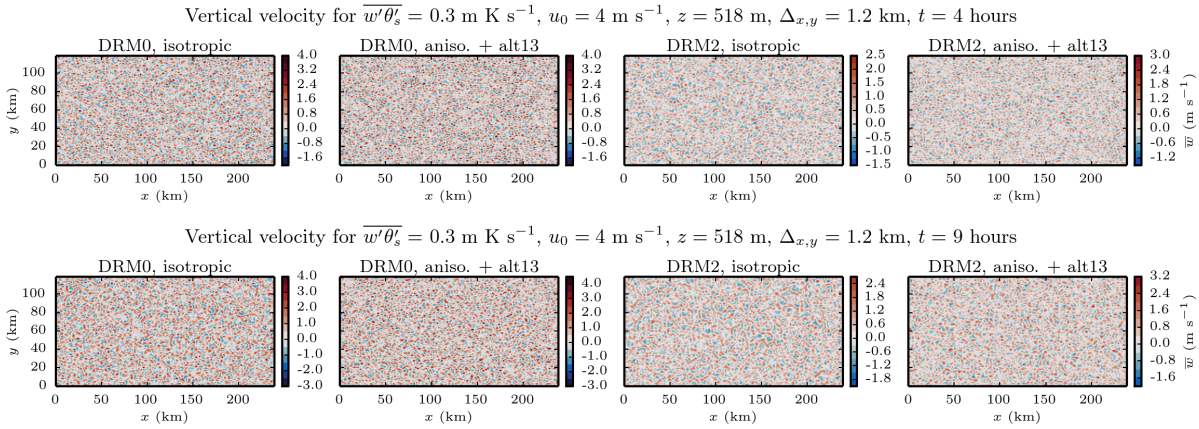

Figure A.6: Resolved vertical velocity, $\overline{w}$, in the $z \approx 518$ m plane at $t = 4$ (top) and 9 (bottom) hours for the $\Delta_{x,y} = 1.2$ km using the DRM0 and DRM2 models with isotropic and anisotropic lengthscales.

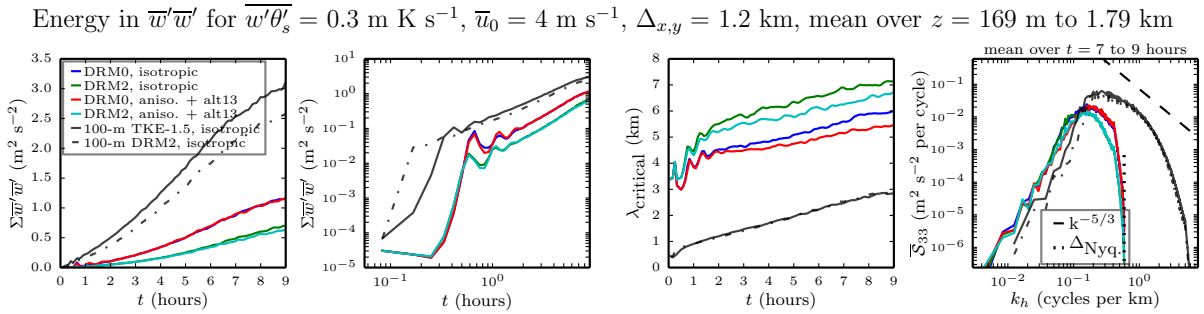

Figure A.7: As in Fig. 3.3 but when $\Delta_{x,y} = 1.2$ km using the DRM0 and DRM2 models with isotropic and anisotropic lengthscales.

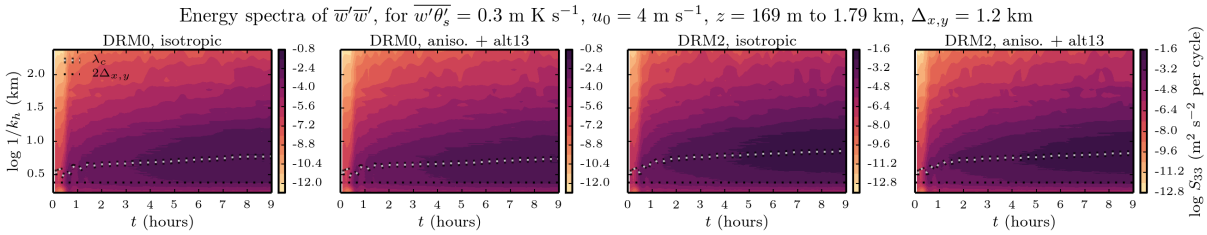

Figure A.8: As in Fig. 3.4 but when $\Delta_{x,y} = 1.2$ km using the DRM0 and DRM2 models with isotropic and anisotropic lengthscales.

Appendix B

Additional test cases with terrain in WRF-LES

This appendix includes preliminary test cases including complex terrain, comparing the DRM to the Smagorinsky-Lilly and TKE-1.5 models for sheared convection. The setup of these cases follows the cases in Chs. 3 and 4 but with the addition of a mountain.

B.1 Results

B.1.1 Coarse isotropic cases

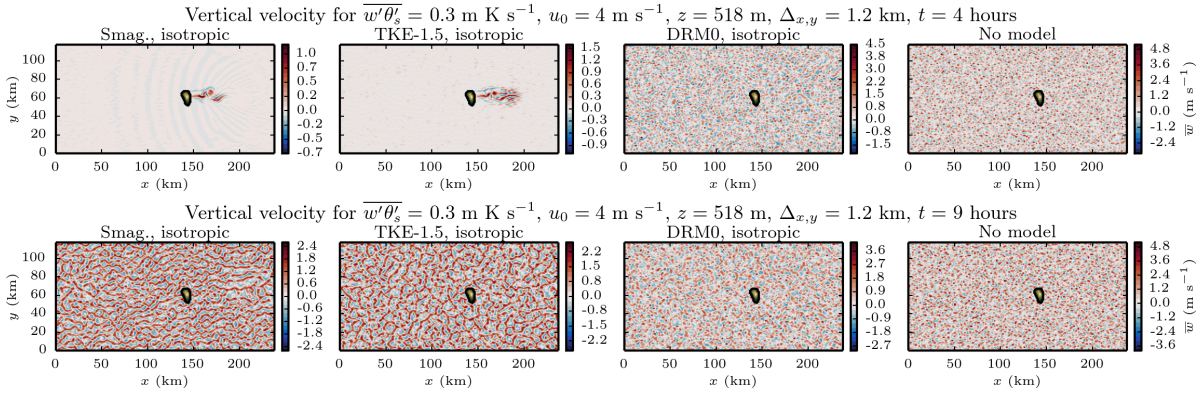

Figure B.1: Vertical velocity, w, at $t = 4$ (top) and 9 (bottom) hours in the $z \approx 518$ m plane for the $\Delta_{x,y} = 1.2$ km cases considered.

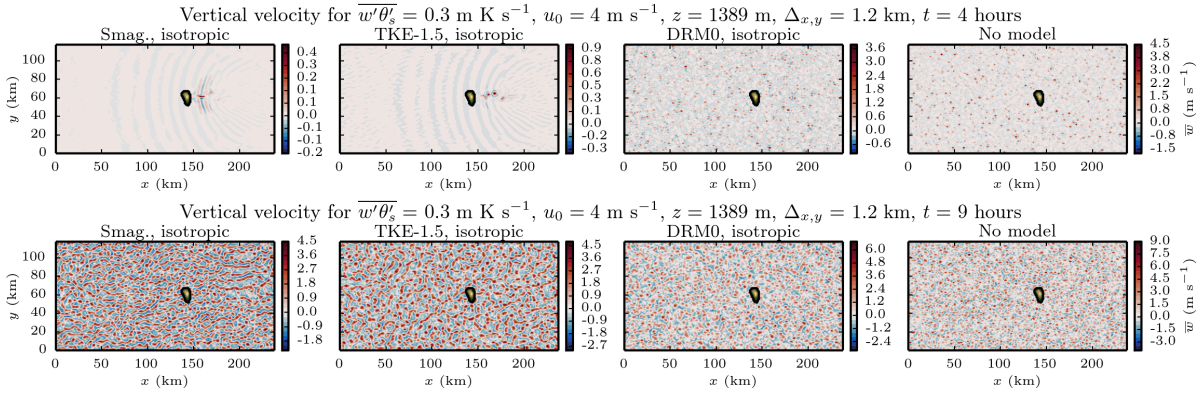

Figure B.2: Vertical velocity, w, at $t = 4$ (top) and 9 (bottom) hours in the $z \approx 1389$ m plane for the $\Delta_{x,y} = 1.2$ km cases considered.

B.1.1.1 Smagorinsky-Lilly model

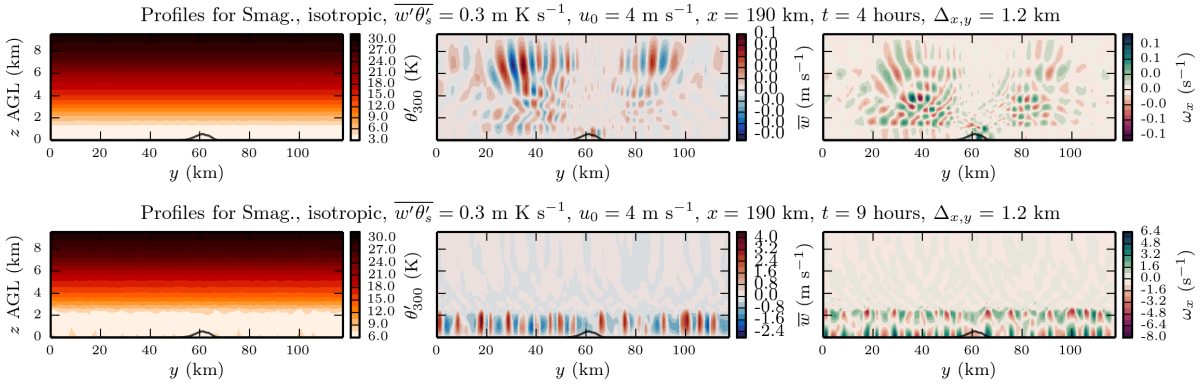

Figure B.3: Slice through the $y-z$ plane at $x = 190$ km using the isotropic Smagorinsky-Lilly model at $t = 4$ (top) and 9 (bottom) hours for the $\Delta_{x,y} = 1.2$ km case.

B.1.1.2 TKE-1.5 model

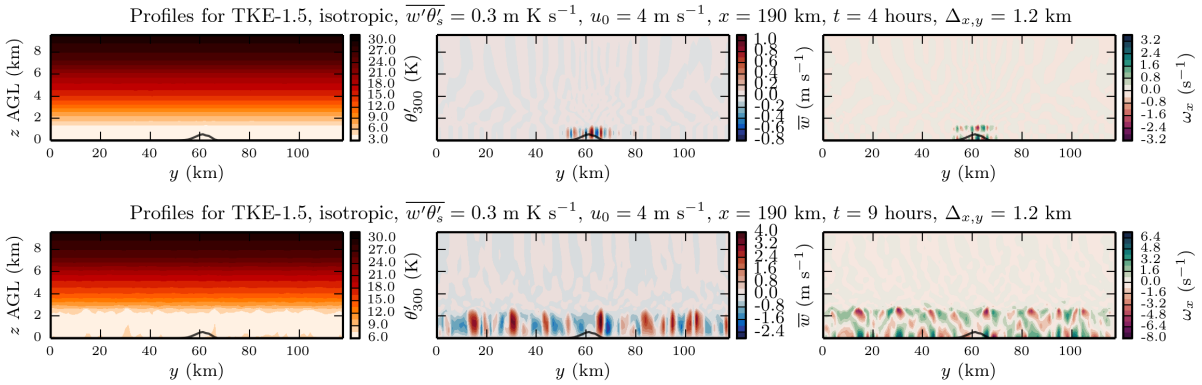

Figure B.4: As in Fig. B.3 but for the isotropic TKE-1.5 model.

B.1.1.3 DRM model

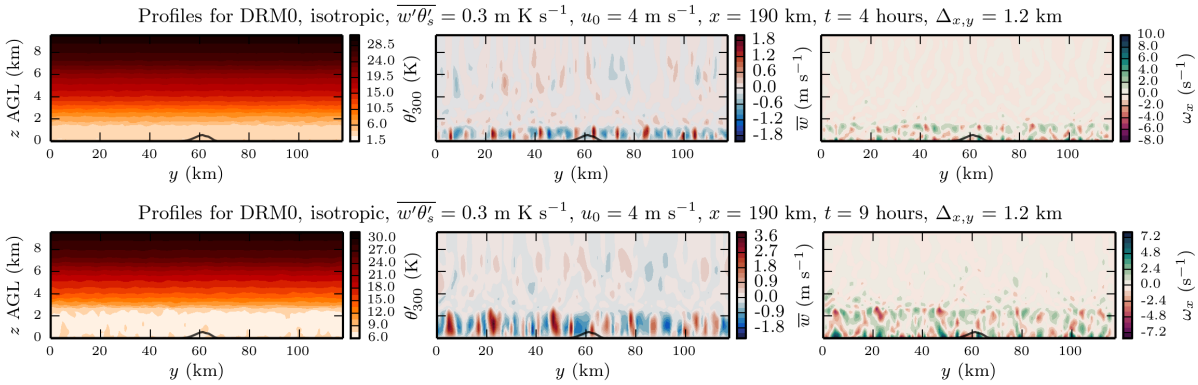

Figure B.5: As in Fig. B.3 but for the isotropic DRM0 model.

B.1.1.4 No model

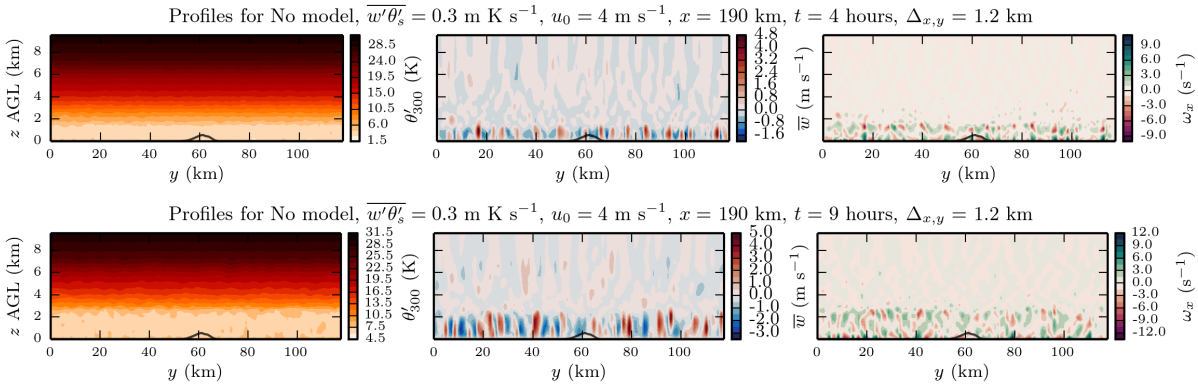

Figure B.6: As in Fig. B.3 but using no model.

Appendix C

Relevant details of the WRF code

C.1 Turbulent diffusion

C.1.1 Diffusion in WRF prior to 3.8.1

In versions of WRF prior to 3.8.1 the turbulent stress terms were coupled to the dry column mass per area, m, (mimicking the prognostic variables U, V, W, Θ) and were simply calculated as the difference in the coupled-stress over the distance of interest. Considering θ as an example, turbulent stress gradients are included in the discrete tendency terms as

$$\frac{\partial \Theta}{\partial t} += -\frac{\Delta \left(m \tau_{\theta 3} \right)}{\Delta z} \tag{C.1}$$

where

$$\tau_{\theta 3} = -\frac{K_v}{\mathrm{Pr}} \frac{\partial \theta}{\partial z}, \tag{C.2}$$

m is column dry air mass per area, K_v is vertical eddy viscosity and Pr is the turbulent Prandtl number.

C.1.2 Diffusion in WRF 3.8.1 onwards

Beginning with WRF 3.8.1 the diffusion terms were updated to conserve mass by coupling the turbulent stresses with the local density rather than the column mass. Due to prognostic variables having units of being coupled to the column mass rather than the local density, this required a reformulation of diffusion terms to a much less intuitive form, becoming (again considering Θ)

$$\frac{\partial \Theta}{\partial t} += g \frac{\Delta \left(\rho \tau_{\theta 3} \right)}{\Delta \eta} \tag{C.3}$$

where

$$\eta = \frac{p_h - p_{ht}}{p_{hs} - p_{ht}} = \frac{p_h - p_{ht}}{m} \tag{C.4}$$

where p_h is the hydrostatic pressure, p_{ht} is the hydrostatic pressure at the top, p_{hs} is the hydrostatic pressure at the surface, ρ is local density. The change in sign is because $\Delta\eta$ is 1 at the surface and 0 at the model top (i.e. positive-down, compared to z which is positive-up). Using the definition of hydrostatic pressure it is relatively simple to find that C.1 and C.3 are equivalent.

C.2 Ideal surface fluxes

C.2.1 Surface heat fluxes in WRF

When a constant surface heat flux is specified in the namelist it is done via `tke_heat_flux`, which has units of [m K s^{-1}], and the diffusion routine takes

$$\tau_{\theta 3,\mathrm{S}} = \texttt{tke\_heat\_flux}, \tag{C.5}$$

$$\frac{\partial \Theta_s}{\partial t} += -g \frac{\rho \tau_{\theta 3,\mathrm{S}}}{\Delta \eta}, \tag{C.6}$$

then calculates

$$\texttt{HFX} = c_{pm} \rho \tau_{\theta 3,\mathrm{S}} \tag{C.7}$$

to provide output in units of [W m^{-2}].

C.2.2 Surface heat and momentum fluxes in the WRF code

```
SUBROUTINE vertical_diffusion_2    ( ru_tendf, rv_tendf, rw_tendf, rt_tendf, &
                                     tke_tendf, moist_tendf, n_moist,        &
                                     chem_tendf, n_chem,                     &
                                     scalar_tendf, n_scalar,                 &
                                     tracer_tendf, n_tracer,                 &
                                     u_2, v_2,                               &
                                     thp,u_base,v_base,t_base,qv_base,mu,tke,&
                                     config_flags,defor13,defor23,defor33,   &
                                     nba_mij, n_nba_mij,                     &
    !JDM
                                     div,                                    &
                                     moist,chem,scalar,tracer,               &
                                     xkmv,xkhv,xkmh,km_opt,                  &
    ! xkmh added
                                     fnm, fnp, dn, dnw, rdz, rdzw,           &
                                     hfx, qfx, ust, rho,                     &
                                     ids, ide, jds, jde, kds, kde,           &
                                     ims, ime, jms, jme, kms, kme,           &
                                     its, ite, jts, jte, kts, kte            )

!-----------------------------------------------------------------------
! Begin declarations.

  !JSS: REMOVED, NOT RELEVANT HERE

! End declarations.
!-----------------------------------------------------------------------

   i_start = its
   i_end   = MIN(ite,ide-1)
   j_start = jts
   j_end   = MIN(jte,jde-1)
!
!-----------------------------------------------------------------------

      CALL vertical_diffusion_u_2( ru_tendf, config_flags, mu,     &
                                   defor13, xkmv,                  &
                                   nba_mij, n_nba_mij,             & !JDM
                                   dnw, rdzw, fnm, fnp, rho,       &
                                   ids, ide, jds, jde, kds, kde,   &
                                   ims, ime, jms, jme, kms, kme,   &
                                   its, ite, jts, jte, kts, kte  )


      CALL vertical_diffusion_v_2( rv_tendf, config_flags, mu,     &
                                   defor23, xkmv,                  &
                                   nba_mij, n_nba_mij,             & !JDM
                                   dnw, rdzw, fnm, fnp, rho,       &
                                   ids, ide, jds, jde, kds, kde,   &
                                   ims, ime, jms, jme, kms, kme,   &
                                   its, ite, jts, jte, kts, kte  )

      CALL vertical_diffusion_w_2( rw_tendf, config_flags, mu,     &
                                   defor33, tke(ims,kms,jms),      &
                                   nba_mij, n_nba_mij,             & !JDM
```

```
54                                        div, xkmh,                          & !Mod from
    RR Oct2013 was xkmv
55                                        dn, rdz, fnm, fnp, rho,             &
56                                        ids, ide, jds, jde, kds, kde,       &
57                                        ims, ime, jms, jme, kms, kme,       &
58                                        its, ite, jts, jte, kts, kte   )
59
60 !****************************************
61 !****************************************
62 !  MODIFICA al flusso di momento alla parete
63 !
64   vflux: SELECT CASE( config_flags%isfflx )
65   CASE (0) ! Assume cd a constant, specified in namelist
66     cd0 = config_flags%tke_drag_coefficient  ! constant drag coefficient
67                                              ! set in namelist.input
68 !
69 !calcolo del modulo della velocita
70     DO j = j_start, j_end
71     DO i = i_start, ite
72         V0_u=0.
73         tao_xz=0.
74         V0_u=     sqrt((u_2(i,kts,j)**2) +          &
75                        (((v_2(i   ,kts,j   )+       &
76                           v_2(i   ,kts,j+1)+        &
77                           v_2(i-1,kts,j   )+        &
78                           v_2(i-1,kts,j+1))/4)**2))+epsilon
79 !SNT -- Fix to diffusion
80 !        tao_xz=cd0*V0_u*u_2(i,kts,j)
                    !old code
81 !        ru_tendf(i,kts,j)=ru_tendf(i,kts,j)             &
                    !old code
82 !                          -0.25*(mu(i,j)+mu(i-1,j))*tao_xz*(rdzw(i,kts,j)+rdzw
    (i-1,kts,j))    !old code
83
84         tao_xz=cd0*V0_u*u_2(i,kts,j)*(rho(i,kts,j)+rho(i-1,kts,j))/2.
                    !new code
85         ru_tendf(i,kts,j)=ru_tendf(i,kts,j) +   g*tao_xz/dnw(kts)
                    !new code
86 !SNT -- End changes
87     ENDDO
88     ENDDO
89
90
91
92   !JSS: REMOVED, SAME AS ABOVE FOR RV_TENDF
93
94   CASE (1,2) ! ustar computed from surface routine
95     DO j = j_start, j_end
96     DO i = i_start, ite
97         V0_u=0.
98         tao_xz=0.
99         V0_u=     sqrt((u_2(i,kts,j)**2) +          &
100                        (((v_2(i   ,kts,j   )+       &
101                           v_2(i   ,kts,j+1)+        &
102                           v_2(i-1,kts,j   )+        &
103                           v_2(i-1,kts,j+1))/4)**2))+epsilon
104        ustar=0.5*(ust(i,j)+ust(i-1,j))
```

```
105 !SNT -- Fix to diffusion
106 !       tao_xz=ustar*ustar*u_2(i,kts,j)/V0_u
                  !old code
107 !       ru_tendf(i,kts,j)=ru_tendf(i,kts,j)            &
                  !old code
108 !                        -0.25*(mu(i,j)+mu(i-1,j))*tao_xz*(rdzw(i,kts,j)+rdzw
    (i-1,kts,j))  !old code
109
110         tao_xz=ustar*ustar*u_2(i,kts,j)*(rho(i,kts,j)+rho(i-1,kts,j))/(2.*V0_u)
                  !new code
111         ru_tendf(i,kts,j)=ru_tendf(i,kts,j) +   g*tao_xz/dnw(kts)
                  !new code
112 !SNT -- End changes
113     ENDDO
114     ENDDO
115
116   !JSS: REMOVED, SAME AS ABOVE FOR RV_TENDF
117
118   CASE DEFAULT
119     CALL wrf_error_fatal( 'isfflx value invalid for diff_opt=2' )
120   END SELECT vflux
121
122
123    CALL vertical_diffusion_s( rt_tendf, config_flags, var_mix, mu, xkhv, &
124                               dn, dnw, rdz, rdzw, fnm, fnp, rho,     &
125                               .false.,                               &
126                               ids, ide, jds, jde, kds, kde,          &
127                               ims, ime, jms, jme, kms, kme,          &
128                               its, ite, jts, jte, kts, kte           )
129
130
131 !****************************************
132 !****************************************
133 !MODIFICA al flusso di calore
134 !
135 !
136   hflux: SELECT CASE( config_flags%isfflx )
137   CASE (0,2) ! with fixed surface heat flux given in the namelist
138     heat_flux = config_flags%tke_heat_flux  ! constant heat flux value
139                                             ! set in namelist.input
140     DO j = j_start, j_end
141     DO i = i_start, i_end
142        cpm = cp * (1. + 0.8 * moist(i,kts,j,P_QV))
143        hfx(i,j)=heat_flux*cp*rho(i,kts,j)          ! provided for output only
144 !SNT -- FIx to diffusion
145 !       rt_tendf(i,kts,j)=rt_tendf(i,kts,j)  &   !old code
146 !            +mu(i,j)*heat_flux*rdzw(i,kts,j)    !old code
147        rt_tendf(i,kts,j)=rt_tendf(i,kts,j)  &    !new code
148             -g*heat_flux*rho(i,kts,j)/dnw(kts)   !new code
149 !SNT -- End changes
150     ENDDO
151     ENDDO
152
153   CASE (1) ! use surface heat flux computed from surface routine
154     DO j = j_start, j_end
155     DO i = i_start, i_end
156
```

```
157         cpm = cp * (1. + 0.8 * moist(i,kts,j,P_QV))
158 !SNT -- Fix to diffusion
159 !         heat_flux = hfx(i,j)/cpm/rho(i,1,j)       !old code
160 !         rt_tendf(i,kts,j)=rt_tendf(i,kts,j)  &    !old code
161 !              +mu(i,j)*heat_flux*rdzw(i,kts,j)     !old code
162         heat_flux = hfx(i,j)/cpm                    !new code
163         rt_tendf(i,kts,j)=rt_tendf(i,kts,j)  &      !new code
164              -g*heat_flux/dnw(kts)                  !new code
165 !SNT -- End changes
166
167       ENDDO
168       ENDDO
169
170     CASE DEFAULT
171       CALL wrf_error_fatal( 'isfflx value invalid for diff_opt=2' )
172     END SELECT hflux
173
174
175
176     !JSS: REMOVED, NOT RELEVANT HERE
177
178
179 END SUBROUTINE vertical_diffusion_2
180
181
182
183 !==========================================================================
184 !==========================================================================
185
186 SUBROUTINE vertical_diffusion_s( tendency, config_flags, var, mu, xkhv,   &
187                                  dn, dnw, rdz, rdzw, fnm, fnp, rho,       &
188                                  doing_tke,                               &
189                                  ids, ide, jds, jde, kds, kde,            &
190                                  ims, ime, jms, jme, kms, kme,            &
191                                  its, ite, jts, jte, kts, kte             )
192
193 !-------------------------------------------------------------------------
194 ! Begin declarations.
195
196     IMPLICIT NONE
197
198     TYPE(grid_config_rec_type), INTENT(IN    ) :: config_flags
199
200     INTEGER ,           INTENT(IN    ) ::        ids, ide, jds, jde, kds, kde, &
201                                                  ims, ime, jms, jme, kms, kme, &
202                                                  its, ite, jts, jte, kts, kte
203
204     LOGICAL,            INTENT(IN    ) ::        doing_tke
205
206     REAL , DIMENSION( kms:kme ) ,                    INTENT(IN    ) ::     fnm
207     REAL , DIMENSION( kms:kme ) ,                    INTENT(IN    ) ::     fnp
208     REAL , DIMENSION( kms:kme ) ,                  INTENT(IN    )       ::   dn
209     REAL , DIMENSION( kms:kme ) ,                  INTENT(IN    )       :: dnw
210
211     REAL , DIMENSION( ims:ime, kms:kme, jms:jme), INTENT(INOUT) ::tendency
212
213     REAL , DIMENSION( ims:ime , kms:kme, jms:jme ) , INTENT(IN) ::    xkhv
```

```
214
215    REAL , DIMENSION( ims:ime , jms:jme ) , INTENT(IN) ::    mu
216
217    REAL , DIMENSION( ims:ime , kms:kme, jms:jme ) ,                    &
218                                            INTENT(IN    )       ::     var, &
219                                                                        rdz, &
220                                                                       rdzw, &
221                                                                        rho
222 ! LOCAL VARS
223
224    INTEGER :: i, j, k, ktf
225
226    INTEGER :: i_start, i_end, j_start, j_end
227
228    REAL , DIMENSION( its:ite, kts:kte, jts:jte)             ::         H3, &
229                                                                    xkxavg, &
230                                                                     rravg
231
232    REAL , DIMENSION( its:ite, kts:kte, jts:jte)             ::   tmptendf
233
234 ! End declarations.
235 !-----------------------------------------------------------------------
236
237    ktf=MIN(kte,kde-1)
238
239    i_start = its
240    i_end   = MIN(ite,ide-1)
241    j_start = jts
242    j_end   = MIN(jte,jde-1)
243
244    IF ( config_flags%open_xs .or. config_flags%specified .or. &
245         config_flags%nested) i_start = MAX(ids+1,its)
246    IF ( config_flags%open_xe .or. config_flags%specified .or. &
247         config_flags%nested) i_end   = MIN(ide-2,ite)
248    IF ( config_flags%open_ys .or. config_flags%specified .or. &
249         config_flags%nested) j_start = MAX(jds+1,jts)
250    IF ( config_flags%open_ye .or. config_flags%specified .or. &
251         config_flags%nested) j_end   = MIN(jde-2,jte)
252       IF ( config_flags%periodic_x ) i_start = its
253       IF ( config_flags%periodic_x ) i_end = MIN(ite,ide-1)
254
255    IF (doing_tke) THEN
256       DO j = j_start, j_end
257       DO k = kts,ktf
258       DO i = i_start, i_end
259          tmptendf(i,k,j)=tendency(i,k,j)
260       ENDDO
261       ENDDO
262       ENDDO
263    ENDIF
264
265 ! H3
266
267    xkxavg = 0.
268
269    DO j = j_start, j_end
270    DO k = kts+1,ktf
```

```
271     DO i = i_start , i_end
272        xkxavg(i,k,j)=fnm(k)*xkhv(i,k,j)+fnp(k)*xkhv(i,k-1,j)
273        xkxavg(i,k,j)=xkxavg(i,k,j)*(fnm(k)*rho(i,k,j)+fnp(k)*rho(i,k-1,j)) !SNT
274        H3(i,k,j)=-xkxavg(i,k,j)*(var(i,k,j)-var(i,k-1,j))*rdz(i,k,j)
275 !       H3(i,k,j)=-xkxavg(i,k,j)*zeta_z(i,j)* &
276 !                 (var(i,k,j)-var(i,k-1,j))/dn(k)
277     ENDDO
278     ENDDO
279     ENDDO
280
281     DO j = j_start , j_end
282     DO i = i_start , i_end
283        H3(i,kts,j)=0.
284        H3(i,ktf+1,j)=0.
285 !       H3(i,kts,j)=H3(i,kts+1,j)
286 !       H3(i,ktf+1,j)=H3(i,ktf,j)
287     ENDDO
288     ENDDO
289
290     DO j = j_start , j_end
291     DO k = kts,ktf
292     DO i = i_start , i_end
293 !SNT -- Fix to vertical diffusion to ensure conservation of mass
294 !       tendency(i,k,j)=tendency(i,k,j)  &                              !old code
295 !                       -mu(i,j)*(H3(i,k+1,j)-H3(i,k,j))*rdzw(i,k,j)   !old code
296        tendency(i,k,j)=tendency(i,k,j)  &                              !new code
297                        +   g * (H3(i,k+1,j)-H3(i,k,j))/dnw(k)          !new code
298 !SNT -- End changes
299     ENDDO
300     ENDDO
301     ENDDO
302
303     IF (doing_tke) THEN
304        DO j = j_start , j_end
305        DO k = kts,ktf
306        DO i = i_start , i_end
307             tendency(i,k,j)=tmptendf(i,k,j)+2.* &
308                             (tendency(i,k,j)-tmptendf(i,k,j))
309        ENDDO
310        ENDDO
311        ENDDO
312     ENDIF
313
314 END SUBROUTINE vertical_diffusion_s
```

C.2.3 Surface roughness-length implementation in the WRF code

In this section, the reader will find the *ad-hoc* method of including a surface roughness in the form of a roughness length, z_0, in the WRF model, as originally implemented by Katherine A. Lundquist and passed down within the Chow Group.

The following code is an excerpt from the subroutine `vertical_diffusion_2` contained in the file `dyn_em/module_diffusion_em.F`:

```
!****************************************
!****************************************
!  MODIFICA al flusso di momento alla parete
!

  vflux: SELECT CASE( config_flags%isfflx )
  CASE (0)  !Assume cd a constant, specified in namelist
        !cd0 = config_flags%tke_drag_coefficient
        !constant drag coefficient set in namelist.input
  Cd_u = 0.
  Cd_v = 0.

  IF (config_flags%tke_drag_coefficient /= 0) THEN
    cd0 = config_flags%tke_drag_coefficient !constant drag coefficient
                                            !set in namelist.input
    DO j = j_start, j_end+1
    DO i = i_start, i_end+1
      Cd_u(i,j)=  cd0
      Cd_v(i,j)=  cd0
    ENDDO
    ENDDO

  !!! ------>>>> START OF KAL'S MODIFICATIONS

  ELSEIF (config_flags%z_rough /= 0) THEN
    !KAL rdz is 1/dz at mass points.  This must be averaged in the horizontal
    !    to find it at u and v horizontal velocity points

    DO j = j_start, j_end+1
    DO i = i_start, i_end+1
      Cd_u(i,j)= (KARMAN / &
        LOG((2./(rdz(i-1,kts,j)+rdz(i,kts,j)))/config_flags%z_rough))**2
      Cd_v(i,j)= (KARMAN / &
        LOG((2./(rdz(i,kts,j-1)+rdz(i,kts,j)))/config_flags%z_rough))**2
    ENDDO
    ENDDO

  !!! ------>>>> END OF KAL'S MODIFICATIONS

  END IF  !end of setting drag coefficient based on
      !tke_drag_coefficient or z_rough from namelist

!calcolo del modulo della velocita
  DO j = j_start, j_end
  DO i = i_start, i_end+1
```

```
46      V0_u=0.
47      tao_xz=0.
48      V0_u=sqrt((u_2(i,kts,j)**2) +          &
49           (((v_2(i   ,kts,j   )+            &
50              v_2(i   ,kts,j+1)+             &
51              v_2(i-1,kts,j   )+             &
52              v_2(i-1,kts,j+1))/4)**2))+epsilon
53
54      tao_xz=Cd_u(i,j)*V0_u*u_2(i,kts,j)*(rho(i,kts,j)+rho(i-1,kts,j))/2.
55      ru_tendf(i,kts,j)=ru_tendf(i,kts,j) +    g*tao_xz/dnw(kts)
56
57    ENDDO
58    ENDDO
59
60    DO j = j_start, j_end+1
61    DO i = i_start, i_end
62      V0_v=0.
63      tao_yz=0.
64      V0_v=sqrt((v_2(i,kts,j)**2) +          &
65           (((u_2(i   ,kts,j   )+            &
66              u_2(i   ,kts,j-1)+             &
67              u_2(i+1,kts,j   )+             &
68              u_2(i+1,kts,j-1))/4)**2))+epsilon
69
70      tao_yz=Cd_v(i,j)*V0_v*v_2(i,kts,j)*(rho(i,kts,j)+rho(i,kts,j-1))/2.
71      rv_tendf(i,kts,j)=rv_tendf(i,kts,j) +    g*tao_yz/dnw(kts)
72
73    ENDDO
74    ENDDO
```

Appendix D

American Meteorological Society full copyright notices

D.1 Full copyright notice for Ch. 2

D.2 Full copyright notice for Ch. 5

References

Arakawa, A. and C.-M. Wu, 2013: A Unified Representation of Deep Moist Convection in Numerical Modeling of the Atmosphere. Part I. *J. Atmos. Sci.*, **70**, 1977–1992, doi:10.1175/JAS-D-12-0330.1.

Aris, R., 1962: *Vectors, Tensors, and the Basic Equations of Fluid Mechanics*. Prentice Hall.

Beare, R. J., 2014: A length scale defining partially-resolved boundary-layer turbulence simulations. *Boundary-layer meteorology*, **151**, 39–55.

Bryan, G. H., J. C. Wyngaard, and J. M. Fritsch, 2003: Resolution Requirements for the Simulation of Deep Moist Convection. *Mon. Wea. Rev.*, **131**, 2394–2416, doi:10.1175/1520-0493(2003)131¡2394:RRFTSO¿2.0.CO;2.

Carper, M. A. and F. Porté-Agel, 2004: The role of coherent structures in subfilter-scale dissipation of turbulence measured in the atmospheric surface layer. *Journal of Turbulence*, **5**, 32–32.

Ching, J., R. Rotunno, M. LeMone, A. Martilli, B. Kosovic, P. A. Jimenez, and J. Dudhia, 2014: Convectively Induced Secondary Circulations in Fine-Grid Mesoscale Numerical Weather Prediction Models. *Mon. Wea. Rev.*, **142**, 3284–3302, doi:10.1175/MWR-D-13-00318.1.

Chow, F. K., 2004: *Subfilter-scale turbulence modeling for large-eddy simulation of the atmospheric boundary layer over complex terrain*. Ph.D. thesis, Stanford University.

Chow, F. K., R. L. Street, M. Xue, and J. H. Ferziger, 2005: Explicit Filtering and Reconstruction Turbulence Modeling for Large-Eddy Simulation of Neutral Boundary Layer Flow. *J. Atmos. Sci.*, **62**, 2058–2077, doi:10.1175/JAS3456.1.

Chow, F. K., A. P. Weigel, R. L. Street, M. W. Rotach, and M. Xue, 2006: High-Resolution Large-Eddy Simulations of Flow in a Steep Alpine Valley. Part I: Methodology, Verification, and Sensitivity Experiments. *J. Appl. Meteor. Climatol.*, **45**, 63–86, doi:10.1175/JAM2322.1.

Clarke, R., A. Dyer, R. Brook, D. Reid, and A. Troup, 1971: The Wangara Experiment: Boundary layer data. *CSIRO Division of Meteorological Physics Technology*.

de Roode, S. R., P. G. Duynkerke, and H. J. J. Jonker, 2004: Large-Eddy Simulation: How Large is Large Enough? *J. Atmos. Sci.*, **61**, 403–421, doi:10.1175/1520-0469(2004)061¡0403:LSHLIL¿2.0.CO;2.

Deardorff, J. W., 1972: Numerical Investigation of Neutral and Unstable Planetary Boundary Layers. *J. Atmos. Sci.*, **29**, 91–115, doi:10.1175/1520-0469(1972)029¡0091:NIONAU¿2.0.CO;2.

— 1974: Three-dimensional numerical study of the height and mean structure of a heated planetary boundary layer. *Boundary-Layer Meteorol*, **7**, 81–106, doi:10.1007/BF00224974.

Efstathiou, G. A. and R. J. Beare, 2015: Quantifying and improving sub-grid diffusion in the boundary-layer grey zone. *Q.J.R. Meteorol. Soc.*, n/a–n/a, doi:10.1002/qj.2585.

Efstathiou, G. A., R. J. Beare, S. Osborne, and A. P. Lock, 2016: Grey zone simulations of the morning convective boundary layer development. *Journal of Geophysical Research: Atmospheres*, **121**, 4769–4782, doi:10.1002/2016JD024860.

Garcia, M., M. zdogan, and P. A. Townsend, 2014: Impacts of forest harvest on cold season land surface conditions and land-atmosphere interactions in northern Great Lakes states. *J. Adv. Model. Earth Syst.*, **6**, 923–937, doi:10.1002/2014MS000317.

Golaz, J.-C., S. Wang, J. D. Doyle, and J. M. Schmidt, 2005: Coamps-Les: Model Evaluation and Analysis of Second-and Third-Moment Vertical Velocity Budgets. *Boundary-Layer Meteorol*, **116**, 487–517, doi:10.1007/s10546-004-7300-5.

Gullbrand, J. and F. K. Chow, 2003: The effect of numerical errors and turbulence models in large-eddy simulations of channel flow, with and without explicit filtering. *Journal of Fluid Mechanics*, **495**, 323–341, doi:10.1017/S0022112003006268.

Honnert, R., V. Masson, and F. Couvreux, 2011: A Diagnostic for Evaluating the Representation of Turbulence in Atmospheric Models at the Kilometric Scale. *J. Atmos. Sci.*, **68**, 3112–3131, doi:10.1175/JAS-D-11-061.1.

Janjic, Z. I., 1977: Pressure gradient force and advection scheme used for forecasting with steep and small scale topography. *Beitr. Phys. Atmos.*, **50**, 186–189.

Kendon, E. J., N. M. Roberts, H. J. Fowler, M. J. Roberts, S. C. Chan, and C. A. Senior, 2014: Heavier summer downpours with climate change revealed by weather forecast resolution model. *Nature Clim. Change*, **4**, 570–576, doi:10.1038/nclimate2258.

Kendon, E. J., N. M. Roberts, C. A. Senior, and M. J. Roberts, 2012: Realism of Rainfall in a Very High-Resolution Regional Climate Model. *J. Climate*, **25**, 5791–5806, doi:10.1175/JCLI-D-11-00562.1.

Khani, S. and M. L. Waite, 2014: Buoyancy scale effects in large-eddy simulations of stratified turbulence. *Journal of Fluid Mechanics*, **754**, 7597, doi:10.1017/jfm.2014.381.

— 2015: Large eddy simulations of stratified turbulence: the dynamic Smagorinsky model. *Journal of Fluid Mechanics*, **773**, 327344, doi:10.1017/jfm.2015.249.

Kirkil, G., J. Mirocha, E. Bou-Zeid, F. K. Chow, and B. Kosovi, 2012: Implementation and Evaluation of Dynamic Subfilter-Scale Stress Models for Large-Eddy Simulation Using WRF. *Mon. Wea. Rev.*, **140**, 266–284, doi:10.1175/MWR-D-11-00037.1.

Klemp, J., W. Skamarock, and O. Fuhrer, 2003: Numerical consistency of metric terms in terrain-following coordinates. *Mon. Wea. Rev.*, **131**, 1229–1239.

Klose, M. and Y. Shao, 2013: Large-eddy simulation of turbulent dust emission. *Aeolian Research*, **8**, 49–58, doi:10.1016/j.aeolia.2012.10.010.

Kurowski, M. J. and J. Teixeira, 2018: A Scale-Adaptive Turbulent Kinetic Energy Closure for the Dry Convective Boundary Layer. *Journal of the Atmospheric Sciences*, **75**, 675–690, doi:10.1175/JAS-D-16-0296.1.

Langhans, W., J. Schmidli, and B. Szintai, 2012: A Smagorinsky-Lilly turbulence closure for COSMO-LES: Implementation and comparison to ARPS. *COSMO newsletter*, **12**, 20–31.

Lean, H. W., P. A. Clark, M. Dixon, N. M. Roberts, A. Fitch, R. Forbes, and C. Halliwell, 2008: Characteristics of High-Resolution Versions of the Met Office Unified Model for Forecasting Convection over the United Kingdom. *Mon. Wea. Rev.*, **136**, 3408–3424, doi:10.1175/2008MWR2332.1.

Leuenberger, D., J. Bettems, and A. Rossa, 2005: Next generation NWP at Meteoswiss and potential contributions of weather radars. *WWRP Symposium on Nowcasting and Very Short Range Forecasting, Toulouse, France*, 5–9.

Lilly, D. K., 1962: On the numerical simulation of buoyant convection. *Tellus*, **14**, 148–172, doi:10.1111/j.2153-3490.1962.tb00128.x.

— 1967: The representation of small-scale turbulence in numerical simulation experiments, paper presented at IBM Scientific Computing Symposium on Environmental Sciences, IBM Data Process. *Div., White Plains, NY*.

Liu, G., J. Sun, and L. Yin, 2011: Turbulence Characteristics of the Shear-Free Convective Boundary Layer Driven by Heterogeneous Surface Heating. *Boundary-Layer Meteorol*, **140**, 57–71, doi:10.1007/s10546-011-9591-7.

Lundquist, K. A., 2010: *Immersed boundary methods for high-resolution simulations of atmospheric boundary-layer flow over complex terrain*. Ph.D. thesis, University of California, Berkeley.

Lundquist, K. A., F. K. Chow, and J. K. Lundquist, 2010a: An immersed boundary method for the Weather Research and Forecasting model. *Mon. Wea. Rev.*, **138 (3)**, 796–817.

— 2010b: Numerical errors in flow over steep topography: analysis and alternatives. *14th Conference on Mountain Meteorology*, American Meteorological Society.

— 2012: An immersed boundary method enabling large-eddy simulations of flow over complex terrain in the WRF-model. *Mon. Wea. Rev.*, in press.

Michioka, T. and F. K. Chow, 2008: High-Resolution Large-Eddy Simulations of Scalar Transport in Atmospheric Boundary Layer Flow over Complex Terrain. *J. Appl. Meteor. Climatol.*, **47**, 3150–3169, doi:10.1175/2008JAMC1941.1.

Mirocha, J. D., J. K. Lundquist, and B. Kosovi, 2010: Implementation of a Nonlinear Subfilter Turbulence Stress Model for Large-Eddy Simulation in the Advanced Research WRF Model. *Mon. Wea. Rev.*, **138**, 4212–4228, doi:10.1175/2010MWR3286.1.

Mirocha, J. D. and K. A. Lundquist, 2017: Assessment of Vertical Mesh Refinement in Concurrently Nested Large-Eddy Simulations Using the Weather Research and Forecasting Model. *Mon. Wea. Rev.*, **145**, 3025–3048, doi:10.1175/MWR-D-16-0347.1.

Moeng, C.-H., P. P. Sullivan, M. F. Khairoutdinov, and D. A. Randall, 2010: A Mixed Scheme for Subgrid-Scale Fluxes in Cloud-Resolving Models. *J. Atmos. Sci.*, **67**, 3692–3705, doi:10.1175/2010JAS3565.1.

Mohd-Yusof, J., 1997: Combined immersed boundary/b-spline methods for simulations of flow in complex geometry. Center for Turbulence Research, Annual Research Briefs, NASA Ames/Stanford University, 317–327.

Pielke, R. A., W. R. Cotton, R. L. Walko, C. J. Tremback, W. A. Lyons, L. D. Grasso, M. E. Nicholls, M. D. Moran, D. A. Wesley, T. J. Lee, and J. H. Copeland, 1992: A comprehensive meteorological modeling systemRAMS. *Meteorl. Atmos. Phys.*, **49**, 69–91, doi:10.1007/BF01025401.

Piotrowski, Z. P., P. K. Smolarkiewicz, S. P. Malinowski, and A. A. Wyszogrodzki, 2009: On numerical realizability of thermal convection. *Journal of Computational Physics*, **228**, 6268–6290, doi:10.1016/j.jcp.2009.05.023.

Pope, S. B., 2004: Ten questions concerning the large-eddy simulation of turbulent flows. *New Journal of Physics*, **6**, 35.

Port-Agel, F., M. B. Parlange, C. Meneveau, and W. E. Eichinger, 2001: A Priori Field Study of the Subgrid-Scale Heat Fluxes and Dissipation in the Atmospheric Surface Layer. *Journal of the Atmospheric Sciences*, **58**, 2673–2698, doi:10.1175/1520-0469(2001)058¡2673:APFSOT¿2.0.CO;2.

Pressel, K. G., C. M. Kaul, T. Schneider, Z. Tan, and S. Mishra, 2015: Large-eddy simulation in an anelastic framework with closed water and entropy balances. *Journal of Advances in Modeling Earth Systems*, **7**, 1425–1456, doi:10.1002/2015MS000496.

Prusa, J. M., P. K. Smolarkiewicz, and A. A. Wyszogrodzki, 2008: EULAG, a computational model for multiscale flows. *Computers & Fluids*, **37**, 1193–1207, doi:10.1016/j.compfluid.2007.12.001.

Romps, D. M., 2008: The Dry-Entropy Budget of a Moist Atmosphere. *Journal of the Atmospheric Sciences*, **65**, 3779–3799, doi:10.1175/2008JAS2679.1.

Schaefer-Rolffs, U., 2017: A generalized formulation of the dynamic Smagorinsky model. *Meteorologische Zeitschrift*, **26**, 181–187, doi:10.1127/metz/2016/0801.

Serrin, J., 1959: The Derivation of Stress-Deformation Relations for a Stokesian Fluid. *Journal of Mathematics and Mechanics*, **8**, 459–469.

Shi, X., F. K. Chow, R. L. Street, and G. H. Bryan, 2019: Key Elements of Turbulence Closures for Simulating Deep Convection at Kilometer-Scale Resolution. *Journal of Advances in Modeling Earth Systems*, **0**, doi:10.1029/2018MS001446.

Shi, X., H. L. Hagen, F. K. Chow, G. H. Bryan, and R. L. Street, 2018: Large-Eddy Simulation of the Stratocumulus-Capped Boundary Layer with Explicit Filtering and Reconstruction Turbulence Modeling. *Journal of the Atmospheric Sciences*, **75**, 611–637, doi:10.1175/JAS-D-17-0162.1.

Simon, J. S., K. A. Lundquist, and F. K. Chow, 2012: Application of the Immersed Boundary Method to Simulations of Flow Over Steep, Mountainous Terrain. *15th Conf. on Mountain Meteorology*, 45.

Simon, J. S., B. Zhou, J. D. Mirocha, and F. K. Chow, 2019: Explicit Filtering and Reconstruction to Reduce Grid Dependence in Convective Boundary Layer Simulations Using WRF-LES. *Monthly Weather Review*, **147**, 1805–1821, doi:10.1175/MWR-D-18-0205.1.

Skamarock, W., J. Klemp, J. Dudhia, D. Gill, D. Barker, M. Duda, X.-Y. Huang, W. Wang, and J. Powers, 2008: A Description of the Advanced Research WRF Version 3. *NCAR Technical Note, NCAR/TN-475+STR*.

Skamarock, W. C., 2004: Evaluating Mesoscale NWP Models Using Kinetic Energy Spectra. *Mon. Wea. Rev.*, **132**, 3019–3032, doi:10.1175/MWR2830.1.

Smagorinsky, J., 1958: On the numerical integration of the primitive equations of motion for baroclinic flow in a closed region. *Monthly Weather Review*, **86**, 457–466.

— 1963: General circulation experiments with the primitive equations. *Mon. Wea. Rev.*, **91**, 99–164, doi:10.1175/1520-0493(1963)091¡0099:GCEWTP¿2.3.CO;2.

Stokes, G. G., 1845: On the theories of the internal friction of fluids in motion, and of the equilibrium and motion of elastic solids. *Transactions of the Cambridge Philosophical Society*, **8**, 287–305.

Stull, R., 1988a: *An Introduction to Boundary Layer Meteorology*. Kluwer Academic Publishers.

— 1988b: *An Introduction to Boundary Layer Meteorology*. Kluwer Academic Publishers, 441 – 443 pp.

Taylor, D. M., F. K. Chow, M. Delkash, and P. T. Imhoff, 2016: Numerical simulations to assess the tracer dilution method for measurement of landfill methane emissions. *Waste Manag*, **56**, 298–309, doi:10.1016/j.wasman.2016.06.040.

Thuburn, J., H. Weller, G. K. Vallis, R. J. Beare, and M. Whitall, 2018: A Framework for Convection and Boundary Layer Parameterization Derived from Conditional Filtering. *Journal of the Atmospheric Sciences*, **75**, 965–981, doi:10.1175/JAS-D-17-0130.1.

Truesdell, C., 1952: The Mechanical Foundations of Elasticity and Fluid Dynamics. *Journal of Rational Mechanics and Analysis*, **1**, 125–300.

— 1954: *The Kinematics of Vorticity*. Indiana University Press.

Truesdell, C. and R. Toupin, 1960: *The Classical Field Theories*, Springer Berlin Heidelberg, Berlin, Heidelberg. 226–858.

van Stratum, B. J. and B. Stevens, 2015: The influence of misrepresenting the nocturnal boundary layer on idealized daytime convection in large-eddy simulation. *Journal of Advances in Modeling Earth Systems*.

Wajsowicz, R. C., 1993: A Consistent Formulation of the Anisotropic Stress Tensor for Use in Models of the Large-Scale Ocean Circulation. *Journal of Computational Physics*, **105**, 333 – 338, doi:https://doi.org/10.1006/jcph.1993.1079.

Wang, H., W. C. Skamarock, and G. Feingold, 2009: Evaluation of Scalar Advection Schemes in the Advanced Research WRF Model Using Large-Eddy Simulations of AerosolCloud Interactions. *Mon. Wea. Rev.*, **137**, 2547–2558, doi:10.1175/2009MWR2820.1.

Wong, V. C. and D. K. Lilly, 1994: A comparison of two dynamic subgrid closure methods for turbulent thermal convection. *Physics of Fluids (1994-present)*, **6**, 1016–1023, doi:10.1063/1.868335.

Wyngaard, J. C., 2004: Toward Numerical Modeling in the Terra Incognita. *J. Atmos. Sci.*, **61**, 1816–1826, doi:10.1175/1520-0469(2004)061¡1816:TNMITT¿2.0.CO;2.

Xue, M., K. K. Droegemeier, and V. Wong, 2000: The Advanced Regional Prediction System (ARPS) A multi-scale nonhydrostatic atmospheric simulation and prediction model. Part I: Model dynamics and verification. *Meteorol Atmos Phys*, **75**, 161–193, doi:10.1007/s007030070003.

Zang, Y., R. L. Street, and J. R. Koseff, 1993: A dynamic mixed subgridscale model and its application to turbulent recirculating flows. *Physics of Fluids A: Fluid Dynamics*, **5**, 3186–3196, doi:10.1063/1.858675.

Zhou, B. and F. K. Chow, 2011: Large-Eddy Simulation of the Stable Boundary Layer with Explicit Filtering and Reconstruction Turbulence Modeling. *J. Atmos. Sci.*, **68**, 2142–2155, doi:10.1175/2011JAS3693.1.

— 2012: Turbulence Modeling for the Stable Atmospheric Boundary Layer and Implications for Wind Energy. *Flow Turbulence Combust*, **88**, 255–277, doi:10.1007/s10494-011-9359-7.

— 2014: Nested Large-Eddy Simulations of the Intermittently Turbulent Stable Atmospheric Boundary Layer over Real Terrain. *Journal of the Atmospheric Sciences*, **71**, 1021–1039, doi:10.1175/JAS-D-13-0168.1.

Zhou, B., J. S. Simon, and F. K. Chow, 2014: The Convective Boundary Layer in the Terra Incognita. *J. Atmos. Sci.*, **71**, 2545–2563, doi:10.1175/JAS-D-13-0356.1.

Zhou, B., M. Xue, and K. Zhu, 2017: A Grid-Refinement-Based Approach for Modeling the Convective Boundary Layer in the Gray Zone: A Pilot Study. *Journal of the Atmospheric Sciences*, **74**, 3497–3513, doi:10.1175/JAS-D-16-0376.1.

— 2018: A Grid-Refinement-Based Approach for Modeling the Convective Boundary Layer in the Gray Zone: Algorithm Implementation and Testing. *Journal of the Atmospheric Sciences*, **75**, 1143–1161, doi:10.1175/JAS-D-17-0346.1.

Zhu, P., B. A. Albrecht, V. P. Ghate, and Z. Zhu, 2010: Multiple-scale simulations of stratocumulus clouds. *J. Geophys. Res.*, **115**, D23201, doi:10.1029/2010JD014400.